Doctoral Dissertation
Doctoral Program in Aerospace Engineering (32nd Cycle)

Turbocharger Design Optimization by Adjoint Method Coupled with CHT Analysis

Alberto Racca
* * * * * *

Supervisors
Prof. T. Verstraete, Supervisor (von Karman Institute for Fluid Dynamics)
Prof. L. Casalino, Supervisor (Politecnico di Torino)

Doctoral Examination Committee:
Prof. A. Arnone, Università degli Studi di Firenze
Prof. R.F. Martinez-Botas, Imperial College London
Prof. K. Giannakoglou, National Technical University of Athens
Prof. F. Millo, Politecnico di Torino
Prof. M. Gherlone, Politecnico di Torino

Politecnico di Torino
September 30th, 2021

I hereby declare that, the contents and organisation of this dissertation constitute my own original work and does not compromise in any way the rights of third parties, including those relating to the security of personal data.

…….....

Alberto Racca

Turin, September 30th, 2021

Summary

The thesis deals with the problem of the multidisciplinary design optimization of thermally stressed turbomachinery components, with focus on a turbocharger radial turbine impeller for automotive applications.

Thermal analyses are usually excluded from standard optimization frameworks because of their high computational cost. Therefore, significant engineering margins are applied to the design process, in order to avoid any unexpected failure related to thermal events appearing during the component validation phase. The shortcoming about this practice is related to the highly constrained problem the optimizer is requested to deal with, resulting in reduced opportunities of identifying the truly optimal solution. Hence, the work herein is devoted to the introduction of the thermal analysis within the scope of the optimization of complex geometries, by the development of a computationally affordable framework based on the discrete adjoint method.

The first part of the manuscript addresses the problem of the thermo-mechanical stresses that develop in the turbomachinery components operating in steady state conditions. The thermal Fluid-Structure Interaction phenomenon is numerically described by the Conjugate Heat Transfer (CHT) method. In particular, a partitioned coupling technique is adopted to separately solve the fluid and the solid domains with dedicated meshes and specialized solvers. The conjugate coupling is based on the heat transfer Forward Flux Back (hFFB) method, which offers stability properties particularly suited to the turbine impeller problem investigated in the present work.

The interaction between the fluid and the solid domains is established by the development of an interface, aimed at allowing the exchange of information between a multiblock structured mesh and an unstructured grid of second order tetrahedral elements. A distance-weighted interpolation technique is adopted

herein because of its robustness in treating meshes of any complexity, as well as cases of locally overlapping grids. The original procedure is revised by multiple improvements addressing the accuracy and the memory footprint of the method.

A heat transfer model based on a FEM linear solver is developed for the evaluation of the energy balance within the solid. Concerning the fluid side, the in-house CFD solver available in CADO is integrated in the present framework. The solid temperature field returned by the iterative hFFB process is transferred to a FEM linear mechanical solver in order to compute the thermal strains in the material, contributing to the prediction of the thermo-mechanical stresses. The latter represent the cost function of the problem, which is seeded for its introduction in an adjoint workflow aimed at computing the sensitivities of the maximum von Mises stress w.r.t. the fluid and the solid grid points coordinates.

The adjoint framework is developed by the manual differentiation of the primal workflow in reverse mode through an Algorithmic Differentiation approach, with the goal of optimizing its memory footprint. In this respect, the perturbations to the state variables are propagated throughout the workflow by walking the primal development in opposite direction, till the original location of the grids generation routines. During the evolution in reverse mode, the relevant adjoint variables are exchanged at the interface of the two domains and the grid sensitivities are accumulated at any call to the fluid and the solid solvers. Finally, those gradients, once multiplied by the sensitivities of the grid coordinates w.r.t. the CAD parameters, are transferred to a Sequential Quadratic Programming algorithm.

The framework is successfully applied to a turbine rotor test case previously optimized under the assumption of adiabatic walls. Hence, it is demonstrated that the thermal evaluations are a necessary means to improve the structural robustness during the design optimization of such components.

The second part of the thesis expands the outreach of the thermal analysis to unsteady conjugate problems with the aim of optimizing the Thermo-Mechanical Fatigue (TMF) lifetime of components experiencing cyclic operations. The transient phenomenon is numerically described by a quasi-dynamic approach leading to the decomposition of a transient manoeuver in separate stretches, each one analyzed by an iterative hFFB approach. The loose coupling framework developed for steady state problems is revised for the scope of the analysis of transient operations by introducing an unsteady FEM non-linear heat transfer solver interfacing with the in-house steady state CFD solver. The mutual exchange of information between the two domains is iterated at each stretch of the

manoeuver till the achievement of convergence of the conjugate coupling. The resulting transient temperature field is transferred to an unsteady FEM linear mechanical solver for the evaluation of the solid thermo-mechanical response along the manoeuver. A set of constitutive equations is included in the prediction of the unsteady displacements field in order to capture any accumulation of local plasticity, under the assumption of the operations in the small-strains region. The evolution of the strains and the stresses in the solid is finally conveyed to the Morrow model, a strain-life method aimed at computing the fatigue lifetime under cyclic conditions.

The durability of the component represents the new cost function, which is seeded to kick off the adjoint workflow. Consistently with the development in steady state conditions, the primal workflow is manually differentiated by a reverse Algorithmic Differentiation technique and the adjoint variables are propagated in opposite direction.

The novel framework is evaluated in the case of a radial turbine impeller experiencing different transient manoeuvers, and proves its effectiveness in capturing the impact of the thermal non-equilibrium during the unsteady computations, thus leading to the development of thermal strains and thermal stresses not present in steady state operations. Finally, the adjoint framework returns the sensitivities of the component lifetime, providing the directions for the perturbations of the grid coordinates necessary to enhance the impeller TMF fatigue resistance.

Acknowledgment

I would like to sincerely thank my supervisor at the von Karman Institute for Fluid Dynamics, Prof. Tom Verstraete, for his invaluable guidance throughout the development of this work. He is one of those people I consider true mentors in my scientific career, who inspired me to embrace a lifelong continuous improvement attitude. His rigorous method and attention to the details grew in me a constructive self-critical approach and the motivation to constantly set the bar higher.

I also express my gratitude to Prof. Tony Arts for having welcomed me in the Turbomachinery and Propulsion Department at VKI in the first place, and to the whole personnel in the Department. In particular, I am in great debt to Dr. Lasse Müller, Ing. Johan Prinsier and Dr. Zuheyr Alsalihi for having walked me through the fine art of turbomachinery design optimization in the early days and for their support during my stay at the Institute.

I wish to acknowledge Politecnico di Torino for having accepted my candidature to the Industrial Ph.D. Program, and in particular my co-supervisor Prof. Lorenzo Casalino, for having welcomed me in the Mechanical and Aerospace Engineering Department. His assistance throughout the several milestones of the academic life and his suggestions during the writing of this manuscript have been fundamental in pursuing this result.

I would like to acknowledge General Motors LLC and PUNCH Torino S.p.A. for the financial support to this Industrial Ph.D. Program and for the permission to publish the material presented in this thesis. Without their trust, this project would not have been possible.

Finally, I wish to thank my family for their relentless encouragements, and for having taught me to keep dreaming and believe the limit to what we can do is the one we set ourselves.

Contents

List of Tables

List of Figures

Chapter 1

Introduction

1.1 Background

The mobility and energy sectors are currently experiencing a profound transformation in response to the common goal of developing a sustainable economy reducing the footprint on the global resources [1]. The aviation industry committed to halve their CO_2 emissions worldwide by 2050 compared to what they were in 2005 [2], while the automotive business declared the mission of hitting net-zero carbon connectivity even earlier. The transition towards these high-end goals requires industry to accelerate the development of new technologies contributing to the climate action mission. However, it is recognized there are different speeds to the decarbonization. In fact, before radical new concepts are developed and brought to readiness to the market, a collaborative effort to a sustainable transition could be played by the evolutionary development path of readily available technologies, which is expected to continue and to contribute to a further 20% improvement in fuel efficiency in the aviation business [3]. A similar advancement is seen in the automotive sector in the pursuit of releasing new lean combustion solutions [4]. In addition to that, new propulsion systems based on synthetic sustainable fuels [5] and hydrogen-powered architectures are under investigation. Hence, while technology improvements are prioritized, a common goal in all the sectors is to maintain a trend of sensible efficiency increase.

A broad scope of different subsystems contributes to the fuel efficiency, but a leap forward in the thermal and propulsive efficiency for the turbomachinery-related technologies is still expected. In such respect, this class of products already exhibits a high level of maturity. For instance, the aerospace business has already achieved about 85% efficiency improvement w.r.t. the jet products released in the 50's [3]. A similar evolutionary trend has also characterized the automotive sector. Hence, the possibility of achieving any further advancement in

the turbomachinery area would reside in a comprehensive review of the design processes, among other means.

Nowadays, the development cycle of turbomachinery components takes advantage of the extensive use of multidisciplinary design optimization techniques [6, 7]. Such methods support the experts in the identification of the most suitable product shape within large design hyperspaces, offering exploration capabilities beyond the human intuition, while fulfilling a diversified set of project targets and requirements [8 – 10]. The increasing complexity in geometries and in flow conditions, along with the need of balancing the machine performance in design and off-design conditions, and of satisfying competing requirements of cost and durability, boosted the development of concurrent design techniques [11, 12]. Their function is to provide a comprehensive view on the problem through the synergic analysis of multiple disciplines, thus capturing their mutual interactions and the impact on the shape under consideration [13, 14]. In fact, a holistic description of the physical phenomena involved in the operations of the product favors the exploration of its design space, thanks to the higher accuracy in the prediction of performance and constraints.

Such approach to the design operations differs from traditional staggered techniques accounting for mono-discipline optimizations performed in cascade. In essence, these simplified computational methods mimic the design procedures widely applied till the twentieth century, in which new designs were generated from the experience gained from previous samples, with an expensive trial-and-error approach relying on iterative prototyping and testing sessions. Similarly, staggered optimization techniques are capable of satisfying a single objective or constraint per time and, therefore, typically lead to longer development cycles to achieve a satisfactory solution. Moreover, the missing interactions among the different disciplines requires the adoption of larger safety margins and may not guarantee the identification of the same solution as the holistic approach, thus leading to suboptimal shapes.

Although the established multidisciplinary optimization methods proved their effectiveness in industrial problems, the new market request for severe reductions in fuel consumption and emissions addresses new challenges to the research community and the need for further advancements in these techniques. The NASA vision for 2040 [15] is expressed in a roadmap of integrated multiscale modelling techniques, and considers the multidisciplinary optimization methods as one of nine core areas of development for the efficient design, manufacturing and certification of future aerospace systems. Similarly, the automotive business requires continuous improvements in efficiency and performance for their turbocharger solutions in order to fulfill the requests of the novel combustion strategies [16, 17].

In order to address these needs, on one side performance enhancements in turbomachinery components are searched for by increasing the details in the geometrical description of the domains and, therefore, through the adoption of a

richer set of design variables during their optimization [18]. In fact, the finer resolution achieved in the discretization of the components allows the exploration of more complex shapes, disclosing hidden interactions among features now present in the design space, hopefully more favorable to performance and constraints aspects.

On the other hand, an improved accuracy in the physical description of the multidisciplinary problem is highly regarded and the aim is twofold. First, the optimizer deals with lumped information concerning the evolution of the response function that is more reliable, as resulting from computations involving a more comprehensive set of physical disciplines and their related interactions. Thus, the optimization benefits from adhering more to the real behavior of the component, and the related output shape requires less validation testing, for the sake of a reduced cost and roll-out time to market. Second, a sophisticated physical description of the multidisciplinary problem allows the introduction of more specific constraints and the relaxation of the safety margins, thus favoring performance-oriented design choices. The optimizer, now enabled by a detailed interpretation of the behavior of the component, may target new exploration paths towards the optimal solution, showing a reduced stiffness in performing the shape modifications.

While such means could support the achievement of the abovementioned advancements in the turbomachinery technology, the benefits herein listed come at the price of more computationally intensive evaluations. Therefore, a feasibility assessment for the adoption of a suitable optimization strategy has to be considered with respect to the two major classes, denoted as Gradient-Free and Gradient-Based optimization methods.

1.2 Optimization methods

1.2.1 Multi-objective optimizations

Optimization problems in the turbomachinery business are typically multi-objective and multi-disciplinary by nature. The reason for the multi-objective description resides in the request of fulfilling competing targets (for instance, performance and durability) at the same time by a unique shape. This condition is formulated by Eq. (1.1):

$$\begin{array}{ccc} \text{Minimize} & f_i(\vec{\boldsymbol{x}}) & i \in (1,m) \\ \text{while satisfying} & C_j(\vec{\boldsymbol{x}}) \leq 0 & j \in (1,n) \\ with & x_{k\_min} \leq x_k \leq x_{k\_max} & k \in (1,p) \end{array} \tag{1.1}$$

in which f_i represents the *i-th* objective function, C_j is the *j-th* equality or inequality constraint, and $x_k \in \vec{\boldsymbol{x}}$ is the *k-th* design variable whose range of variation is limited by a minimum and a maximum value. A design improvement is attainable through the minimization of the set of objective functions, while its feasibility is guaranteed by the simultaneous fulfillment of all the constraints.

Since the objectives may be conflicting, it is unlikely a single design could satisfy the entire problem. Instead, a so-called Pareto front [19] can be described with the scattering of non-dominated solutions, from which a sample can be selected by trade-off among the obtained cost functions. Figure 1.1 shows an example with only two objectives reported on the axes: it is understood an improvement in f_1 corresponds to a deterioration in f_2.

According to [20], an established method for the selection of the best candidate in an optimization is by the reduction of the multi-objective problem into a single-objective formulation, as reported in Eq. (1.2):

$$Minimize: \qquad F(\vec{x}) = \omega \cdot f_1 + (1 - \omega) \cdot f_2 \tag{1.2}$$

with $\omega \in (0,1)$ as weighting parameter between the two objectives f_i.

The compounded function $F(\vec{x})$ appears in Figure 1.1 as a set of lines whose inclination is determined by the weighting parameter. Therefore, the location of the best solution is uniquely identified by the intersection between the line returning the lowest value of the function F and the Pareto front itself.

The formulation reported in Eq. (1.2) can be generalized to any number of objective functions f_i, each one associated to a corresponding weight ω_i, whose sum equals unity.

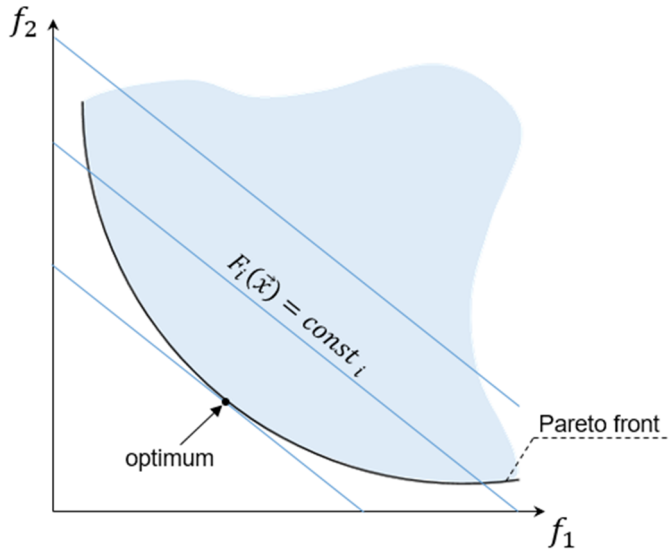

Figure 1.1 Exemplary Pareto front for optimization problem with two objective functions.

For more details, the reader interested in optimal control theory is addressed to [21 – 24].

1.2.2 Multidisciplinary optimizations

The multidisciplinary footprint of the optimization problems in the turbomachinery space is defined by the mutual interactions between the fluid and the solid domains. In fact, while a pure aerodynamic shape optimization focuses on fluid aspects only, the geometrical impact on the structural mechanics of the component cannot be overlooked to generate a sound design fulfilling the set of constraints. Ultimately, a Fluid Structure Interaction (FSI) problem is instantiated [25, 26], and a suitable computational framework addressing CFD and FEM analyses has to be identified in order to support the numerical formulation of the problem.

In general, the computational effort associated to the solution of a multidisciplinary problem can be expressed in relation to the selected coupling strategy. These techniques are grouped in three major families:

1. *Fully decoupled approach*: The multidisciplinary problem is split in multiple single-discipline sub-problems, each one addressing the solution of the corresponding physical domain through a specialized solver [27]. This class of methods is by far the less demanding from computational perspectives, because each discipline is treated separately from the others and contributes to the compounded function $F(\vec{x})$ with its own objective function f_i. Such approach may be deemed correct in case of unrelated physical aspects (e.g. the computation of the fluid dynamic performance of a blade and the numerical evaluation of its first natural frequency), while it would represent a simplification of the reality in all the other cases.
2. *Loose coupling approach*: The multidisciplinary problem exhibits a series of disciplines exchanging information at their domains interface, whose combined solution results in the evaluation of the objective function f_i. This class of methods is suitable for the solution of FSI problems, among others. In its simplest form, a relation is expressed by a "one-way coupling" between two solvers, the first one passing some information to the second one, but not the other way around [28]. An example is represented by a thermo-mechanical problem, in which the heat transfer solver calculates the thermal field within the domain and passes the temperature information to the structural solver for the calculation of the thermal strains. No information is returned to the heat transfer solver (for instance, the thermal deformation of the structure is supposed to yield a negligible impact on the heat transfer solution), and the exchange of physical variables is performed only once. A more complex framework is instead represented by the "two-way coupling" technique, in which the solvers are iteratively engaged in multiple loops and physical quantities are mutually exchanged till achieving their continuity at the boundaries [29]. Such method reveals a trade-off between the computational effort in performing the iterative process till convergence, and the possibility of adopting specialized meshers and solvers for each domain, resulting in a higher robustness of the solution process for the numerical problem.

Moreover, this approach is convenient in the case of physical phenomena presenting very different time scales, as explained in Chapter 4.

3. *Tight coupling approach*: The problem is treated by a single multi-physics solver dealing with the different media through a unique large system of equations, and the whole domain is discretized by a single meshing strategy (either structured or unstructured) [30]. This method implicitly exchanges boundary conditions between the involved domains (e.g. fluid and solid), and directly solves the global system of equations avoiding any iterative cross-discipline workflow, unlike the loose coupling case. The advantage resulting from the shorter computational time has to be evaluated w.r.t. the more involved development of the solver and the robustness of the selected meshing strategy when dealing with domains of complex shape. Moreover, this method is less suited for FSI problems involving phenomena with very different time scales.

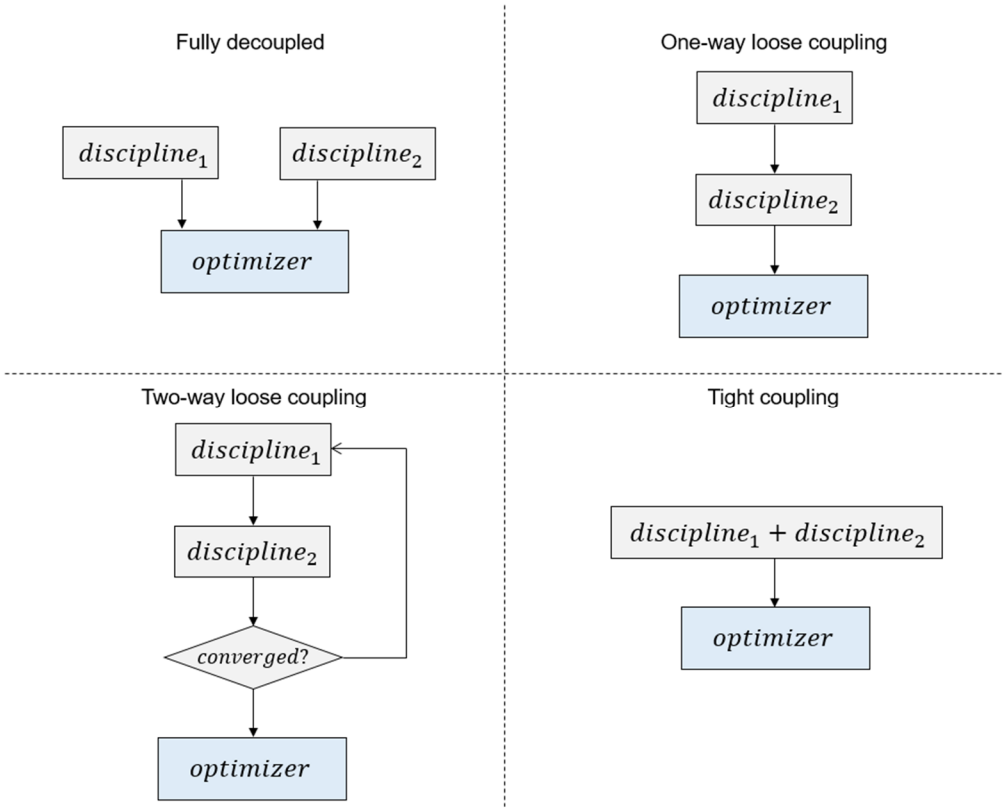

Figure 1.2 Workflows for numerical solution of multi-disciplinary problems.

The finalization of the multi-objective and multi-disciplinary aspects of the design problem would eventually lead to the selection of a suitable optimization technique between two classes, known as Gradient-free and Gradient-based methods. The following sections provide a concise description of such two families, as complementary information to the remaining portion of the chapter.

1.2.3 Gradient-free optimization methods

Gradient-free optimization methods, also known as "zero-order" methods from the order of the derivatives of their cost functions, represent a wide class of techniques for the solution of optimization problems, as described in Eq. (1.1) and Eq. (1.2). The commonality among the different algorithms existing in literature resides in the evaluation of the objective function $F(\vec{x})$ through the screening of a large population of samples, each one represented by a vector $\vec{x}$ of design variables.

The simplest method is the "random search" [31], which proposes the evaluation of individuals with characteristics that are randomly distributed within the ranges of the selected design space. The higher the complexity of the optimization problem, the larger the population of candidates to be analyzed in order to identify a sample that simultaneously satisfies all the constraints, while minimizing the objective function. Therefore, this method may be inefficient in case of computationally expensive FVM or FEM simulations invoked for the characterization of each candidate, because of the prohibitive number of solutions necessary to identify the optimal sample.

Such technique opposes to other methods, like the random walk [32], the simulated annealing [33] or the Particle Swarm Optimization [34], which present an evolution of individuals based on the promotion of the most fitting samples. At each iteration, the new design replaces the previous one if it is considered to be a better solution in terms of objective function and feasibility w.r.t. the constraints. The algorithm benefits from this selection in the search for the optimal candidate, leading to a faster convergence. Additionally, the simulated annealing and the Particle Swarm algorithms introduce some randomness in the selection process, with the aim of preserving the diversity in the population and therefore the possibility of escaping local optima to seek a better solution.

Of particular interest are the optimization methods in the class of the Evolutionary Algorithms [35, 36], because of their wide acceptance in turbomachinery design problems. Such techniques mimic the Darwinian theory of natural evolution and, in this respect, evaluate the fitness of each candidate w.r.t. the optimization objectives and constraints, in order to promote the best samples to the creation of the next generation of individuals. This process involves a crossover of the characters of pairs of candidates, called "parents" and represented by binary vectors $\vec{x}$, and returns new vectors, called "offspring", exhibiting different binary combinations. The selection process of the parents is based on mechanisms aimed at identifying the pair of fittest samples at each iteration, till having exhausted all the individuals in the population. Despite the elitism in the process of mating two candidates for the generation of new samples, the possibility of coupling a promising individual with another one showing a low fitness value is maintained, with the goal of preserving the diversity in the generation of the new population. This aspect is also enforced by some mutation mechanisms, introducing a random alteration of a character in the binary vectors of the offspring at the completion of the crossover. Finally, during the transition

from a generation to the following one, the fittest candidate from the previous iteration is recovered if it overcomes the performance of the best offspring. This entire framework allows the population to progress in the direction of improvement, maintaining a historic knowledge of the evolution process and guaranteeing the possibility of escaping the local optima in favor of a wide screening of the design space.

Although the Evolutionary Algorithms proved their robustness in industrially relevant optimizations, it is recognized that thousands of generations are necessary in order to identify the global optimum. Since in turbomachinery problems the fitness of each individual has to be characterized through FVM and FEM analyses, the simple execution of the method would bring a considerable (or even unacceptable) computational budget. Therefore, low fidelity models, also called "surrogate models", have been combined with the accurate three-dimensional analyses in the wider framework of the Metamodel Assisted Evolutionary Algorithms [37]. An exemplary workflow is reported in Figure 1.3, from the in-house multidisciplinary design optimization platform "CADO" developed at the von Karman Institute for Fluid Dynamics [38].

Such low fidelity models, for instance represented by heuristics like Artificial Neural Networks [39] or Kriging [40, 41], are non-physical approximations of the design hyperspace performed through the information of the previously analyzed samples. Their intrinsic advantage is in the fast execution of the evaluation of the fitness of the individuals, which allows considering them as a convenient means for the screening of a large population [42]. However, the lower computational involvement is contrasted by a reduced accuracy in the estimation of a candidate's performance w.r.t. the high fidelity simulations. Therefore, some compensation techniques, like the "offline training", are introduced. With reference to the workflow in Figure 1.3, the Evolutionary Algorithm invokes the metamodel for the investigation of the fitness of the population during its evolution. After evaluating a predetermined number of generations, only the best candidate identified by the metamodel is analyzed through the three-dimensional solvers. Therefore, the resulting accurate information is added to the database, comprising only the candidates evaluated by the high-fidelity simulations. Hence, a new loop of the evolutionary process starts.

During the execution of this workflow, the error between the fitness estimated by the metamodel and the high-fidelity results is tracked. Such difference may be large at the first iterations, but tends to progressively decrease in the following loops. In fact, the information continuously added to the database favors more accurate interpolations of the design space by the surrogate model: this process is called "adaptivity".

In conclusion, the Metamodel Assisted Evolutionary Algorithm enables a vast exploration of the design space through thousands of generations, while only few tens or hundreds of individuals are processed by the expensive three-dimensional simulations.

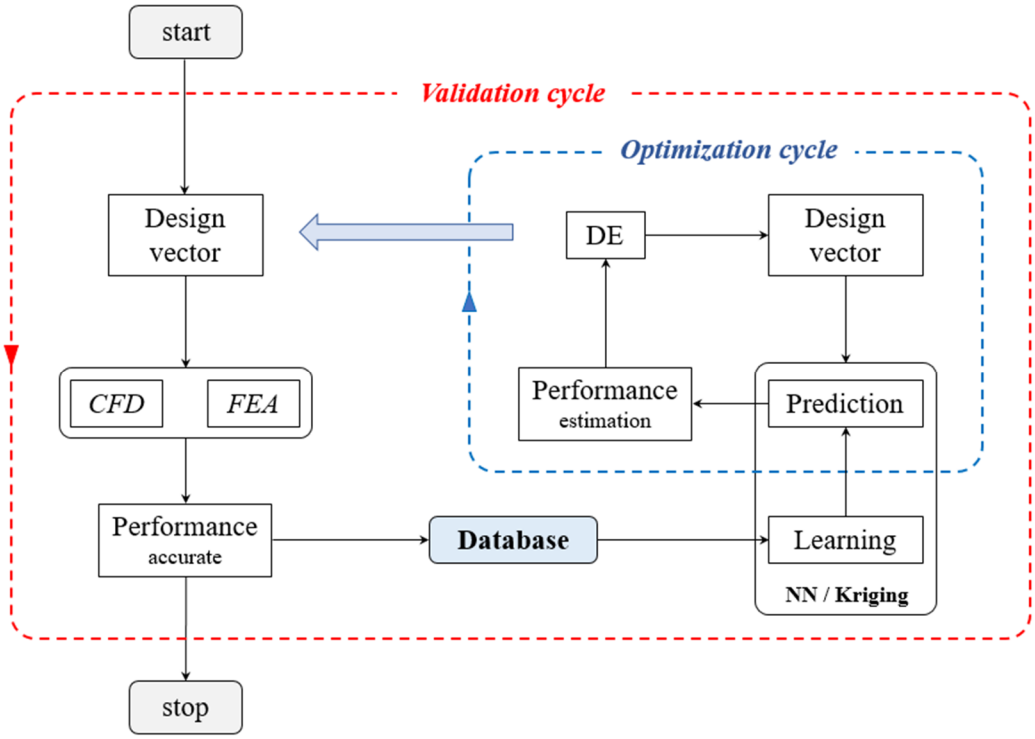

Figure 1.3 Workflow for Metamodel Assisted Evolutionary Algorithm developed in CADO. Source [38].

Despite the efficacy of this optimization strategy, the technique suffers from the limitation in the maximum number of design variables. In fact, a common drawback affecting the Gradient-free methods is known as "curse of dimensionality" [43], which indicates the exponential growth of the dimensions of the design space with the increase of the number of optimization variables. Therefore, the higher the number of design parameters, the wider the hyperspace, the higher the number of evaluations (or generations) required by the Evolutionary Algorithm to correctly locate the global optimum. Since high-fidelity simulations are invoked at each generation, a typical limit of few tens of design variables is recommended to ensure the exploration of the design space within an acceptable computational budget. In case the component under optimization presents a complex geometry not suitable for the abovementioned limitation, it is common practice to split the entire domain in sub-regions, each one treated with a dedicated optimization process, with frozen boundary conditions. The underlying approximation, missing the interactions between the evolving sub-components, results in some performance deviations once the full assembly is analyzed for validation purposes. The extent of such difference is case-dependent and up to the experience of the designer. Therefore, this aspect intrinsic of zero-order methods poses a severe constraint to the attempt of further improving the design optimization procedures by increasing the level of detail in the geometrical description, as requested in the introduction.

Moreover, the iterative nature of Gradient-free methods demands efficient high-fidelity solvers in order to saturate the exploration of the design space within an acceptable timeframe. Despite the existence of hybridized [44] and parallelized

[45] techniques aimed at accelerating the search for the global optimum, the introduction of multidisciplinary analyses (such as the FSI) would anyhow imply more involved computations. This scenario could potentially impact the time necessary to complete the evaluation of each generation, along with the complexity of identifying the path to convergence of the optimization process. Hence, the sustainability of this framework in the effort of increasing the fidelity of the domain analysis is a critical aspect to be considered with regards to the expected advancements in the design of turbomachinery components.

Concerning the identification of an exhaustive answer to this problem, the second class of optimization methods, known as Gradient-based methods, is briefly described in the next section.

1.2.4 Gradient-based optimization methods

Gradient-based methods make use of the sensitivity information of the function of interest in the search of the optimal solution [46, 47]. In the course of this manuscript, we focus on "first-order methods", from the order of the derivatives of the cost functions. Since these algorithms do not need to sample the entire design space, but evolve a geometry following the direction of descent towards the minimum as indicated by the gradients, they are deemed more computationally efficient than Gradient-free methods (Figure 1.4). In particular, for each design iteration the derivatives, computed by one of the techniques described hereafter, are provided in input to the gradient-based optimizer, which identifies a direction of search and a corresponding step length to be followed for the modification of the candidate design through the alteration of its input parameters. Several different optimizers are available in the literature for the interested reader [48], which mostly differ in the algorithms determining the search direction.

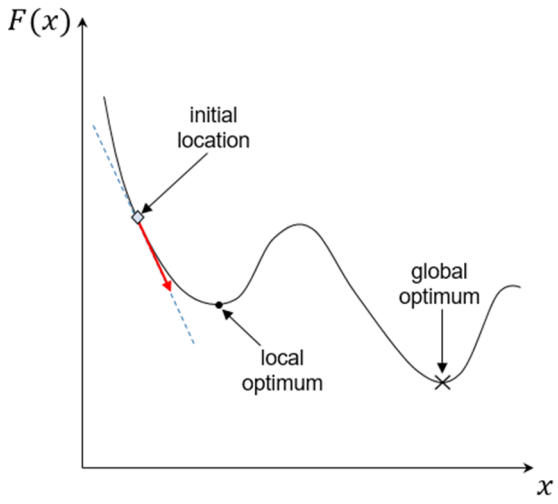

Figure 1.4 Search for local optimum by a Gradient-Based optimization method.

The procedure adopted for the computation of the gradients is a distinctive aspect of the Gradient-based methods. [49] provides a summary of the available techniques. The application of Finite Differences is the simplest approach to the evaluation of the derivatives, but on the other side their accuracy is strongly dependent on the step size adopted for their computation. Moreover, the method implies the execution of a dedicated field solution for the perturbation of each design variable in order to compute the correspondent sensitivity of the cost function. Therefore, the computational cost scales up with the number of design parameters and the number of iterations required to identify the optimum. The evaluation of the gradients by the Complex Step method [50] shares the same drawback, despite the fact it produces accurate results because it is not affected by any round-off error. Similarly, the tangent linearization method may be adopted for the computation of the sensitivities, but a field solution would be required for the perturbation of each optimization parameter. Hence, it is obvious that the computational cost of such methods would likely become prohibitive in design optimization problems of complex components, especially in the presence of a large number of design variables and in case of disciplines involving expensive computations. Therefore, they may be less suited to address the issues previously raised for turbomachinery products. However, if the number of objective functions is lower than the number of optimization parameters, an efficient calculation of the gradients can be obtained by the adoption of the adjoint methods [51, 52].

This family of Gradient-based techniques was first introduced by [53] for fluid problems, and is characterized by a cost for the computation of the sensitivity derivatives of the objective function that is essentially independent from the number of design variables. Hence, it is particularly suited for problems requiring detailed geometrical descriptions with many degrees of freedom.

Among the different techniques available in literature for the development of an adjoint framework, one of the two methods recurrent in this thesis is the computation of the adjoint equations through the linear algebraic approach discussed in [54], and herein repeated for sake of convenience.

Given a cost function J, such as

$$J\big(x, y(x)\big), \tag{1.3}$$

with x as the vector of input variables (for instance, the nodal grid coordinates) and y representing the state variables, a set of governing equations can be defined as follows:

$$R\big(x, y(x)\big) = 0\,. \tag{1.4}$$

Eq. (1.4) relates a change in the values of the state variables y to the perturbation of the input parameters x, for instance determined by a modification of the component shape. The derivatives of the cost function w.r.t. the input variables resulting from the application of the chain rule of differentiation is the following:

$$\frac{dJ}{dx} = \frac{\partial J}{\partial x} + \frac{\partial J}{\partial y}\frac{dy}{dx} \ . \tag{1.5}$$

The evaluation of the last term on the RHS of Eq. (1.5), *dy/dx*, could be computationally involved because requiring a field solution (for instance, through a differentiation of a CFD or a FEM simulation) to characterize the perturbation of each input variable *x*. Therefore, the computational cost would scale up with the number of degrees of freedom. In order to circumvent such limitation, the adjoint method eliminates the dependence of the cost function sensitivities on the term *dy/dx*. In particular, starting from the differentiation of the governing equations,

$$\frac{dR}{dx} = \frac{\partial R}{\partial x} + \frac{\partial R}{\partial y}\frac{dy}{dx} = 0 \ , \tag{1.6}$$

$$\frac{dy}{dx} = -\left(\frac{\partial R}{\partial y}\right)^{-1}\frac{\partial R}{\partial x} \ . \tag{1.7}$$

Eq. (1.7) is introduced in Eq. (1.5) returning

$$\frac{dJ}{dx} = \frac{\partial J}{\partial x} - \frac{\partial J}{\partial y}\left(\frac{\partial R}{\partial y}\right)^{-1}\frac{\partial R}{\partial x}, \tag{1.8}$$

from which the adjoint variable ψ is defined:

$$\psi^T = \frac{\partial J}{\partial y}\left(\frac{\partial R}{\partial y}\right)^{-1} \quad \rightarrow \quad \left(\frac{\partial R}{\partial y}\right)^T \psi = \left(\frac{\partial J}{\partial y}\right)^T. \tag{1.9}$$

Eq. (1.9) describes the adjoint system of equations whose solution would finally lead to the computation of the cost function sensitivities w.r.t. the input variables:

$$\frac{dJ}{dx} = \frac{\partial J}{\partial x} - \psi^T \frac{\partial R}{\partial x} \ . \tag{1.10}$$

Therefore, Eq. (1.9) and Eq. (1.10) demonstrate that the computational cost of the calculation of the objective function sensitivities is essentially independent from the number of input variables. In fact, the evaluation of the terms $\partial J/\partial x$ and $\partial R/\partial x$ appearing in Eq. (1.10) does not require any expensive field solution. Instead, the calculation of the adjoint variables in Eq. (1.9), whose size is the same as the vector of the state variables, implies a system solution of similar complexity as the standard primal (but then linearized) field problem. Hence, the cost of the calculation of the sensitivities is reduced to an additional system solve only, irrespectively from the number of input parameters. For this reason, the adjoint methods are addressed as a promising means for the advancement of the optimization techniques in case of complex physical problems demanding rich domain spaces and more involved numerical models, yet at an affordable computational cost.

A second methodology available for the computation of the adjoint sensitivities, widely adopted in the framework of the present work, refers to the

Algorithmic Differentiation (AD) technique [55]. Starting from Eq. (1.3) and introducing the design variables α such that $J = J\left(\alpha, y\left(x(\alpha)\right)\right)$, by applying the chain rule of differentiation, the "forward mode" of AD is obtained as follows:

$$\frac{dJ}{d\alpha} = \frac{\partial J}{\partial \alpha} + \frac{\partial J}{\partial y}\frac{\partial y}{\partial x}\frac{\partial x}{\partial \alpha}. \tag{1.11}$$

Since $\partial x/\partial \alpha$ appears at the last term at the RHS of Eq. (1.11), a perturbation to any design variable would propagate throughout the entire differentiation chain. Therefore, for each variation of a design parameter α, a re-evaluation of $\partial y/\partial x$ through a dedicated field solution is necessary to compute the corresponding sensitivity of the cost function $dJ/d\alpha$.

The adjoint approach is realized by the application of the "reverse mode" of AD, consisting in a rearrangement of Eq. (1.11) by transposing its terms:

$$\left(\frac{dJ}{d\alpha}\right)^T = \left(\frac{\partial J}{\partial \alpha}\right)^T + \left(\frac{\partial x}{\partial \alpha}\right)^T \left(\frac{\partial y}{\partial x}\right)^T \left(\frac{\partial J}{\partial y}\right)^T. \tag{1.12}$$

Eq. (1.12) presents as rightmost term of the chain of differentiation the sensitivity of the cost function J w.r.t. the state variables y, which needs to be computed only once if the cost function is unique. Now the derivative w.r.t. the design variables α appears only in the leftmost position of the transposed product and, therefore, has no influence on the other terms in the chain. Hence, consistent with the demonstration of the linear algebraic method, the evaluation of the sensitivities of the cost function w.r.t. the design parameters $dJ/d\alpha$ requires only one additional system solve to address the term $\partial y/\partial x$, while the computational effort for the calculation of the other derivatives in Eq. (1.12) is almost negligible.

A remarkable aspect of the reverse mode AD is the back-tracing of the perturbations, from the formulation of the objective function in backward direction till the original locations in the mesh, where the nodal coordinates are stored, and finally to the design parameters. Therefore, differently from the previous technique and the formulation in Eq. (1.9), in this case the adjoint variables ψ do not explicitly appear anymore. Instead, the sensitivities of the cost function w.r.t. the design variables are directly computed, as reported in Eq. (1.12). The new solver addressing the reverse mode computations mirrors the primal solver, as thoroughly discussed in Chapter 3.

The implementation of the adjoint field equations can be performed in two different ways:

- Continuous adjoint method: This approach relies at first on the linearization of the system of equations and their recombination through the Lagrange multipliers [56], while their discretization follows. This technique is the one adopted in the pioneering works of [53, 46] and its main advantages consist in the accurate linearization of the system of equations and the high performance of the code in terms of runtime.
- Discrete adjoint method: Opposite to the previous method, this approach requires the discretization of the primal system of equations at first,

followed by its linearization to formulate the adjoint equations [57]. The main advantage of this technique resides in the full consistency between the primal and the adjoint system of equations (i.e. considering their discrete framework, the adjoint equations are exact w.r.t. their primal version). Moreover, it is open to the possibility of verifying the accuracy of the derivatives line-by-line in the code by comparison with the Complex Step method, and eventually it allows also adopting automatic procedures for the development of the adjoint code [58].

Both methods present their own advantages and disadvantages and there is an almost equal share in the community of adjoint code developers. The work presented herein is executed by adopting the discrete adjoint approach and, more precisely, by developing the whole adjoint framework by "manual differentiation".

Despite the advantages of the adjoint methods are now evident to the reader, their large scale adoption for the solution of industrial problems has been limited so far. In fact, among the drawbacks of such technique, there is the requirement of having a well-conditioned design space in order to enable the calculation of the derivatives. This limitation may interfere with the need of evaluating complex geometries in off-design operative conditions, which is usually the case in internal aerodynamics problems for turbomachinery applications, like in the turbocharger field. In order to cope with the continuous demand of enhancements of the operative range and the efficiency of such machines, complex flow fields characterized by large flow separations must be tackled. Since the adjoint equations inherit the stiffness of the primal system, their solution may be challenging in such situations. In this respect, recent advancements in the robustness of the solvers are attributed to [59, 60], whose work on the JT-KIRK scheme allowed to expand the usability of the method. This new solution strategy, embraced in the recent development of the CADO flow solver by [54] (integrated in the framework of this thesis), proved its effectiveness in the design optimization of turbines and compressors for industrial applications [61 – 64], paving the way to a larger adoption of the adjoint techniques in the engineering community.

1.2.5 Hybrid optimization frameworks

Gradient-free optimization methods are also known as "global search" methods, because their explorative capability offers the opportunity of identifying the global optimum in the design space, provided that a sufficient number of candidates is evaluated. Instead, gradient-based methods, despite their efficient identification of the minimum of the objective function, may stagnate in local optima (cf. Figure 1.4), whose distance from the global optimum depends on the characteristics of the baseline candidate. The exploration capability of the adjoint method is investigated by [54] in comparison with a Differential Evolution

algorithm in the framework of the optimization of a radial turbine impeller. The author shows how three different initial geometries scattered in the design space could all convergence to the same optimal solution by application of the adjoint method, and even extend the Pareto front constructed by the Gradient-free counterpart. Another example leading to a similar outcome is reported in [65] for the optimization of a turbine inlet guide vane. Therefore, it is possible to conclude that the actual performance of the adjoint method depends on the "morphology" of the design hyperspace of the problem under consideration, which is not known a priori.

In order to support the designers in the early stages of a design optimization, hybrid techniques were recently explored, like in [66], proposing the combination of a Gradient-free algorithm with a Gradient-based method. The advantage of this set-up is the preservation of the exploration capabilities of the Gradient-free technique, while a Gradient-based method invoked at each iteration allows accelerating the convergence of the optimization. [67] presents a more efficient framework combining a Differential Evolution algorithm with an adjoint method, which is dynamically invoked during the evolution process with a number of calls progressively increasing as the candidate design approaches the region of the global optimum. Such new algorithm shows improved convergence performance for the optimizer.

In case a hybrid optimization method is not available, a pragmatic approach is represented by the early investigation of the optimization problem through a Gradient-free method, for instance a Differential Evolution algorithm, followed by the switch to an adjoint framework. The transition from the first to the second method is recommended as soon as the rate of exploration of the gradient-free technique tends to saturate, thus focusing on a mature baseline design in input to the gradient-based framework. This transition point can be recognized by visualizing the history of the design variables and the performance parameters along the iterations of the optimization, stopping the DE as soon as the amplitude of the oscillations (qualitatively reported in Figure 1.5) decreases and a quasi-monotone path of convergence is identified. At this point, the last individual could be considered as the initial design for an adjoint optimization, with the benefit of addressing this second step by a much higher number of design variables, along with augmented objective function and constraints obtained with more involved physical disciplines (like the FSI). Hence, the goal of increasing the level of detail in the shape modifications and to improve the fidelity of the physical predictions is achieved, while reducing the risk of being trapped in local optima, as it may happen instead with the direct application of an adjoint method since the early stages of the design exploration.

The proposed framework may be a suitable means to respond to the needs of the turbomachinery community introduced at the beginning of this chapter.

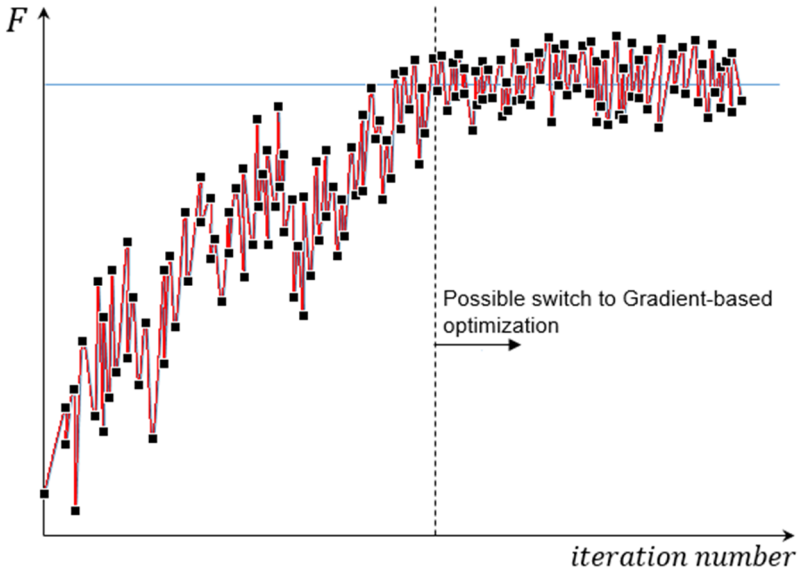

Figure 1.5 Qualitative history of a performance parameter during a Gradient-free optimization and suggested switch to a Gradient-based optimization.

However, the full exploitation of the adjoint methods still requires significant developments in the field of multidisciplinary simulations. In particular, the following section analyzes the problem of the design of a radial turbine impeller for turbocharger applications, exposing some critical gaps requiring further advancements in the technique. Hence, this thesis focuses on the expansion of the adjoint method to more involved physical disciplines with the aim of directly addressing some sensible aspects of the product robustness throughout its optimization.

1.3 Turbocharger turbine technology

Turbochargers are highly engineered components essential for the achievement of the future emissions regulations in the field of internal combustion engines, despite the selected fuel. Their introduction in a reciprocating architecture allows achieving improved power and efficiency, along with the actuation of more refined control strategies aimed at limiting soot formation and NOx emissions, while enhancing the powertrain transient response for increased elasticity at vehicle level [68 – 70]. The range of applications comprehends passenger cars, naval, rail and light-aviation products, large off-highway machines, and stationary power plants. These turbomachines consist of a radial turbine driving a radial compressor through its connecting shaft. The compressor is aimed at dynamically increasing the pressure level in the engine intake system in order to modulate the mass flow rate entering the cylinders. On the exhaust side, a turbine is demanded to convert the enthalpy of the exhaust gases in mechanical energy to the shaft [71]. [72] offers an interesting overview of the early stages of the development of a charging system and its matching w.r.t. the

engine requirements for a light application of the general-aviation industry. In particular, the integration process of the turbomachine in the reciprocating architecture is described following the steps of the preliminary performance and fuel consumption estimates. The trade-off studies guiding the stage layout selection and its conceptual design, the evaluation of the materials, control mechanisms and bearing technology, the aerodynamic and structural design of the wheels, and finally the definition of the technology impact on the market are analyzed, as well as the technological contents necessary to achieve a cost-effective large scale production. Nowadays, the analytical methods reported in the paper are replaced by multi-scale modelling techniques aimed at simulating the engine behavior in steady state operative conditions and transient manoeuvers, and therefore predicting the interactions between the turbocharger and the surrounding systems [73 – 75]. Therefore, the performance of the turbomachines are evaluated at engine or vehicle level and such information results in a set of requirements for the detailed machine design [76].

1.3.1 Turbines for automotive applications

The engineers dedicated to the development of turbines for the automotive business are continuously demanded to provide cost-effective technologies with increased operative range and improved efficiency all over the engine map. In fact, differently from the aeronautical applications, the typical duty cycles for passenger cars span the whole envelop of the engine performance curve, from very low mass flow rates in urban driving conditions, up to peak power. The capability of delivering the required boost pressure in any of those operative points is a key ingredient for the emissions control and the responsiveness of the engine. In order to cope with these requests, the Variable Geometry Turbine (VGT) technology emerged in the past decades, with a recent increase in popularity in the new gasoline applications adopting Miller cycle-based lean combustion strategies [4]. This turbine architecture, exemplarily reported in Figure 1.6, mainly consists of three elements:

- A volute collecting the entire mass flow from the combustion chambers, except the portion dedicated to the recirculation towards the intake manifold through the short-route circuit.
- The Variable Geometry Nozzle mechanism, comprehensive of a set of vanes arranged in a cartridge, rotating around their pivots. The change in the vanes setting angle determines a variation of the flow passage towards the wheel with the aim of regulating the flow incidence angle at the rotor blades leading edge.
- A rotor, typically a radial or mixed-flow impeller, for the conversion of the enthalpy of the exhaust gases in mechanical energy to drive the compressor.

The main advantage of a VGT layout, in comparison with standard systems equipped with a wastegate valve, is related to the wider operative range at high efficiencies, since the machine is capable of managing the entire flow exhausted by the combustion chambers with no need of any external bypass channel. Additionally, it can adjust the rotor inlet flow tangential component by means of the inlet guide vanes. Therefore, more enthalpy is available for the extraction of power at the turbine wheel and near-optimal conditions are achieved according to Euler's equation. This is reflected in faster accelerations of the compressor and higher boost targets realized by the turbocharger, finally disclosing more opportunities in the refinement of the calibration of the selected combustion package. In the specific case of a Miller cycle, [77] shows that eventually the VGT technology may deliver the boosting capabilities necessary to design an architecture for higher Miller rates, thus leading to further improvements in fuel consumption.

In order to deal with the wide span of operative conditions, statistical approaches have been refined to synthesize the information in a discrete number of key points in the engine map, whose flow characteristics are extracted for the determination of the boundary conditions to be imposed to the turbine domain.

Figure 1.6 Variable Geometry Turbine components: volute, vanes, rotor. Courtesy of General Motors.

This information, typically represented by mass flow averaged figures retrieved from the engine performance models, results in a set of steady state operative conditions that the turbine design has to be confronted with, aiming at a balanced solution according to the engine requirements. Since compact layouts are generally necessary to fulfill the most diverse project goals (from transient response, to boosting capability at low mass flow rates, and reduced heat rejection to the external environment), the turbine is demanded to operate over a wide range of vane positions, increasing the complexity in the design operations. Moreover, this technology presents a clearance between vane-shroud and rotor-housing of

the order of few hundreds of microns, whilst the typical thermal operative range spans from ambient temperature up to 1050°C in gasoline applications, this without the possibility of any dedicated blade cooling circuit. These considerations add up to other targets for a production-intent design, like the structural integrity to centrifugal and fluid-induced stresses for operations in excess of 300k RPM in small applications, the robustness to the engine and fluid-induced vibrations, creep resistance and a minimum fatigue lifetime, along with the fulfillment of cost, mass and packaging constraints. Such scenario clearly demonstrates the challenges the designer is confronted with during the product development process. Therefore, it is indeed recognized that a design practice based on the experts' intuition alone would be likely inconvenient. Hence, multidisciplinary optimization methods play a fundamental role.

1.3.2 Turbine design optimization

The standard process for the design optimization of turbine components is multidisciplinary and multipoint, resulting in customized geometries responding to specific engine functional requirements [78]. Given a set of operative conditions (OPs), the optimization problem may be described by a compounded objective function, as presented in Eq. (1.2), synthesizing the performance information collected by the analyses executed in most (if not all) the key points. At the same time, a set of constraints is applied to some OPs, against which the turbine geometry is assessed. In general, the optimizer performs the shape modifications in such a way the investigation of the design space is driven by the need of satisfying the constraints set at first, in order to identify some feasible geometries, followed by a minimization of the objective function. The values of the weights ω_i in case of a single-objective function (ref. Eq. 1.2) are application dependent and based on the designer's experience. Therefore, the process can assume different convergence paths leading to non-unique solutions, hopefully in proximity of the global optimum.

Examples of optimization problems for turbocharger applications are discussed in [27] for the case of a centrifugal compressor, and in [79] for the development of a radial turbine impeller. In the latter, the novelty is represented by the additional constraints applied to the blade in order to respond to the flow vibrational excitations induced by the VGT vanes, without having the nozzles explicitly represented in the domain. Both the optimizations are performed by the direct application of an adjoint method to a baseline geometry, either obtained from a previous Gradient-free optimization or from a diligent manual design. These efficient processes prove that an optimal solution can be achieved in few iterations (respectively 18 and 20), resulting in a significant time saving w.r.t. a Gradient-free optimization performed on the same baseline turbine rotor [80], which leads to a computational budget of about nine times higher. Therefore, it follows the opportunity of trading the less expensive optimization by the adjoint

method with the implementation of more involved physical disciplines. The benefit is twofold:

- On one side, the optimizer equipped with more comprehensive models would be influenced by their predictions and may select a different path of convergence towards a solution which is deemed the “truly optimal candidate”, as affected by less assumptions and simplifications. In this regard, the best shape would behave consistently during the validation process performed after the completion of the optimization, as most of (if not all) the relevant disciplines, even the more computationally demanding, were already considered by the optimizer itself. Therefore, the risk of incurring in unfeasible shapes is drastically reduced.
- On the other side, the reliability of such models would support a wider adoption of numerical simulations in place of the experimental testing, thus limiting it to the final stage of the validation only. This scenario would give access to a significant cost saving and a faster product roll-out to the market. Moreover, the higher the model accuracy, the lower the safety margins applied to the design and, therefore, the higher the chance of identifying promising solutions.

Since the advantages of surcharging the adjoint method with more complex disciplines are known, it is necessary to focus on the missing aspects in turbocharger radial turbines optimizations. [78, 79] present the treatment of aerodynamic related parameters (such as efficiency, pressure ratio, permeability, etc.), along with the evaluation of centrifugal stresses and vibrational modes. Geometrical aspects, like the inertia, are also included. [80] discusses an efficient implementation of Uncertainty Quantification evaluations within the framework of a Gradient-free optimization, with the scope of accounting for the manufacturing deviations and their impact on the previous performance figures. However, a commonality among these optimizations is the assumption of adiabatic walls all over their domains. This simplification (mostly inherited from the past, when adjoint methods were less popular and the calculation resources more limited) is due to the significant computational overhead implied by the accurate evaluation of three-dimensional heat transfer phenomena between solid and fluid media.

[81] analyzes the problem of the Fluid-Structure Interaction in radial turbines, in relation to the thermal loads induced by the fluid in contact with the blades. Their effort is to accurately predict the heat transfer mechanisms between the two media for a reliable estimation of the loads to the rotor in dynamic operative conditions. The study shows the most impacted regions of the wheel are those ones exposed to the highest difference in Reynolds number w.r.t. the main flow in the blade channel, i.e. the areas affected by secondary flows like the blade leading edge, the tip and the trailing edge. Hence, the authors suggest considering the inclusion of the impact of the thermal field on the structure, on top of the standard computation of the centrifugal stresses.

The integration of the heat transfer analysis within an optimization process is a topic of recent interest [82 – 84]. The physical phenomenon is described through the application of a Conjugate Heat Transfer (CHT) procedure as originally proposed by [85, 86], which involves the thermal interaction between a solid body and its surrounding fluid by a coupled solution of the two domains. The challenge in the implementation of this methodology within the landscape of a multidisciplinary optimization of a complex geometry consists in the trade-off between the accuracy and its computational overhead, so far limiting the thermal predictions only to the validation phase in industrial design procedures. In fact, it is a common practice during an optimization to replace such intensive computations with reduced order models or safety margins based on empirical experience. However, it is recognized that most of the previously cited benefits are lost with such simplifications and the competitiveness of the product might be impacted.

Therefore, since the CHT analysis is less suited for a Gradient-free optimization framework, a new optimization approach based on a highly multidisciplinary adjoint method is investigated in this work.

In conclusion, the introduction of thermal evaluations within the optimization of industrially-relevant geometries is still at an early stage of development. To the best of our knowledge, the literature presents only few studies considering the CHT analysis in adjoint-based optimizations [87, 88], a limited number of them adopts a discrete adjoint formulation [89 – 91], and none extends the problem to thermo-mechanical evaluations for complex three-dimensional geometries, with their consequences on the lifetime of the component. Therefore, this work is aimed at covering critical gaps in the design of radial turbines.

1.4 Objectives of the work

The thesis deals with the problem of the durability control with respect to the operative thermal loads, which is a fundamental aspect in the design of turbochargers for automotive applications. Because of the highly dynamic duty cycles of these machines, it may be inconvenient to relegate the lifetime assessment to the late phase of the geometry validation, as any potential failure might be difficult to interpret by the sole experts' intuition. Moreover, a manual correction of the design could affect other figures, previously dealt by the optimizer (such as performance related parameters or other structural constraints). Therefore, this work is aimed at facilitating the integration of some aspects of the product lifecycle control within the established optimization process, defining a strategy that is self-reliant and compatible with the standard timing of industrial workflows.

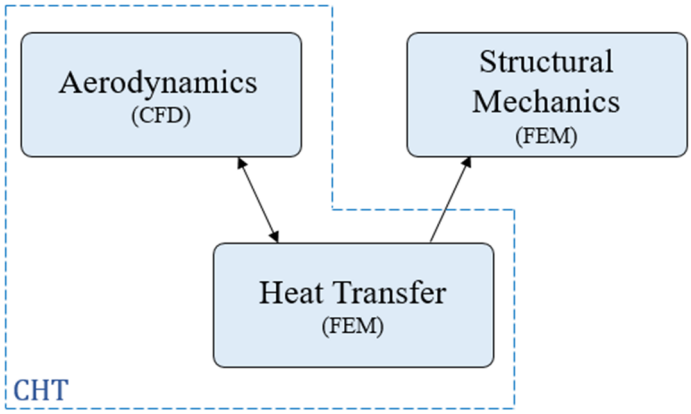

Figure 1.7 Schematic representation of the problem framework in primal mode, with CHT closure between the involved disciplines.

In light of this objective, the main goals of the thesis are the following:

1. Development of a framework for the execution of the CHT analysis, with the aim of predicting the temperature field in the solid domain and the related impact in terms of thermo-mechanical stresses. The introduction of the CHT analysis promotes the closure between the fluid and the structural disciplines, so far treated separately (Figure 1.7).

2. Development of an adjoint-based optimization framework compatible with the requirements of such multidisciplinary analysis. With reference to the workflow discussed in [54], the goal is to enrich the current multidisciplinary outlook with an additional constraint, as qualitatively reported in Figure 1.8, enforcing the path of convergence of the optimizer to a robust solution.

3. Validation of the framework and application to a turbocharger radial turbine rotor in steady state operative conditions. Analysis and interpretation of the results.

4. Extension of the method to the evaluation of the Thermo-Mechanical Fatigue problem experienced in engine dynamic operative conditions.

5. Validation of the transient adjoint framework, application to a turbocharger radial turbine rotor test case and interpretation of the results.

The algorithm is developed in the C++ programming language and is integrated in the in-house optimization platform “CADO”.

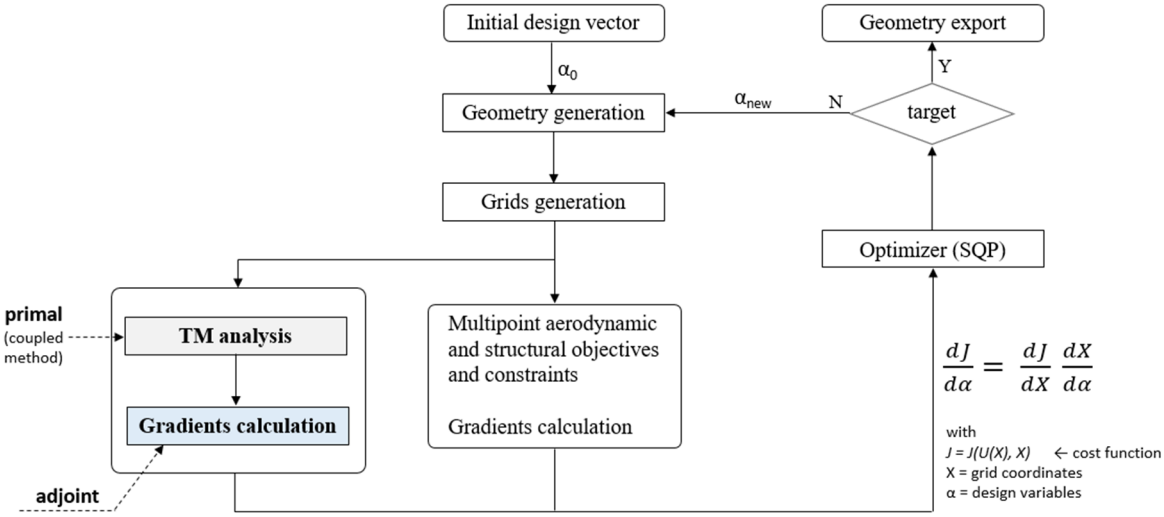

Figure 1.8 Simplified adjoint multidisciplinary optimization workflow in CADO.

1.5 Thesis outline

The remainder of this thesis describes the development of a gradient-based multidisciplinary optimization framework for thermo-mechanical evaluations and presents its application to the test case of a radial turbine rotor geometry. In particular, the manuscript is structured as follows.

Chapter 2 introduces the mathematical framework for the development of the heat transfer analysis in the body of the optimization. The problem of the interface between the solid and the fluid domains is treated, as well as the validation of the CHT solver in steady state operative conditions and the definition of the most convenient mesh settings for a radial turbine rotor test case. The calculation of the thermal field allows the inclusion of the thermal strains in the solid domain and the prediction of their impact on the stresses, which are computed in demanding engine operative points. Hence, the field of thermo-mechanical stresses is compared to a similar prediction following the adiabatic walls assumption, as a demonstration of the implications of the thermal loads on the robustness of the structure.

Chapter 3 addresses the development of a discrete adjoint framework tailored to the implementation of the thermo-mechanical analysis in steady state operative conditions. Concerning the adoption of a gradient-based method, the development of a system supporting the calculation of the constraint function sensitivities w.r.t. the solid and the fluid grids coordinates is discussed, along with the validation of the gradients, with the aim of including this analysis in a Sequential Quadratic Programming-based optimizer [92].

Chapter 4 expands the evaluation of the thermal stresses to engine transient operative conditions, such as in cyclical manoeuvers representative of real-driving conditions. In this respect, the problem of the Thermo-Mechanical Fatigue (TMF) in the turbocharger turbines is addressed, with the aim of optimizing the turbine impeller durability. The primal and the adjoint solvers treating the conjugate problem in transient conditions and the structural-mechanic history of the component are discussed with focus on the requirements of computational budget, with the aim of creating a framework suitable for industrial applications.

Finally, Chapter 5 presents the conclusions drawn from this study, along with some proposals of possible future steps complementary to the current findings.

Chapter 2

Thermo-mechanical stresses in primal solver

2.1 Turbocharger thermal analysis

Thermal analyses of turbocharger components are typically executed to address two different scopes.

The first one is related to the improvement of the accuracy of the performance predictions by the engine models, influenced by the approximated interactions of the turbocharger with the surrounding subsystems. In fact, a cause of mismatch between simulated and measured performance resides in the simplified treatment of the thermal losses within the turbomachine, which is imported in the one-dimensional engine model in the simplified form of maps containing lumped data, measured in nominal conditions [93 – 95]. In order to increase the reliability of those predictions, [96] offers an extensive overview of the state-of-the-art research activities aimed at characterizing the heat transfer phenomena in turbochargers, considering both one-dimensional and three-dimensional modelling techniques. The goal is to create thermal maps of the prototype part or its virtual mock-up in steady state and transient operative conditions. Such extensive dataset enables the exploration of enriched one-dimensional approaches, capable of reacting to the variations of the boundary conditions from the engine model, yet still preserving the advantage of a low computational budget [97 – 99]. Hence, the expensive three-dimensional thermal simulations are replaced by efficient zero- or one-dimensional models (Figure 2.1-a) improving the fidelity of the engine performance estimations at an affordable cost.

The second approach to the turbocharger thermal analysis follows an opposite direction, consisting in a two-step process starting at system level and ending up with detailed evaluations (Figure 2.1-b). At first, the turbomachine is analyzed with reference to the engine performance envelop, and its operations are synthesized in a discrete number of characteristic points from the engine map. The

relevant boundary conditions at the inlet and at the outlet of the turbocharger component, extracted from the one-dimensional engine model, are applied to its three-dimensional representation. Hence, a thermal analysis of the turbomachine is performed with the coupling of the three-dimensional fluid and solid domains through a Conjugate Heat Transfer (CHT) technique, with the goal of generating a detailed virtual thermal map. This data is directly evaluated against the constraint of maximum temperature (aimed at avoiding the formation of any severe local hot spot), or addressed to secondary analyses of critical subcomponents requiring the characterization of the temperature field as input [100, 101].

Concerning these two scenarios, the thermal FSI problem undertaken in this thesis pertains to the second area of focus. In particular, the scope herein is to address detailed thermo-mechanical evaluations of a turbocharger turbine impeller by means of an optimization framework, with the aim of enhancing its robustness against any critical thermal event possibly encountered along its duty cycle.

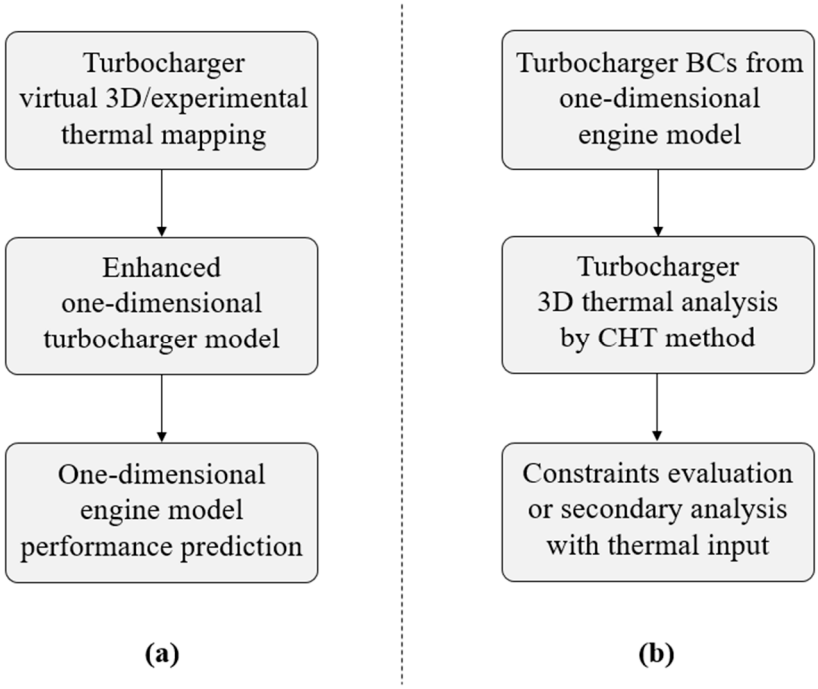

Figure 2.1 Workflows for turbocharger thermal analyses.

2.2 Thermal evaluations by the Conjugate Heat Transfer analysis

2.2.1 The conjugate problem

Heat transfer phenomena in a solid surrounded by a fluid occur any time a temperature gradient is established between the two media (Figure 2.2). The thermal exchange in the fluid domain develops through the convection

mechanism, which involves diffusion processes at molecular level and advection at macroscopic scales due to the motions in the bulk flow. Instead, the solid field exhibits only diffusion mechanisms by conduction processes, which account for the energy exchange within the material through particles collisions at microscopic level [102]. The heat transfer between the two domains takes place at their interface. This is the case for instance in turbomachinery applications, and in particular in turbine blades, experiencing a convective loading q_{fl} from the hot exhaust gases, and developing a thermal conductive path within the solid towards the inner cooling elements.

The numerical description of this problem of fields coupling is performed through the Conjugate Heat Transfer method, as originally proposed by [85, 86]. Such technique, either formulated as a two-way loose coupling approach or a tight coupling approach, opposes to simplistic methods referring to a one-way coupling philosophy. In fact, the latter usually computes the convective heat transfer coefficient by means of the sole fluid solution, by running dedicated CFD analyses with imposed wall temperatures. It follows a Robin boundary condition, which is assigned to the solid for the determination of its inner temperature field. This technique, despite the advantage of a rather inexpensive computational framework, offers only a rough estimate of the development of the thermal boundary layer [103], since it neglects the local temperature evolution in the solid. Instead, a more accurate representation of the heat transfer phenomena is offered by the coupling method known as the "conjugate problem" [104].

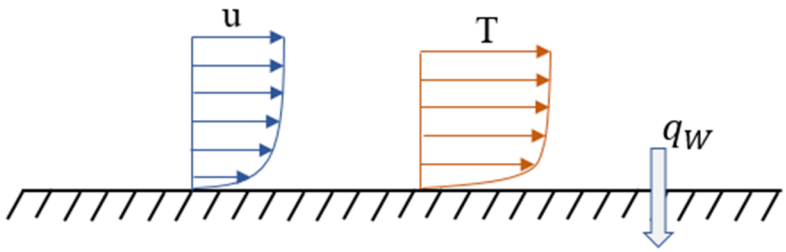

Figure 2.2 Heat transfer phenomenon between fluid and solid media in contact.

With reference to this last approach, the work herein presented adopts a two-way loose coupling technique for the development of a CHT framework according to [105], in which a fluid and a solid solver are sequentially called in an iterative process with mutual exchange of boundary conditions, till reaching the convergence of the temperature at their interface. As anticipated in Section 1.2.2, the advantages of this partitioned coupling technique are related to the efficient solution of each domain by the use of specialized solvers, and the flexibility offered by the adoption of the most suitable meshing strategy for each medium. Moreover, in case of an unsteady operating condition, a faster convergence of the thermal coupling is achieved through the partial decoupling of the two fields,

which show very different characteristic time scales, as will be discussed in Chapter 4.

The literature offers many numerical techniques to describe the conjugate problem. [106] adopts the Finite Volume Method (FVM) with structured meshes for both the fluid and the solid domains. [107] develops a coupling procedure between a research CFD code using FVM structured meshes and a commercial code adopting a FVM unstructured grid on the solid side. [108] analyzes a CHT problem in turbomachinery applications through FVM unstructured grids over the entire computational domain. Hybrid methods are presented by [109, 110] modelling the convection by a FVM and solving the solid through a Boundary Element Method (BEM), while [111] makes use of a scheme comprehensive of a Finite Difference Method (FDM) and a BEM. [112] presents a localized Radial Basis Function (RBF) meshless method extended to the fluid-solid coupling in CHT problems. [113] develops a conjugate model using a Volume Average Technique (VAT) applied to the momentum and energy equations in the domains coupling, solving the system of equations by a Galerkin method. A recent contribution from [114] presents a coupled lattice Boltzmann FVM for the solution of this problem.

The present work addresses the solution of the fluid domain through a FVM, while a Finite Element Method (FEM) is adopted for the analysis of the solid medium.

2.2.2 Domains discretization

The problem under investigation is represented in Figure 2.3, in which a turbine rotor is analyzed considering a periodic sector. A multi-block structured fluid grid with boundary layer refinement is interfaced to an unstructured solid mesh of second-order tetrahedral elements for the computation of the heat fluxes between the two domains.

The choice of discretizing the fluid domain with a structured grid is justified by the higher accuracy returned in the flow solution, in particular in the region of the boundary layer. Moreover, since the turbine impeller presents a highly staggered shape, a multi-block mesh [115] supported by a topology-based approach is adopted to split the domain in fourteen sub-regions. The benefit is twofold: maintaining a conformal curvilinear grid at the periodic boundaries, and preserving the flexibility necessary to generate a high quality mesh throughout the domain by a Transfinite Interpolation technique [116].

The solid domain, instead, is discretized with an unstructured grid of tetrahedral elements generated by a three-dimensional Delaunay method [117]. A hierarchical approach is adopted for the grid generation, starting from the vertices, edges and faces laying on the CAD surface, followed by the distribution of inner nodes in the volume. This technique allows approximating the original blade shape with high fidelity, regardless its complexity, thus supporting the accuracy of

the structural computations in the most stressed regions, like the hub fillet. Moreover, it ensures the conformity of the solid grid with the geometry, which is updated at each iteration during an optimization.

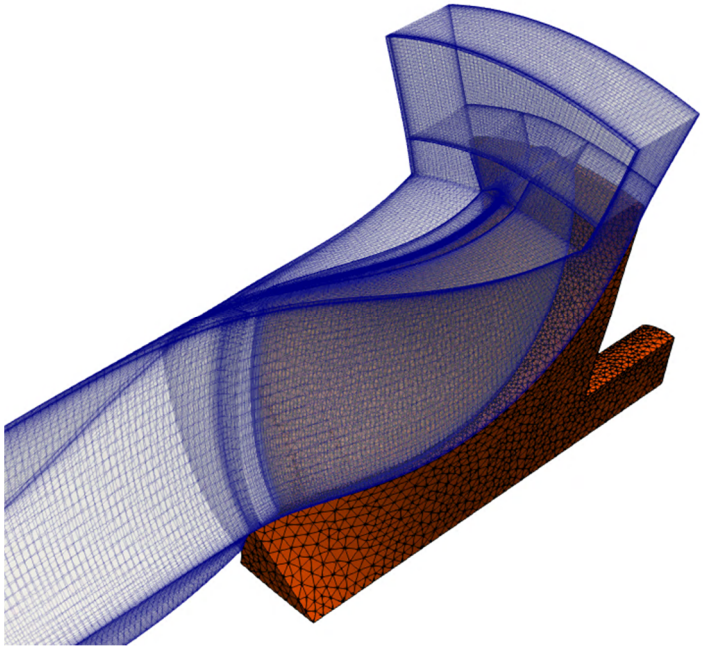

Figure 2.3 Radial turbine rotor: Fluid and solid meshes.

While the solid mesh is tightly coupled to the original CAD surface, the fluid grid approximates the region of the blade hub fillet, as shown in Figure 2.4, because not significantly impacting the aerodynamic results. On the contrary, the blade tip clearance w.r.t. the housing is rigorously discretized in order to compute the secondary flows developing in the shroud region. This set-up determines the generation of locally overlapping non-matching grids, as discussed in the next section.

The reader interested in the details of the mesh generation process is addressed to [54, 118].

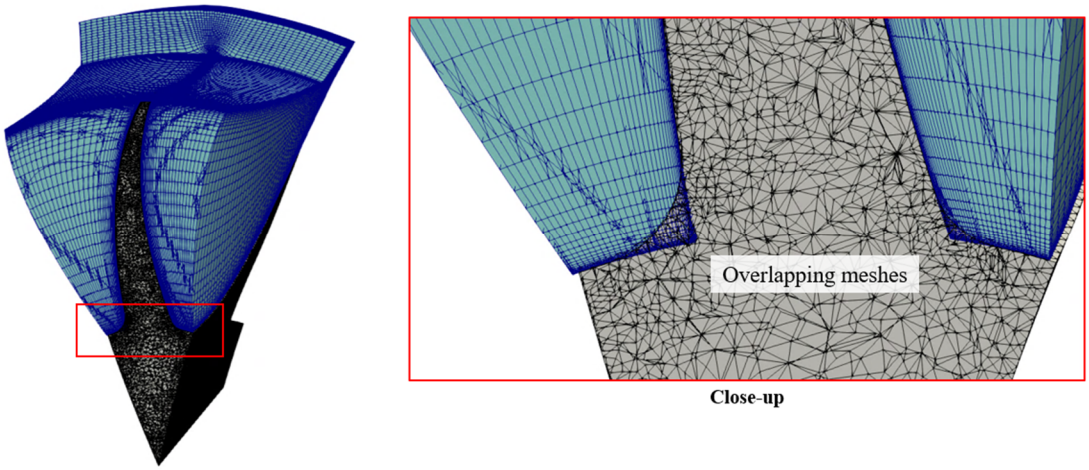

Figure 2.4 Locally overlapping fluid and solid meshes at blade hub fillet.

2.2.3 Fluid-Solid interface mapping

The conjugate problem is determined by the iterative exchange of information between the fluid and the solid domains at their interface. Since the two grids are non-matching and even overlapping in certain regions, a suitable technique must be implemented for the identification of the correspondences between fluid cells and solid nodes. An eligible method has to be robust w.r.t. the fluid mesh stretching in regions of high velocity gradients, and the solid nodes refinements at thin edges. Moreover, it has to be capable of dealing with quadratic finite elements, which present curvilinear edges.

[119] discusses four interpolation approaches: three techniques imply the use of projection methods in the three-dimensional space, while the fourth one adopts a generic search algorithm. The latter is adopted in the present work because of its demonstrated robustness in treating meshes of any complexity, despite being a non-conservative technique introducing some small losses in accuracy [119]. In its original formulation, this method, named Distance-Weighted Interpolation (DWI) [120], implies the definition of a search radius drawing a circular area in 2D or a sphere in 3D, whose origin is placed in correspondence of a reference cell center (or solid node). All the nodes (or cells) trapped into the search region are mapped as "the closest neighbors" of the target cell (or node). Hence, the exchange of information between the two grids takes place through a weighted average of the data from the population captured into the search region. The weighting function is based on the mutual distance of each node w.r.t. the target cell (or viceversa):

$$X_j = \frac{\sum_{i=1}^{N} \frac{X(i)}{dist(i)^2}}{\sum_{i=1}^{N} \frac{1}{dist(i)^2}} \tag{2.1}$$

with X representing the information to be exchanged between the two grids, j indicating the target cell center or node, *dist* standing for the distance between each node i within the search region and the target cell center j (or viceversa).

Although this approach benefits from its generality, it presents two weaknesses. First, the construction of a spherical search region in the three-dimensional space may lead to intercepting neighboring nodes (or cells) belonging to wrong regions of the physical domain. It is the case of a search sphere in proximity of thin walls, like at the blade tip (Figure 2.5-a): in the proposed example, the simplistic application of the method would mate the solid node at pressure side with some fluid cells located on the suction side, leading to a corrupted data averaging. In principle, a proper calibration of the search radius may help avoiding such circumstances, but this workaround loses generality at the hub fillet, where the two grids, detached from each other (ref. Figure 2.4), could create missing intersections preventing the data exchange. In order to address this problem, the solid and the fluid domains are split in sub-regions (named blade

pressure side, suction side, hub, tip, etc.). Therefore, the search algorithm is activated only between corresponding fluid-solid zones, instead of attempting the coupling of the two fields through a global search within the entire domain, thus avoiding any wrong averaging (Figure 2.5-b). This approach brings also a reduction in the computational cost for the mapping of the interface, as for each fluid cell (or solid node) the search of the neighbors is limited only to the nodes (or cells) belonging to the corresponding sub-space, instead of invoking the entire mesh.

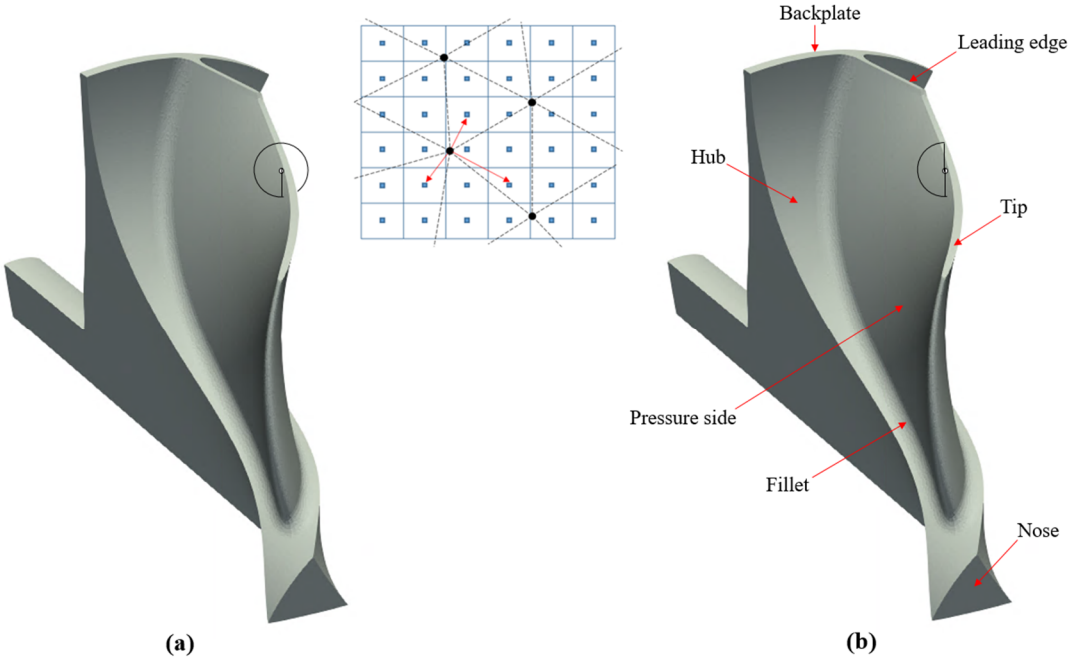

Figure 2.5 Search region shortcomings (a) and application of domain split (b).

The second issue refers to the application of the method in locations with high mesh stretching on fluid side. Figure 2.6-a shows a cut of the scene in a direction perpendicular to the wall: the target solid node, laying far from the cell centers, would intercept a search region involving fluid cells not in direct contact with the surface, as a result of the aspect ratio returned by the stretching. Since the thermal boundary layer is a region presenting high temperature gradients, the weighted averaging among cells not in direct contact with the wall could induce a locally false estimation of the heat fluxes. In order to compensate for this situation, only the fluid cells belonging to the domain layer in actual contact with the solid surface are invoked in the mapping procedure (Figure 2.6-b), and their temperature at the face in contact with the wall is considered (as discussed in the next section). Thus, a positive side effect is the further reduction of the computational overhead of the DWI because of the smaller number of mating elements. Moreover, the concept of “search radius” is dismissed in favor of a ranking assigned to each node or cell according to their mutual distance. This approach avoids the need of any local adjustment of the size of the search region based on the different meshes refinements.

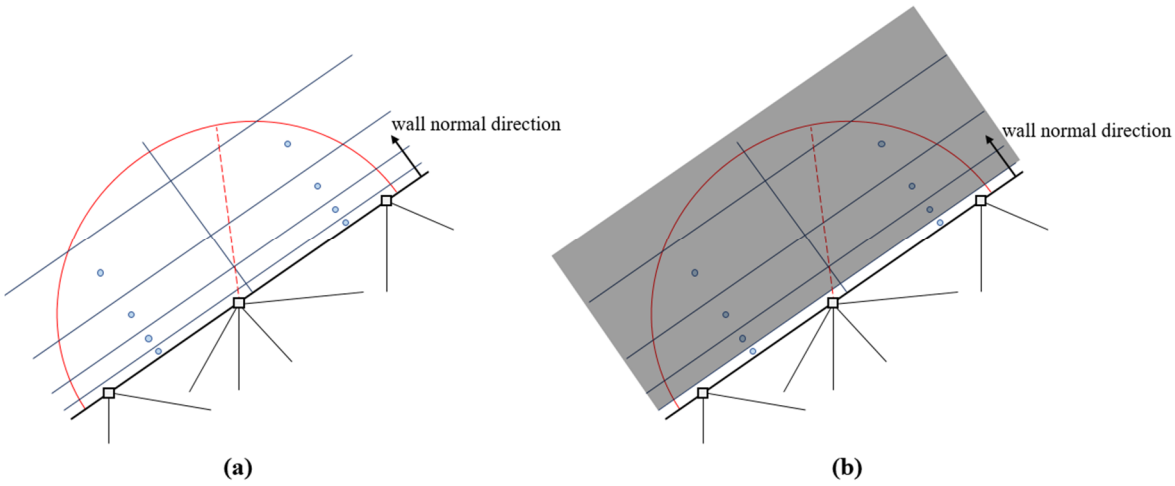

Figure 2.6 Search region across the thermal boundary layer (a) or through the first layer of the fluid domain (b).

Despite such improvement, the fluid mesh stretching could also take place in a direction parallel to the wall, as also discussed in [119]. This scenario would lead to solid nodes capturing information from cells located along the stretching direction, hence not being on top of them (Figure 2.7-a).

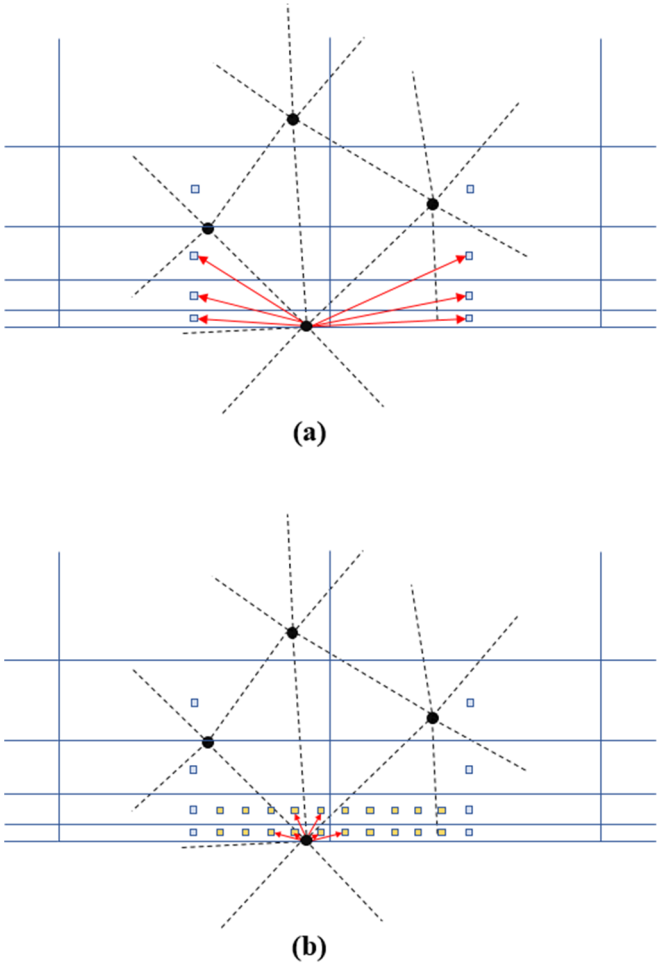

Figure 2.7 Search region across fluid mesh stretching parallel to the wall (a). Search through isotropic virtual fluid points distribution (b).

Because of the possibility of large temperature gradients also in this direction, the interpolated information would suffer in accuracy. This issue is tackled by the construction of a "virtual fluid grid" aimed at creating a locally isotropic distribution of virtual points around each solid node. The distance between two neighboring cell centers is covered by a distribution of virtual points, whose number depends on the cells aspect ratio. Each virtual point contains the information obtained through linear interpolation from the closest cell centers. Indeed, the goal is to increase the density of the attractors in proximity of each solid node, avoiding possible inconsistencies generated from gathering the information from fluid cells located too far away. Therefore, the search algorithm applied to the target solid node would intercept a majority of close virtual points from the isotropic pattern, bringing higher accuracy in the DWI procedure (Figure 2.7-b).

The result of such implementations is shown in Figure 2.8, describing the pattern of fluid temperatures at the wall as resulting from the CFD computation (Figure 2.8-a), and the corresponding interpolated temperatures applied to the solid surface as returned by the DWI procedure (Figure 2.8-b).

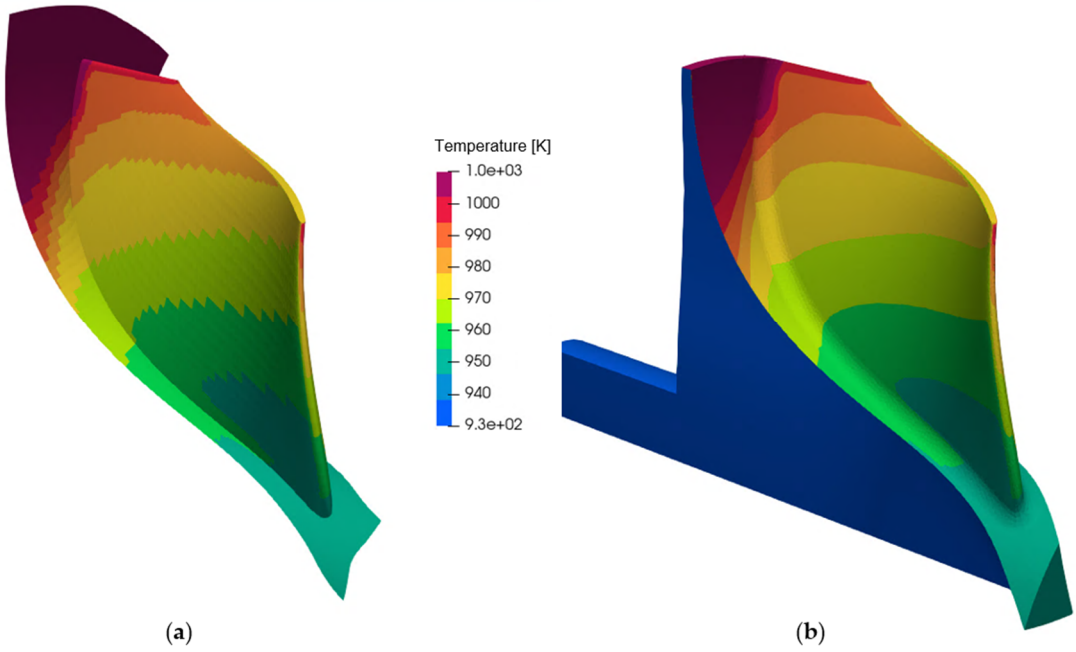

Figure 2.8 Distance-weighted interpolation method applied to the exchange of information between solid and fluid domains: (a) fluid temperature at walls, (b) interpolated fluid temperature assigned to the solid surface.

2.2.4 Coupling method

The partitioned coupling method separately solves each field involved in the multidisciplinary problem, generating boundary conditions for the other one. The non-synchronous solutions of the two domains determine numerical stability problems associated with the interface treatment, which are specific for the

method adopted in the coupling process. This characteristic distinguishes the loose coupling approach from the monolithic one, which is essentially unconditionally stable [121].

In the case of the conjugate problem, [122] discusses the stability properties of four coupling techniques, reported in Table 2.1, which rely on the Dirichlet or the Neumann boundary conditions at fluid and solid side, or on the Robin boundary condition applied to the solid. In summary, the convergence rate depends on the local Biot number, which expresses the ratio between the conductive over the convective thermal resistances:

$$Bi = \frac{h\,L}{k} \tag{2.2}$$

with h indicating the convective heat transfer coefficient, L the characteristic length at the wall, and k the solid thermal conductivity coefficient, while L/k is the conductive thermal resistance.

In complex geometries, as in the case of a radial turbine impeller, the Biot number may locally change to values greater or lower than unity, according to the variations in the blade thickness (affecting L) and in the local flow conditions (mostly contributing to the variations in h). This situation is inconvenient for the Flux Forward Temperature Back (FFTB) method [123] or the Temperature Forward Flux Back (TFFB) method [124], because their stability regions hold respectively for $|Bi| < 1$ and $|Bi| > 1$. Therefore, such techniques are unsuitable for locally swapping conditions around unity. Instead, the methods characterized by a Robin boundary condition, either the heat transfer Forward Temperature Back (hFTB) [125] or the heat transfer Forward Flux Back (hFFB) [126], exhibit a wider stability region. In fact, they provide the possibility of controlling the Biot number ranges in which stability is obtained through a user-imposed "virtual heat transfer coefficient" $\tilde{h}$ (introduced later), thus promoting the convergence of the fluid-solid coupling. Finally, [127] presents a recent development with Robin boundary conditions applied to both the domains, demonstrating the technique in a one-dimensional incompressible test case.

Method	Fluid BCs	Solid BCs
FFTB	Dirichlet	Neumann
TFFB	Neumann	Dirichlet
hFTB	Dirichlet	Robin
hFFB	Neumann	Robin
hFRB	Robin	Robin

Table 2.1 Partitioned coupling methods for the conjugate problem.

The hFFB method is selected in the present study since a heat flux boundary condition imposed to the fluid domain would generally improve the convergence stability of the CFD computation compared to an imposed wall temperature

boundary condition. The corresponding workflow is presented in Figure 2.9 and discussed hereafter.

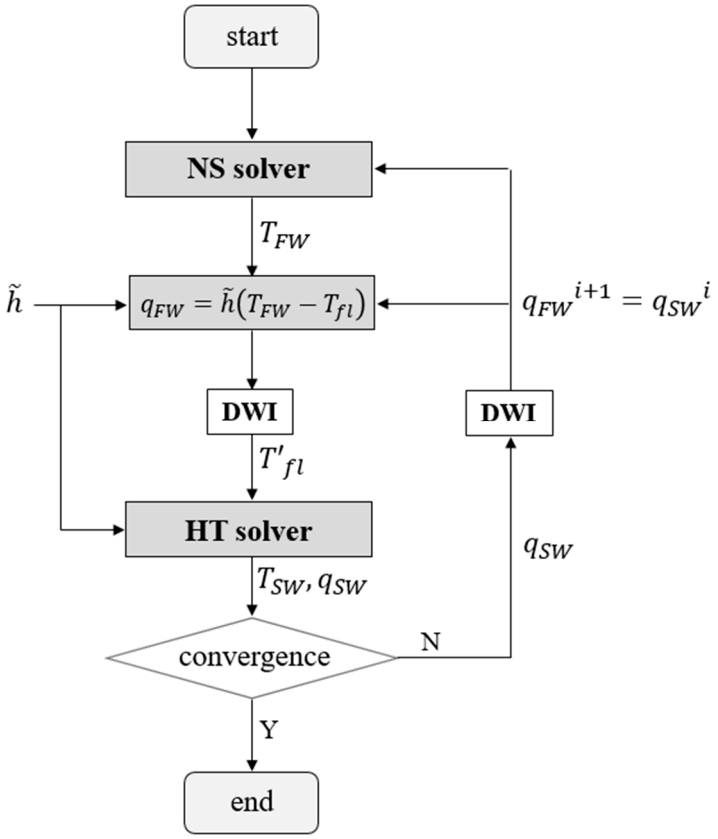

Figure 2.9 hFFB coupling method for the CHT analysis.

The conjugate problem is addressed with an initial CFD computation considering adiabatic walls. The fluid temperature T_{FW} and the heat flux normal to the walls q_{FW} are retrieved at the boundaries in contact with the solid, and a virtual fluid bulk temperature T_{fl} is calculated as:

$$T_{fl} = T_{FW} - \frac{q_{FW}}{\tilde{h}} \tag{2.3}$$

with $\tilde{h}$ indicating a constant user-defined virtual heat transfer coefficient.

Since the initial fluid simulation is adiabatic, Eq. (2.3) returns a virtual fluid bulk temperature equal to the fluid temperature at the walls. The DWI procedure computes the interpolated T'_{fl} field associated with the solid grid nodes.

Consequently, $\tilde{h}$ and T'_{fl} are assigned to the FEM heat transfer model, such that the convective load to the solid results from the following boundary condition:

$$q_{SW} = \tilde{h}(T - T'_{fl}) \tag{2.4}$$

with T as the unknown solid nodal temperatures.

After solving the FEM heat transfer problem, the temperature and the heat flux distributions at this boundary are known. Therefore, the heat flux at the interface is calculated from the solid temperature field *T* by means of the Fourier's law applied to all the finite elements exposing at least one face to the fluid:

$$q_{SW} = -k\frac{dT}{dn} \tag{2.5}$$

with dT/dn indicating the temperature gradient normal to the wall and *k* the thermal conductivity coefficient.

The heat flux q_{SW} is processed by the DWI routine, returning the heat flux q_{FW} assigned to the fluid cells at the interface. A new CFD simulation, now accounting for an external heat flux at the viscous walls, is recomputed and the entire workflow is re-iterated for several loops, till the achievement of the continuity of the temperature at the interface between the two fields. [122] demonstrates that

$$if\ \left|q_{FW}^{i+1} - q_{FW}^{i}\right| \to 0 \quad then\ \begin{cases}\left|T_{SW}^{i} - T_{FW}^{i}\right| \to 0\\ \left|q_{SW}^{i} - q_{FW}^{i}\right| \to 0\end{cases}. \tag{2.6}$$

The user-imposed virtual heat transfer coefficient $\tilde{h}$ does not affect the final solution of the coupling problem, but it influences the predicted wall heat fluxes at any intermediate cycle of the conjugate procedure, thus determining the convergence path of the thermal analysis. In the case of the hFFB method, [119] shows that a suitable choice of the virtual coefficient $\tilde{h} < 2h$, with h as the physical value of the convective heat transfer coefficient, would guarantee the convergence of the CHT problem for any local value of the Biot number. The higher the value of $\tilde{h}$ within the stable region, the faster the convergence of the partitioned coupling method. A discussion about the determination of a suitable $\tilde{h}$ value for a problem of industrial relevance is reported in Section 2.4.2.

2.3 Primal solvers

2.3.1 Solid heat transfer solver

The heat transfer phenomena within the solid domain are modelled through a steady linear FEM solver, developed according to [128].

The governing equation for the energy balance in a solid medium is defined as:

$$\rho c\frac{dT}{dt} = \nabla \cdot q + Q \tag{2.7}$$

with *T* indicating the solid temperature and *q* the heat flux, ρ is the material density, *c* is the heat capacity, *t* is the time, and *Q* is the internal heat source.

The weak form of Eq. (2.7) is obtained by multiplying each term by a small perturbation of the unknown temperature δT, and integrating it over the entire volume [129]:

$$\int_V \rho c \frac{dT}{dt} \delta T \, dV = -\int_V \nabla \cdot q \, \delta T \, dV + \int_V Q \, \delta T \, dV \, . \tag{2.8}$$

Since the conjugate problem under analysis is about a steady state operating condition and there is no internal heat source, Eq. (2.8) reduces to

$$\int_V \nabla \cdot q \, \delta T \, dV = 0 \, . \tag{2.9}$$

Eq. (2.9) is integrated per parts, resulting in the following:

$$\int_S q \, \delta T \, dS - \int_V q \, \nabla(\delta T) dV = 0 \, . \tag{2.10}$$

The heat flux q is described by the Fourier's law: $q = -k\nabla T$. Concerning the surface integral at the first term, if the solid surface consists in $S = \partial\Omega_1 + \partial\Omega_2 + \partial\Omega_3$, the relevant boundary conditions will be distinguished in the following families:

- Dirichlet – Constant temperature applied to the reference surface Ω_1:

$$T|_{\Omega 1} = const \, . \tag{2.11}$$

- Neumann – Heat flux q imposed to the reference surface Ω_2:

$$-k\nabla T|_{\Omega 2} = q \, . \tag{2.12}$$

  If q=0, an adiabatic wall boundary condition is defined.

- Robin – Convection boundary condition applied to the reference surface Ω_3:

$$-k\nabla T|_{\Omega 3} = \tilde{h}\left(T|_{\Omega 3} - T'_{fl}\right) . \tag{2.13}$$

  Here, the heat flow is proportional to the temperature difference between the wall and the surrounding fluid. For sake of consistency with the hFFB coupling method presented in Section 2.2.4, the virtual convective heat transfer coefficient $\tilde{h}$ and the interpolated virtual fluid bulk temperature T'_{fl} are reported in Eq. (2.13).

The implementation of such boundary conditions is discussed in Section 2.5 through the modelling of a radial turbine test case.

On the boundaries where the heat transfer between the fluid and the solid is established through the application of a Robin boundary condition, Eq. (2.10) can be reformulated as

$$\int_V k\nabla T \; \nabla(\delta T) dV = -\int_S \tilde{h}\left(T - T'_{fl}\right) \delta T \, dS \, . \tag{2.14}$$

The solid domain is discretized through an unstructured mesh of second order tetrahedral elements. The temperature is interpolated in the domain by an isoparametric formulation based on the shape functions φ [130], such that

$$T = \sum_{i=1}^{N} \varphi_i T_i$$
$$\delta T = \sum_{j=1}^{N} \varphi_j \delta T_j \tag{2.15}$$

with N as the number of nodes in a finite element.

Therefore, Eq. (2.14) is discretized as follows:

$$\sum_e \sum_i \sum_j \underbrace{\left[\int_{V_e} \mathrm{k}\, \nabla\varphi_i \nabla\varphi_j \, dV_e \right]}_{A_{cond}} T_i \delta T_j = -\sum_e \sum_i \sum_j \underbrace{\left[\int_{S_e} \tilde{h} \varphi_i \varphi_j dS_e \right]}_{A_{conv}} T_i \delta T_j + \sum_e \sum_j \left[\int_{S_e} \tilde{h} T'_{fl} \varphi_j dS_e \right] \delta T_j \tag{2.16}$$

with e representing the number of finite elements comprised in the domain.

Therefore, Eq. (2.16) results in the following linear system:

$$A\, \boldsymbol{T} = b\,. \tag{2.17}$$

$\boldsymbol{T}$ indicates the unknown temperature field. The LHS matrix A, comprising the conductive and the convective terms $A = [A_{cond} + A_{conv}] \in R^{n,n}$, is symmetric positive definite (SPD). Finally, the RHS vector $b \in R^n$ accounts for the fluid boundary condition.

Further details about the domain discretization are reported in Section A.1 and A.2.

The system in Eq. (2.17) is solved through an iterative Conjugate Gradient method [131], returning the temperature field in the solid domain.

Finally, for each finite element in contact with the fluid, the normal component of the heat flux at the solid surface is computed by applying Fourier's law (cf. Eq. 2.5). Such heat fluxes are imported in the DWI procedure for an interpolation and later assignment to the neighboring fluid cells.

2.3.2 Fluid solver

A sensible aspect in the choice of a loose coupling scheme is the possibility of adopting already existing and well-established solvers. It is the case for the fluid dynamic analysis, relying on the three-dimensional compressible Reynolds-Averaged Navier–Stokes solver developed by [54].

The fluid domain is discretized through a cell-centered finite volume scheme defined on a multi-block structured grid. The solver computes the convective fluxes by Roe's upwind scheme with MUSCL extrapolation, while a central discretization is applied to the calculation of the viscous fluxes. The eddy viscosity hypothesis is adopted for the treatment of the turbulence, which is represented by the negative Spalart–Allmaras model. The N-S equations are solved through an implicit integration scheme resulting in the linear system formulated in Eq. (2.18):

$$\left[\frac{V}{\Delta t} I + \left.\frac{\partial R}{\partial U}\right|_n\right] \Delta U = -R(U_n) \tag{2.18}$$

with R indicating the flow residuals, U the conservative variables, and V the cells volumes.

The implementation of the time marching technique follows the JT-KIRK scheme proposed in [61], whose convergence rate to a fully steady state solution is pivotal to the achievement of an improved stabilization of the discrete adjoint solver. Acceleration techniques are implemented through the local time-stepping and the multigrid approaches.

In order to attain a conjugate coupling, the original adiabatic walls assumption is replaced by a Neumann boundary condition weakly imposed to the viscous walls. The heat fluxes, computed in the solid domain and interpolated through the DWI procedure (cf. Eq. 2.1), are assigned to the relevant cells centers on the fluid block boundaries in contact with the solid, leveraging the concept of the dummy cells [132]. Figure 2.10 shows the two layers of ghost cells, named *G1* and *G2*, present in the finite volume discretization with the aim of facilitating the computation of the inviscid and viscous fluxes at the interfaces. *D1* is the first layer in the inner (physical) domain.

According to the thin shear layer approximation [133], the fluid temperature in *D1* is detected from the previous solver iteration, and the ghost cell temperature in *G1* is updated as follows:

$$T_{G1} = T_{D1} - q_{FW} \frac{\Delta n}{k_{fl}} \tag{2.19}$$

with Δn as the characteristic length represented by the distance of the two adjacent cells centers, and k_{fl} as the locally computed fluid conductivity. Similarly, the temperature in G2 is updated in cascade, following Eq. (2.19) with the newly computed T_{G1}in place of T_{D1}, and a consistent value for the thermal resistance.

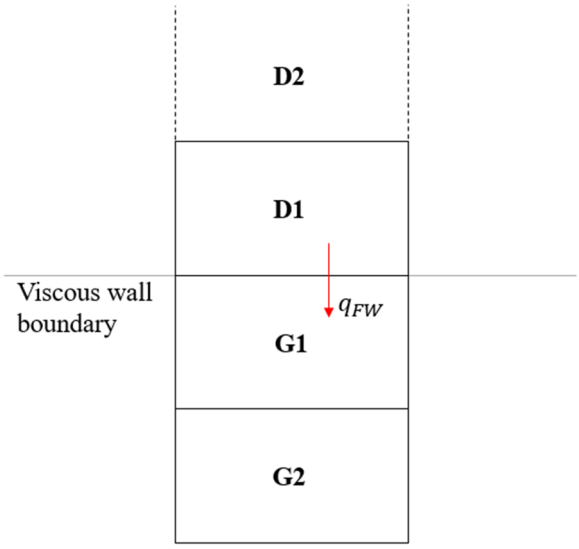

Figure 2.10 Heat flux through ghost layers at wall boundaries.

The thermal field computed in the ghost cells supports the computation of the corresponding densities by means of the ideal gas law, under the assumption of a zero-order pressure extrapolation in wall-normal direction. Additionally, the no-slip condition at the walls is satisfied by reversing the components of the flow velocities in the ghost layers w.r.t. the first two inner layers.

In order to preserve the unconditional stability of the integration scheme, the boundary condition in Eq. (2.19) is linearized, providing contributions to the linearized flow residuals $\partial R/\partial U$ at the LHS of the system in Eq. (2.18). In this respect, [54] reports that the Jacobian matrix of the inviscid and viscous fluxes at a boundary F_{bnd} can be computed with the chain rule of differentiation as follows:

$$\frac{dF_{bnd}}{dU_{D1}} = \left[\frac{\partial F_{bnd}}{\partial V_{D1}} + \frac{\partial F_{bnd}}{\partial V_{G1}}\frac{\partial V_{G1}}{\partial V_{D1}}\right]\frac{\partial V_{D1}}{\partial U_{D1}} \tag{2.20}$$

with V_x indicating the primitive variables, and $\partial V_{G1}/\partial V_{D1}$ as the 5x5 flow transformation matrix from the ghost cell to the first inner layer. In the case of viscous fluxes at a solid wall, its formulation is the following:

$$\frac{\partial V_{G1}}{\partial V_{D1}} = \begin{bmatrix} a & 0 & 0 & 0 & 0 \\ 0 & -1 & 0 & 0 & 0 \\ 0 & 0 & -1 & 0 & 0 \\ 0 & 0 & 0 & -1 & 0 \\ 0 & 0 & 0 & 0 & 1 \end{bmatrix} \tag{2.21}$$

The central terms on the diagonal reflect the no-slip condition. The last term refers to the zero-order pressure extrapolation. The first term, indicated with a, is equal to unity in case of an adiabatic wall assumption. However, because of the newly implemented Neumann condition, this term is computed as

$$a = \frac{\partial \rho_{G1}}{\partial \rho_{D1}} = \frac{1}{1 - \frac{q_{FW} \Delta n}{k_{fl} T_{D1}}} \tag{2.22}$$

Eq. (2.22) is discussed in Section A.4

The rate of convergence of the integration scheme in presence of a Neumann boundary condition is influenced by the actual value of the heat flux appearing in Eq. (2.19). Since the current implementation relies on the hFFB method, no under-relaxation factors are necessary for the update of the ghost cells temperatures, because they are replaced by a suitable choice of the virtual heat transfer coefficient $\tilde{h}$, determinant for the stability of the coupling process [119].

2.3.3 Solid mechanical solver

The workflow presented in Figure 2.9 completes with the achievement of the continuity of temperatures and heat fluxes at the fluid-solid interface. Hence, the thermal field in the solid domain is exported for the computation of the thermo-mechanical stresses.

The mechanical solver in primal mode is based on the work of [134] and consists in a FEM linear elastic solver with volume discretization through quadratic tetrahedral elements. The problem is described according to the following equilibrium equations in a three-dimensional Cartesian coordinates system [130]:

$$\begin{cases} \frac{\partial \sigma_{xx}}{\partial x} + \frac{\partial \sigma_{yx}}{\partial y} + \frac{\partial \sigma_{zx}}{\partial z} + f_x = \rho \frac{\partial^2 u}{\partial t^2} \\ \frac{\partial \sigma_{xy}}{\partial x} + \frac{\partial \sigma_{yy}}{\partial y} + \frac{\partial \sigma_{zy}}{\partial z} + f_y = \rho \frac{\partial^2 v}{\partial t^2} \\ \frac{\partial \sigma_{xz}}{\partial x} + \frac{\partial \sigma_{yz}}{\partial y} + \frac{\partial \sigma_{zz}}{\partial z} + f_z = \rho \frac{\partial^2 w}{\partial t^2} \end{cases} \tag{2.23}$$

with σ_{ij} indicating the normal and the shear stresses, (u, v, w) as the three components of the displacements, ρ as the density, and f_i corresponding to the loads in the x-y-z directions.

Because of the constitutive equation, the stresses σ can be formulated as a function of the strains tensor ε, following Hooke's law:

$$\sigma = E\, \varepsilon \tag{2.24}$$

with *E* representing the elasticity matrix.

Moreover, the relation between strains and displacements is expressed by Eq. (2.25):

$$\begin{Bmatrix}\varepsilon_{xx}\\ \varepsilon_{yy}\\ \varepsilon_{zz}\\ \gamma_{xy}\\ \gamma_{yz}\\ \gamma_{xz}\end{Bmatrix} = \begin{bmatrix}\partial/\partial x & 0 & 0\\ 0 & \partial/\partial y & 0\\ 0 & 0 & \partial/\partial z\\ \partial/\partial y & \partial/\partial x & 0\\ 0 & \partial/\partial z & \partial/\partial y\\ \partial/\partial z & 0 & \partial/\partial x\end{bmatrix}\begin{Bmatrix}u\\ v\\ w\end{Bmatrix}$$
$$= \begin{bmatrix}\partial/\partial x & 0 & 0\\ 0 & \partial/\partial y & 0\\ 0 & 0 & \partial/\partial z\\ \partial/\partial y & \partial/\partial x & 0\\ 0 & \partial/\partial z & \partial/\partial y\\ \partial/\partial z & 0 & \partial/\partial x\end{bmatrix}\begin{Bmatrix}\sum_i \varphi_i u_i\\ \sum_i \varphi_i v_i\\ \sum_i \varphi_i w_i\end{Bmatrix} = B\,U \tag{2.25}$$

Eq. (2.25) presents the isoparametric formulation discussed in Section A.1. Thus, the strain-displacements relation is established through the strain matrix B in a finite element formulation.

Hence, the system of equations (2.23) can be described in compact form as:

$$M\ddot{U} + SU = f \tag{2.26}$$

with $M \in R^{n,n}$ indicating the mass matrix at the RHS of (2.23), $f \in R^n$ as the force vector, $U \in R^n$ enclosing the whole displacements field, and $S \in R^{n,n}$ representing the derivatives matrix also known as stiffness matrix. Both the matrices M and S are SPD.

The thermo-mechanical problem under consideration pertains to a steady state operative condition. Thus, the mass matrix term is neglected. After applying a small perturbation δU to Eq. (2.26) and interpolating the displacements field through an isoparametric formulation like in Eq. (2.15), the integration of the system (2.23) over the solid domain by the finite element method results in the following explicit form [129]:

$$\sum_e \sum_i \sum_j \underbrace{\left[\int_{V_e} B^T \mathrm{E}\,\mathrm{B}\, dV_e\right]}_{S_e} U_i \delta U_j$$
$$= \sum_e \sum_j \left[\int_{V_e} \rho \varphi_j b(\omega) dV_e\right] \delta U_j$$
$$+ \sum_e \sum_j \left[\int_{V_e} B^T E \varepsilon_{th} dV_e\right] \delta U_j$$
$$+ \sum_e \sum_j \left[\int_{S_e} \varphi_j t\, dS_e\right] \delta U_j \tag{2.27}$$

Eq. (2.27) presents a load vector *f* at the RHS comprising three contributions. The first term refers to the centrifugal forces, function of the wheel rotational speed ω. The second term introduces the thermal strains ε_{th}, defined as:

$$\varepsilon_{th} = \alpha(T)\left(T - T_{ref}\right) \tag{2.28}$$

with *α(T)* indicating the thermal expansion coefficient of the material (dependent on the local temperature), *T* as the temperature field returned by the heat transfer solver, and T_{ref} as a reference temperature at which no thermal stresses are present in the solid. In the current work, we refer to T_{ref} as the ambient temperature. Through the thermal strains, the stresses in the material depend on the outcome of the CHT computation, which increases the complexity of the gradients calculation, as presented later on.

The last term at the RHS of Eq. (2.27) is the boundary condition of imposed displacement or traction (for instance, a pressure loading) which is assigned to the solid surface.

It is worth mentioning the solid mesh adopted by the heat transfer solver is shared with the mechanical computations in order to avoid any temperature re-interpolation. This choice is particularly convenient during the development of the adjoint solvers, as discussed in Chapter 3.

Finally, once the displacement field *U* is computed, the workflow is completed by the calculation of the maximum von Mises stress, which takes place through a p-norm function:

$$\sigma_{\max\_VM} \approx \lim_{p\to\infty} \sqrt[p]{\frac{\int \sigma_{VM}^{p} dV}{\int dV}} \,. \tag{2.29}$$

A value of $p = 75$ is selected herein in order to avoid any numerical overflow issue induced by too high values of the exponent. Moreover, it is interesting to note Eq. (2.29) establishes a weighting over the spatial extent of the stress concentration as well. In fact, in case two regions of the domain exhibit the same peak value of σ, but one of them is much smaller than the other, the p-norm function gives priority to the location where the peak stress is spread over a wider area, hence addressing the focus of the optimizer on the most severe location first.

Eq. (2.29) is a continuous function and is globally differentiable, hence fulfilling the requirements for an adjoint development.

In conclusion, instead of an elastic solution accounting only for the centrifugal loading, the present framework allows considering also the impact of the thermal stresses, whose contribution is non-negligible in solid regions experiencing high temperature gradients. This statement is consolidated by the assessment offered in Section 2.5.

The outcome of Eq. (2.29) represents the cost function (or constraint) of the optimization problem, whose gradient computation kicks off the adjoint framework in reverse mode, as discussed in Chapter 3.

2.4 Applications

2.4.1. Flat-plate

The CHT workflow discussed in Section 2.3 is validated with reference to the conjugate problem of a flat plate, whose analytic solution is offered by [86]. The thin plate experiences an incompressible flow with zero incidence angle and temperature T_∞, while the bottom face presents a constant sink temperature $T_c < T_\infty$. The thermal coupling of the two domains takes place at their interface, identified in the plate upper surface. A thermal boundary layer develops in correspondence of it and the flow imposes its convective loading, while a conductive path develops within the material.

Table 2.2 summarizes the domains dimensions, the corresponding mesh settings and the boundary conditions. The fluid domain is discretized by a structured mesh comprising two blocks. The mesh stretching in correspondence of the blocks interface and on the flat plate upper surface (Figure 2.11) provides a proper representation of the boundary layer. A no-slip condition is assigned to the flat plate top face, while all the other surfaces are treated as symmetry planes. The solid domain is discretized by an unstructured mesh of second order tetrahedral elements. Therefore, the non-conformal meshes rely on the DWI procedure for the exchange of information at their interface.

The thermal conductivity coefficient k adopted for the solid phase is aimed at obtaining an average Biot number around unity, while the virtual heat transfer coefficient $\tilde{h}$ is selected as a compromise between convergence rate and stability.

Figure 2.12 shows the convergence history of the conjugate problem, determined by the maximum temperature difference L_∞ between two consecutive fluid-solid interactions.

$$L_\infty = \left| T_s^{i+1} - T_s^i \right|_{max} \tag{2.30}$$

Domain Settings	Value
Fluid domain length/height	0.25 m/0.1 m
Fluid mesh cells count	365,000
Plate thickness/length	0.01 m/0.2 m
Solid mesh nodes count/elements count	35,000
Fluid type	Air
Inlet flow total pressure $p°_\infty$	1.03×10^5 Pa
Inlet flow total temperature $T°_\infty$	1000 K
Outlet flow static pressure p_{out}	1.029×10^5 Pa
Plate temperature at bottom face T_c	600 K
Plate thermal conductivity k	0.29 W/m K
Virtual heat transfer coefficient $\tilde{h}$	100 W/m^2 K

Table 2.2 Flat plate domain characteristics and boundary conditions.

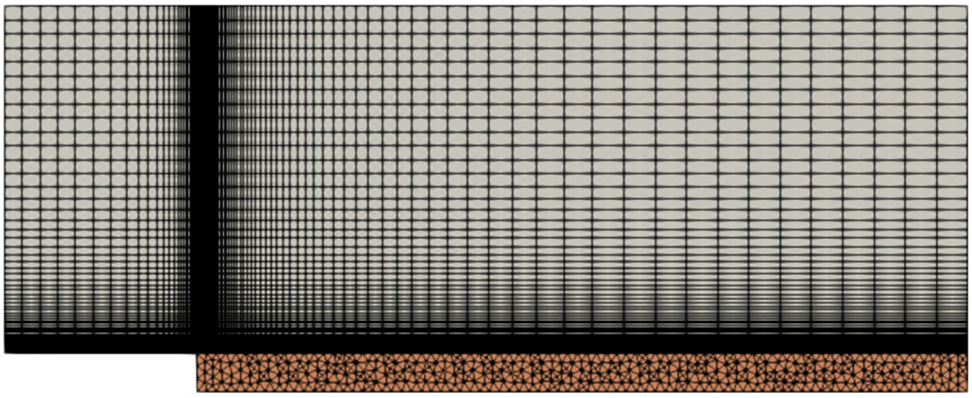

Figure 2.11 Heat flux through ghost layers at wall boundaries.

In the present case study, a threshold of 1K is selected as stabilization criterion for the model.

The comparison of the temperature distribution at the domains interface w.r.t. the analytic solution obtained through Luikov's differential heat transfer (DHT) method is reported in Figure 2.13-a. Figure 2.13-b shows the temperature profiles in a vertical section along the plate in correspondence of the axial coordinate x = 0.05m. In both cases, the conjugate computation returns a solution in sufficient agreement with the analytic one, and within the limits of the DHT approach, which cannot account for the lateral conductivity in the solid domain, and the consequent impact on the temperature evolution in streamwise direction, as discussed in [127].

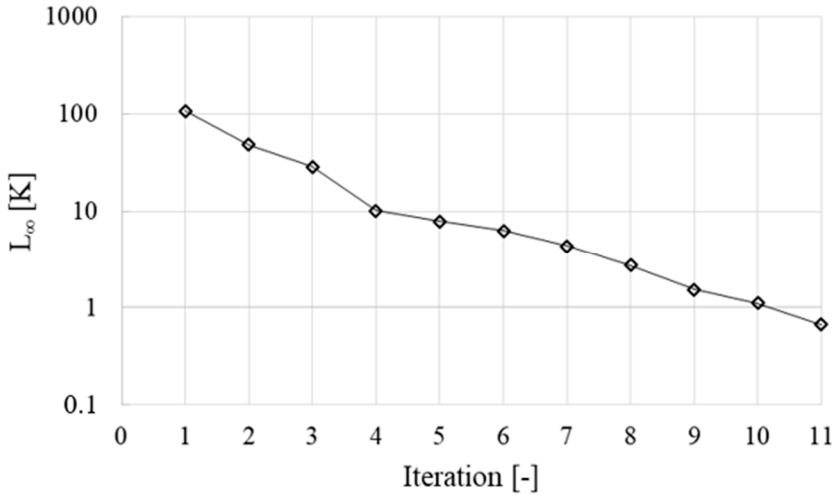

Figure 2.12 Convergence history of $\boldsymbol{L}_\infty$.

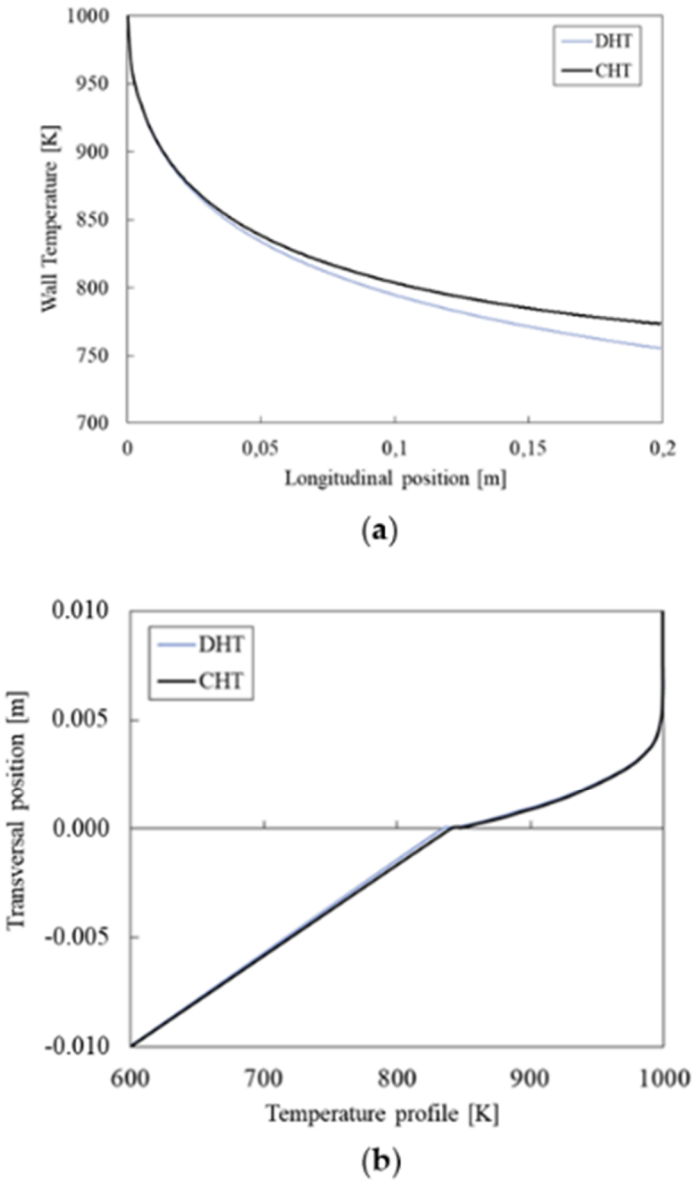

Figure 2.13 CHT problem for flat plate: a) temperature at the domains interface, b) temperature profile at x=0.05m. Numerical Vs. analytic solutions.

2.4.2. Radial turbine mesh sensitivity analysis

A sensitivity study is conducted with the goal of defining the settings for the execution of the CHT analysis on a three-dimensional test case, i.e. a radial turbine impeller presented in [54]. The wheel is characterized by a diameter of 50.0mm, an axial length of 25.0mm, and ten blades with a tip clearance w.r.t. the housing of 0.3mm. Figure 2.14 reports a projection of the rotor on its meridional plane, highlighting the locations where the boundary conditions are imposed.

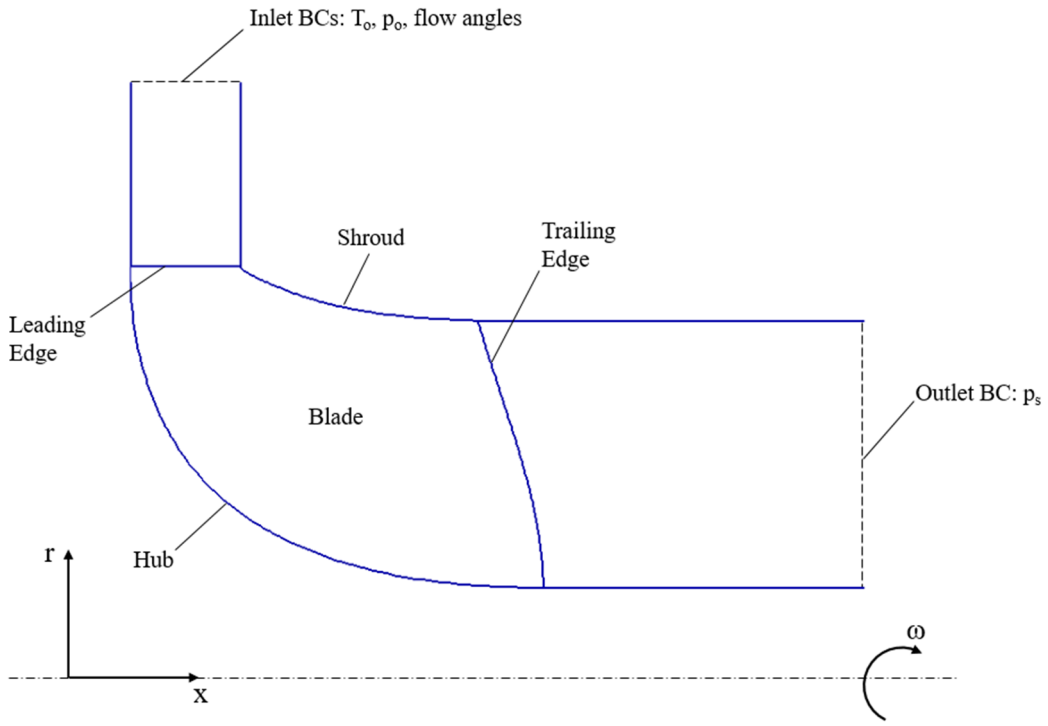

Figure 2.14 Turbine rotor meridional view and location of the boundary conditions.

The method of the characteristics [133] is adopted to establish the number of physical conditions to be assigned at the inflow and outflow boundaries. The total upstream temperature and pressure are specified at the inlet of the domain, along with the flow velocity components in the corresponding coordinate system. At the subsonic outflow boundary, a single flow variable is imposed, specifically the downstream static pressure. The boundary conditions applied to the problem are summarized in Table 2.3, in which the impeller rotational speed is also included.

Boundary conditions	**Value**
Inlet total pressure p_0	173 kPa
Inlet total temperature T_0	1080 K
Inlet flow angle α from radial direction	62 deg
Outlet static pressure p_s	101 kPa
Blade rotational speed ω	140000 RPM

Table 2.3 Turbine rotor boundary conditions.

The sensitivity analysis is performed through the method of the Orthogonal Array [135]. Three variables relevant for the solution of the conjugate problem are considered herein: the fluid mesh size, the solid mesh size, and the virtual heat transfer coefficient $\tilde{h}$. Each "factor" is explored over three levels of refinement (cf. Table 2.4), generating nine combinations according to the L9 Orthogonal

Array scheme, as presented in Table 2.5. Such matrix of test cases favors the exploration of the mutual interactions of the parameters, with the goal of identifying for each of them the most suitable value, in accomplishment of the minimization of an objective function presented hereafter. The target is the achievement of an optimal trade-off between computational cost and accuracy with the aim of introducing the CHT analysis into the optimization process.

All the simulations are run till convergence at a relative residuals drop of 10^{-8} for the CFD solver and 10^{-10} for the FEM solver, while the CHT workflow is stopped for a maximum deviation in wall temperature between two successive fluid-solid iterations L_∞ below 1K. y+ values below unity are obtained for the "mid" and "fine" levels of the fluid grid refinement, while the coarsest one exhibits a peak in y+ around 2.5 at the blade leading edge.

Factors Levels	**Value**
Fluid domain "coarse"—cells count	0.8 M
Fluid domain "mid"—cells count	1.3 M
Fluid domain "fine"—cells count	2.1 M
Solid domain "coarse"—nodes count	105 k
Solid domain "mid"—nodes count	295 k
Solid domain "fine"—nodes count	1.1 M
$\tilde{h}$ low–mid–high (W/m² K)	800–1000–1300

Table 2.4 Fluid and solid mesh refinements, $\tilde{h}$ levels.

Test case number	**CFD Mesh**	**FEM Mesh**	$\tilde{h}$ **[W/m^2 K]**
1	coarse	coarse	800
2	coarse	mid	1000
3	coarse	fine	1300
4	mid	coarse	1000
5	mid	mid	1300
6	mid	fine	800
7	fine	coarse	1300
8	fine	mid	800
9	fine	fine	1000

Table 2.5 L9 Orthogonal Array applied to the turbine rotor CHT analysis.

The results of the nine simulations are presented in Table 2.6. In general, the prediction of the maximum temperature in the solid domain reveals a low sensitivity w.r.t. the factor levels under investigation, except in the first case, in which coarse meshes are considered for both the media. In fact, the quality of the interpolation of the information at the interface of the domains may suffer in case of too coarse grids, despite the presence of virtual nodes on the fluid side, as

described in Section 2.2.3. On the contrary, finer solid meshes increase the resolution of the convective loads imported in the FEM computations, resulting in more accurate predictions of the temperature field and the heat fluxes. Figure 2.17 compares two solid grids of different quality, the first one set at a coarse level (cf. Figure 2.17-a), and the second one with elements of medium size (cf. Figure 2.17-b) and with the addition of a local refinement at the trailing edge, as discussed hereafter. In the case of the finer solid grid, the interpolation procedure returns a richer temperature pattern at the interface, closely mirroring the fluid conditions at the walls; instead, the coarsest one approximates the thermal loading distribution, with the highest deviation localized in the blade tip region – where large secondary flows and leakages are present – and at the trailing edge.

Case #	#CHT Loops to Convergence [-]	Norm. Computational Time for CHT Iteration	Computational Time: CFD—FEM w.r.t. Total	Maximum Solid Temperature [K]	Delta Temperature Integral
1	11	1.0×	97.0–0.5%	1019	0.121
2	10	1.02×	95.2–1.9%	1025	0.053
3	9	1.36×	71.3–25.0%	1027	0.045
4	8	1.76×	98.3–0.3%	1026	0.092
5	10	1.78×	97.2–1.1%	1028	0.038
6	12	2.12×	81.6–16.1%	1028	0.023
7	11	2.4×	98.6–0.2%	1026	0.074
8	11	2.44×	97.2–0.8%	1028	0.019
9	8	2.76×	86.5–12.4%	1028	0.000

Table 2.6 Fluid-solid grid sensitivity: summary of CHT computations.

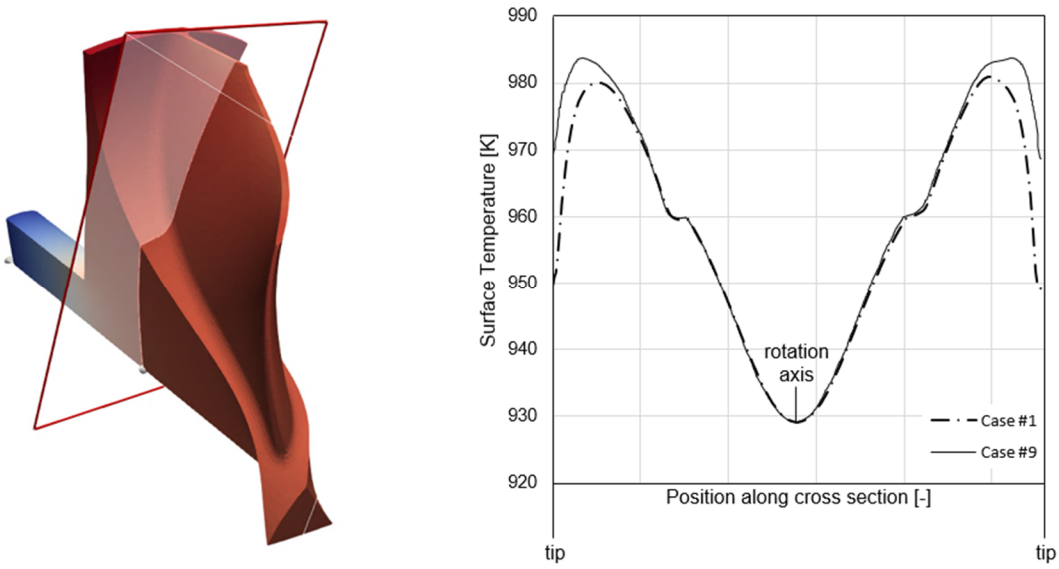

Figure 2.15 Temperature contours for test case 1 and test case 9 at the planar cross section on the blade.

An analysis of the temperature distribution on the blade surface is performed considering a cross section located at roughly 25% of the chord. This is a challenging location for the interpolation routine because of the presence of high convective perturbations due to the severe flow detachment at the blade leading edge and the high local mixing. Figure 2.15 shows the plane where the surface temperature distributions are detected for the nine test cases, as well as a comparison of temperature profiles for two extreme set-ups. For each candidate model, the integral of the temperature deviations w.r.t. the case 9 (elected as reference because showing the finest grids) is evaluated and reported in Table 2.6. It is possible to conclude the FEM coarsest mesh overestimates the temperature drop. This assessment is supported by the comparison of the two temperature contours in Figure 2.15, showing the case 1 with a more pronounced temperature decay, despite the high thermal gradients revealed by both the models around the thin region of the blade tip exposed to the flow vorticity.

The computational time associated to each set-up of the model is recorded and compared in Table 2.6. The data is normalized w.r.t. the total duration of the CHT analysis, therefore including also the hFFB procedure. All the tests are compared w.r.t. case 1, showing the coarsest fluid and solid meshes. The data post-processing reveals that, while the CFD simulations largely determine the cost of the thermal analysis, a noticeable rise in the computational timing is associated to the FEM when adopting the finest grid level. Such information enters the evaluation of the cost function, expressed as:

$$S = \omega A + (1 - \omega)B, \tag{2.31}$$

with the term A enclosing the normalized difference between the maximum temperature predicted by the test case of interest and test case 9, B representing the normalized computational time, and ω as the weighting coefficient. In the current study, $\omega = 0.7$ in order to bias the objective function towards the accuracy of the coupling process. Indeed, the factor levels finally expected from this study are the ones minimizing the signal S.

Figure 2.16 summarizes the outcome of the analysis of the Orthogonal Array, revealing the dependence of the signal S on the three factors and their correspondent levels. The goal is to identify the combination of parameters minimizing the cost function. In this respect, the chart illustrates that the virtual heat transfer coefficient $\tilde{h}$ is chosen at the highest possible level within the region of stability of the Biot number, as discussed in [119]. In fact, this parameter influences the B term in Eq. (2.31) by determining the rate of convergence of the CHT coupling process. In this study, $\tilde{h}$ = 1000 W/m^{2}K is the optimal value, since the highest factor level approaches the limit of the stability region, with incipient oscillations in the heat flux exchanged at the interface, before reaching convergence.

The solid mesh size determines the quality of the interpolation of the information exchanged at the domains interface and contributes to the cost function mainly through the A term in Eq. (2.31). The analysis favors the finest

grid levels, despite a negligible deterioration of the B term induced by the increased computational time. On the contrary, the sensitivity to the fluid mesh refinement reveals an opposite trend, because its influence on the A term is less pronounced since the coarsest grid level already provides good quality results. In this case, the driver for the selection is the computational budget, severely impacted by the finest fluid mesh.

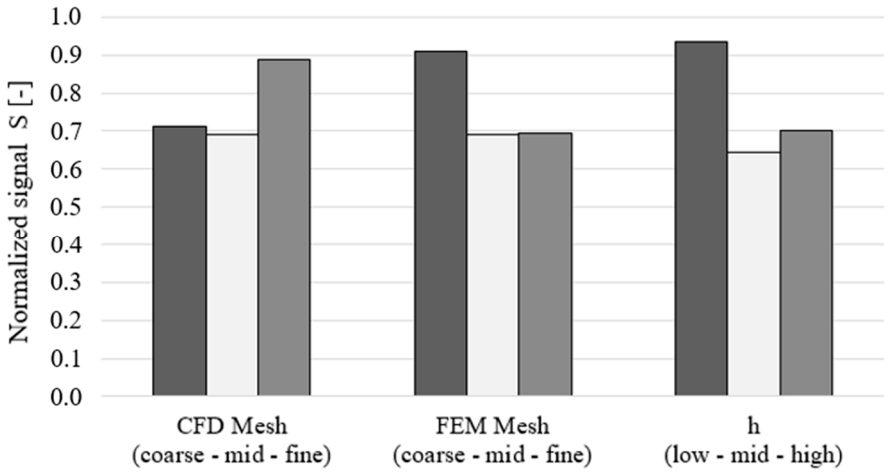

Figure 2.16 Normalized signal S dependence from factor levels in the Orthogonal Array.

Since the weighting coefficient ω in Eq. (2.31) privileges the accuracy of the CHT coupling process, the final selection of the factor levels results in the intermediate values for the refinements of both the grids and for the virtual heat transfer coefficient. However, it is recognized that smaller sizes for the solid finite elements improve the stability of the CHT coupling process, since they avoid any local poor quality in the discretization of the blade surface in correspondence of thin regions. For instance, Figure 2.17-a exhibits a coarse representation of the blade trailing edge, with sharp edges and local spikes. Such scenario generates a local alteration of the characteristic length L in Eq. (2.2), potentially inducing drops in the local Biot number and, therefore, inconsistencies with the selected $\tilde{h}$ value from a stability standpoint, even in the case of the hFFB method. Hence, this issue is addressed by the generation of a "hybrid" mesh configuration (cf. Figure 2.17-b), envisaging a local solid mesh refinement in correspondence of the blade tip surface and the trailing edge, whilst maintaining the intermediate elements size in the rest of the domain.

This last setup increases the mesh density to a total count of about 420k nodes, leading to a satisfactory trade-off between convergence rate of the conjugate problem and computational accuracy.

The analysis of the L9 Orthogonal Array is re-evaluated by modifying Eq. (2.31) with the assignment of the integral of the temperature deviations to the A term. The outcome is reported in Figure 2.18 and confirms the previous factors selection, except for the fluid mesh size, which promotes a trend towards the coarsest level because still providing sufficiently accurate results. However, since

the timing penalization on the signal *S* between the coarse and intermediate meshes is moderate, the previous choice of a medium size grid will be pursued for the sake of an improved prediction accuracy.

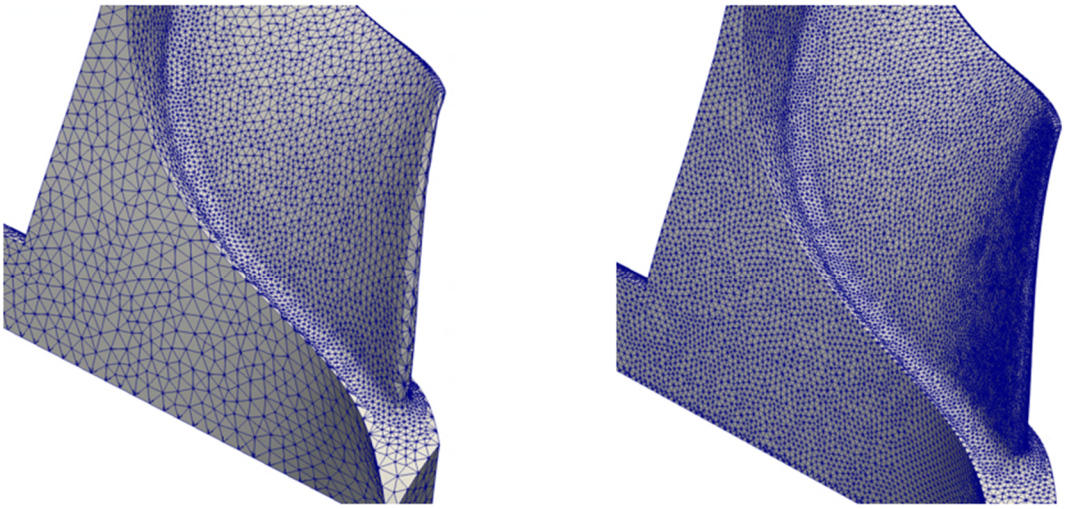

Figure 2.17 Comparison of solid mesh refinements: (a) coarse grid, (b) hybrid-mid grid.

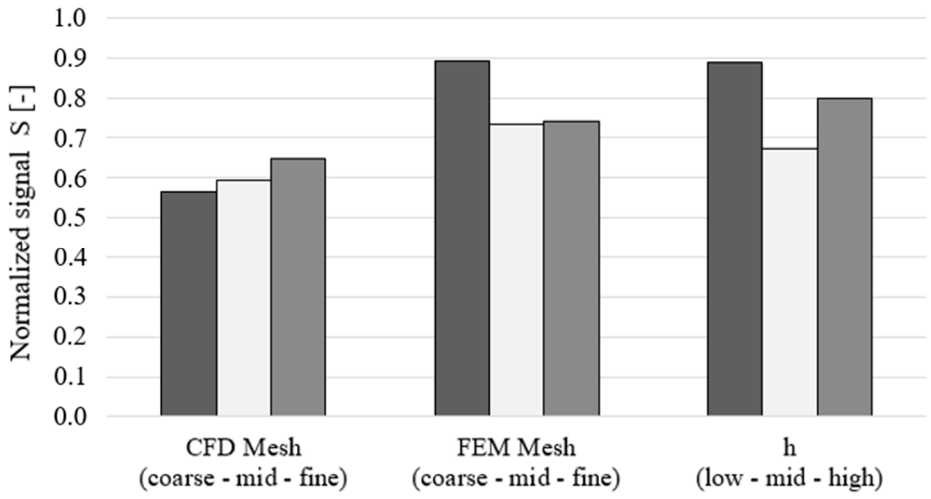

Figure 2.18 Normalized signal *S* dependence from factor levels in Orthogonal Array – integral of temperate deviation assigned to term *A*.

Based on such considerations, the settings returned by the analysis of the Orthogonal Array are considered for the further assessments of the coupling problem.

2.5 Closure

The thermo-mechanical workflow herein discussed is applied to the three-dimensional test case of the radial turbine impeller introduced in Section 2.4.2. The goal is to compare the resulting pattern of von Mises stresses w.r.t. the correspondent one computed with a fully decoupled structural mechanic approach insensitive to the convective loading.

The rotor operative condition is described in Table 2.3, along with an additional Dirichlet boundary condition of 500K assigned to the turbine shaft end section, with the aim of emulating the heat sink represented by the oil cooling system in the bearing housing of the real turbocharger application. The domain discretization is compliant with the conclusions of the mesh sensitivity analysis in the previous section. In particular, the fluid domain is represented by a multi-block structured mesh of about 1.3M cells with boundary layer refinement. The solid domain accounts for an unstructured grid of approximately 420k nodes and second-order tetrahedral elements.

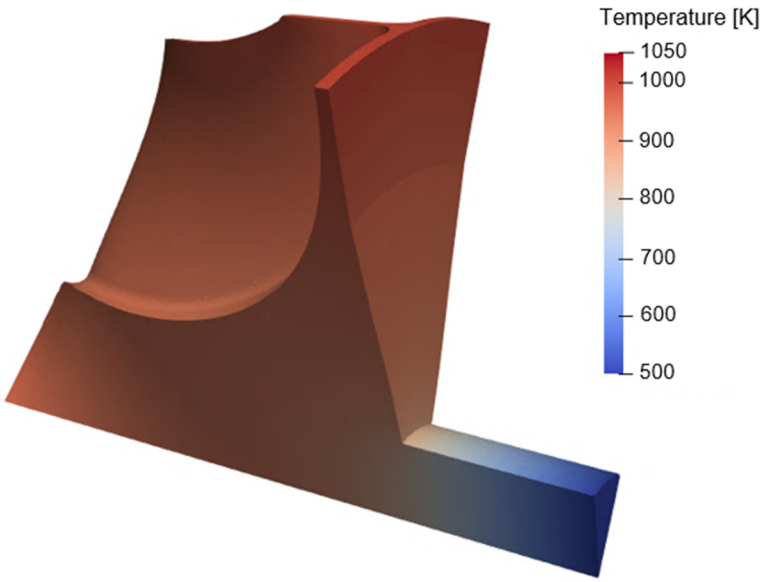

Figure 2.19 Solid temperature distribution with rotor experiencing convective loading from the exhaust gases and shaft cooling.

The CHT analysis results in the steady state temperature field reported in Figure 2.19. The highest thermal gradient is located in the region of the connection of the rotor back-plate with the shaft. The local thermal footprint is responsible for a variation in thermal strains according to Eq. (2.28) enhancing the generation of localized stresses. This statement is confirmed by the outcome of the mechanical computations performed with and without thermal loading, as reported in Figure 2.20. The normalized view of the distribution of von Mises stresses in the domain reveals a significant deviation in correspondence of the bulky area of the rotor, and in particular around the connection with the shaft. Therefore, it demonstrates that the analysis considering only the centrifugal forces

(cf. Figure 2.20-a) lacks in accuracy as it underestimates the local stresses with a maximum error of about 20%. Moreover, the material properties and the structural limit are temperature dependent parameters. Hence, the lack of knowledge about the temperature field would not allow accurately estimating the robustness of the component.

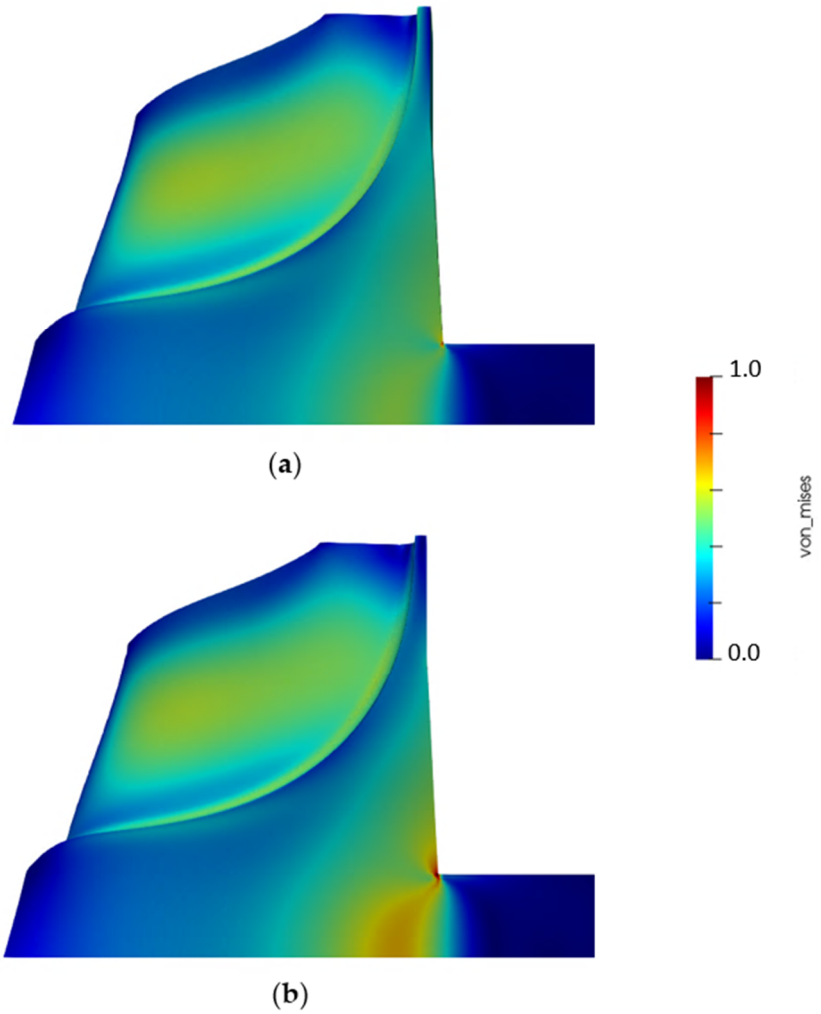

Figure 2.20 Normalized von Mises stresses pattern comparison in baseline layout: (a) mechanical versus (b) thermo-mechanical.

In conclusion, the test case under investigation demonstrates the need of a CHT evaluation during the design optimization of such critical component. In fact, the current impeller shape results from a previous optimization neglecting the thermal loading. Since the original stress pattern in Figure 2.20-a is at the limit of the elastic region for the material, it turns out the robustness of this design is impaired by the actual input of its own operative environment. In absence of any sophisticated framework, it is a common practice to assign large safety margins to the structural constraints. However, this approach poses a severe limitation to the optimization algorithm in the search for a viable solution. Starting from these considerations, the next chapter is devoted to the development of an adjoint framework capable of efficiently handling this class of problems.

Chapter 3

Thermo-mechanical stresses in adjoint solver

3.1 Adjoint gradients evaluation

The CHT analysis discussed in the previous chapter is an involved process because of its iterative nature in the achievement of the convergence of the conjugate problem. Therefore, it is recognized this discipline is less suited for gradient-free optimization methods, since the coupling technique presented in Section 2.2.4 would be associated to the assessment of each individual of a prohibitively large population, in the search for the global optimum.

An opportunity for the introduction of accurate thermal predictions in the optimization process arises from the adoption of a gradient-based technique. In fact, this family of methods accounts for a significantly lower number of candidates evaluations before reaching the locally optimal solution, since they rely on a more guided search in the design hyperspace. Moreover, this approach is particularly appealing when associated to an adjoint method for the computation of the derivatives of the state variables, as this technique is almost insensitive to the number of design variables. Therefore, it is suited to answer the new design requirements presented in the introduction.

The development of an adjoint method for the evaluation of the sensitivities of a cost function J w.r.t. the design variables $\alpha \in R^n$ is a two-step process. Figure 3.1 shows a general workflow applicable to any fluid or structural analysis. The first step involves the generation of a mesh with points coordinates $X \in R^m$, referred to the geometry resulting from the set of design variables α. It is followed by the execution of the primal solver(s) and the related post-processing routines, returning the response function J. Starting from this outcome, the second step is devoted to the computation of the sensitivities of the cost function w.r.t. the grid coordinates dJ/dX, as well as the evaluation of the sensitivities of the grid coordinates w.r.t. the design variables $dX/d\alpha$. Therefore, the sensitivities of the

cost function w.r.t. the CAD parameters can be expressed by the chain rule of differentiation as:

$$\frac{dJ}{d\alpha} = \frac{dJ}{dX}\frac{dX}{d\alpha}. \tag{3.1}$$

The first term at the RHS of Eq. (3.1), i.e. the sensitivities of the cost function w.r.t. the grid coordinates, is computed through a discrete adjoint method, as anticipated in Section 1.2.4. The next sections will be devoted to the discussion of the related differentiation scheme developed in reverse mode.

The second term at the RHS of Eq. (3.1), i.e. the sensitivity of the grid points coordinates w.r.t. the design variables $dX/d\alpha$, is traced back to the CAD-based parametrization approach implemented in CADO. In fact, during an optimization the grid coordinates are subjected to a perturbation based on the values of the term $\partial J/\partial X$. However, such local gradients may lead to very irregular shapes that could be in violation of some manufacturing constraints. Moreover, the conversion of the optimal geometry into a CAD model during the post-processing phase is inconvenient because it may induce some approximations, with a potential loss of details that may be detrimental for the achievement of the component performance. Therefore, a more robust approach consists in keeping the CAD parameters within the optimization loop [118].

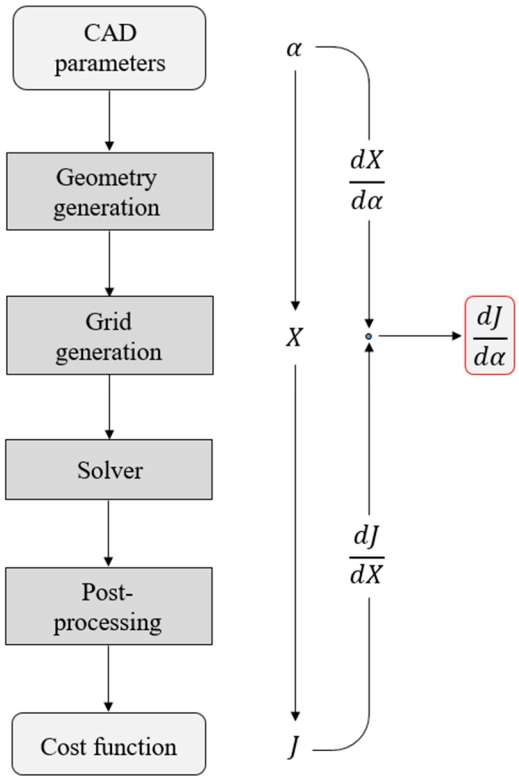

Figure 3.1 Workflow for primal and adjoint evaluations in fluid and solid analyses.

As described in Figure 3.1, any candidate geometry during the optimization is originated by the set of CAD parameters α, which can also be adopted to define some geometrical constraints aimed at supporting the fulfillment of the manufacturing requirements. The CAD kernel uses the design variables to create the CAD model through Bezier and B-spline curves [136]. Hence, the accurate computation of the derivatives $dX/d\alpha$ is performed by differentiating the CAD kernel and the grid generation tool through an Algorithmic Differentiation technique in forward mode [137].

The CAD surface determines the interface between the fluid and the solid domains, respectively discretized by a structured mesh and an unstructured grid. Therefore, in case of a FSI problem in which both domains collaborate to the determination of the cost function, the sensitivities w.r.t. the CAD parameters involve both the grids. Hence, Eq. (3.1) can be reformulated as follows:

$$\left(\frac{dJ}{d\alpha}\right)_{FSI} = \frac{dJ}{dX_{fl}}\frac{dX_{fl}}{d\alpha} + \frac{dJ}{dX_{sl}}\frac{dX_{sl}}{d\alpha}, \tag{3.2}$$

with X_{fl} indicating the fluid grid points coordinates, and X_{sl} as the corresponding solid grid points coordinates. Despite Eq. (3.2) appears as a combination of sensitivities separately computed in their own domains, the terms dJ/dX_{fl} and dJ/dX_{sl} are mutually influenced by the exchange of some adjoint variables through the interface, as will be thoroughly discussed in the next sections.

Finally, the cost function sensitivities w.r.t. the design variables are evaluated by an SQP-based algorithm, providing the descent direction for the multidisciplinary optimization problem and addressing the necessary shape perturbations. At every optimization iteration, instead of generating a completely new solid mesh, the update is executed by application of a morphing technique to the original FEM grid, with the aim of preserving the number of nodes and the original elements connectivity. Such means guarantees a more pronounced continuity in the variation of the sensitivities along the execution of the optimization and, therefore, a gradual evolution of the shape. The reader interested in the details of the different morphing techniques is addressed to [118] for a review of the Inverse Distance Method, and to [62] for the alternative concept of the Linear Elastic Analogy. Conversely, the structured fluid grid is recreated for any new geometry because self-preserving the finite volume mesh characteristics.

3.2 The adjoint thermo-mechanical workflow

The development of the adjoint workflow for the thermo-mechanical evaluations is consistent with the choice of a loose coupling approach performed in primal mode. The method differs from the tight coupling technique discussed in [138] accounting for the cross-discipline Jacobian terms to implicitly exchange

the boundary conditions between the two domains, and therefore directly solving the global adjoint system at once. Instead, the selected partitioned coupling method, despite being an iterative technique, is less intrusive in the structure of the fluid and solid solvers, allowing the integration of the adjoint CFD solver developed by [54] in the present workflow. This approach is advantageous in case of continuously growing multidisciplinary optimization platforms, and particularly suited to the treatment of transient operative conditions, as will be clarified in Chapter 4.

The complete thermo-mechanical workflow is shown in Figure 3.2. The iterative structure of the solution of the primal solver is maintained by the adjoint counterpart represented by the branch on the right.

The sensitivities of the cost function J_{TM} are computed by an Algorithmic Differentiation technique in reverse mode, as discussed in Eq. (1.12). The adjoint workflow is developed through the manual differentiation of the primal code. Even if more involved from development standpoint, the choice of the manual differentiation allows optimizing the memory footprint for the gradients evaluation, as no recording on tapes is necessary (as typically done by any automatic differentiation software [139]). This aspect is peculiar in case of extensive iterative workflows like the present one. Moreover, any incompatibility issue arising from the interactions between such software and the existing solvers is avoided.

The most computationally demanding terms in Eq. (3.2) are the sensitivities of the response function w.r.t. the grid points coordinates, dJ/dX. In case

$$J = J(X, u(X)) , \tag{3.3}$$

with u denoting the vector of the state variables, the application of the chain rule of differentiation to Eq. (3.3) results in the following:

$$\frac{dJ}{dX} = \frac{\partial J}{\partial X} + \frac{\partial J}{\partial u}\frac{du}{dX} . \tag{3.4}$$

The second term at the RHS is the partial derivative of the cost function w.r.t. the state variables. Because of the multidisciplinary nature of the FSI problem in Figure 3.2, the output state variables contributing to the calculation of the maximum von Mises stress depend on the intermediate states resulting from the previous CFD and FEM computations, such that

$$J = J\left(u_3\left(u_2(u_1)\right)\right) . \tag{3.5}$$

According to the "principle of the reverse differentiation" [140], we choose the output variable u_3, whose sensitivity dJ/du_3 is known, and calculate its sensitivities w.r.t. each intermediate state, till reaching the initial one:

$$\frac{dJ}{du_3}\ known$$
$$\frac{dJ}{du_2} = \frac{dJ}{du_3}\frac{du_3}{du_2} \tag{3.6}$$
$$\frac{dJ}{du_1} = \frac{dJ}{du_2}\frac{du_2}{du_1}$$

Therefore, the sensitivity of the cost function w.r.t. the initial state variable is finally obtained by Eq. (3.6).

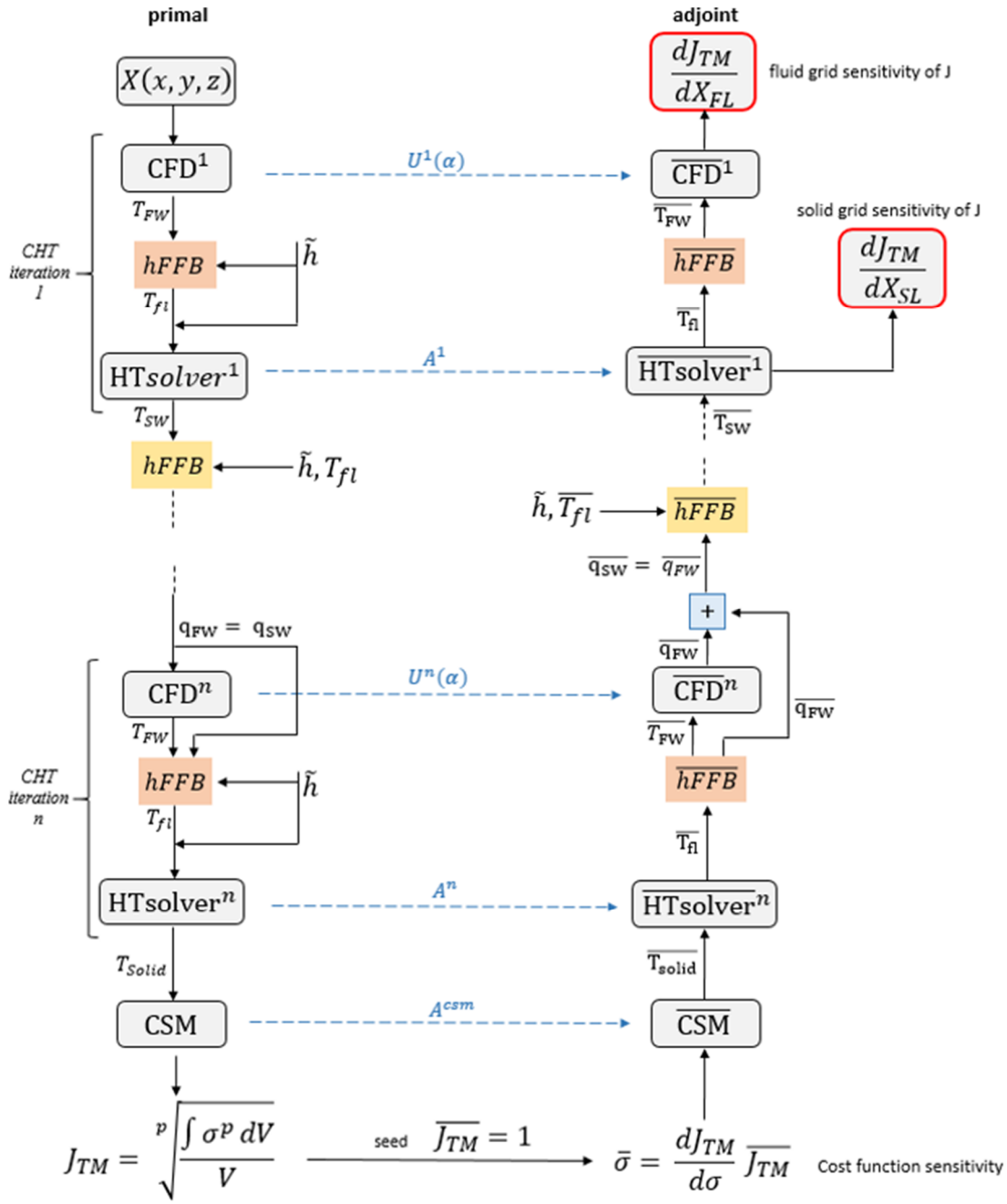

Figure 3.2 Workflow for the primal and adjoint computations of steady-state thermo-mechanical constraints.

If we rename the cost function J with y, we can associate to any state variable u_i a corresponding adjoint state variable $\bar{u}_i$ such that:

$$\bar{u}_i = \frac{dy}{du_i}. \tag{3.7}$$

The upper bar notation presented in Eq. (3.7) reflects the convention adopted by [140] for the adjoint variables.

The concept expressed by Eq. (3.6) is expanded to the entire workflow in Figure 3.2. Hence, the chain rule of differentiation is applied walking through the original trace in backward mode, propagating the adjoint variables in opposite direction w.r.t. the physical ones computed from the primal solvers.

In case a physical variable is provided as input to multiple routines along the workflow, in reverse mode each routine returns a contribution to the correspondent adjoint variable (Figure 3.3). All the contributions to the adjoint variable are summed up, a process also known as "accumulation". For instance, the wall heat flux q_{FW} entering the CFD solver and the hFFB routine in Figure 3.2 is reflected in two perturbations in reverse mode which are accumulated in the adjoint variable $\bar{q}_{FW}$.

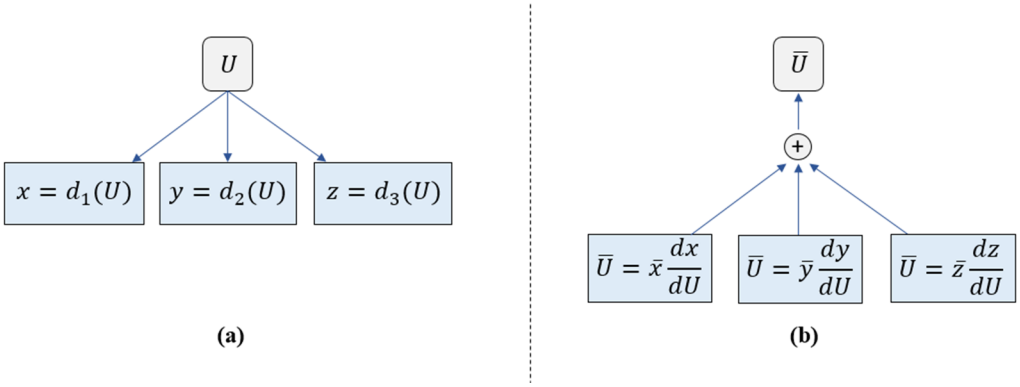

Figure 3.3 a) Physical variable contributing to multiple solvers. b) Accumulation of perturbations to the adjoint variable.

In primal mode, the fluid and the solid grids, which are generated upfront, are invoked by the CFD and the FEM solvers at any intermediate step along the convergence history of the conjugate problem. Moreover, since the structural solver adopts the same mesh as the heat transfer solver, the solid grid contributions extend till the computation of the cost function by the p-norm. Hence, in reverse mode any perturbation of the fluid grid or the solid grid contributes to the correspondent adjoint vector, either dJ/dX_{fl} or dJ/dX_{sl}, and is accumulated throughout the workflow, till achieving the final grid sensitivities at the top of Figure 3.2. The next section discusses in detail the process of accumulation of the adjoint grids sensitivities.

Despite the adjoint solid and fluid grids contributions are separately accumulated in the respective vectors, their evaluation is influenced by the

contributions of the other domain. In fact, the exchange of heat fluxes and fluid bulk temperatures through the interface in the physical domain corresponds in the reversed FSI problem to the backpropagation of the respective adjoint quantities. Thus, the fluid and the solid domains influence each other in the evaluation of the sensitivities of the cost function w.r.t. the grids coordinates.

Finally, the convergence of the conjugate coupling in primal mode is achieved through multiple loops of the hFFB workflow discussed in Section 2.2.4. Each loop is linked to the next one through the exchange of heat fluxes at the interface. Therefore, the adjoint workflow resembles the same structure with the propagation of the adjoint heat fluxes in the opposite direction, thus generating a bridge between two consecutive stages of the adjoint CHT process. Conversely, any physical variable showing only a local influence during the execution of the primal workflow appears in reverse mode in the corresponding position, but is not affected by any accumulation.

The adjoint flowchart in Figure 3.2 ends up with the final sensitivities of the cost function w.r.t. the solid and fluid grids coordinates, respectively released after the completion of the adjoint heat transfer solver and the adjoint CFD solver at the last CHT iteration in reverse mode. Such sensitivities account also for the contributions from the adjoint interface from the hFFB process in reverse mode, as will be discussed in the next section. Hence, the final sensitivities enter Eq. (3.2) for the calculation of the gradients of the cost function w.r.t. the CAD parameters.

3.3 Adjoint solvers

3.3.1 Adjoint response function

The adjoint workflow is initiated by seeding the cost function, i.e. the constraint of the maximum von Mises stress $\sigma_{\max\_VM}$. Since $\sigma_{\max\_VM} = J_{TM} = y$, from the definition of the adjoint variable in Eq. (3.7), it turns out the input to the adjoint trace is

$$\bar{\sigma}_{\max\_VM} = \bar{J}_{TM} = \frac{dy}{dJ_{TM}} = 1\,. \tag{3.8}$$

The maximum von Mises stress is expressed by the continuous p-norm function from Eq. (2.29) and repeated here for convenience:

$$\sigma_{\max\_VM} \approx \sqrt[p]{\frac{\int \sigma_{VM}^{p} dV}{\int dV}}\,. \tag{3.9}$$

The solution of Eq. (3.9) in primal mode is achieved through the application of the numerical integration technique discussed in Section A.2. Therefore, the integrals at the numerator and the denominator result from the sum of the

contributions of each finite element. Hence, the element-wise adjoint von Mises stress is obtained as follows:

$$\bar{\sigma}_{\mathrm{e\_}VM} = \frac{dy}{d\sigma_{e\_VM}} = \frac{dJ_{TM}}{d\sigma_{e\_VM}} \bar{J}_{TM} = \frac{d}{d\sigma_{e\_VM}} \sqrt[p]{\frac{\sum_e \int_{V_e} \sigma_{e\_VM}^p dV}{\sum_e \int_{V_e} dV}}. \tag{3.10}$$

The von Mises stress is a function of the components of the Cauchy stress tensor. It follows that for each element the adjoint components of the stress tensor are computed as:

$$\begin{aligned} \bar{\sigma}_{\mathrm{i,j}} &= \frac{dy}{d\sigma_{i,j}} = \bar{\sigma}_{\mathrm{e\_}VM} \frac{d\sigma_{e\_VM}}{d\sigma_{i,j}} \\ &= \bar{\sigma}_{\mathrm{e\_}VM} \frac{d}{d\sigma_{i,j}} \left(\sqrt{\frac{1}{2}[(\sigma_{11}-\sigma_{22})^2 + (\sigma_{22}-\sigma_{33})^2 + (\sigma_{33}-\sigma_{11})^2 + 6(\sigma_{12}^2+\sigma_{23}^2+\sigma_{31}^2)]} \right) \end{aligned} \tag{3.11}$$

Moreover, the explicit dependence of the two volume integrals in Eq. (3.9) on the solid grid coordinates results in the accumulation of the related sensitivities:

$$\bar{X}_{sl} = \frac{dy}{dX_{sl}} += \frac{dJ_{TM}}{dX_{sl}} \bar{J}_{TM} = \frac{d}{dX_{sl}} \sqrt[p]{\frac{\int \sigma_{VM}^p dV}{\int dV}}. \tag{3.12}$$

In Eq. (3.12) the operator "+=" is reported to emphasize the concept of accumulation of the cost function sensitivities w.r.t. the solid grid coordinates that are back-propagated throughout the adjoint workflow, till the grid generation procedure. Herein, the $\bar{X}$ notation is adopted for sake of simplicity, while in reality the sensitivities over the three dimensions *(x,y,z)* are accounted in the development.

In the remaining portion of the chapter the notations dy/du_i and dy/dX will be replaced by the more convenient notations $\bar{u}_i$ and $\bar{X}$.

3.3.2 Adjoint mechanical solver

The mechanical solver described in Section 2.3.3 receives as input the solid grid originally developed by the grid generation tool and adopted by the heat transfer solver, as well as the temperature field in the solid domain. Since the same mesh of second order tetrahedral elements is implemented in the two FEM solvers, the temperature field T and the correspondent adjoint temperature field $\bar{T}$ are exchanged with no need of re-interpolations. The execution of the structural solver in primal mode returns the displacements field, which is processed to compute the distribution of stresses. Figure 3.4 illustrates the primal process and addresses the correspondent adjoint workflow evolving in reverse mode.

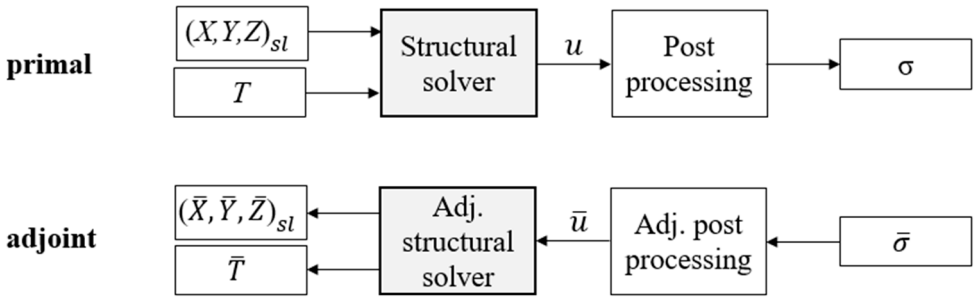

Figure 3.4 Evaluation by mechanical solver: primal and adjoint modes.

The back-propagation of the adjoint variables starts from the adjoint stress tensor developed in Eq. (3.11). In the physical domain the stress tensor is a function of the elasticity matrix E characteristic of the material under consideration, as well as of the strain components, respectively of mechanical nature ε_m and of thermal nature ε_{th}:

$$\sigma_{\mathrm{i,j}} = E(T)\left(\varepsilon_{m\_ij} - \varepsilon_{th_{ij}}(T)\right). \tag{3.13}$$

Hence, three contributions are derived in reverse mode:

$$\begin{cases} \bar{E}(T) = \bar{\sigma}_{i,j}\left(\varepsilon_{m\_ij} - \varepsilon_{th_{ij}}(T)\right) \\ \bar{\varepsilon}_{m\_ij} = \bar{\sigma}_{i,j}\, E(T) \\ \bar{\varepsilon}_{th\_ij} = -\bar{\sigma}_{i,j}\, E(T) \end{cases}. \tag{3.14}$$

Since the elasticity matrix depends on the nodal temperatures, the adjoint elasticity matrix $\bar{E}$ provides the contributions to the adjoint temperature field $\bar{T}$ by walking in opposite direction through the matrix assembly process.

$$\bar{T} += \bar{E}(T)\frac{dE(T)}{dT}. \tag{3.15}$$

Similarly, the thermal strains defined as

$$\varepsilon_{\mathrm{th\_ij}}(T) = \alpha(T)\left(T - T_{ref}\right) \tag{3.16}$$

with *α(T)* indicating the thermal expansion coefficient, convey their relative contributions to the adjoint temperature field $\bar{T}$ as follows:

$$\begin{cases} \bar{T} += \bar{\varepsilon}_{th\_ij}\,\alpha(T) \\ \bar{T} += \bar{\varepsilon}_{th\_ij}\left(T - T_{ref}\right)\dfrac{d\alpha(T)}{dT} \end{cases}. \tag{3.17}$$

Thus, the resulting temperature sensitivities are back-propagated to the adjoint CHT process.

The mechanical strains in Eq. (3.14) are a function of the strain matrix B and the displacement field u [141]:

$$\varepsilon_m(i) = B(i,j)\,u(j). \tag{3.18}$$

In reverse mode, the following adjoint terms are derived:

$$\begin{cases} \bar{B}(i,j) = \bar{\varepsilon}_m(i)\, u(j) \\ \bar{u}(j) = \bar{\varepsilon}_m(i)\, B(i,j) \end{cases} . \tag{3.19}$$

The strain matrix assembly process is walked in opposite direction in order to accumulate the contributions to the solid grid sensitivities:

$$\bar{X}_{sl} \mathrel{+}= \bar{B}\, \frac{dB}{dX_{sl}} . \tag{3.20}$$

Eq. (3.20) is discussed in detail in Section B.1.

The adjoint nodal displacements $\bar{u}$ in output of the reversed post-processing routine (cf. Figure 3.4) are provided as input to the adjoint mechanical solver.

The iterative linear system solver presented in Eq. (2.26), and limited to its steady state formulation, is not directly differentiated. In fact, such approach would require the same Krylov subspace and the same number of inner iterations as the primal solver, leading to possible errors in the computation of the adjoint variables, that would eventually propagate throughout the adjoint CHT workflow. Instead, the following adjoint formulation of the linear system is adopted [142], with the adjoint nodal displacements appearing at RHS:

$$S^T \bar{f} = \bar{u} . \tag{3.21}$$

The system in (3.21) is solved for the adjoint load vector $\bar{f}$ by an iterative Conjugate Gradient method. The transposed stiffness matrix at the LHS equals the stiffness matrix *S* previously calculated in primal mode, because of its symmetric form. Therefore, the adjoint system matrix $\bar{S}$ is obtained from Eq. (3.22), where the nodal displacements computed in primal mode appear at the RHS:

$$\bar{S}_{ij} = -u_j\, \bar{f}_i . \tag{3.22}$$

The process leading to the definition of Eq. (3.21) and Eq. (3.22) is demonstrated in Section B.2.

Finally, the system assembly process is algorithmically differentiated, returning the contributions of the mechanical solver to the grid sensitivities accumulation:

$$\bar{X}_{sl} \mathrel{+}= \bar{S}\, \frac{dS}{dX_{sl}} + \bar{f}\, \frac{df}{dX_{sl}} . \tag{3.23}$$

The differentiation process in Eq. (3.23) is presented in Section B.3. It is important to notice the adjoint matrix $\bar{S}$ is no more symmetric. Such consideration is relevant for the derivation of its contributions to the sensitivities of the solid grid coordinates. Moreover, the system differentiation accumulates also the contributions to the adjoint Single and Multiple Point Constraints (introduced in Section A.3) which will be propagated till the grid generation routine. The

algorithmic differentiation of the system assembly provides also further contributions to the adjoint temperature field $\bar{T}$, as discussed in Section B.3.

3.3.3 Adjoint heat transfer solver

The adjoint temperature field $\bar{T}$ establishes a link between the adjoint mechanical solver and the adjoint CHT workflow.

In primal mode, the heat transfer solver is invoked multiple times during the convergence history of the conjugate coupling, receiving in input the virtual bulk fluid temperature T'_{fl} and the virtual heat transfer coefficient $\tilde{h}$ defining the Robin boundary condition. Concerning the output, the thermal solver delivers the heat flux to the hFFB routine during an intermediate loop to convergence, and the temperature field to the mechanical solver once the continuity of the heat fluxes at the interface is achieved. Hence, while walking the flowchart in Figure 3.2 in opposite direction, at the kick-off of the adjoint CHT process the temperature field is seeded. Figure 3.5 shows the input and output variables to the heat transfer solver at the last loop of convergence of the CHT process. Since the solid grid is invoked by the primal solver for the system assembly, a contribution is accumulated in reverse mode.

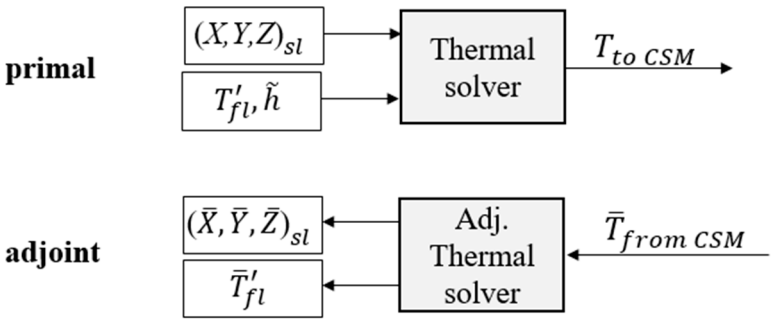

Figure 3.5 Evaluation by the heat transfer solver at convergence of the CHT process: primal and adjoint modes.

In case an intermediate CHT loop is considered instead, the temperature field returned by the thermal solver is processed by a routine with the aim of computing the heat flux that is to be interpolated and assigned as boundary condition to the CFD solver. Thus, in adjoint mode the post-processing routine is evaluated in opposite direction, as represented in Figure 3.6, resulting in the adjoint temperature field that is assigned to the adjoint thermal solver. The differentiation of the post-processing routine for the computation of the heat fluxes is reviewed in Section B.4.

Consistently with the approach discussed in the previous section, the iterative linear system solver from Eq. (2.17) is not directly differentiated. Instead, a two-step method is undertaken, first addressing the computation of the adjoint load vector $\bar{b}$ and then evaluating the adjoint stiffness matrix $\bar{A}$.

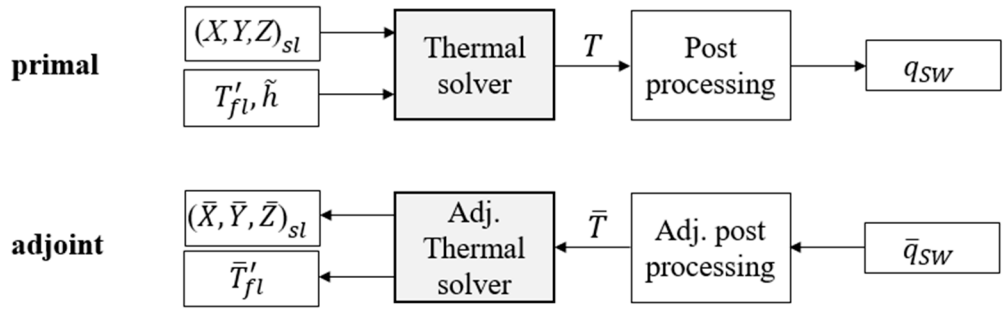

Figure 3.6 Evaluation by the heat transfer solver at an intermediate loop of the CHT process: primal and adjoint modes.

$$A^T \bar{b} = \bar{T} \tag{3.24}$$

$$\bar{A}_{ij} = -T_j \bar{b}_i \tag{3.25}$$

Eq. (3.24) shows the transposed stiffness matrix A^T accounting for the conductive and convective terms previously calculated in primal mode. Since the stiffness matrix is SPD, it follows that $A^T = A$. The adjoint temperatures $\bar{T}$ are imposed at the RHS. The system is solved by an iterative Conjugate Gradient method, returning the adjont load vector $\bar{b}$ that is assigned to Eq. (3.25), together with the temperature solution stored at the correspondent CHT loop in primal mode. Hence, the adjoint stiffness matrix $\bar{A}$ is computed.

The process leading to the definition of the two previous systems is compliant with the demonstration reported in Section B.2 for the structural solver.

Similarly to Eq. (3.23), the system assembly process is algorithmically differentiated and the adjoint contributions to the solid grid coordinates are accumulated. Since the thermal solver and the mechanical solver share the same grid, a unique vector of solid grid sensitivities is accumulated and propagated backwards throughout the CHT workflow.

$$\bar{X}_{sl} \mathrel{+}= \bar{A} \frac{dA}{dX_{sl}} + \bar{b} \frac{db}{dX_{sl}}. \tag{3.26}$$

The computation of the derivatives in Eq. (3.26) is discussed in Section B.5.

The adjoint load vector $\bar{b}$ computed in Eq. (3.24) is invoked to link the adjoint thermal solver to the adjoint hFFB procedure. In primal mode, the Robin boundary condition is imposed to the heat transfer solver, with the virtual bulk fluid temperature appearing at the RHS in Eq. (2.17). Hence, in reverse mode it follows that

$$b_i = \tilde{h}\, T'_{fl_i} \quad \rightarrow \quad \bar{T}'_{fl_i} = \bar{b}_i\, \tilde{h}\,. \tag{3.27}$$

The adjoint virtual bulk fluid temperature $\bar{T}'_{fl}$ is not accumulated along the adjoint CHT workflow, but recomputed at every loop in reverse mode and then passed to the adjoint hFFB process, consistently to the primal mode.

3.3.4 Adjoint hFFB procedure (solid → fluid)

The hFFB method presented in Section 2.2.4 is invoked in primal mode for the coupling process transferring information from the fluid domain to the solid one. The heat flux and the fluid temperatures at the walls, together with the virtual heat transfer coefficient $\tilde{h}$, are introduced in Eq. (2.3) for the computation of the virtual fluid bulk temperature T_{fl}. The latter is processed through the DWI routine, assigning an interpolated T'_{fl} field to the solid nodes.

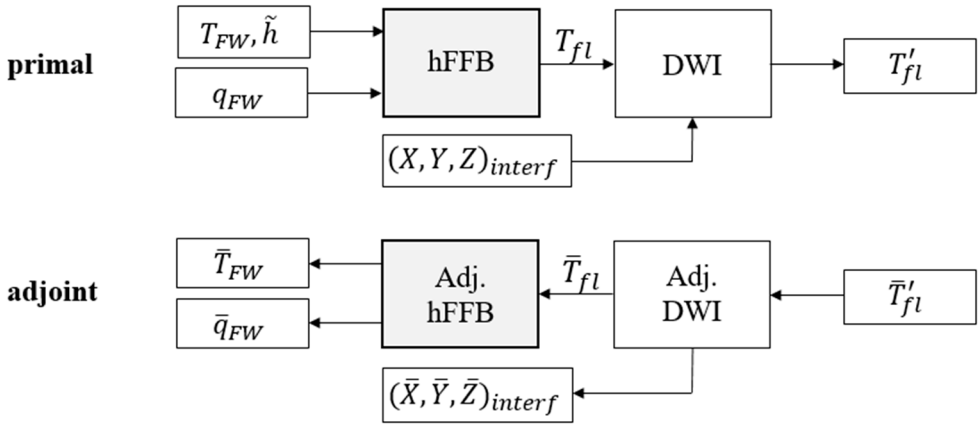

Figure 3.7 hFFB procedure between fluid domain and solid domain: primal and adjoint modes.

In reverse mode, the adjoint virtual fluid bulk temperature field $\bar{T}'_{fl}$ from Eq. (3.27) is introduced to the DWI procedure, which is treated by algorithmic differentiation in order to obtain the adjoint virtual fluid bulk temperature field $\bar{T}_{fl}$ associated to the fluid cells. In primal mode, the temperature associated to the solid node j is calculated through a weighted interpolation of the temperatures contained in the cluster of $i \in (1, N)$ fluid cells identified as close neighbors. The backward differentiation of the interpolation expressed by Eq. (2.1) is the following:

$$T'_{fl}(j) = \frac{\sum_{i=1}^{N} \frac{T_{fl}(i)}{\left(dist(i)\right)^2}}{\sum_{i=1}^{N} \frac{1}{\left(dist(i)\right)^2}} \quad \rightarrow \quad \bar{T}_{fl}(i) \mathrel{+}= \bar{T}'_{fl}(j) \, \frac{\frac{1}{(dist(i))^2}}{\sum_{i=1}^{N} \frac{1}{(dist(i))^2}} \tag{3.28}$$

The operator "+=" in Eq. (3.28) stresses the fact each fluid cell i may belong to multiple "neighboring clusters" associated to different solid nodes j. Hence, the accumulation of the adjoint variables in reverse mode follows.

Eq. (3.28) suggests also that a contribution to the accumulation of the sensitivities of the fluid and solid grids coordinates derives from the adjoint vector of the mapped distances between each solid node and its neighboring fluid cells. Therefore, it follows that:

$$\overline{dist(i)} = \bar{T}'_{fl}(j)\,\frac{dT'_{fl}(j)}{d(dist(i))}\,. \tag{3.29}$$

Such adjoint distances are accumulated along the CHT workflow, till achieving the routine dedicated to the interface generation.

Finally, the algorithmic differentiation of Eq. (2.3) results in the adjoint temperatures at the fluid walls $\bar{T}_{FW}$, which are used as input to the adjoint CFD solver, and in the adjoint heat flux $\bar{q}_{FW}$, which is stored for a later accumulation.

$$T_{fl} = T_{FW} - \frac{q_{FW}}{\tilde{h}} \quad \rightarrow \quad \begin{cases} \bar{T}_{FW} = \bar{T}_{fl} \\ \bar{q}_{FW} = \bar{T}_{fl}\left(-\frac{1}{\tilde{h}}\right) \end{cases}. \tag{3.30}$$

3.3.5 Adjoint fluid solver

The choice of a partitioned coupling technique, as discussed in Section 2.2.4, discloses the possibility of non-intrusive calls to the in-house adjoint CFD solver.

In primal mode, the fluid grid, the wall heat flux and the converged flow solution from the previous CHT loop U^{i-1} are invoked by the fluid solver, which provides as output the updated flow solution U^i and the temperature at the walls T_{FW} (cf. Figure 3.8). In reverse mode, the linearization is performed around the converged flow solution U^i previously stored at the correspondent system solve in primal mode. The viscous wall temperatures in the ghost cells layers are updated imposing the Neumann boundary condition reported in Eq. (2.19).

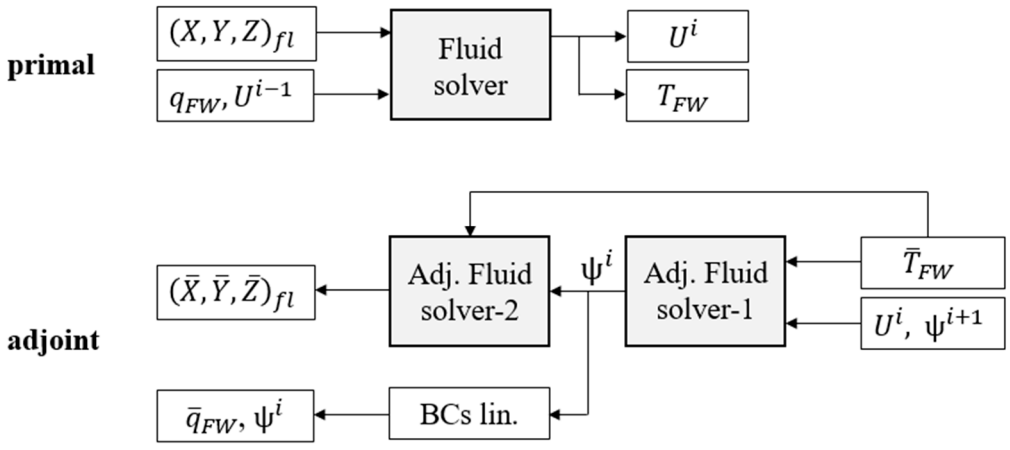

Figure 3.8 Fluid solver: primal and adjoint modes.

In accordance with the linear algebraic approach adopted for the computation of the adjoint equations, the vector of the adjoint variables ψ derives from the solution of the system (1.9), here repeated for convenience:

$$\left(\frac{\partial R}{\partial U}\right)^T \psi = \left(\frac{\partial J}{\partial U}\right)^T \tag{3.31}$$

with U indicating the conservative flow variables, R as the non-linear residuals of the primal flow solver, and J the objective or constraint function. Since the primal solver is initialized with the converged flow solution at the previous CHT iteration, the adjoint system in (3.31) is initialized with the vector of the adjoint variables ψ computed at the previous CHT step in reverse mode.

The adjoint fluid temperature $\bar{T}_{FW}$, obtained from the reversed hFFB procedure at the previous section, contributes to the linearization of the cost function. Thus, the term at the RHS of Eq. (3.31) is linearized at the viscous walls exposed to the heat flux, as follows:

$$\begin{aligned}\frac{\partial J}{\partial U} = \frac{\partial J}{\partial V_{bnd}}\frac{\partial V_{bnd}}{\partial V_{domain}}\frac{\partial V_{domain}}{\partial U_{domain}} = \frac{\partial J}{\partial T_{FW}}\frac{\partial T_{FW}}{\partial V_{bnd}}\frac{\partial V_{bnd}}{\partial V_{domain}}\frac{\partial V_{domain}}{\partial U_{domain}} \\ = \bar{T}_{FW}\frac{\partial T_{FW}}{\partial V_{bnd}}\frac{\partial V_{bnd}}{\partial V_{domain}}\frac{\partial V_{domain}}{\partial U_{domain}}\end{aligned} \tag{3.32}$$

with V_{bnd} as the primitive variables computed at the wall boundary of interest, V_{domain} as the corresponding variables from the interior of the fluid domain, and the last term $\partial V/\partial U$ indicating the transformation matrix from primitive to conservative variables. Hence, $\partial T_{FW}/\partial V_{bnd}$ indicates the derivatives of the face-centered temperature w.r.t. the primitive variables at the face center point of those cells laying at the wall. Moreover, the flow transformation matrix $\partial V_{bnd}/\partial V_{domain}$ is compliant with the definition reported in Section A.4.

Since in primal mode the response function J is affected only by the temperature values detected at the first layer of the inner domain and of the ghost cells, from Eq. (3.32) it turns out in adjoint mode only the correspondent cells around a non-adiabatic wall are seeded to a non-zero value.

The solution of the system in (3.31) returns the adjoint vector ψ allowing the computation of the cost function sensitivities w.r.t. the fluid grid coordinates:

$$\frac{dJ}{dX_{fl}} = \frac{\partial J}{\partial X_{fl}} - \psi^T \frac{\partial R}{\partial X_{fl}} \ . \tag{3.33}$$

Here, the linearization of the cost function at the viscous walls with heat flux is affected by the contribution of the adjoint fluid wall temperatures from the hFFB procedure:

$$\frac{\partial J}{\partial X_{fl}} = \frac{\partial J}{\partial V_{bnd}}\frac{\partial V_{bnd}}{\partial X_{fl}} = \frac{\partial J}{\partial T_{FW}}\frac{\partial T_{FW}}{\partial V_{bnd}}\frac{\partial V_{bnd}}{\partial X_{fl}} = \bar{T}_{FW}\frac{\partial T_{FW}}{\partial V_{bnd}}\frac{\partial V_{bnd}}{\partial X_{fl}} \ . \tag{3.34}$$

The sensitivities in Eq. (3.33) are referred to the face centers at the walls. Therefore, their contribution to the fluid grid takes place by summing up the values collected at the four cells surrounding each grid vertex (cf. Figure 3.9). The resulting grid perturbations $\bar{X}_{fl}$ are accumulated along the entire adjoint CHT workflow, till the grid generation process.

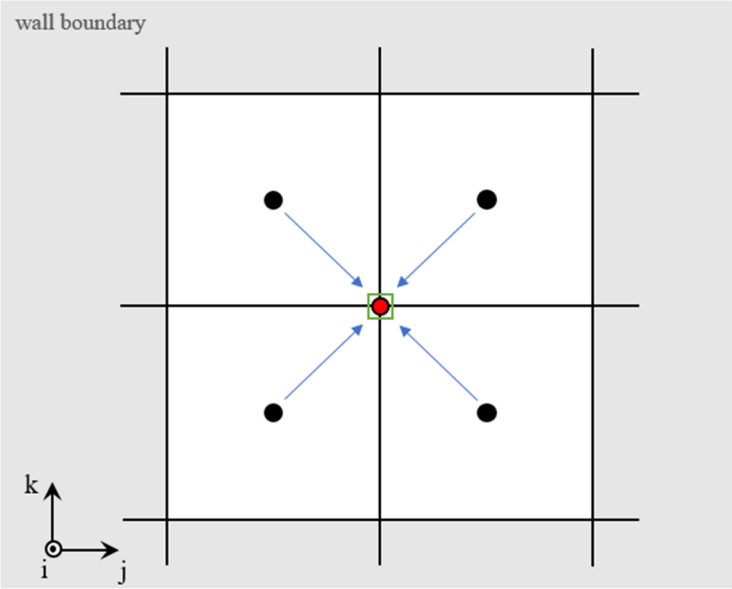

Figure 3.9 Two-dimensional view of cells faces at non-adiabatic wall boundary on (j,k) plane: Cost function sensitivities at each fluid grid vertex (red) from the surrounding four cells face centers (black).

Finally, for the principle of the reverse accumulation, the wall heat flux term, entering in primal mode as the update of the boundary conditions in Eq. (2.19), results in an adjoint fluid wall heat flux $\bar{q}_{FW}$ that is computed once the adjoint CFD solver approaches full convergence. This contribution is summed up with the $\bar{q}_{FW}$ returned in Section 3.3.4 by the adjoint hFFB procedure:

$$\bar{q}_{FW} = \bar{q}_{FW\_hFFB} + \bar{T}_{G1}\frac{\Delta n}{k_{fl}} \,. \tag{3.35}$$

A further contribution derives also from the second layer of ghost cells, not reported in Eq. (3.35) for the sake of simplicity.

Moreover, the term Δn appearing in Eq. (2.19) indicates the distance between the cell centers of the pairs (D1-G1) and (G1-G2) according to the thin shear layer approximation. Therefore, such term results in additional contributions to the solid and the fluid grids sensitivities, which are computed by algorithmic differentiation of the Neumann boundary condition.

3.3.6 Adjoint hFFB procedure (fluid → solid)

The partitioned coupling scheme in reverse mode completes by transferring the adjoint terms from the fluid to the solid domain (cf. Figure 3.10). The accumulated adjoint heat flux $\bar{q}_{FW}$ obtained in the previous section and referred to the fluid cells is processed through the DWI routine by application of the algorithmic differentiation technique. Consistently with the reverse interpolation call discussed in Eq. (3.28), the adjoint heat flux associated to the solid nodes is obtained as follows:

$$q_{FW}(j) = \frac{\sum_{i=1}^{N} \frac{q_{SW}(i)}{(dist(i))^2}}{\sum_{i=1}^{N} \frac{1}{(dist(i))^2}} \rightarrow \bar{q}_{SW}(i) \mathrel{+}= \bar{q}_{FW}(j) \frac{\frac{1}{(dist(i))^2}}{\sum_{i=1}^{N} \frac{1}{(dist(i))^2}} . \qquad (3.36)$$

The "+=" operator in Eq. (3.36) highlights the accumulation justified by the fact each solid node *i* may belong to multiple clusters of "neighboring points" associated to different fluid cells *j*.

Similarly to Eq. (3.29), further contributions to the interface sensitivities result from the adjoint terms of mapped distances $\overline{dist(i)}$ that are obtained by differentiating the interpolation procedure. Such sensitivities are accumulated throughout the adjoint CHT workflow, till the grid generation procedure, discussed at the next section.

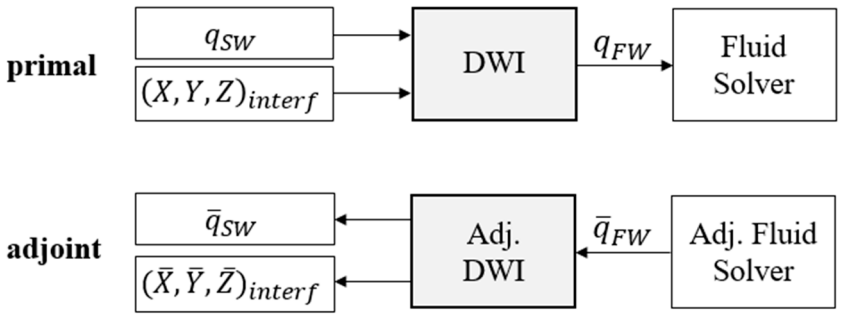

Figure 3.10 hFFB procedure between fluid domain and solid domain: primal and adjoint modes.

Finally, the adjont heat flux $\bar{q}_{SW}$ is passed to the solid domain (cf. Figure 3.6), in which the differentiated post-processing routine returns the new field of adjoint solid temperatures $\bar{T}_{SW}$ in input to the system solve in Eq. (3.24). Since the adjoint heat flux accounts only for the solid nodes laying on the interface, consistently with the case of the adjoint fluid solver, only the temperatures in the nodes of the finite elements belonging to the surface are seeded, while the remaining portion of the adjoint field is posed to zero. The interested reader may find more details about the algorithmic differentiation procedure in Section B.4.

Hence, the whole adjoint CHT loop completes with the closure offered by the adjoint thermal solver described in Section 3.3.3. The workflow is repeated in

reverse mode for as many loops as the one performed during the history of the primal computations till the convergence of the conjugate coupling.

3.3.7 Adjoint interface sensitivities to fluid and solid grids

The completion of the adjoint CHT workflow results in the two grid sensitivities $\partial J/\partial X_{fl}$ and $\partial J/\partial X_{sl}$ accumulating the contributions from the respective fluid and solid solvers calls and appearing on top of Figure 3.2.

The intermediate calls to the differentiated DWI routine accumulate the sensitivities of the response function w.r.t. the interface perturbations, as represented by the adjoint clusters of distances between the neighboring fluid-solid and solid-fluid pairs introduced in Section 3.3.4 and 3.3.6. In fact, in primal mode any perturbation to the solid or fluid grids, determined by the optimizer's modifications to the component shape, would lead to some differences in the definition of the interface. Thus, the alteration of the fluid-solid mating process would be reflected in some differences in the exchange of heat flux between the two domains, finally affecting the evaluation of the response function. In reverse mode, the impact of these perturbations must be captured, providing further contributions to the grids sensitivities $\bar{X}_{fl}$ and $\bar{X}_{sl}$ by walking the interface generation process in backward direction, including the displacement of the virtual fluid grid points, as discussed in Section B.6.

Finally, the grids sensitivities, enclosing the contributions of the entire multidisciplinary chain, are imported in Eq. (3.2) for the computation of the cost function sensitivities w.r.t. the CAD parameters. Hence, $dJ/d\alpha$ is evaluated by the SQP-based optimizer in order to operate a geometry update, opening the path to a new thermo-mechanical assessment within the history of the gradient-based shape optimization problem.

3.4 Gradients calculation

3.4.1 FEM solvers gradients validation

The heat transfer solver and the mechanical solver presented in the previous section rely on the manual differentiation of their own processes to provide accurate computations of the sensitivities of the response function by the reverse Algorithmic Differentiation technique. Hence, the validation of the computed gradients is discussed herein, with reference to the turbine rotor test case introduced in Section 2.4.2.

The cost function J considered for the thermal solver is the maximum temperature in the solid domain, calculated through a p-norm function, similarly to Eq. (2.29). Instead, the mechanical solver refers to the maximum von Mises stress, including the contribution of the thermal strains. In both cases, the list of

design variables α adopted for the evaluation of the sensitivities $dJ/d\alpha$ is reported in Table 3.1 and referenced in Figure 3.11.

	Design Variables α
1	Rotor hub meridional contour: Y-coordinate at 20% chord;
2	Rake angle;
3	Back-plate thickness;
4	Turbine shaft diameter;
5	Turbine shaft length;
6	Rotor maximum diameter;
7	Blade height at leading edge;
8	Back-plate/shaft connection axial position;
9	Blade hub thickness ;
10	Blade hub fillet radius.

Table 3.1 Design variables adopted in the $\boldsymbol{dJ/d\alpha}$ gradients validation.

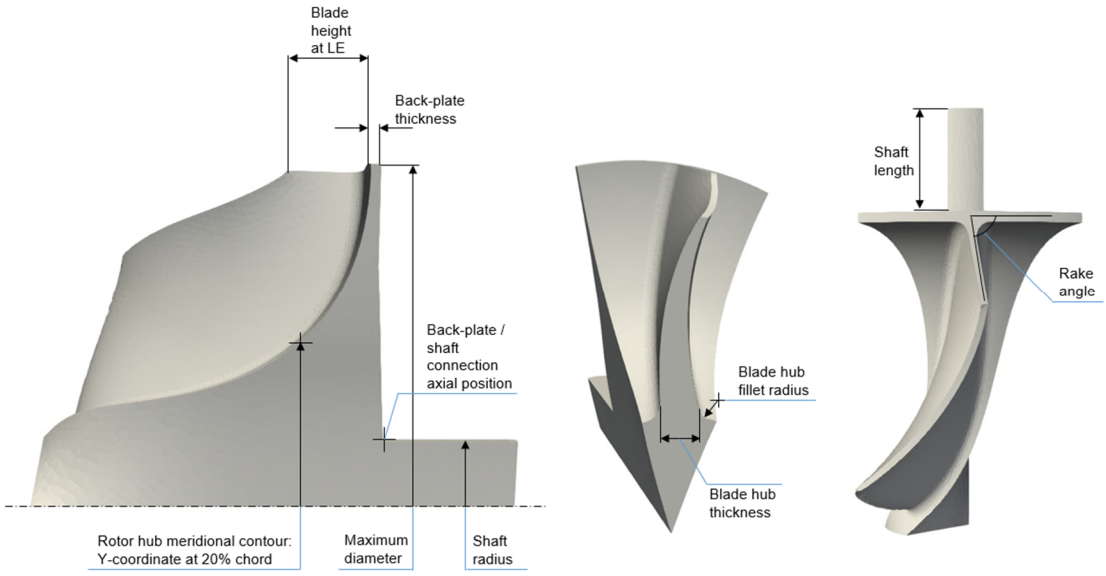

Figure 3.11 Design variables from Table 3.1.

The sensitivities computed by the adjoint method are compared to the correspondent gradients calculated by the Finite Differences (FD) technique. The latter adopts a central differencing scheme for sake of improved accuracy, while the optimal step size is searched for each design variable with the aim of accurate gradient computations. An exemplary case is reported in Figure 3.12, referred to the seventh variable from Table 3.1 evaluated in the framework of the thermal solver: a suitable step size is identified at a value of 10^{-6} m. The curve indicating the gradient evolution derives from the computation of the cost function

sensitivities at each step size, by solving the linear system obtained after applying a perturbation of the mesh through the morphing technique described in [118]. In general, the magnitude of such perturbations must avoid too-small values because turning in round-off errors; at the same time, they have to avoid too-large values as well, because potentially introducing significant truncation errors.

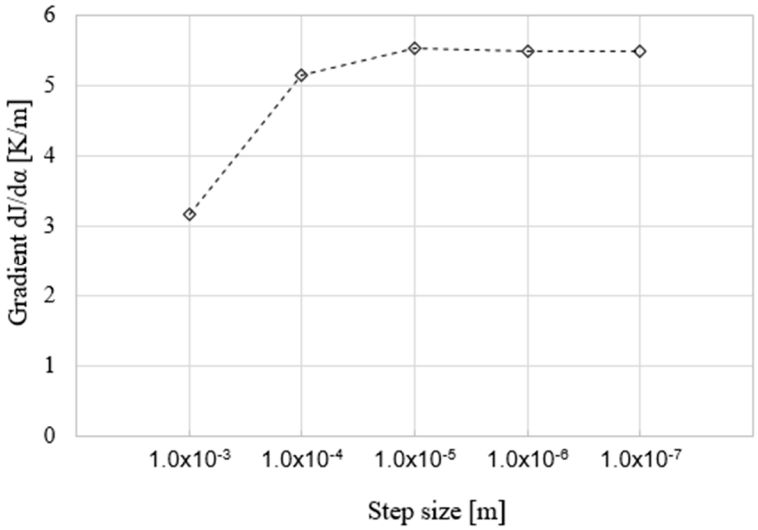

Figure 3.12 Step size evaluation for the computation of $\boldsymbol{dJ/d\alpha}$ by Finite Differences: Heat transfer solver, variable #7.

The sensitivities of the maximum solid temperature to the perturbations of the ten design variables are summarized in Figure 3.13-a, which shows a close agreement between the two methods, both in sign and magnitude.

To understand the sensitivity analysis in detail, let us consider the thermal paths in the turbine rotor experiencing the convective loading resulting from the operative condition reported in Table 2.3. Additionally, a convective condition is imposed on the back-plate surface with a uniform fluid temperature of 950K, and a Dirichlet boundary condition of 500K is assigned to the extreme section of the shaft.

According to Figure 3.14, the maximum solid temperature is detected at the nodes in the hub region, in proximity of the leading edge. The computation of the gradients of this constraint reveals a marked sensitivity to the back-plate thickness (i.e. variable #3), whose enlargement would reduce the cooling influence of the convective boundary condition imposed at the back-plate outer surface. Similarly, an increase in blade height at the leading edge (i.e. variable #7) would extend the thermal path to the colder areas highlighted at the tip, while an elongation of the shaft (i.e. variable #5) would reduce the gradient field by locating the heat sink with the Dirichlet boundary condition further away from the rotor hub surface. Conversely, an increase in the shaft diameter (i.e. variable #4), an advancement of the axial position of the intersection point between the back-plate and the shaft (i.e. variable #8), and an enlargement of the blade hub thickness (i.e. variable #9) would favor the cooling of the hub upper region. Such sensitivities provide the

direction of descent for a constrained optimization problem aimed at limiting the maximum rotor temperature for sake of extended lifetime.

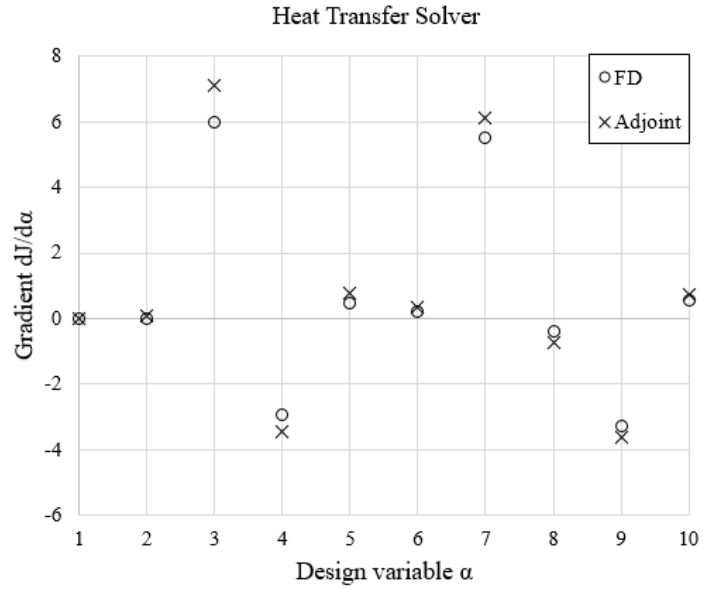

(a)

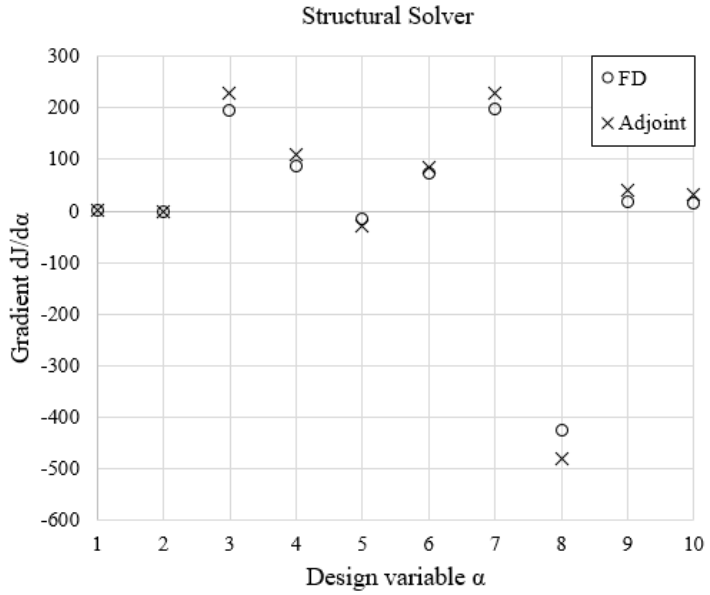

(b)

Figure 3.13 Comparison of the $\boldsymbol{dJ/d\alpha}$ sensitivities of the solid maximum temperature (a), and of the maximum von Mises stress (b): Gradients computed by the adjoint method vs. Finite Differences.

The sensitivities of the maximum von Mises stress w.r.t. the ten design variables are shown in Figure 3.13-b. The accuracy of the adjoint structural solver is assessed by comparison with the same gradients computed by the Finite Differences, confirming the suitability of the manually differentiated framework.

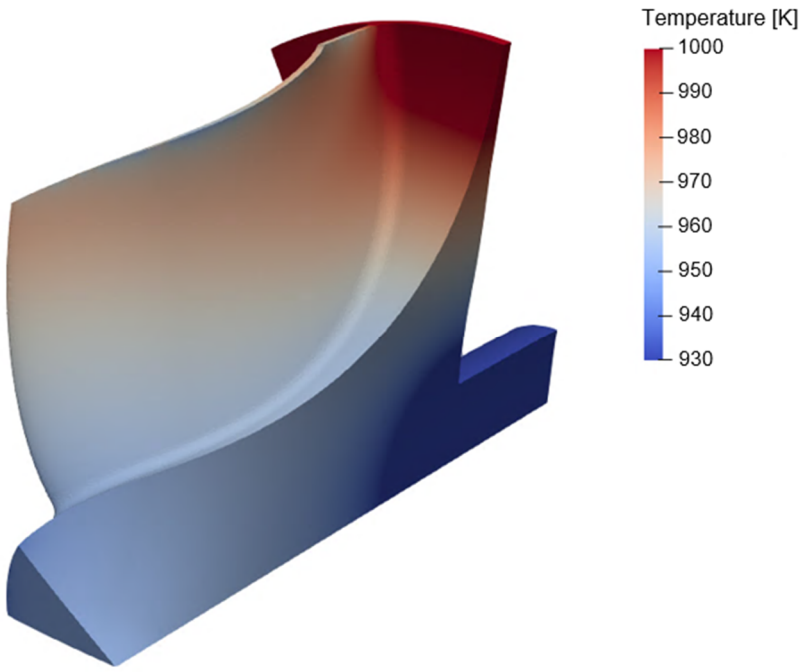

Figure 3.14 Close-up of solid temperatures in turbine rotor (operative condition from Table 2.3).

Finally, the performance of the two adjoint FEM solvers was investigated by measuring the computational time required for the evaluation of the sensitivities fields. Given X as the time required to perform the computation of the multidisciplinary workflow in primal mode, if the problem involves n design variables, the gradients evaluation by FD would approximately cost $n \cdot X$. On the contrary, the application of the adjoint method herein described costs about $8.6X$ for the heat transfer solver and $2.3X$ for the structural module. Hence, the choice of an adjoint method proves its advantage in the case of problems defined by a rich design space, as presented in the introduction. The cost figures herein presented mostly depend on the assembly process of the differentiated system (cf. Eq. (3.23) and Section B.3), rather than the solver itself. Thus, the thermal solver is the most impacted in terms of upscaling because accounting only for one d.o.f. in primal mode (i.e. the vector of unknown temperatures), while dealing with three adjoint variables in reverse mode (the three-dimensional coordinates sensitivities).

3.4.2 CFD solver convergence history

The loose coupling approach herein adopted allows the direct integration of the in-house adjoint CFD solver in the multidisciplinary framework under discussion. Hence, the present work benefits from the accuracy of the computed gradients as was already demonstrated by the same author.

The focus of this section is in the verification of the convergence rate of the solver, being the adiabatic walls assumption dismissed in favor of the wall heat

fluxes. The test case under consideration refers to the radial turbine impeller presented in Section 2.4.2, in which all rotor surfaces exchange heat with the surrounding fluid, while the turbine housing contour is considered adiabatic (since the scroll metal domain is not included in the model). The whole CHT workflow in Figure 3.2 is run in primal and adjoint modes and the performance data of the CFD solver is extracted at an intermediate hFFB cycle for a closer assessment.

Figure 3.15 presents the rate of convergence of the density residuals for the primal flow solver and the adjoint flow solver. As thoroughly discussed in [54], the two convergence rates are similar because the LHS matrices adopted by the respective solvers contain the same eigenvalues. However, such traces do not coincide because, consistently with the approach adopted for the FEM solvers, the JT-KIRK scheme [61] herein adopted is not directly reversed in adjoint mode.

In order to achieve a consistent path of convergence for the adjoint solver, the primal flow solver with heat fluxes has to be run till approaching a relative residual drop around machine level accuracy. In this respect, Figure 3.15 reveals a final residual value of about 10^{-15} with the appearance of "white noise" at the multigrid cycle 700. Hence, a smooth convergence path for the adjoint fluid solver is achievable.

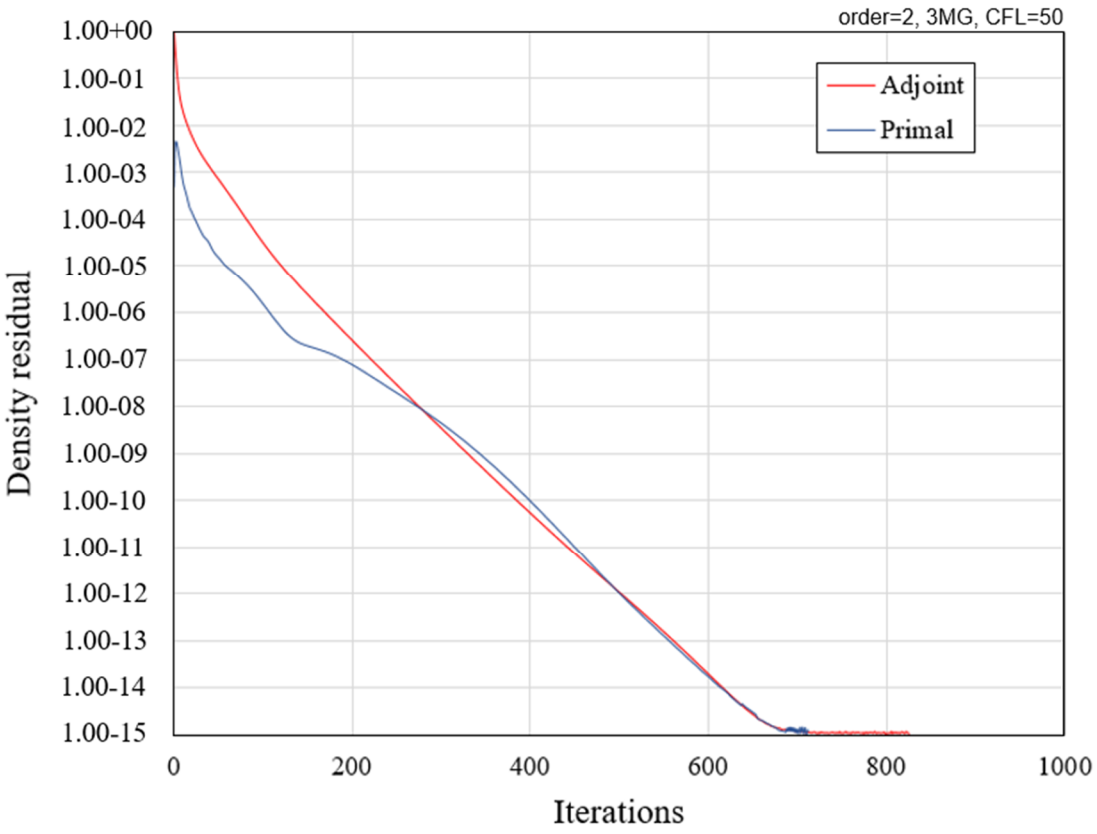

Figure 3.15 Convergence rate of the density residual for the primal and the adjoint CFD solvers with wall heat fluxes.

3.5 Closure

The radial turbine rotor analyzed in Section 2.5 is considered herein for the evaluation of the sensitivities of the response function, i.e. the gradients of the maximum von Mises stress accounting for the thermal strains w.r.t. the CAD parameters.

The geometry under assessment is about a turbine rotor previously optimized with a simpler decoupled approach, in which the aerodynamic performance and the structural constraints were separately treated. The later verification of the impact of the thermal operative environment, as resulting from Figure 2.20, highlights the presence of a region of concentrated stresses, not visible in the original optimization results and now exceeding the limit of safe operation for the component. Hence, the purpose of the current investigation is to address a second step in the optimization process, while accounting for a more holistic perspective on the problem.

For sake of simplicity, only the most critical operative condition is addressed to the thermo-mechanical constraint assessment. In order to identify such key point, at first the list of rotor working conditions reported in Table 3.2 is investigated by means of the workflow in primal mode (cf. left side branch in Figure 3.2). The points represent turbine steady state working conditions extracted from a set of ascending loads in the engine map, with the variable geometry vanes progressively opening while considering higher loads, as demonstrated by the variation in inlet flow angles. The maximum von Mises stress for each case is summarized in Table 3.3, in accordance with the stress patterns shown in Figure 3.16. The normalization refers to the value obtained in the test case #1. It is then confirmed that case #5, already analyzed in Chapter 2, is the most severe condition; hence, it is eligible for the application of the adjoint workflow.

Operative point #	Inlet tot pressure [kPa]	Inlet tot temperature [K]	Inlet flow angle [deg]	Outlet static pressure [kPa]	Rotational speed [RPM]
1	122	604	81	98.5	30000
2	131	677	78	98.5	60000
3	148	843	72	98.5	90000
4	167	1011	65	98.5	120000
5	173	1080	62	98.5	140000

Table 3.2 Boundary conditions for rotor operating points.

Operative point #	Normalized maximum von Mises stress [-]
1	1.0
2	4.7
3	9.3
4	15.3
5	20.1

Table 3.3 Normalized maximum von Mises stress for test cases in Table 3.2.

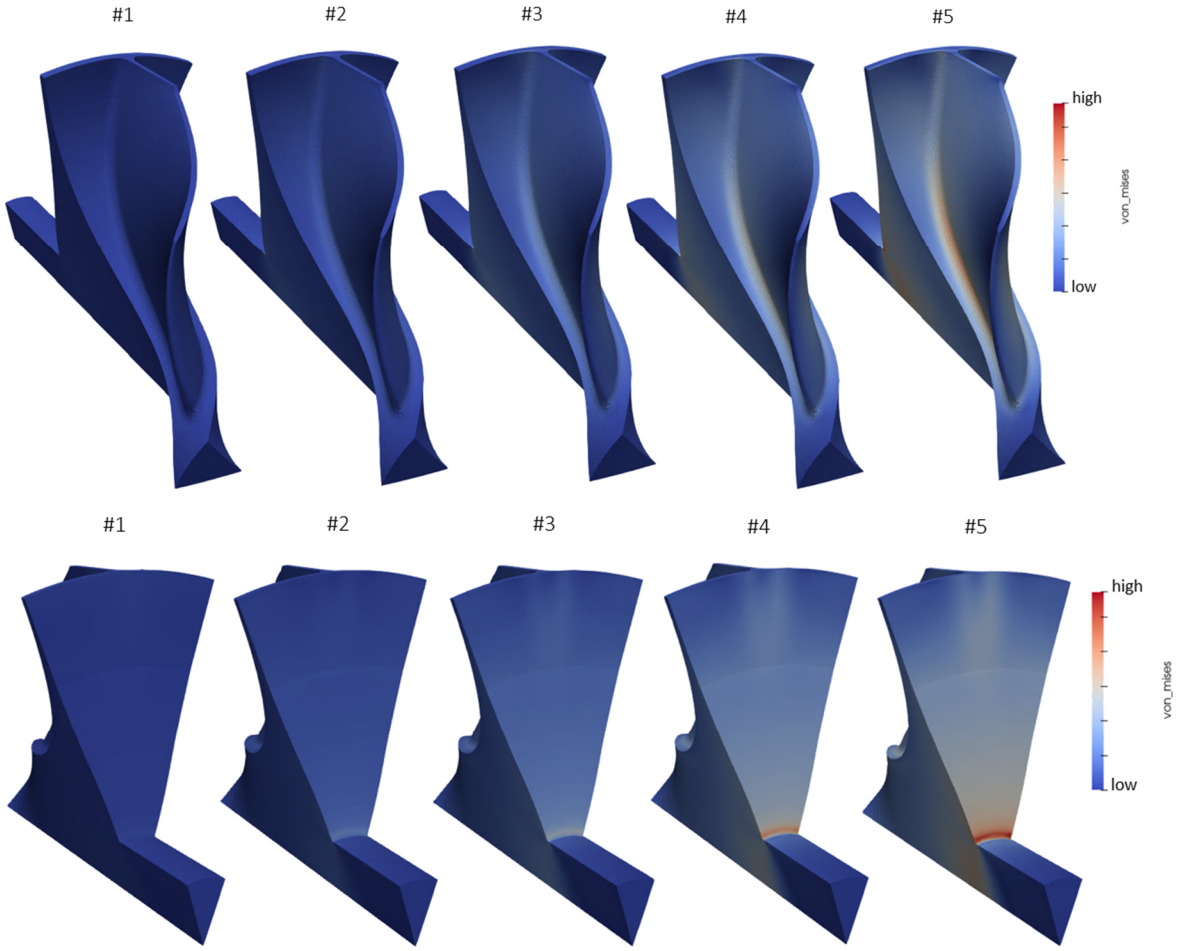

Figure 3.16 von Mises stresses distributions for test cases reported in Table 3.2.

The output of the adjoint thermo-mechanical assessment in Figure 3.17 reveals the distribution of the sensitivities of the maximum von Mises stress w.r.t. the grid coordinates, identifying the most stressed region at the connection of the rotor back-plate with the shaft, where the highest local thermal gradients are present (cf. Figure 2.19). The finding is consistent with Figure 3.13-b, which shows a more pronounced sensitivity for the eighth design variable w.r.t. the other ones. In particular, the sign of the gradient illustrates a stress reduction is achievable by an advancement of the location of the connection point in axial direction. Hence, the result of the grid perturbation is reported in Figure 3.18, which compares the von Mises stresses distribution of the baseline geometry (left) and the updated layout (right). It is demonstrated that a reduction of the local von Mises stresses in excess of 35% is achievable in the most critical area through a modification of the back-plate profile. The increased curvature promotes a more gradual evolution of the local displacements field and a smoother temperature transition, thus lowering the impact of the thermal strains and returning a more gradual mechanical pattern at the intersection of the two elements. The new shape is compliant with the limit defined by the Yield strength of the material and,

therefore, is in line with the goal of satisfying the thermo-structural constraint within an optimization problem.

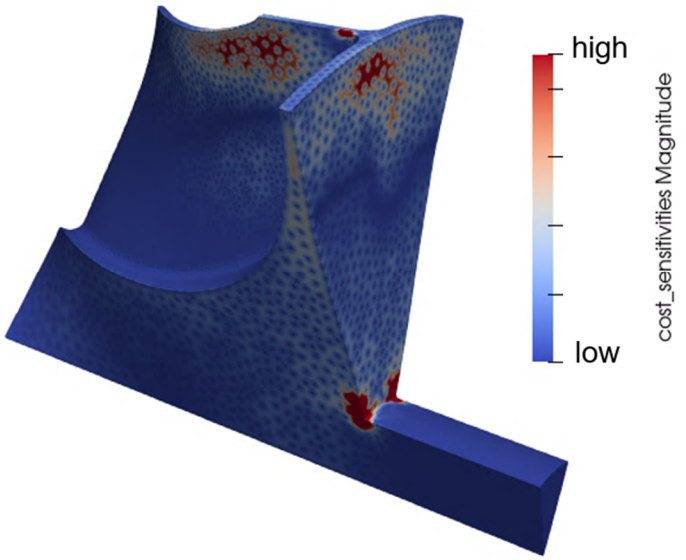

Figure 3.17 Sensitivities of thermo-mechanical constraint w.r.t. grid coordinates.

Other areas of the blade are highlighted by the sensitivity patterns in Figure 3.17, in particular at high blade span and in the upper portion of the back-plate. However, they exhibit a lower magnitude and refer to locations where the stresses do not exceed the constraint, because already addressed by the original decoupled optimization. For instance, the reddish island in the sensitivity plot at high blade span, in proximity of the leading edge, brings the attention to a blade section at 25% of the chord presenting a locally mild non-radial fibered configuration, also visible in Figure 3.11.

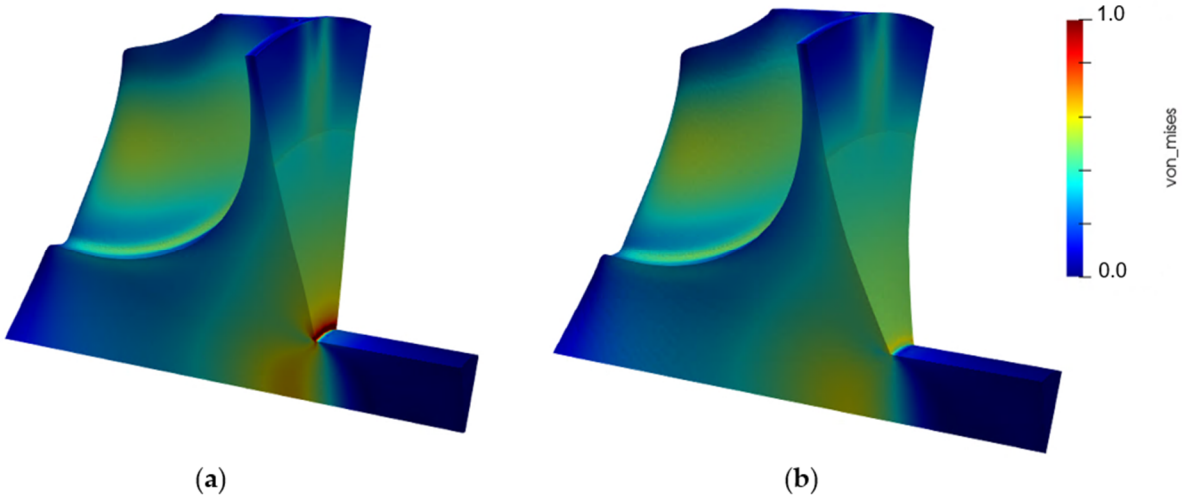

Figure 3.18 Normalized von Mises stresses distribution in radial turbine impeller experiencing thermo-mechanical loading: a) baseline configuration, b) updated geometry.

This layout is responsible for the stresses at the hub fillet in the corresponding axial position, which however are within the elastic limit of the material. Therefore, the constraint is locally inactive, the sensitivity is neglected, and the original blade shape with its aerodynamic performance can be preserved.

Finally, a further positive aspect of the implementation of the CHT analysis within the design loop is about the more accurate prediction of the actual turbine efficiency, as no more adiabatic walls assumptions are in place. The deviation in the total-to-static efficiency w.r.t. an adiabatic simulation is about 0.2% in the selected operative condition while considering the sole impeller. However, more marked differences are expected in case the CHT analysis is extended to the whole turbine stage, including the volute and the nozzle guide vanes.

Chapter 4

Thermo-Mechanical Fatigue optimization

4.1 The Thermo-Mechanical Fatigue problem

The optimization framework discussed in the previous chapters deals with the problem of the fulfilment of the multipoint performance targets and constraints in steady state conditions. In fact, it is a common practice to analyze the performance envelope of the machine in order to extract a diversified set of key operating points to address the shape modifications. However, such approach lacks of generality when transient operative conditions are prominent in the duty cycle of the device. It is the case of a radial turbine for automotive turbocharger applications, whose durability is affected by the transient loads induced by the dynamic change in engine working points. Figure 4.1 shows an exemplary driving cycle synthesized from fleet data [143].

The highly dynamic trace, described as vehicle speed in time, suggests the turbine continuously operates in transient conditions, since it experiences variations in inlet mass flow rate, inlet temperature, and consequently in transient centrifugal loads determined by the varying trace of turbocharger speed.

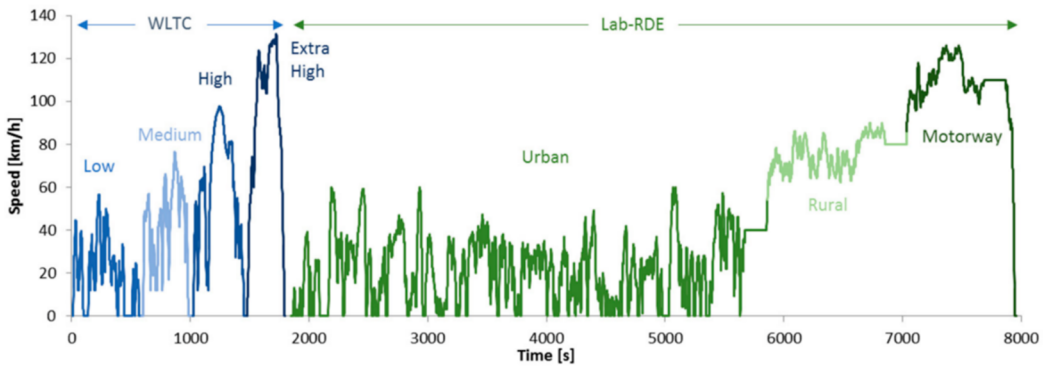

Figure 4.1 Exemplary vehicle speed trace for passenger car application. Source [143].

The highly dynamic trace, described as vehicle speed in time, suggests the turbine continuously operates in transient conditions, since it experiences variations in inlet mass flow rate, inlet temperature, and consequently in transient centrifugal loads determined by the varying trace of turbocharger speed.

Such considerations inevitably pose the question about the fatigue lifetime problem in these applications.

[144] defines the fatigue in metals as the consequence of repeated reversals of inelastic deformations. Solids temporarily operating in their inelastic regime accumulate non-recoverable deformations, eventually leading to a mechanical failure. The process is simplified through the evaluation of repeated cyclic operations, like the ones presented in Figure 4.2. In case the component operates within the boundaries of its material elastic regime, the deformations are always recoverable and the fatigue lifetime is quantified in tens or even hundreds millions cycles. Hence, the component is considered as experiencing an "infinite fatigue lifetime", since each loading cycle may take from few seconds to few minutes to complete. However, if the cycle extends to the inelastic regime, irrespectively of the permanence time, some irreversible deformations occur because of the dislocations movement in the solid crystal structure [145, 146], determining a hysteresis loop in the material mechanical properties. If the deformations are small and localized, hundreds of thousands cycles must be accumulated to induce actual failure. Instead, in case of high activation energies, the deformations may be larger and facilitate the dislocations movements, progressively reducing the yield strength of the material. Hence, mechanical failure may occur earlier, even in few thousands cycles or less.

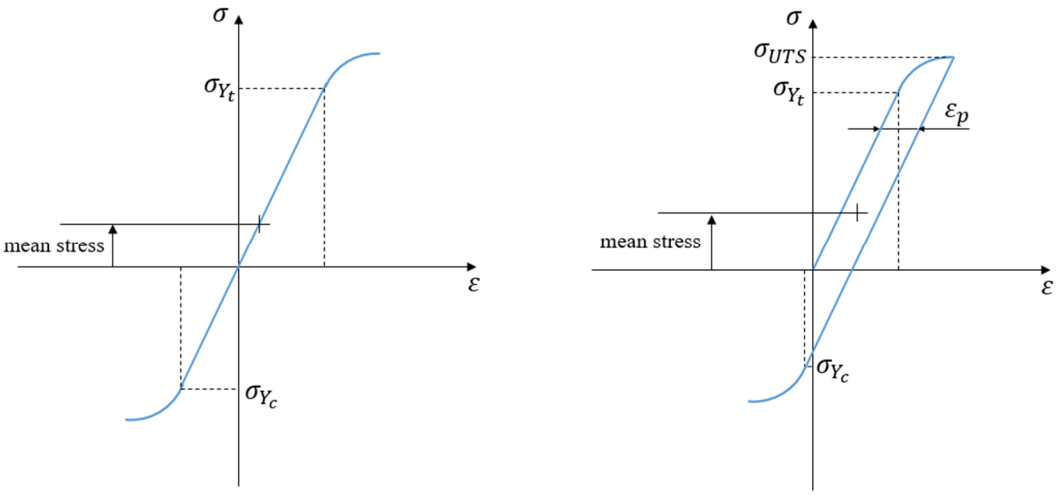

Figure 4.2 Thermo-mechanical cyclic operations: a) elastic regime, b) elasto-plastic regime.

Thus, we refer to Low-Cycle Fatigue (LCF) to indicate the phenomena inducing mechanical failure in thousands or few hundreds of thousands cyclic repetitions, in contrast to High-Cycle Fatigue (HCF), usually appointed to fluid-

structure interaction problems causing failure in tens of millions cycles, but occurring in a short amount of time because of the high-frequency of the alternating process. An intuitive representation of the two regimes is offered by Manson's method of the Universal Slopes [147] reported in Figure 4.3 according to the following formulation:

$$\Delta\varepsilon_{tot} = \Delta\varepsilon_e + \Delta\varepsilon_p = \left[3.5\frac{\sigma_{UTS}}{E}(N_f)^{-0.12}\right] + \left\{\left[ln\left(\frac{1}{1-RA}\right)\right]^{0.6}(N_f)^{-0.6}\right\} \quad (4.1)$$

with ε indicating the strains (total, elastic or plastic), N_f as the number of cycles to failure, σ_{UTS} as the ultimate tensile strength, E indicating the modulus of elasticity, and RA defined as the percentage of reduction of area (obtained from uniaxial tension tests).

Eq. (4.1) results in the total strain range curve reported in Figure 4.3, whose elastic and plastic components are visualized as the curves A and B, each one characterized by its own slope. In particular, curve A defines a relation between the elastic strain range and the number of cycles to failure; accordingly, curve B reports the same relation for the plastic strain range. The point of intersection between the two lines, defined "transition point", is commonly referred as the switching point between the LCF region on the left, where the plastic deformations are dominant, and the HCF regime on the right, in which the elastic deformations prevail.

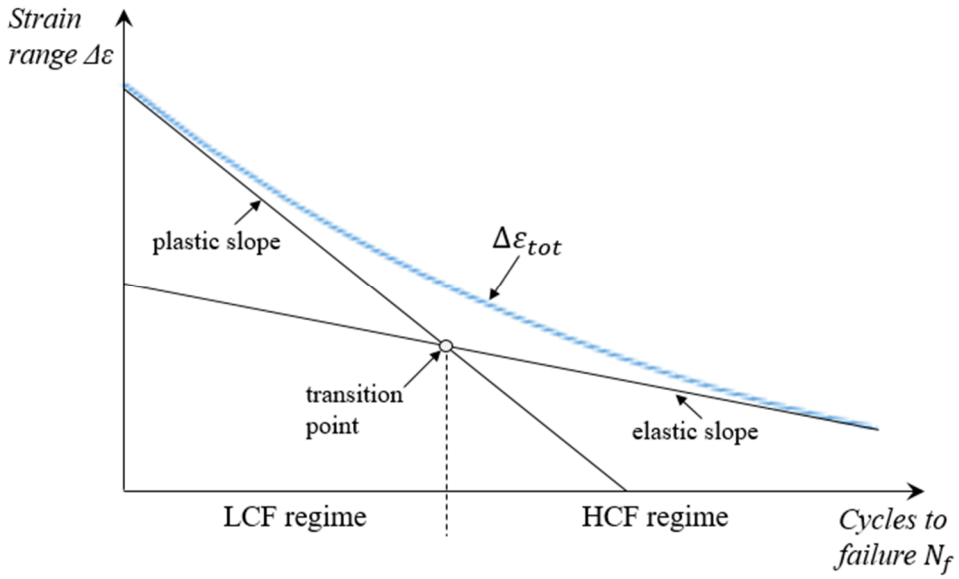

Figure 4.3 Fatigue regimes for material experiencing repeated cyclic loading.

The LCF phenomena are distinguished by the type of forcing function leading to the deformations. The most obvious case is the one related to the isothermal fatigue [148, 149], characterized by the repeated application of external or body forces at constant temperature. It is the case, for instance, of the specimens tested in laboratory in controlled conditions, in order to determine the materials fatigue characteristics.

On the other hand, thermal fatigue [150, 151] is related to the application of cyclic thermal loads inducing stresses because of the varying temperature gradients within the solid associated to its constrained differential thermal expansion. It is the case of high temperature structures experiencing repeated variations in the local thermal strains (ref. Eq. 2.28) by the alternating heating and cooling conditions. The deformations are facilitated at high temperatures, since the energy in the atoms vibrational level increases. According to [152], the material elastic modulus decreases almost linearly with the increase of temperature: thus, the cyclic elastic strain range decreases as the material weakens under higher and higher temperatures, enabling the generation of earlier plastic deformations. The thermal fatigue problems belong to the class of the LCF because of the low frequency characterizing the development of the cyclic phenomenon in the solid.

Turbomachinery applications experience the combination of the previous two cases, since both alternating stresses and varying thermal loads are present in their duty cycles. Hence, these machines are affected by Thermo-Mechanical Fatigue (TMF) problems, defined by [144] as mechanical fatigue superimposed to varying temperature cycles. In particular, the two loads could be “in-phase” if the maximum (tensile) stress is experienced at the highest temperature; otherwise, they could be “out-of-phase” when the minimum (compressive) stress takes place at the maximum temperature; or any intermediate condition of stress and temperature may happen. In the case of a turbine blade, the critical areas are the zones of concentration of unit stresses, i.e. the areas of pronounced section variations, like at the rotor connection with the shaft, or in case of holes or joining of flanges. The blade leading and trailing edges are critical areas too, because during a transient manoeuver their heating-up and cooling-down phases are faster than in the mid-chord region, with a consequent larger local expansion or contraction. Therefore, they are prone to an accelerated crack initiation when experiencing alternating conditions [153].

The study of high-temperature TMF phenomena has to deal with the accuracy in the prediction of the component lifetime, whose complex estimation is affected by the correct determination of the material properties while subjected to controlled laboratory conditions. In the past, the TMF was evaluated by adopting an isothermal fatigue approach relying on some simplifications. Either the fatigue resistance was assumed at the maximum alternating temperature, or the lowest isothermal fatigue resistance identified within the range of operative temperatures was attributed to the whole cycle. An attempt of covering the gap between the isothermal fatigue and the TMF derives from the introduction of the Bithermal Fatigue approach [154], an experimental procedure dividing the cycle in tensile and compressive halves isothermally imposed at two very different temperatures. The highest temperature is chosen in the time-dependent creep regime of the material, while the lowest temperature is selected in a regime where the time dependencies are neglected because of the lack of thermal activation. The reader interested in a more detailed treatment of the problem is addressed to [155 – 161].

The reason for the abovementioned simplifications is traced back to the possibility of collecting reliable material data at different loading conditions, while during real-life operations the material experiences transient multiaxial mechanical and thermal states. Hence, the true evolution of those micro-mechanisms appearing in thermal cyclic conditions cannot be accurately captured during the laboratory characterizations. For instance, [153] highlights that in alloys with strengthening precipitates the distribution of cyclic strains would experience localized alterations related to the thermal cycles, because of the differential thermal expansion between the precipitates and the matrix itself. In case of an isothermal test, such superimposing effect does not take place and therefore is neglected by the material characterization. In this respect, such limitations are also reflected in the traditional fatigue lifetime models [162, 163], as will be discussed in Section 4.3. The later introduction of more comprehensive macroscopic inelastic constitutive equations, like Chaboche's lifetime model [164] discussed in Section C.4, allows considering alternating conditions in a closer fashion w.r.t the natural evolution of the mechanical stresses and the thermal loadings along the cycle.

The reason for pursuing the prediction of LCF phenomena in the present work resides in the opportunity of integrating their treatment in the framework of a holistic multidisciplinary optimization. In fact, in the case of turbochargers for automotive applications, it is a common practice to perform TMF lifetime verifications in the post-processing phase of the design operations of a turbine impeller. The motivations behind this workflow are the same as discussed for the thermo-mechanical stresses in Chapter 1. Consistently with the previous argumentations, an unexpected failure revealed during the validation of a geometry would impair the outcome of the preceding optimization, thus requiring a new design loop with arbitrarily more stringent engineering margins on the constraints. Such an iterative scenario would be expensive because slowing down a development program. Moreover, the exploration capabilities of the optimizer may be limited if excessive precautions are taken on the standard mechanical constraints, which would only indirectly affect the fatigue problem. Therefore, the capability of tracing back the durability aspect of the component to the grid coordinates would expand the envelope available for the performance improvement, for instance by allowing an increase in maximum operative temperature and rotational speed, addressing the original request presented in the introduction of this manuscript.

Hence, the present chapter offers an attempt in addressing this issue by exploiting the convenient convergence capabilities of the adjoint methods, and the possibility of introducing more complex disciplines in a framework suitable for fatigue lifetime optimizations.

4.2 Modelling strategies

[165] discusses the problem of TMF for different automotive components. The turbocharger operations respect a rotational speed limit aimed at guaranteeing, by design, the safe operations of the turbine and compressor rotors within the elastic regime of their respective materials. However, the control of such turbocharger speed, performed by direct or indirect sensors measurements, is affected by uncertainties related to the accuracy band of the sensors themselves (accounting for shifts and aging), as well as the dynamics of the vehicle manoeuvers. Hence, some limited excursions in the inelastic region of the wheel's materials might occur. Moreover, on the exhaust side the impact of the thermal cycles is not precisely predictable, thus inducing further chances of accumulating plastic deformations in the turbine rotor. Therefore, even if the problem pertains to the category of "small strains" (or small deformations), yet the lifetime assessment is a fundamental aspect in the validation of such components.

The LCF evaluation along an entire driving cycle may be inconvenient, or even prohibitive within the framework of an optimization. Hence, a reduction strategy could be implemented by breaking down the whole trace in elementary samples classified by their peculiar characteristics [153]. For instance, several stretches of the original cycle may present large excursions till the region of the highest stresses and temperatures, thus representing the most extreme operative conditions for the component. An exemplary shape for a base cycle obtained from such sampling process is shown in Figure 4.4. The manoeuver is conveniently classified in terms of engine load over time, since the former parameter provides the experts with an intuitive understanding of the severity of the operating condition. The trace starts with a plateau representing a stabilization of the initial conditions, followed by a load rise, which corresponds to a progressive increase in the turbine inlet mass flow rate and rotational speed.

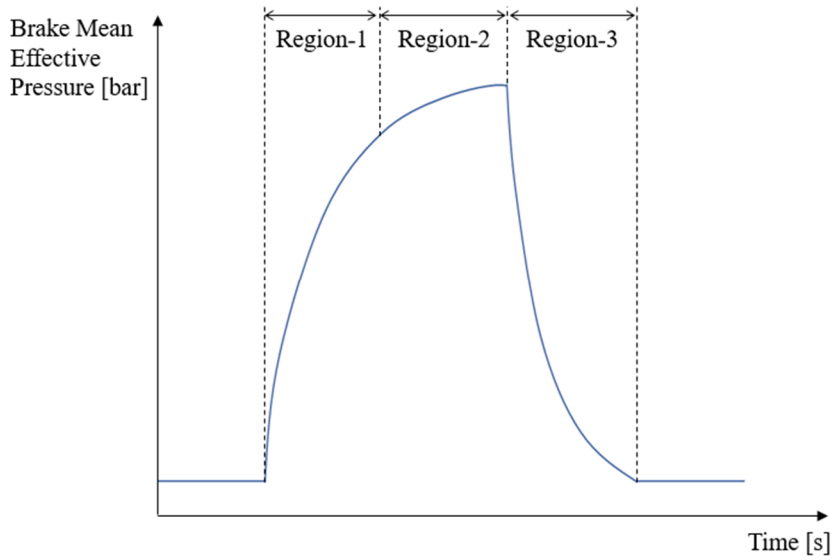

Figure 4.4 Exemplary cyclic manoeuver for the LCF evaluation of a turbine rotor.

Hence, the impeller experiences both the highest centrifugal forces and the highest internal temperature field at the end of this second section. After that, a sudden drop in engine load follows, determining a significant reduction in the rotor inlet mass flow rate and inlet flow temperature: therefore, the component is subjected to a rapid decrease in rotational speed followed by a fast cooling-down in "Region-3". Finally, a new stabilization stretch is present at the end of the cycle, with the aim of completing the dynamics of the thermal event.

The duration of the sampled event is not entirely predictable, as it depends on the vehicle dynamics and its coupling with the engine. However, a reference timeframe may vary from less than ten seconds to few tens of seconds. Despite the actual length of the manoeuver is rather short, a suitable computational framework must be selected in order to affordably model this FSI problem within an optimization task. The goal is to treat the predicted TMF lifetime as a constraint, in order to maximize the turbine rotor durability under the reference trace.

A literature review of the most relevant coupling strategies would address the problem of the unsteady Conjugate Heat Transfer by means of several numerical simplifications, since a disparity exists in the time scales between conduction and convection [166].

In this respect, [167] discusses a "quasi-dynamic" coupling approach aimed at creating a bridge between the slow response of the metal heat conduction and the change in operative conditions of the turbomachinery component. A purely unsteady coupling between the two domains requires the CFD analysis to be run over the entire duration of the thermal event within the solid region. However, the timescale should be as small as the one characteristic of the convection in order to solve for the small disturbances: thus, the fluid-solid coupling would take place at each small time step. Such approach, despite being the most accurate, would not be affordable within an optimization. Hence, the author proposes an algorithm minimizing the computational budget by focusing on the solid dynamic response with information exchanged and updated at the interface with a static flow solution. With reference to Figure 4.5, the manoeuver is split in intermediate stretches, and steady state CFD simulations are performed at the two extremes (respectively indicated as "*t1*" and "*t2*"). Hence, the solid domain is evaluated by an unsteady thermal analysis executed between the two fluid instances. At any inner time-step t_k, the solid is assigned with a boundary condition obtained by interpolating the two neighboring fluid states. Once the transient solution is available, the heat fluxes from the solid domain are imposed to the fluid domain at *t2* and a static fluid solve is called with the updated boundary condition. Hence, the process is reiterated between *t1* and *t2* leveraging the revised convective loading projected to the solid domain, till achieving convergence of the conjugate coupling. After that, the workflow continues by invoking the next stretch of manoeuver from *t2* to *t3*. It is recognized that the larger the distance between two consecutive flow solutions, the higher the number of iterations necessary to lead

the FSI coupling to convergence at each step. Hence, the overall computational budget must be optimized in this respect.

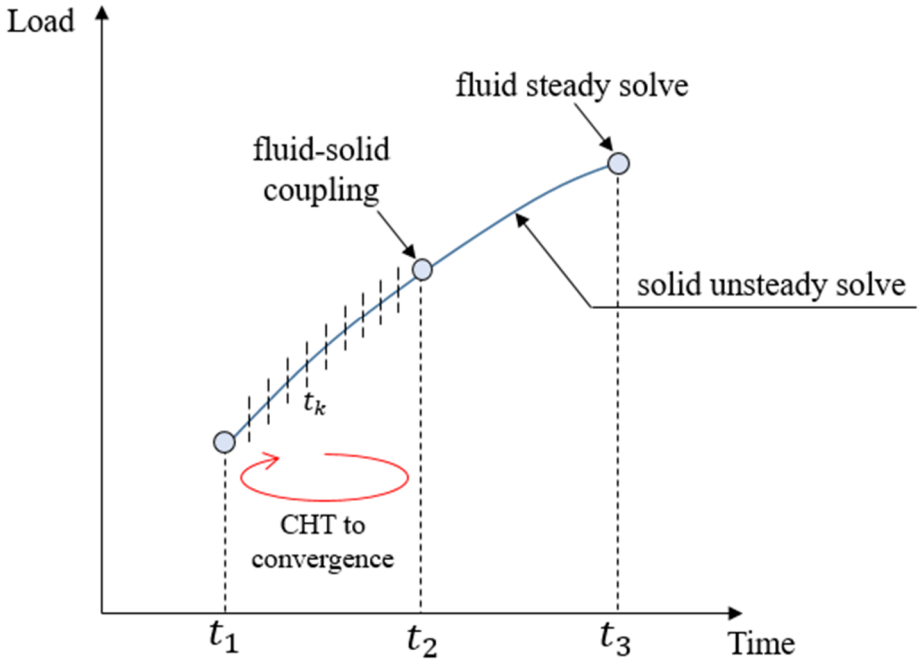

Figure 4.5 Quasi-dynamic approach for unsteady conjugate coupling.

A slight modification to the previous approach is undertaken by [168] who confirms the negligible impact of the flow unsteadiness in the evaluation of this conjugate problem. The authors adopt a workflow similar to the one at the previous step, but introducing a further simplification indicated by the Energy Equation Only method. In fact, the re-computation of the steady state fluid domain with the updated boundary condition involves only the energy equation, bypassing the continuity and momentum equations for a further reduction of the computational time. The method is supported by the assumption that there are conditions in which the fluid properties are almost independent from the temperature and therefore the energy equation has no influence on the flow field. Moreover, an automated approach for the adjustment of the solid inner time step to perform the unsteady FEM analysis is proposed. In fact, given three successive time steps t_k, a node-wise temperature interpolation is performed by a piecewise linear and parabolic curve fitting: in case the gap between the two interpolations exceeds a certain threshold, the solid time step is refined.

A more involved method is developed by [169]. With reference to the workflow by [167], while the continuity and momentum equations in the fluid are solved through steady state simulations at the update of the heat flux at the interface, the fluid energy equation is invoked concurrently with the solid domain through a transient coupling scheme. In this case, the steady state fluid computations are called according to a coarser schedule, defined by a sufficiently large threshold in the change of the Nusselt number necessary to influence the flow velocity distribution. Hence, this approach, despite being more

computationally expensive than the previous ones, attempts to minimize the number of calls to the steady state flow solver by means of empirical evaluations of the temperature change at the domains interface along the specific manoeuver.

[170] proposes a simplification to the coupling problem by attempting the elimination of the FSI iterations presented in the first scheme herein discussed. In fact, in absence of such repetitions of the conjugate coupling for each stretch of manoeuver, the authors discuss the possibility of simply enforcing the continuity of energy exchanged at the interface by applying a corrective factor, according to their "estimation of the conservative correction" approach. Three different techniques are compared for the imposition of such correction, to be assigned either before or after the domains coupling, or even during the same domains integrations. Despite the significant reduction of the computational budget, the method demonstrates some shortcomings in terms of robustness from stability perspectives, especially in case of Neumann boundary conditions.

Finally, [171] discusses a technique aimed at surpassing the quasi-dynamic approach in order to provide a CHT framework applicable to a wide range of time scales, by getting closer to a direct time-accurate integration. Starting from the consideration of the significant disparity in time scales between the fluid and the solid domains involved in the conjugate problem, the authors propose a loose coupling approach in which the flow is subjected to a decomposition in two time scales. The small temporal resolution is the typical one adopted to solve the small perturbations self-excited by the flow unsteadiness. The large scale is obtained by imposing a low-pass filtering and captures only the long-wavelengths disturbances. Hence, the flow domain is efficiently solved in transient mode over the two time scales, while the time-averaged heat fluxes computed on the larger scale are passed to the solid domain. On the other side, the solid provides the temperature information at the interface, which is imposed to the fluid domain as a boundary condition for the large-scale solver. Thus, thanks to the assumption of the milder influence of the temperature variations on the flow velocities, the fine scale fluid disturbances can be accurately resolved in their own time step, without invoking a full transient multi-domain solution.

Despite this methodology is attractive from accuracy standpoint, the present work is based on the quasi-dynamic approach previously described, mainly for two reasons. First, the TMF analysis focuses on the solid dynamic response, and the literature agrees on the mild influence of the fluid domain unsteadiness on the solid temperature evolution in this kind of FSI problems, because of the marked disparity in time scales. On the other side, this scenario is supported by the high blade pass frequency (in the range of 5-50 kHz within the operative envelope of the turbine) w.r.t. a minimum duration of each stretch of manoeuver as low as some decimals of second: hence, from aerodynamic standpoint, the blade perceives the engine load transition as a sequence of steady state events. Second, the selected method must be affordable within the iterative framework of an optimization, in compliancy with the typical duration of such manoeuvers. Conversely, oversimplifications like in the case of the conservative correction

approach are not envisaged, because the method is aimed at being applicable to any manoeuver, despite the local steepness of its profile.

Hence, the previous sample manoeuver is split in several stretches, each one extending from t_i to t_{i+1}, according to a user-defined step in engine load (Figure 4.6). Steady state CFD computations are called at the two extremes of each section, which are walked in the solid domain through an unsteady solution. Since each section of the cycle presents a different load gradient, the solid inner time step is adapted accordingly, in order to preserve the expected accuracy and numerical stability even in the steepest stretches. Finally, the last portion of the alternating profile aimed at establishing a thermal equilibrium is not considered anymore in the following discussion, as no considerable fatigue event occurs in this last time step.

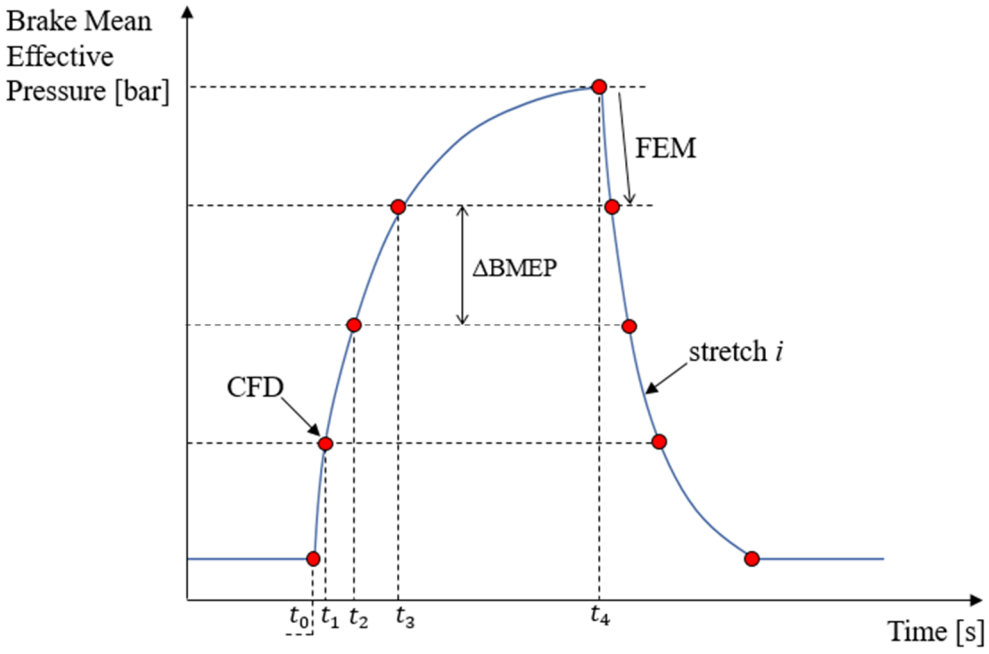

Figure 4.6 Sample manoeuver split in sub-sections.

4.3 Thermo-Mechanical Fatigue evaluation: Primal solvers

4.3.1 The workflow

The quasi-dynamic approach selected for the evaluation of the TMF lifetime presents significant similarities with the thermo-mechanical workflow discussed for steady state problems. In fact, the loose coupling approach calls the static flow solutions at predetermined time steps: hence, the in-house CFD solver can be directly implemented in the new procedure. Moreover, since the conjugate coupling between the two domains takes place only at the end of each stretch of manoeuver (once the unsteady FEM computation is completed), the new

framework inherits the hFFB routine presented in Chapter 2. In fact, the heat flux at the interface – computed at the end of each solid transient event – is assigned as a boundary condition to the steady state CFD, which returns the updated Robin boundary condition to the solid domain, while the user-imposed virtual heat transfer coefficient $\tilde{h}$ is fixed. Hence, the conjugate problem is re-iterated till convergence, before moving forward with the following stretch of the manoeuver.

The conjugate coupling provides the temperature field to an unsteady thermo-mechanical solver, which shares the same mesh and inner time step with the transient heat transfer solver. Therefore, a one-way partitioned coupling is established between the two FEM solvers with no need of any interpolation, consistently with the steady state workflow. With reference to Figure 4.7, at each stretch of manoeuver, the temperature fields stored at all the inner steps t_k of the last CHT loop at convergence are provided as input to the mechanical solver. Thus, the solid dynamic response benefits from a continuously updated temperature field at each inner step, conveying a corresponding local adjustment of the temperature-dependent material properties.

At the end of the manoeuver, the entire history of stresses and deformations is evaluated by a lifetime model, with the goal of predicting the number of cycles to failure.

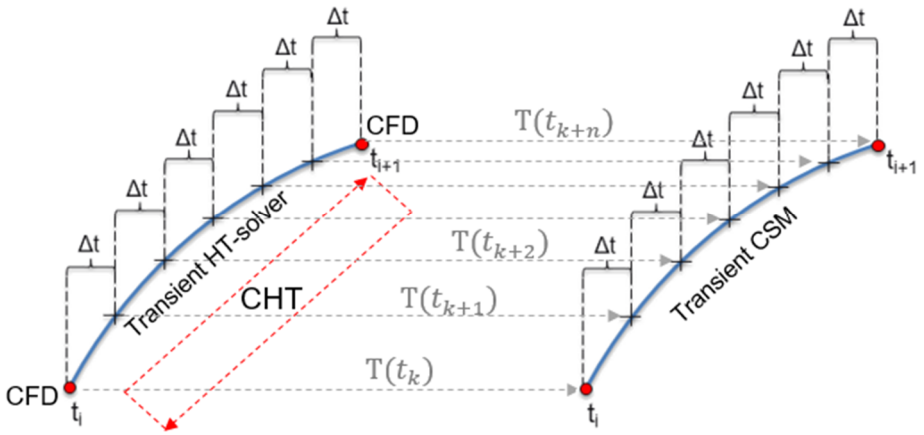

Figure 4.7 Loose coupling for unsteady conjugate problem and transient thermo-structural prediction.

In conclusion, the previous considerations support the initial choice of a partitioned coupling approach for the steady state thermo-mechanical problem, since the present TMF lifetime estimation develops as a natural extension of the original workflow. Figure 4.8 shows the flowchart updated to the alternating manoeuver, in which the FEM solvers are replaced by their unsteady counterparts, as well as a new routine for the computation of the constraint function is implemented.

4.3.2 Steady state flow solver

The steady state in-house flow solver introduced in Chapter 2 is invoked by the partitioned coupling workflow shown in Figure 4.8. Heat flux boundary conditions are assigned at the viscous walls.

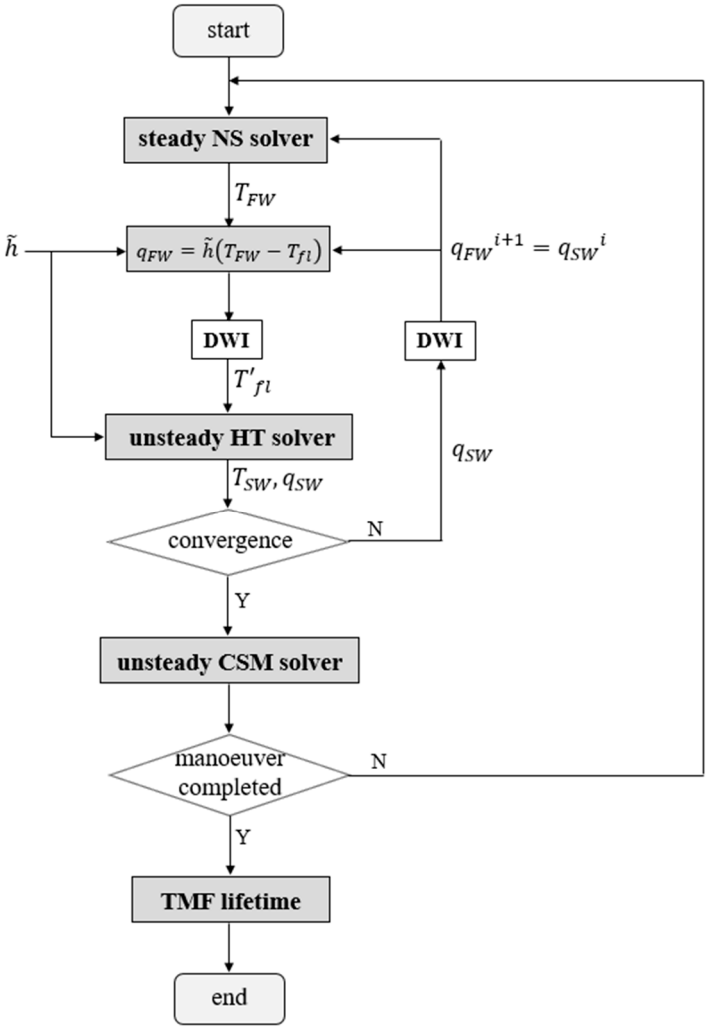

Figure 4.8 Partitioned coupling method for the TMF analysis.

Since the entire manoeuver is split in several stretches extending from t_i to t_{i+1}, in each one the flow field has to be resolved at the two extreme points prior to the solid, in order to start the conjugate coupling. Therefore, at first the heat flux computed in t_i at the end of the previous stretch is assigned to the CFD solver in t_{i+1}, and the flow field is preliminarily resolved. The two flow states at the extremities of the stretch are linearly interpolated in order to provide the convective loads to the solid at each inner time step along the unsteady integration. At the completion of the transient computation, the solid returns a new heat flux to the fluid domain; thus, a new steady state flow solution is performed with the updated boundary condition, resulting in a more accurate Robin boundary condition assigned to the solid at the following hFFB loop.

The conjugate coupling is iterated till convergence. After that, the calculations are executed at the following stretch, until the full manoeuver is processed.

4.3.3 Transient non-linear heat transfer solver

An unsteady non-linear FEM heat transfer solver is developed for the computation of the temperature field along the transient conjugate coupling.

With reference to Eq. (2.7), repeated here for convenience,

$$\rho c_p \frac{dT}{dt} = \nabla \cdot q + Q \tag{4.2}$$

in case of a convective load and in absence of internal heat sources, it is possible to derive its weak form as follows:

$$\int_V \rho c_p \frac{dT}{dt} \delta T \, dV + \int_V k \nabla T \; \nabla(\delta T) dV = -\int_S \tilde{h}\left(T - T'_{fl}\right) \delta T \, dS \,. \tag{4.3}$$

The discretization of Eq. (4.3) leads to

$$\begin{aligned} &\sum_e \sum_i \sum_j \underbrace{\left[\int_{V_e} \rho(\mathrm{T}) c_p(\mathrm{T}) \, \varphi_i \varphi_j \, dV_e\right]}_{Mass} \frac{dT_i}{dt} \delta T_j \\ &+ \sum_e \sum_i \sum_j \underbrace{\left[\int_{V_e} \mathrm{k(T)} \, \nabla\varphi_i \nabla\varphi_j \, dV_e\right]}_{A_{cond}} T_i \delta T_j \\ &+ \sum_e \sum_i \sum_j \underbrace{\left[\int_{S_e} \tilde{h} \varphi_i \varphi_j dS_e\right]}_{A_{conv}} T_i \delta T_j \\ &= \sum_e \sum_j \left[\int_{S_e} \tilde{h} T'_{fl} \varphi_j dS_e\right] \delta T_j \,. \end{aligned} \tag{4.4}$$

The solver non-linearity is expressed by the temperature-dependent material properties, i.e. the density, the heat capacity and the thermal conductivity. This characteristic allows achieving a higher accuracy in the unsteady computations of the temperature field, when deep loading or unloading manoeuvers are performed in a short amount of time, especially because of the more pronounced temperature sensitivity shown by the density and the heat capacity terms.

The stretch of manoeuver under consideration is divided in N time steps Δt. Hence, the integration of Eq. (4.4) can be written in implicit form as:

$$M(T_k^{n+1})\,\frac{T_k^{n+1}-T^n}{\Delta t}+A(T_k^{n+1})\,T_k^{n+1}=b\,. \tag{4.5}$$

Here, $T_k^{n+1}\in R^n$ indicates the unknown temperature field at the end of the time step, while $T^n\in R^n$ is the known temperature at the beginning of it. $M(T_k^{n+1})\in R^{n,n}$ represents the first integral term in Eq. (4.4) and is commonly referred as the mass matrix. The matrix A comprises the conductive and the convective terms $A=[A_{cond}+A_{conv}]\in R^{n,n}$. Both the matrices at the LHS of Eq. (4.5) are SPD. Finally, the RHS vector $b\in R^n$ accounts for the convective load. Since in the hFFB method the virtual heat transfer coefficient $\tilde{h}$ is fixed, b does not depend on the solid temperature.

The non-linear system in (4.5) is solved through the application of the Newton-Raphson method, as discussed in detail in Section C.1. At each time step, the convective load is updated by a linear interpolation of the two extreme fluid states computed in Section 4.3.2, thus leading to a new T'_{fl}.

The resulting temperature field integrated over the stretch of manoeuver is post-processed by the routine presented in Section B.4 in order to compute the heat fluxes at the interface. Finally, such heat fluxes are passed to the hFFB routine for an interpolation before being assigned to the fluid domain.

The exchange of information between the unsteady FEM solver and steady state CFD is iterated multiple times. Once the thermal coupling in the reference stretch of manoeuver reaches convergence, the temperature field initializes the next loading or unloading section, while in parallel the structural solver acquires the thermal input to compute the evolution of the stresses.

4.3.4 Transient linear mechanical solver

The solid structural response is computed through an unsteady linear FEM mechanical solver. In this case, the linearity is associated to the material, which relies on the linear elastic hypothesis. In fact, despite the material properties are temperature dependent, the elasticity is expressed by stresses that are linearly proportional to the strains. This assumption is supported by the fact that turbocharger operations normally respect a limit of maximum rotational speed within the elastic regime of the wheel's material (with some margins w.r.t. the yield strength). Hence, the machine is supposed to continuously work in the region of "infinite life". However, in Section 4.2 it was anticipated that, in case of very aggressive manoeuvers, some limited excursions in the inelastic region might occur. Therefore, despite the permanence time, some accumulations of plasticity would follow.

Since this phenomenon is limited, it is assumed the rotors operate in the "small strain" region, in which the linearized theory of elasticity holds because of the small deformations, and the strain is supposed to depend on the effective stress. For this reason, no modification to the shape of the body is operated during the analysis because of the effect of the local plasticity. The reader interested in

more details about modelling techniques for non-linear problems with finite deformations is addressed to [172].

Hence, this assumption allows treating the cases of material yielding through a post-processing routine, described in the next section, which divorces the TMF lifetime assessment from the FEM simulation [165].

According to such precondition, the unsteady evolution of the displacements field is described by Eq. (2.23) repeated here for convenience:

$$\begin{cases} \dfrac{\partial \sigma_{xx}}{\partial x} + \dfrac{\partial \sigma_{yx}}{\partial y} + \dfrac{\partial \sigma_{zx}}{\partial z} + f_x = \rho \dfrac{\partial^2 u}{\partial t^2} \\ \dfrac{\partial \sigma_{xy}}{\partial x} + \dfrac{\partial \sigma_{yy}}{\partial y} + \dfrac{\partial \sigma_{zy}}{\partial z} + f_y = \rho \dfrac{\partial^2 v}{\partial t^2} \\ \dfrac{\partial \sigma_{xz}}{\partial x} + \dfrac{\partial \sigma_{yz}}{\partial y} + \dfrac{\partial \sigma_{zz}}{\partial z} + f_z = \rho \dfrac{\partial^2 w}{\partial t^2} \end{cases} \tag{4.6}$$

Following the development discussed in Section 2.3.3, the weak form of Eq. (4.6) is discretized as

$$\begin{aligned} \sum_e \sum_i \sum_j \underbrace{\left[\int_{V_e} \rho(T) \varphi^T \varphi \, dV_e \right]}_{M_e} \frac{\partial^2 U_i}{\partial t^2} \delta U_j \\ + \sum_e \sum_i \sum_j \underbrace{\left[\int_{V_e} B^T \mathrm{E}(T) \, \mathrm{B} \, dV_e \right]}_{S_e} U_i \delta U_j \\ = \sum_e \sum_j \left[\int_{V_e} \rho(T) \varphi_j b(\omega) dV_e \right] \delta U_j \\ + \sum_e \sum_j \left[\int_{V_e} B^T E(T) \varepsilon_{th}(T) dV_e \right] \delta U_j \\ + \sum_e \sum_j \left[\int_{S_e} \varphi_j t \, dS_e \right] \delta U_j \end{aligned} \tag{4.7}$$

in which the first term, i.e. the mass matrix, is added to the formulation previously encountered in steady state. It is important to note the material parameters exhibit a temperature dependence, as expressed by the density, the elasticity matrix and the thermal expansion coefficient $\alpha(T)$ included in the definition of the thermal strains (beside their direct dependence over the temperature difference w.r.t. ambient). The temperature field is known at each time step along the transient computation, as deriving from the converged thermal coupling at the previous section. Hence, the material properties are continuously

updated. Since the mechanical solver shares the same mesh and the same time steps as the thermal solver, no interpolations are necessary. This choice results particularly convenient in adjoint mode.

Moreover, no damping term (related to the hysteresis of the material) appears in Eq. (4.6) and Eq. (4.7), because negligible in the case of low-frequency transient excitations as discussed in this chapter.

The system of equations in (4.7) is expressed in compact form as

$$M\ddot{U} + SU = f \tag{4.8}$$

and is solved by a discrete approximation in time through the Newmark method [173]. The presence of the inertial term requires the identification of three variables at each discrete time t^n:

$$\left\{U, \dot{U}, \ddot{U}\right\} = \{u, v, a\}\,. \tag{4.9}$$

The Newmark method is a one-step technique that computes the state at t^{n+1}, given its value at t^n. Since there are three quantities in Eq. (4.9), the method adopts a system of four equations to advance the solution in time:

$$\begin{cases} \hat{u}_{n+1} = u_n + \Delta t\, v_n + \left(\frac{1}{2} - \beta\right)\Delta t^2 a_n \\ [M + \beta\Delta t^2 S]\, a_{n+1} = f_{n+1} - S\hat{u}_{n+1} \\ v_{n+1} = v_n + (1-\gamma)\Delta t\, a_n + \gamma\Delta t\, a_{n+1} \\ u_{n+1} = u_n + \Delta t\, v_n + \left(\frac{1}{2} - \beta\right)\Delta t^2 a_n + \beta\Delta t^2\, a_{n+1} \end{cases}. \tag{4.10}$$

The first equation in (4.10) describes the formulation of the predictor $\hat{u}_{n+1}$, whose quantities at t^n are all known. The predictor is called by the second equation, which is a residual formulation of the equilibrium equation (4.8) and is solved w.r.t. the independent variable a_{n+1}, i.e. the acceleration at time t^{n+1}. The solution allows updating the velocities and the displacements fields. Hence, the next time step is approached.

The system in (4.10) presents the coefficients (β, γ) whose values determine the stability and the dissipation properties of the scheme. In the present work, the implicit formulation of the Newmark method, obtained with $\beta = 1/4$ and $\gamma = 1/2$, is adopted because it is unconditionally stable and does not imply any numerical dissipation. This arrangement is also known as “trapezoidal rule” or “constant acceleration method”.

The advantage of choosing an implicit method resides in the possibility of freely adopting the same time steps as the heat transfer solver, with the aim of avoiding any interpolation of the temperature fields exchanged between the two frameworks. Moreover, also the thermal solver adopts an implicit method, in order to guarantee the possibility of adapting the time step to the local steepness

of the profile of the transient manoeuver. Thus, the efficiency of the unsteady computations is favored, with no constraints from numerical stability standpoint.

At each time step, once the transient displacements field is solved, the post-processing routine aimed at computing the strains is invoked, followed by the evaluation of the stresses according to the linear elastic assumption. Hence, the verification of the material yielding is performed by the constitutive model discussed in the next section.

4.3.5 Constitutive model for inelastic deformations

The constitutive model is used to characterize the material non-linearity and intervenes only in case of yielding. As previously mentioned, adopting the constitutive equations only in the phase of post-processing of the FEM solution is admissible because the reference application operates in the "small strains" region.

The model is described in detail in Section C.2. It starts with a verification of inelasticity: in case any nodal stress exceeds the Yield surface, an appropriate evaluation of the plastic strains and stresses is operated by the method. During this operation, the displacements field is corrected as well, before advancing the solution to the following time step.

In case no local plasticity is identified, the constitutive equations are not invoked, and the solver is allowed to move to the next time step.

4.3.6 Lifetime evaluation model

The alternating manoeuver is analyzed through the partitioned coupling workflow shown in Figure 4.8, iterating over the whole set of stretches. Once the trace is completed, the history of nodal stresses and strains is available: hence, it is possible to evaluate the TMF lifetime of the component.

A crack-initiation model is considered in the present work. In fact, once the crack is originated at the free surface of the solid, the forces driving its propagation usually decrease as the crack grows [144]. For this reason, it is necessary to prevent or delay as much as possible the initiation event by design; hence, no attempts in modelling the crack propagation were undertaken as deemed irrelevant in the present scenario.

The definition of the singular event leading to a cyclic crack initiation is a topic of debate, partially because of the difficulty in accurately characterizing the TMF phenomenon by controlled specimens testing. Moreover, the fatigue strength of the materials tends to decrease at high temperatures, and this phenomenon is difficult to generalize in the inelastic regime, especially in the case of the temperature dependence of the total strain range, which is invoked by the lifetime estimation models. However, considerable research was conducted to link the

initiation event at the surface with the bulk properties of the material, and predictive correlations were established. The reader interested in a review of the conducted activities is addressed to [174].

The literature offers many TMF lifetime models [175, 176], and their selection cannot ignore the availability of a comprehensive characterization of the material properties. The present study focuses on the Morrow model [163], which belongs to the family of the strain life methods.

Following the work by Manson [151], the Morrow model plots the fatigue life in terms of the total strain range $\Delta\varepsilon^{tot}$ (cf. Figure 4.3). Differently from the stress life analysis techniques, the adoption of the total strain range allows gaining further resolution in the lifetime prediction at low numbers of cyclic repetitions (i.e. in the LCF regime), because the strain range curves present non-unique solutions in that region. Conversely, the correspondent stress amplitude curves would exhibit an almost flat profile for low number of cycles to failure [165], hence making an appropriate estimation of the TMF lifetime difficult.

The relation between the total strain range and the fatigue life is expressed as follows:

$$\Delta\varepsilon^{tot} = \Delta\varepsilon^{e} + \Delta\varepsilon^{p} = \frac{2\left(\sigma_f' - \sigma_{mean}\right)}{E}\left(2N_f\right)^{b} + 2\varepsilon_f'\left(2N_f\right)^{c} \qquad (4.11)$$

with $2N_f$ indicating the number of cyclic repetitions, the total strain range obtained by summing up the elastic and plastic components (as schematically shown in Figure 4.9), σ_f' representing the fatigue strength coefficient and ε_f' as the fatigue ductility coefficient (both tabulated as material properties), and E as the elastic modulus. The two terms at the RHS of Eq. (4.11) represent the elastic and plastic components already anticipated by the method of the Universal Slopes (ref. Eq. 4.1), and their slopes are determined by Basquin's exponent b and the fatigue ductility exponent c, which represent respectively the material sensitivities to cyclic stressing and alternating straining. The relevant data adopted in the present study is available in [163]. Figure 4.9 offers a qualitative distinction between the amplitude of the plastic strain range w.r.t. the total strain range, the former obtained by subtracting the elastic tensile and compressive parts.

Since the fatigue properties are usually defined for a zero mean stress testing condition, a corrective factor is adopted in Eq. (4.11) by altering the fatigue strength of the material by an amount corresponding to the mean stress σ_{mean} over the cycle. This correction allows generalizing the application of the lifetime estimation model to any working condition, as non-zero mean stresses are usually encountered in real life operations (cf. Figure 4.2).

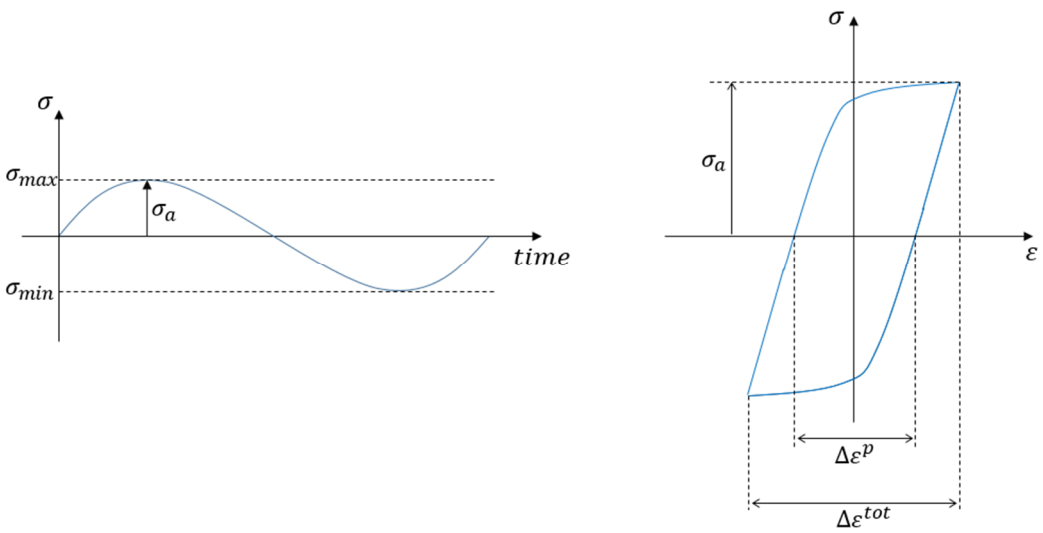

Figure 4.9 Schematic representation of strain range composition. Source [163]

The application of the Morrow model in the code is performed on a nodal basis, i.e. by separately analyzing the strain histories along the transient manoeuver for each node in the FEM mesh. Therefore, each grid point brings its own total strain range, from which the number of cycles to failure is computed. At this stage of development, some approximations in the lifetime estimation have been accepted. In fact, each node in the mesh experiences a thermal cycle along the manoeuver, while the abovementioned fatigue properties (i.e. $\sigma_f', \varepsilon_f', b, c$) are assigned w.r.t. a nodal reference temperature evaluated along the transient event. In case of lack of an extensive dataset, fatigue properties measured at a unique reference temperature may be assigned to the whole mesh, thus incurring in the accuracy limitations previously described in the case of the isothermal fatigue evaluations.

This shortcoming was overcome by the Chaboche TMF lifetime model [164], whose development is discussed in Section C.4. The rest of the chapter follows the original approach by Morrow, as not all the experimental data necessary to operate the Chaboche model are available to the present work.

Eq. (4.11) requires the total strain range and the mean stress in input to the lifetime calculation. With reference to Figure 4.9, the former is obtained by evaluating the whole history of the nodal strains along the alternating manoeuver, such that

$$\Delta\varepsilon^{tot} = \varepsilon^{tot}_{max} - \varepsilon^{tot}_{min} \,. \tag{4.12}$$

Eq. (4.12) presents the difference between the total strain values, which are obtained from the FEM solution (or corrected by the constitutive model, in case of plasticity), according to the von Mises equivalent strain definition. The formulation is repeated here for convenience:

$$\varepsilon_{eq\_vM} = \frac{2}{3}\sqrt{\frac{3}{2}\left(\varepsilon_{xx}^2 + \varepsilon_{yy}^2 + \varepsilon_{zz}^2\right) + \frac{3}{4}\left(\gamma_{xy}^2 + \gamma_{yz}^2 + \gamma_{zx}^2\right)}\,. \tag{4.13}$$

For sake of compliance with the requirements of the adjoint implementation, both the terms in Eq. (4.12) are computed by p-norm functions.

Instead, the mean stress is simply obtained by averaging the nodal history of von Mises stresses.

In conclusion, since Eq. (4.11) is non-linear, it is solved by using the Newton-Raphson method, discussed in Section C.1, as follows:

$$\begin{gathered} R = \Delta\varepsilon^{tot} - \frac{2\left(\sigma_f' - \sigma_{mean}\right)}{E}\left(2N_f\right)^b - 2\varepsilon_f'\left(2N_f\right)^c \\ \frac{dR}{dN_f}\,\Delta N_f = -R\,. \end{gathered} \tag{4.14}$$

In order to speed up the solution process, a refinement of the initial guess is executed by application of a regula falsi. Hence, the nodal TMF lifetime is obtained eventually, and the minimum lifetime over the whole set of grid points is simply computed by means of a p-norm function such that $min = \sqrt[k]{\sum_i x_i^k}$, $k \to -\infty$, thus completing the evaluation of the cost function J_{LCF} in primal mode.

4.4 Thermo-Mechanical Fatigue evaluation: Adjoint solvers

4.4.1 The workflow

The present section is devoted to the computation of the TMF lifetime sensitivities w.r.t. the CAD parameters α in order to impose the minimum lifetime as a further constraint in the turbine optimization problem.

The workflow presented in Figure 4.10 is consistent with the trace of the cyclic manoeuver shown in Figure 4.6. The branch on the left presents the development of the primal solvers discussed in Section 4.3. It is important to note that at first the workflow engages the steady state thermo-mechanical algorithm described in Chapter 2, before moving to the unsteady counterpart. This is in line with the presence of a flat stretch at the beginning of the manoeuver, whose function is to guarantee the thermal equilibrium as an initial condition. Once the convergence of the steady state portion is achieved, the quasi-dynamic computations take place, iterating over the rest of the manoeuver. Finally, the Morrow model is engaged for the lifetime estimation.

The development of the adjoint branch starts by seeding the minimum lifetime. Hence, the workflow shown on the RHS of Figure 4.10 propagates the

adjoint variables in opposite direction, maintaining its consistency with the iterative framework walked in primal mode.

Since the flow is treated by steady state simulations, the correspondent adjoint field is solved in steady state conditions as well, by means of the in-house adjoint CFD solver presented in Section 3.3.5. Moreover, the conjugate coupling in adjoint mode inherits the adjoint hFFB routine from the thermo-mechanical development: thus, adjoint variables are exchanged at the interface of the two domains.

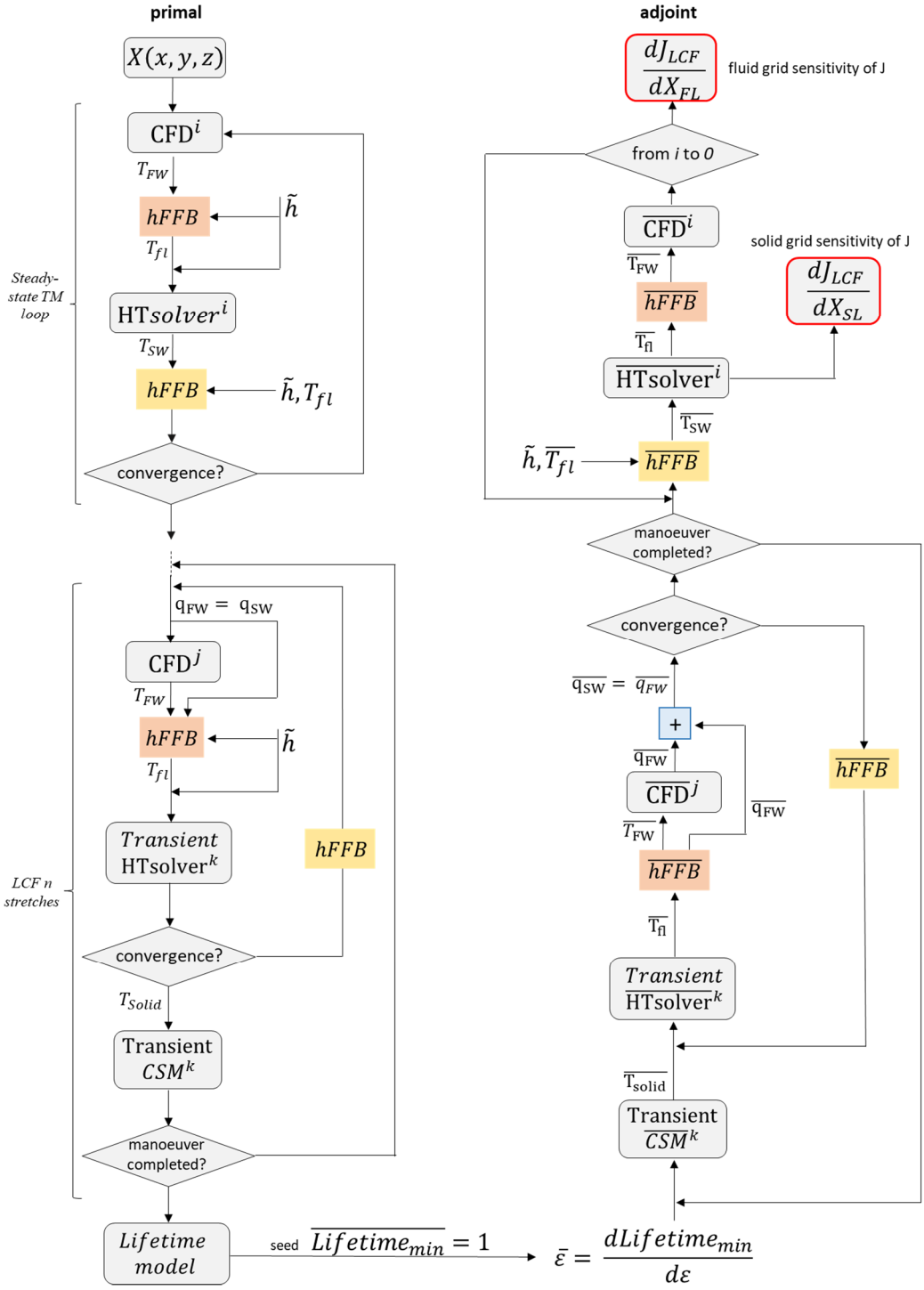

Figure 4.10 Workflow for the primal and adjoint computations of thermo-mechanical fatigue lifetime constraints.

The major novelty is represented by the two adjoint FEM solvers, whose unsteady development is discussed in the next sections. The process of accumulation of the adjoint variables maintains its consistency with the previous treatment and the fluid and solid grids, invoked multiple times along the iterative procedure, accumulate their sensitivities, till reaching the grid generation routine on top of the chart.

Consistently with the steady state algorithm discussed in Chapter 3, the adjoint TMF workflow terminates with the accumulated grids sensitivities, which are finally processed through Eq. (3.2) for the evaluation of the constraint $(dJ/d\alpha)_{LCF}$.

The extent of the framework presented in Figure 4.10 supports the choice of manually differentiating the whole branch in reverse mode, as a matter of achieving an optimal memory footprint. In fact, in case of adopting an automatic differentiation software, the entire primal workflow would have had to be recorded on the tape, making the process computationally inconvenient.

4.4.2 The adjoint lifetime evaluation model

The evaluation of the Morrow model in reverse mode follows the adjoint framework discussed in Section C.2.

Starting from the seeded value of the minimum lifetime over the entire domain, the adjoint nodal lifetimes are obtained by reverse differentiation of the p-norm function (cf. Section 4.3.6):

$$\begin{aligned} \overline{Lifetime}_{\min} &= \bar{J}_{LCF} = \frac{dy}{dJ_{LCF}} = 1 \\ \overline{N_f(i)} &= \frac{dy}{dN_f(i)} = \frac{d}{dN_f(i)} \sqrt[p\_min]{\sum_{j=1}^{N} \left[N_f(j)\right]^{p\_min}} \quad . \end{aligned} \tag{4.15}$$

Since at each iteration of the Newton-Raphson method in primal mode $N_f^{k+1} = N_f^k + \Delta N_f$, in reverse mode the linearization around the converged solution leads to

$$\begin{aligned} \overline{\Delta N_f} &= \overline{N_f}^{\,k+1} \\ -\frac{dR}{dN_f}\,\bar{R} &= \overline{\Delta N_f} \quad . \end{aligned} \tag{4.16}$$

Hence, for each solid grid node, the adjoint residual is computed by linearizing around the converged solution. Since the residual formulation in Eq. (4.14) involves the total strain range and the mean stress, these variables are respectively seeded. In the case of the adjoint mean stress, the process of seeding the nodal von Mises stress is trivial, and is followed by the algorithmic differentiation of the von Mises stress formula, in order to calculate the adjoint stresses $\bar{\sigma}$. Concerning the adjoint total strain range, it follows that

$$\begin{aligned} \overline{\varepsilon_{max}^{tot}} &= \overline{\Delta\varepsilon^{tot}} \\ \overline{\varepsilon_{min}^{tot}} &= -\overline{\Delta\varepsilon^{tot}} \end{aligned} \quad . \tag{4.17}$$

Therefore, the nodal values of the von Mises strains are seeded by differentiating the two p-norm formulations (like in Eq. 4.15). Finally, the nodal strains are seeded by algorithmic differentiation of the definition in Eq. (4.13).

4.4.3 The adjoint unsteady thermo-mechanical solver

The unsteady computations of the thermo-mechanical response of the solid rely on the transient temperature field and the solid grid as input, as well as the updated rotational speed at each time step. Section 4.3.4 discusses the motivation behind the adoption of a linear elastic solver, whose output is corrected by the constitutive equations in case of any occurrence of local plasticity. The corrections, affecting the displacements, as well as the strains and the stresses, are passed to the following time step in the advancement of the solution along the transient manoeuver, and finally to the TMF lifetime model. The process is schematically represented on top of Figure 4.11.

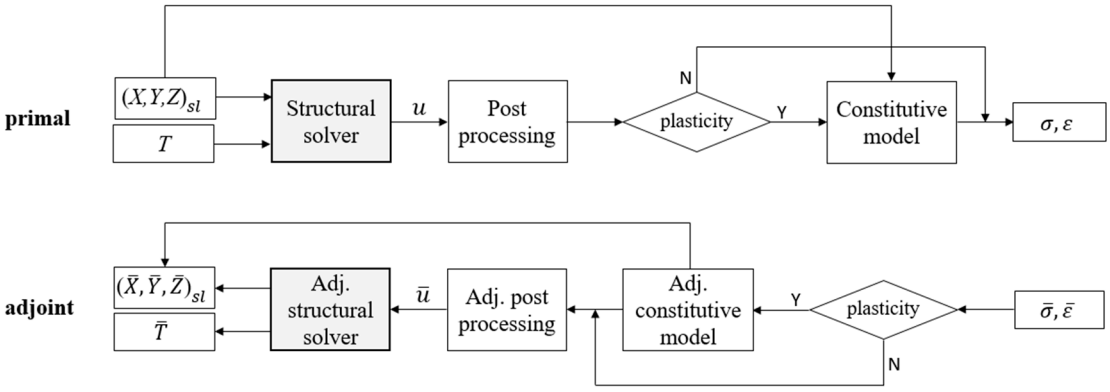

Figure 4.11 Adjoint workflow for unsteady thermo-mechanical computations at time step *k*.

The propagation of the adjoint variables in reverse mode starts from the seeded stress and strain fields released by the adjoint lifetime model. Hence, for each stretch of manoeuver and for every inner time step along the unsteady computation, the workflow on the bottom of Figure 4.11 applies. In particular, at the instant t^{n+1} the grid points are checked for any occurrence of local plasticity (this indication is stored in a supporting vector during the primal computations). If the assessment is affirmative, the adjoint stresses and strains are imported in the adjoint constitutive model, whose development is discussed in Section C.3. The routine completes by seeding the original stress and strain fields, obtained by the linear elasticity theory, as well as contributing to the accumulation of the solid grid sensitivities. Instead, in case the plasticity check is negative, the adjoint

constitutive model is simply bypassed, because not affecting the primal computations.

Afterwards, the reverse post-processing routine computing the strains and the stresses from the displacements field is engaged. The discussion follows the steps already undertaken in Section 3.3.2. Such routine seeds the displacements field, which is passed to the linear elastic solver, and accumulates further contributions to the grid sensitivities.

Hence, the adjoint structural solver is invoked. The unsteady structure of the solver in adjoint mode differs from the steady state counterpart, as the Newmark method is differentiated. According to the structure of the equations in (4.10), the following reverse schedule is deduced:

1. The variables u_n, v_n, a_n, a_{n+1} are seeded from the third and fourth equations in (4.10), and their sensitivities are accumulated.
2. A new linear system is created in (4.18), consistently with the mechanical solver in steady state, and the adjoint load vector is computed first. Here, $F_{n+1} = f_{n+1} - S\hat{u}_{n+1}$. The computation of the adjoint LHS matrix follows.

$$\begin{cases} [M + \beta\Delta t^2 S]^T \ \bar{F}_{n+1} \ = \ \bar{a}_{n+1} \\ \overline{[M + \beta\Delta t^2 S]}_{ij} \ = \ -a_{n+1}(j)\, \bar{F}_{n+1}(i) \end{cases} \tag{4.18}$$

3. The contributions to the adjoint temperatures and to the grid sensitivities are accumulated by differentiating the system assembly process for the LHS matrix and the load vector. The procedure is described in Section C.5.
4. The predictor $\hat{u}_{n+1}$ is seeded through the adjoint load vector $\bar{F}_{n+1}$, and the differentiation of its definition allows accumulating the sensitivities to the displacement, velocity and acceleration terms at the time t^n. Such sensitivities are passed to the next time step Δt in backward direction.
5. The sensitivities of the temperature field are provided in input to the adjoint unsteady heat transfer solver, in order to contribute to its computations over the same time step, thus creating a reverse one-way coupling between the two solvers. Since the solvers share the same mesh and time step schedule, no interpolation of $\bar{T}$ is necessary.

The process is iterated for all the inner time steps within a stretch of the manoeuver, and for all the stretches in backward direction along the transient profile. Finally, the accumulated sensitivities of the displacements field are passed as input to the steady state adjoint mechanical solver to complete the workflow in Figure 4.10.

4.4.4 The adjoint unsteady heat transfer solver

The unsteady evaluation of each stretch of the manoeuver in primal mode requires the conjugate coupling between the solid and the fluid domains to be repeated multiple times, till convergence. The solution of the temperature field at time t^n initializes the domain at the next time step. At the end of the transient event, a post-processing routine computes the heat fluxes at the interface, to be transferred to the hFFB module for an interpolation, before the assignment to the fluid cells. At the last conjugate loop, the converged temperature information is passed at each time step to the mechanical solver. The routine is schematically represented on top of Figure 4.12.

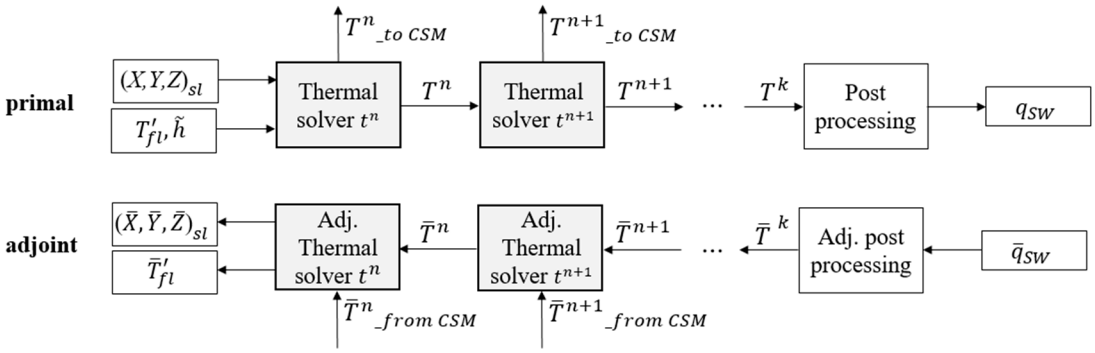

Figure 4.12 Adjoint workflow for unsteady heat transfer solver along a stretch of manoeuver.

In reverse mode, the algorithmically differentiated post-processing routine discussed in Section B.4 seeds the temperature field at the last time step along the stretch of manoeuver. After that, the sequence of calls to the unsteady heat transfer solver is walked in backward direction and at each time step the system solve thoroughly discussed in Section C.2 is invoked.

During the first iteration of the conjugate coupling in reverse mode, at each time step the thermal solver collects also the contributions to the sensitivities of the temperature field derived from the correspondent adjoint mechanical computation. Such contributions are summed up with the one deployed by the adjoint heat transfer solver at the previous time step in reverse mode. For instance, $\bar{T}^n = \bar{T}^n_{from\ CSM\ at\ t^n} + \bar{T}^n_{from\ thermal\ \ solver\ at\ t^{n+1}}$, thus walking in opposite direction through the branching in the distribution of the temperature field operated in primal mode.

At every time step, the adjoint heat transfer solver increments the contributions to the solid grid sensitivities and to the convective loading $\bar{T}'_{fl}$. In this respect, since in primal mode the convective loading at each inner time step results from the interpolation of the two loads computed by the CFD solver at the extreme points of the stretch, in reverse mode the contributions to $\bar{T}'_{fl}$ account for the algorithmic differentiation of the interpolation routine.

The process is repeated for all the stretches of manoeuver, until the initial plateau is reached. Hence, the steady state adjoint workflow is operated. In this respect, the adjoint unsteady heat transfer solver enables the transition by passing the seeded temperature field to its steady state counterpart.

4.4.5 Conjugate coupling in reverse mode

The quasi-dynamic approach implemented in the present work allows invoking the adjoint steady state CFD solver already discussed in Section 3.3.5, in compliancy with the same workflows. In return, the flow solver accumulates the contributions to the fluid grid sensitivities and to the adjoint wall heat flux $\bar{q}_{FW}$. The latter is processed in reverse mode by the differentiated hFFB routine in order to close the loop with the interpolated adjoint heat flux $\bar{q}_{SW}$, entering the adjoint workflow as shown in Figure 4.12.

Therefore, no alteration to the adjoint hFFB procedure is necessary, either to pass the information from the fluid to the solid domain or vice versa, and the related algorithms discussed in Section 3.3.4 and Section 3.3.6 still hold. This is reflected also in a continuous accumulation of contributions to the sensitivities of the interface (identified in the clusters of distances between neighboring fluid cells and solid nodes), which finally convey their increments to the grids sensitivities $\bar{X}_{fl}$ and $\bar{X}_{sl}$, as discussed in Section 3.3.7.

4.5 FEM solvers gradients validation

The unsteady heat transfer solver and the unsteady thermo-mechanical solver introduced in the previous sections rely on the manual differentiation of the primal code through a reverse Algorithmic Differentiation technique, in order to compute accurate derivatives of the response function. The validation of the two procedures is discussed hereafter.

Consistently with the discussion in Section 3.4.1, the gradients computed by the adjoint method are compared to the equivalent ones derived by the application of the Finite Differences (FD) technique. The radial turbine rotor introduced in Section 2.4.2 represents the baseline geometry for the study. The comparison between the two techniques is performed by perturbing the ten design variables α previously reported in Table 3.1.

The transient manoeuver adopted to test the two FEM solvers is defined by the exemplary sequence of events in Table 4.1. In particular, the boundary conditions assigned at the extreme points of each stretch of manoeuver are listed herein.

Stretch #	Inlet tot pressure [kPa]	Inlet tot temperature [K]	Inlet flow angle [deg]	Outlet static pressure [kPa]	Rotational speed [RPM]	Init. time [s]
1	122	604	81	98.5	30000	0.0
2	131	677	78	98.5	60000	1.1
3	148	843	72	98.5	90000	2.4
4	167	1011	65	98.5	120000	3.6
5	173	1080	62	98.5	140000	4.8

Table 4.1 FEM solvers: Boundary conditions for rotor operating points along transient manoeuver.

The response functions assigned to the two solvers are respectively the solid maximum temperature and the maximum von Mises stress evaluated along the transient computations, both represented by p-norm functions.

For sake of consistency with the steady state treatment, the development of the cost functions sensitivities with the FD method accounts for a study concerning the correct step size to be assigned to each design variable. Hence, the evaluations avoid being misled by round-off errors or truncation errors.

Figure 4.13 reports the sensitivities computed by the adjoint method and the FD technique for the non-linear unsteady heat transfer solver. The comparison results in a sufficiently accurate agreement, both in sign and magnitude.

The physical interpretation of the gradients results in a marked influence of the third design variable (i.e. the back-plate thickness), whose sign is opposite to the steady state case. In fact, during a transient manoeuver starting from relatively low conditions, an increase in the thermal mass represented by this element tends to slow down the temperature rise at the hub surface, in proximity of the blade leading edge, location where the nodes exhibiting the highest temperatures reside.

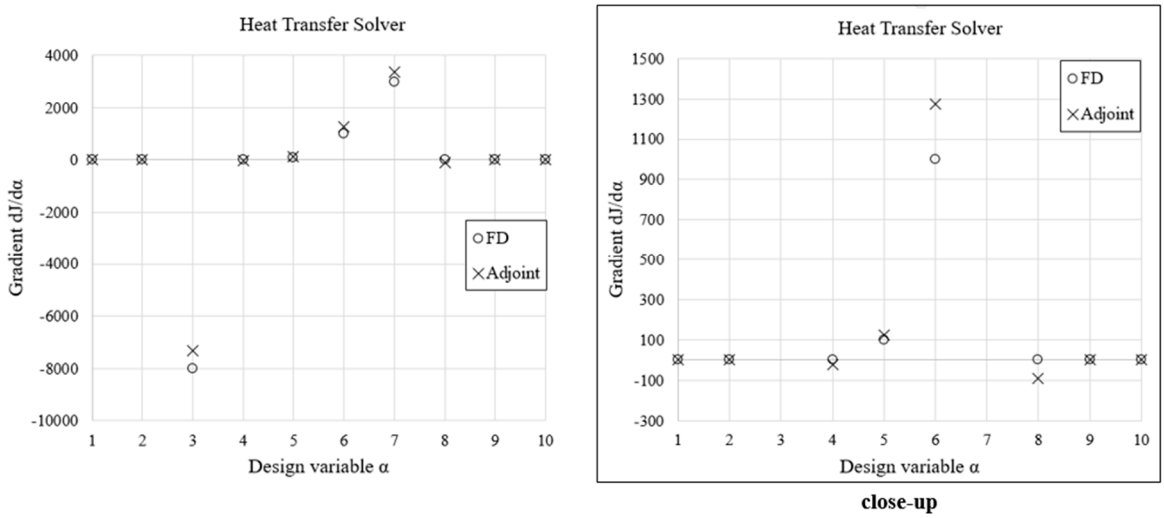

Figure 4.13 Comparison of the $\boldsymbol{dJ/d\alpha}$ sensitivities of the solid maximum temperature for unsteady computations: Gradients evaluated by the adjoint method vs. Finite Differences.

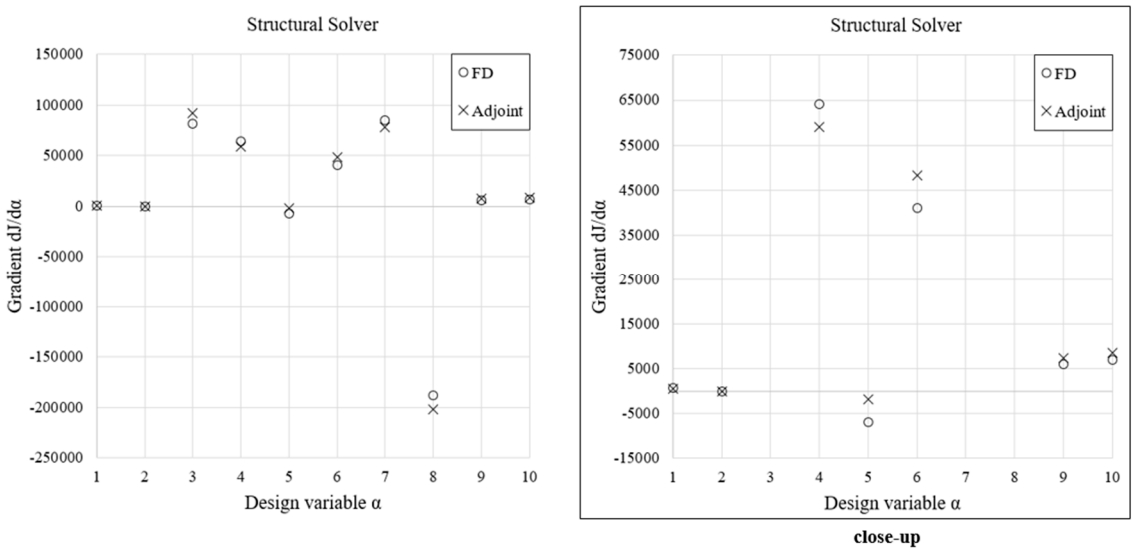

Figure 4.14 Comparison of the $\boldsymbol{dJ/d\alpha}$ sensitivities of the maximum von Mises stress for unsteady computations: Gradients evaluated by the adjoint method vs. Finite Differences.

Conversely, an increase in the sixth and in the seventh design variables, respectively the rotor diameter and the blade span at the leading edge, favors the build-up of higher temperature spots because this increases their distance from the heat sinks located at the rotor shaft and at the blade tip.

Figure 4.14 shows the sensitivities of the maximum von Mises stress computed by the adjoint method and the FD technique for the unsteady mechanical solver. The gradients demonstrate a sufficient accordance, and their trend is aligned with the results discussed in steady state operating conditions. Also in this unsteady manoeuver, the axial position of the connection of the rotor back-plate with the shaft drives the evolution of the stresses.

Finally, the computational performance of the two adjoint solvers is compared to the effort necessary to calculate the derivatives with the FD technique. Given *X* as the time required to evaluate the unsteady temperature field or the unsteady stress field by the primal solver, the application of the adjoint methods herein described costs about *4.6X* for the heat transfer solver and *2.8X* for the structural module. As in the steady state case, these cost figures mostly depend on the system assembly process in reverse mode, and in the case of the heat transfer solver are more impacted because of the different number of d.o.f. handled by the adjoint solver w.r.t. the primal one.

However, it once more confirms the expectation of efficiently addressing the evaluation of the sensitivities of the cost function by the adjoint method in case of problems dealing with rich design spaces.

4.6 Applications

The radial turbine rotor presented in Section 2.4.2 is adopted to address the quasi-dynamic evaluations of the fatigue phenomenon through the workflow reported in Figure 4.10. Two different manoeuvers are discussed hereafter, in order to assess the algorithm response in evaluating the fatigue lifetime and the correspondent sensitivities w.r.t. the grid coordinates.

4.6.1 Test case #1

The unsteady trace addressed by the first test case is reported in Table 4.2. The manoeuver starts from a condition of low engine load and, after an initial stabilization time, a BMEP increase is associated to a ramp-up in turbine rotational speed. At the completion of the fifth stretch of the manoeuver, the engine load suddenly drops at a higher rate than in the ascending part of the profile. Such condition is associated to the evolution of the rotor inlet temperature and pressure. However, the wheel presents an inertial lag and the rotational speed decreases more significantly only from the seventh stretch onwards.

Stretch #	Inlet tot pressure [kPa]	Inlet tot temperature [K]	Inlet flow angle [deg]	Outlet static pressure [kPa]	Rotational speed [RPM]	Init. time [s]
1	122	604	81	98.5	30000	0.0
2	131	677	78	98.5	60000	0.8
3	148	843	72	98.5	90000	1.9
4	167	1011	65	98.5	120000	3.6
5	173	1080	62	98.5	140000	4.8
6	162	816	60	98.5	130000	5.3
7	143	738	60	98.5	108000	5.9
8	132	643	60	98.5	75000	6.7
9	122	604	60	98.5	30000	7.5

Table 4.2 TMF manoeuver #1: Boundary conditions for rotor transient operating points.

The manoeuver is initially assessed in primal mode, and Figure 4.15 shows the evolution of the von Mises stresses corresponding to different stretches from the previous list. Not all the stretches from Table 4.2 are visualized herein. In fact, the execution of the workflow demonstrates the most critical portion of the transient event is about the ascending branch (i.e. Region-1 and Region-2 in Figure 4.4), since the fatigue resistance of the material decreases at higher temperatures, which correspond also to the highest centrifugal forces. Instead, during the engine load drop, the cooling effect by the convective loading restores the conditions for higher values of the Young's modulus and the Poisson's ratio and, therefore, results in lower stresses.

It is interesting to note the boundary conditions reported in Table 4.2 at the first five stretches correspond to the steady state boundary conditions from Table 3.2 assigned to the rotor while exploring different steady state operative points in the engine map. The current test case differs from the previous one in Section 3.5 because of the unsteady transition through such operating conditions. Hence, the von Mises distributions in Figure 4.15 can be compared to the ones in Figure 3.16, as they are plotted w.r.t. the same scale.

The first three stretches in unsteady conditions show a localized region of high stresses in correspondence of the blade trailing edge at the hub. Such critical spot is not present in steady state working conditions because characterized by the thermal equilibrium. Instead, the sudden engine load increase experienced in the Region-1 of the manoeuver leads to a quicker heat-up of the thinner blade sections compared to the bulk.

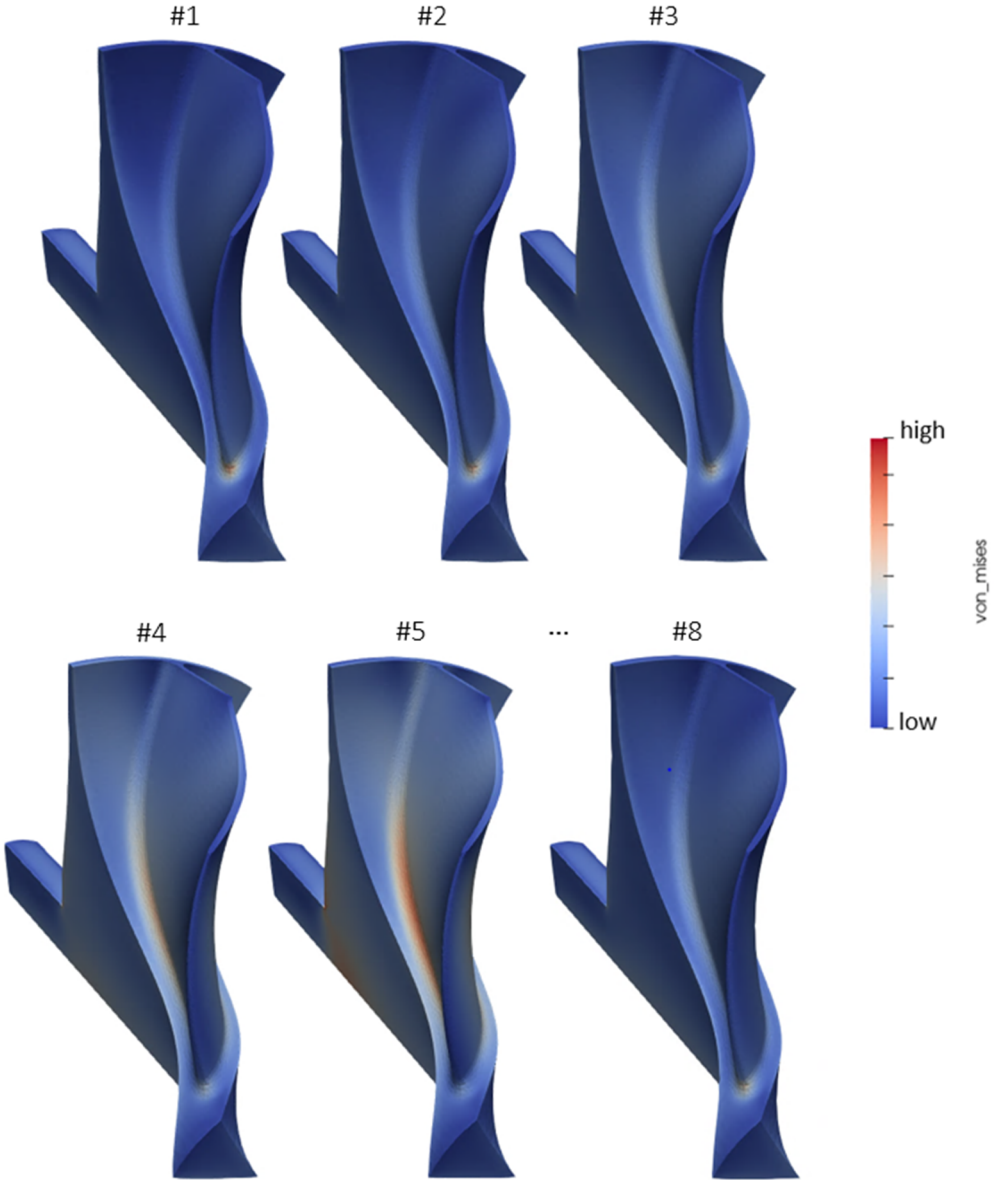

Figure 4.15 von Mises stress evolution at different stretches of the manoeuver described in Table 4.2.

Moreover, the location of the trailing edge is the most exposed to the thermal gradients between the blade pressure side and suction side: hence, the uneven distribution of thermal strains favoring the formation of high stress spots. It is also noticeable that such localized stress tends to progressively decrease at higher engine loads, despite the increased centrifugal forces, as a consequence of the more homogenous thermal field developed in the rotor. Finally, in the fifth stretch (approaching the peak of the load), the localized spot completely disappears relieving the trailing edge, and a stress pattern closely resembling the one experienced in steady state conditions is established. A similar stress concentration appears again during the last stages of the descending branch (Region-3) because of the new influence of the thermal gradients.

The behavior shown by Figure 4.15 finds confirmations in literature [153], and is discussed in detail by [81], whose application to a scalloped turbine rotor exhibits also a second critical spot located at the leading edge. In particular, the CHT analysis performed by the authors identifies the root cause of the thermal stresses at the trailing edge in the high flow separation and mixing between the blade pressure and suction sides. Hence, they found a correlation between the most structurally impacted regions in the blade and those ones experiencing significant convective loads, which are in correspondence of the fluid regions with the highest difference in Reynolds number w.r.t. the main flow in the blade channel.

Beside the stress conditions at the trailing edge, the centrifugal forces exhibit their impact in the fourth and fifth stretch, and two critical locations are identified in correspondence of the hub fillet radius at mid chord on the pressure side, and at the connection between the back-plate and the shaft. In particular, this last region prevails in terms of maximum von Mises stresses (Figure 4.16), because of the superimposed effect of the thermal strains induced by the temperature gradients between the bulk of the rotor and the heat sink located at the shaft end section. Since the fourth and the fifth stretch present a longer duration, a condition of almost thermal equilibrium is achieved at the peak of the manoeuver. Thus, the pattern of von Mises stresses closely resembles the one developed in the fifth steady state operating point in Figure 3.16.

Such considerations are in line with the discussion in [81], whose findings along a different transient manoeuver match the present review, and identify the connection with the shaft as a critical region.

The next step is about the lifetime evaluation performed by the Morrow model. Since it pertains to the category of the strain life methods, the focus shifts from the evolution of the von Mises stresses to the history of the nodal total strains, in order to identify the location experiencing the largest total strain range. Because of the impact of the high thermal gradients, the region of the connection of the back-plate with the shaft is confirmed being the one suffering for the shortest lifetime to the crack-initiation event.

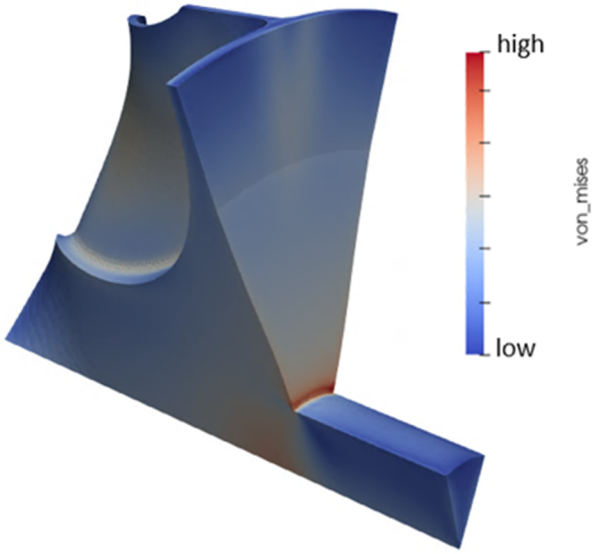

Figure 4.16 Distribution of von Mises stresses in Stretch #5.

Figure 4.17-a highlights also other regions of the blade potentially showing weaknesses to the thermo-mechanical fatigue, such as the blade hub fillet and the blade surface at mid span. These areas are respectively affected by the centrifugal stresses and by the thermal strains, thus highlighting different fatigue mechanisms developing in the blade. However, the current shape exhibits the minimum lifetime value at the connection with the shaft, and this is confirmed by the pattern of cost function sensitivities in Figure 4.17-b, attributing the highest priority to this area. During an optimization, a correction of the back-plate profile as presented in Section 3.5 would relieve this connection region, favoring the exploration of new geometrical modifications involving other locations of the blade affected by the fatigue phenomenon.

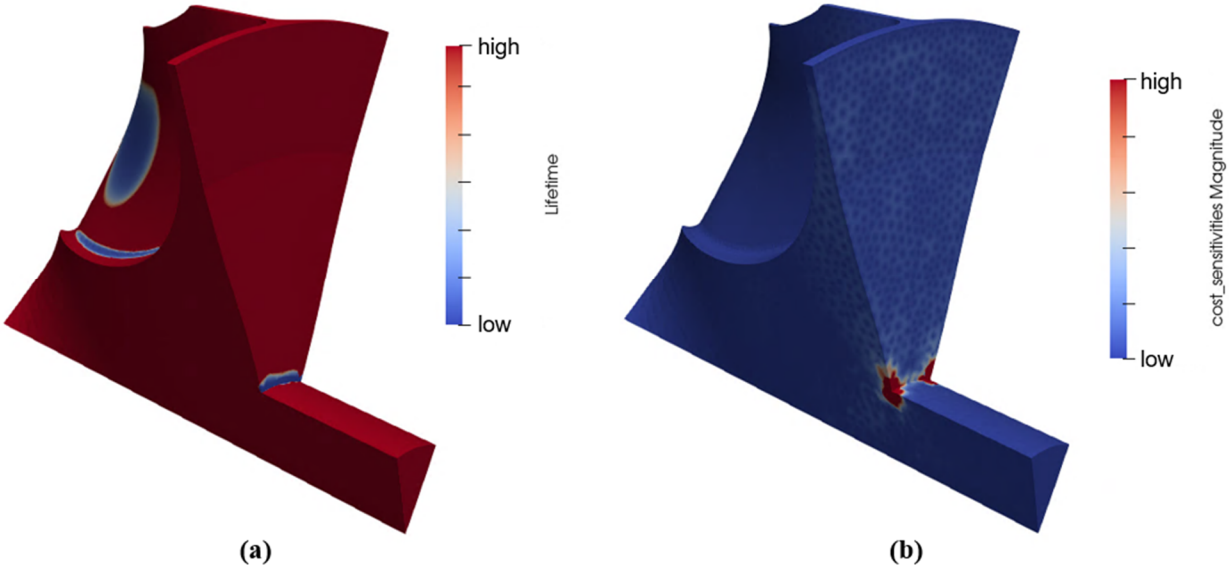

Figure 4.17 TMF lifetime prediction corresponding to transient manoeuver in Table 4.2 (a); sensitivity of TMF lifetime w.r.t. grid coordinates (b).

4.6.2 Test case #2

The second manoeuver under investigation is about a less severe rise in engine load corresponding to a softer drive profile. Such a scenario is expected to be less critical from TMF lifetime standpoint; however, it is relevant to evaluate the consistency of the response of the workflow.

The boundary conditions assigned to the rotor are summarized in Table 4.3. The manoeuver presents a rapid rise in the first two stretches, which are followed by a prolonged permanence at intermediate loads, before experiencing a sudden drop in engine load. The peak inlet temperature and inlet pressure are lower with respect to the ones in the previous manoeuver; additionally, the transition through the Region-2 of the profile shows a less pronounced gradient in rotational speed.

Stretch #	Inlet tot pressure [kPa]	Inlet tot temperature [K]	Inlet flow angle [deg]	Outlet static pressure [kPa]	Rotational speed [RPM]	Init. time [s]
1	122	604	81	98.5	30000	0.0
2	131	677	78	98.5	60000	0.8
3	148	843	72	98.5	90000	2.4
4	154	938	69	98.5	100000	4.3
5	132	643	60	98.5	75000	6.0
6	122	604	60	98.5	30000	7.8

Table 4.3 TMF manoeuver #2: Boundary conditions for rotor transient operating points.

Figure 4.18 shows the evolution of the von Mises stresses during some key stretches. The scale adopted in the present figure is narrower than the one in Figure 4.15, with the aim of emphasizing the transient evolution of stresses, which are less severe than in the previous test case.

The current manoeuver determines the appearance of a localized stress spot in correspondence of the trailing edge at the hub fillet. In fact, this region is per se susceptible to the centrifugal loads, and the superimposition of the thermal strains promotes the rise of localized stresses. Consistently with the previous discussion, it is apparent how the thermal strains represent the locally dominant factor in the description of the stress pattern. In fact, from the second stretch onwards, the progressive achievement of a local thermal equilibrium in the bulk material diminishes the magnitude of the critical spot, regardless the operative conditions presenting higher and higher centrifugal loads due to the rising rotational speed.

The analysis of the remaining portion of the blade highlights a gradual increase of stresses at the hub fillet radius at mid chord on the pressure side. This evolution is related to the increasing body forces because of the rotational speed. However, such stresses are by far below the yield limit of the material.

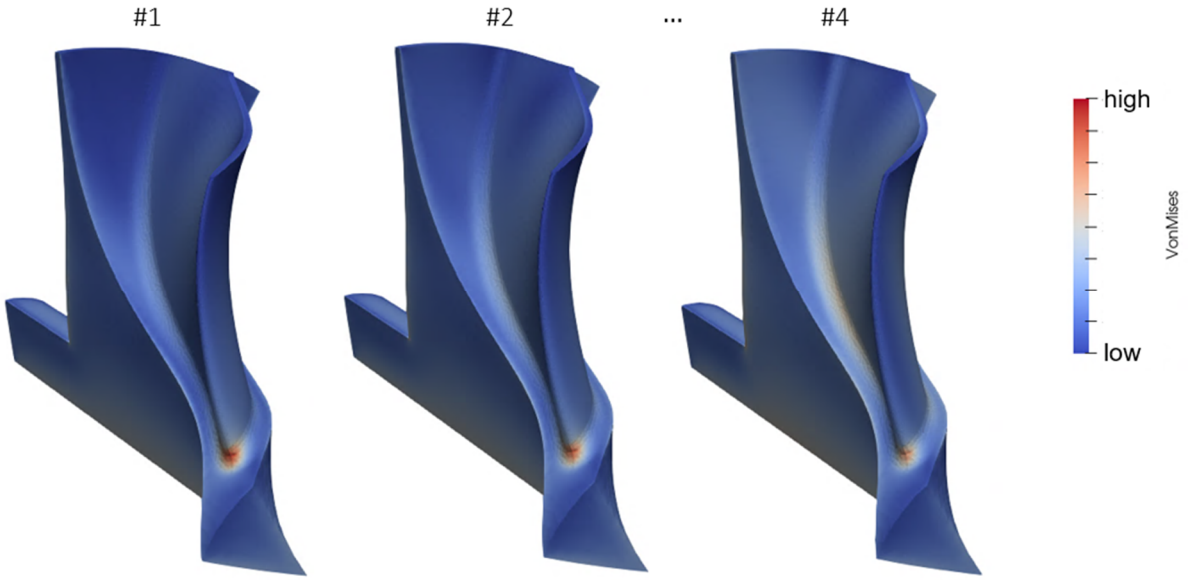

Figure 4.18 von Mises stress evolution at different stretches of the manoeuver described in Table 4.3.

Figure 4.19-a presents the TMF lifetime assessment for this sample. The fatigue resistance of the rotor operating under the alternating maneuver defined in Table 4.3 is significantly higher than in the previous case, such that the component operates in the “infinite life” region of the Universal Slopes diagram. However, the Morrow model can provide a lifetime estimate even in case of pure elastic cycles. The lifetime mapping highlights two regions: a weak spot is located at the trailing edge, in correspondence of the stress island visualized in Figure 4.18, and a second area of interest resides at the blade hub fillet on the pressure side. Despite the highest instantaneous von Mises stresses are located at the trailing edge, the minimum lifetime is recognized by the p-norm function at the hub fillet. This non-intuitive finding is justified by the larger variation in total strains experienced in this location, because of its closer proximity to the shaft, which represents a heat sink for the structure.

Therefore, the accumulated grid sensitivities in Figure 4.19-b provide the directions for the nodes perturbations necessary to improve the fatigue lifetime, with indications of the corrections to the blade metal angles and to the thickness distribution along the span. In particular, the same blade region at mid chord and at intermediate-high spans is highlighted, as already shown in Figure 3.17. The reason is about a local slightly non-radial fibered blade configuration, visible also in Figure 3.11, which was accepted in the original adiabatic optimization because inducing hub stresses not activating the constraint.

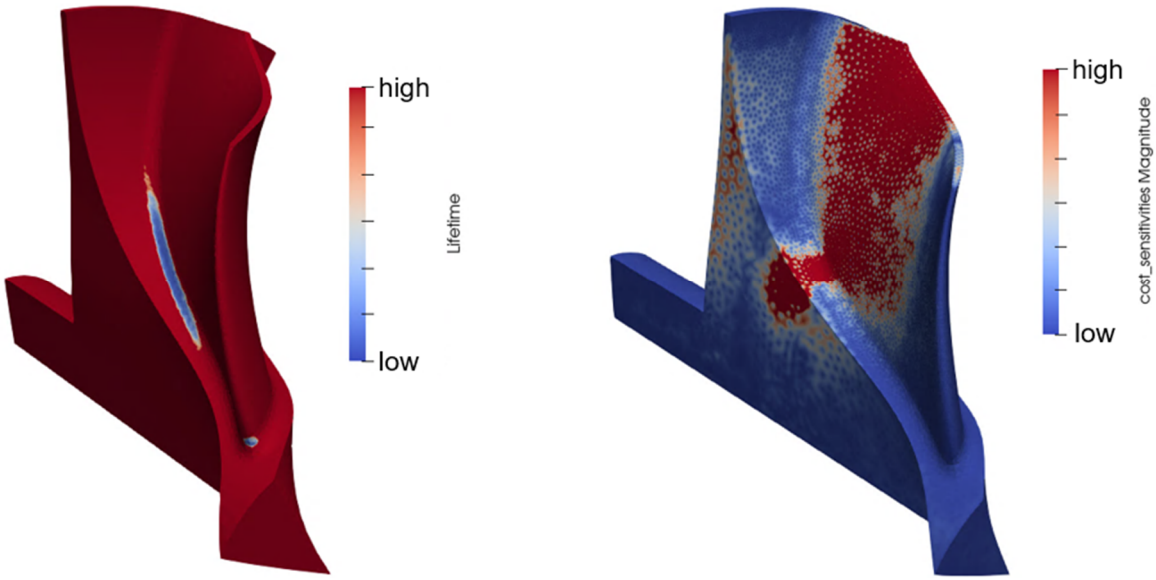

Figure 4.19 TMF lifetime prediction corresponding to transient manoeuver in Table 4.3 (a); sensitivity of TMF lifetime w.r.t. grid coordinates (b).

Finally, a localized enlargement of the hub fillet radius at mid chord of the blade pressure side would support an improved durability of the rotor, as also testified by the red spot sitting on the hub surface. At more advanced stages of the optimization, the framework would eventually identify the weakest spot at the trailing edge, providing indications for its reshaping.

Chapter 5

Summary and conclusions

5.1 Conclusions

5.1.1 The thermal Fluid-Structure Interaction problem

This thesis presents the development of a multidisciplinary optimization framework addressing the thermal Fluid-Structure Interaction problem in turbomachinery components operating at high-temperatures, with focus on the turbocharger radial turbine application. The objective of the work is related to the possibility of introducing thermal evaluations within the framework of the optimization of complex components, with the aim of improving the accuracy in the prediction of the structural robustness to their own operative environments. Moreover, the method is requested to be flexible in handling a high number of design parameters, in order to allow executing optimizations in rich design spaces.

Based on the choice of a discrete adjoint method outlined in Chapter 1, the present work delivers the possibility of computing the sensitivities of the thermo-mechanical stresses developed in the solid experiencing steady state operative conditions, as well as the gradients of the thermo-mechanical fatigue lifetime under cyclic conditions. Such robustness figures are treated as additional constraints within the framework of an SQP-based optimization workflow offered in CADO, in parallel to the evaluation of the sensitivities of other aerodynamic and vibrational cost functions.

Hence, the first objective is to interface the fluid domain, discretized by a multi-block structured grid, with the solid medium, treated through an unstructured mesh of second order tetrahedral elements. In this respect, the exchange of information between the non-matching grids is realized through the implementation of a distance-weighted interpolation technique whose robustness is proven for general meshes related to geometries of any complexity. This choice demonstrates to be particularly suitable for the treatment of critical areas in the turbine impeller, like the blade hub fillet region, presenting some approximations

in the discretization of the fluid domain, thus leading to locally intersecting meshes. The robustness of the search algorithm in charge of identifying the correspondences between the fluid cells and the solid nodes is enhanced by the implementation of multiple refinements to the original mapping technique. In particular, the effort is in increasing the accuracy of the interpolation method by including a virtual fluid grid introducing a more isotropic distribution of fluid points on the interface, as well as in excluding false interactions between elements that in reality are not in physical contact. Therefore, the original concept of "search radius" is dismissed, in favor of a more effective classification technique attributing a ranking to the couples of fluid cells and solid nodes in close proximity.

A conjugate coupling between the two domains is established by the adoption of a partitioned coupling technique. The advantage of this method is twofold. First, this approach allows analyzing the fluid and the solid domains with specialized meshers and solvers, with the aim of improving the accuracy and efficiency in the investigation of the FSI phenomenon. Hence, the present framework benefits from the implementation of the in-house CFD solver already available in CADO. Second, the work herein expands the outreach to the evaluation of transient thermal phenomena, showing a considerable disparity between the characteristic time scales in the two media. A literature review about the successful attempts in efficiently dealing with unsteady conjugate problems supports the choice of a loose coupling technique, deemed the most suited, especially in the framework of an iterative process, like an optimization. Therefore, the CHT workflow is developed through the "heat Transfer Forward Flux Back" technique (hFFB) and is validated by considering the flow over a flat plate, a conjugate problem whose analytical solution is available. The test is run at the edge of a Biot number around unity, in order to verify the robustness of the convergence of the method while transitioning through such threshold, being a critical measure for the different loose coupling algorithms. The hFFB –based workflow confirms the robustness in dealing with such problem, as well as in analyzing the thermal coupling of a relevant three-dimensional geometry of a radial turbine impeller. In fact, this application presents a shape with local variations in the Biot number, as resulting from the complex flow field and the presence of considerable secondary flows in off-design conditions. A sensitivity analysis about the fluid and solid mesh settings, as well as the imposed value of the virtual heat transfer coefficient $\tilde{h}$, is undertaken in order to identify the optimal set-up for accurate, yet robust and computationally efficient solutions of the thermal coupling. The analysis provides some insights about the most appropriate settings that are implemented in all the test cases throughout this thesis, highlighting the need of localized refinements in the solid mesh concerning the thinner regions of the blade.

5.1.2 Steady state thermo-mechanical stresses

The solid temperature field computed by such framework is transferred to a FEM structural solver by a one-way loose coupling technique. Since the thermal and the mechanical solvers share the same mesh, no interpolation is necessary during this exchange of information. The linear solver is enriched by the possibility of evaluating the thermal strains in addition to the centrifugal loads affecting the reference application. Hence, the pattern of the newly computed thermo-mechanical stresses in the rotor is compared with the original von Mises stresses prediction, neglecting the impact of the temperature gradients: it is confirmed that the simplistic approach ignoring the convective load from the operative environment underestimates the local von Mises stresses at the connection of the back-plate with the shaft by 20%. The issue is relevant since the region is susceptible for the body forces, and the superimposing effect of the thermal field leads to the instantiation of maximum stresses exceeding the yield limit of the material. Therefore, the test proves the original optimization would have missed a local plasticity, potentially impairing the robustness of the component, and demonstrates the need of including thermal evaluations within the design optimization of such thermally stressed applications.

In this respect, a thermo-mechanical workflow in reverse mode is developed by closely resembling the primal structure of the code, in order to maintain the consistency in the propagation of the adjoint variables in backward direction. Since the cost function, represented by the maximum von Mises stress accounting for the thermal strains, is affected by the interactions of the FEM and the FVM solvers within the iterative hFFB loop, the adjoint workflow follows the same schedule. Thus, the adjoint variables are exchanged through the interface of the two domains, and the sensitivities of the response function w.r.t. the grids points coordinates are accumulated throughout the workflow. The adjoint framework is developed with a reverse Algorithmic Differentiation technique applied through a manual differentiation of the entire code. The advantages of approaching this development by means of a manual differentiation are about an optimized memory footprint, as an extensive recording on the tape operated by automatic differentiation software is avoided, as well as the possibility of excluding any issues in the interactions of such external software with the multidisciplinary solvers. The gradients of the cost function computed by the two FEM solvers through the adjoint method are validated against the equivalent sensitivities evaluated by a Finite Differences technique. Moreover, the robustness of the convergence of the adjoint CFD solver with the newly implemented heat transfer boundary condition is demonstrated by means of a test case showing the requirement of a deep convergence of the primal solver till machine level accuracy to correctly initialize the adjoint computations. Finally, the application of the framework to the previous radial turbine impeller test case correctly highlights the region of the connection between the rotor back-plate and the shaft as the most critical from structural standpoint, offering the gradients for the grids perturbations expected to improve the cost function. The application of such shape

modifications affects only the profile of the back-plate, delivering a localized reduction in von Mises stresses in excess of 35%, thus bringing the component back to the operation within the elastic region of the material. Finally, the framework is suitable to compute the rotor aerothermal efficiency, as the assumption of adiabatic walls is dismissed.

5.1.3 Thermo-Mechanical Fatigue

The second part of the thesis is devoted to the problem of the Thermo-Mechanical Fatigue (TMF) in structures that are thermally and mechanically stressed under cyclic conditions. In particular, the problem of the lifetime estimation is undertaken after a comprehensive literature review, demonstrating the opportunities offered by the currently available prediction models, as well as the limitations related to the availability of consistent datasets of material properties. In this respect, following the choice of a partitioned coupling technique, the well-proven quasi-dynamic method is selected for the analysis of the unsteady conjugate problem. The transient manoeuver is split in several stretches, each one showing two extreme points in which the coupling between the two domains takes place. While a FEM unsteady non-linear heat transfer solver is developed for the analysis of the stretch in transient mode, the starting condition and the ending one are treated by the fluid solver through a steady state simulation. Hence, the conjugate coupling is executed at the end of each stretch and the two domains exchange the relevant information at the wall through the same interpolation routine adopted in steady state conditions. The coupling of the fluid and solid media is performed through the hFFB method, which defines an iterative framework between the two fields till convergence, before advancing the solution to the following stretch of the manoeuver. Hence, the correct conditions at the interface are still respected, avoiding the effort of solving the flow field with the time scale characteristic of a URANS, while dealing with the slow thermal event developing in the solid.

As soon as the temperature field is resolved in a stretch of the manoeuver, the information is passed to a FEM linear unsteady structural solver for the evaluation of the correspondent solid thermo-mechanical response. The choice of a solver relying on the linear elasticity assumption is justified by the operations of the reference turbine application within the region of the “small strains”. Hence, no geometry deformation induced by the inelastic event is modelled herein. However, the possible occurrence of infrequent transitions in the plasticity region of the material is treated by a post-processing of the displacements and strains fields by means of a constitutive model. In particular, the Return-Map Algorithm is implemented with the aim of correcting such fields before advancing the solution to the next time step. Finally, the thermo-mechanical history of the component is investigated through the Morrow model, a strain life technique aimed at evaluating the fatigue resistance of the component by means of the node-wise evaluation of the total strain range. The resulting lifetime represents the new

cost function introduced by this framework, whose sensitivities w.r.t. the grids coordinates are computed through an adjoint framework.

Coherently with the steady state development, the backward propagation of the adjoint variables through the workflow in reverse mode mirrors the interactions of the primal solvers. Differently from the steady state implementation, in this case the adjoint mechanical solver participates to the whole event by evolving in a synchronous way with the quasi-dynamic CHT framework, and the adjoint variables are consistently exchanged between the two. The choice of a loose coupling approach allows the direct integration of the in-house adjoint steady state CFD solver in this development. The entire framework is manually differentiated by a reverse Algorithmic Differentiation technique, with the aim of optimizing the memory footprint. Hence, the adjoint sensitivities delivered by the two unsteady FEM solvers are validated against the corresponding ones computed by the Finite Differences techniques.

The application of the new framework is finally assessed against two transient manoeuvers. Both test cases adopt the radial turbine impeller presented during the steady state verifications. Hence, it demonstrates the capability of the primal solvers in capturing the transient evolution of the von Mises stresses, impacted by the local thermal non-equilibrium. If compared to an equivalent trace analyzed through steady state operating points, the unsteady evolution determines the appearance of uneven distributions of thermal strains originated by the significant temperature gradients in the material, thus leading to stress spots, not occurring in static operations. The most affected regions in the blade are the ones presenting large variations in the cross section, since the thinner areas tend to heat up and cool down more quickly than the bulk of the rotor. This result is in compliance with the investigations performed by separate research groups and available in literature, which identify the blade regions exposed to high differences in Reynolds number compared to the main flow in the blade channel (i.e. those regions experiencing localized large flow separations) as the ones most likely to be involved in the appearance of localized peaks in transient stresses. The consistency of the primal workflow is proven in two manoeuvers leading to different fatigue lifetime expectations. Finally, the sensitivities of the cost function computed by the correspondent adjoint framework are analyzed, finding a good conformity between the directions of the suggested perturbations of the grid coordinates and the design corrections expected by the application experts.

5.2 Perspectives and future work

The present thesis delivers an effective means to treat the optimization of the thermo-mechanical stresses and fatigue lifetime within an adjoint framework. However, during such development, new opportunities arose to improve the computational efficiency of the current framework and to expand its outreach to additional turbomachinery applications.

Concerning the conjugate coupling framework, the hFFB method is chosen for its superior convergence properties w.r.t. the other classical methods, and for the numerical stability experienced by the CFD solver by imposing a heat transfer boundary condition (instead of an imposed wall temperature). However, recent advancements in the CHT technique are present in literature, and the new "heat transfer Forward Resistance Back" method (hFRB) [127] discloses promising results in terms of amplitude of the stability region and convergence rate. Such technique has been only demonstrated with the flat plate test case so far, and it would require further testing with more complex three-dimensional geometries. If promising, it may substitute the hFFB technique currently implemented.

The choice of a loose coupling method in the present work is justified in Chapter 1, and is deemed necessary in the case of unsteady conjugate problems, like in the case of the TMF lifetime. However, the current iterative framework would benefit from the application of acceleration techniques in order to lower the computational budget necessary to deal with the fluid domain. In this respect, an opportunity may arise from the implementation of a One Shot Method [177, 178], whose tolerance to the partial convergence of the primal and the adjoint CFD solvers would reduce the overall computational time for the conjugate framework. This emerging technique should be tested in the specific case of complex geometries with an imposed wall heat transfer, since in the current work it is found necessary to achieve a deep drop in residual of the primal computation to safeguard the robustness of the adjoint counterpart.

The turbocharger turbine application considered herein normally operates in the elastic regime of its material and the mild excursions to the inelastic region allow accepting the assumption of the "small strains" operations. However, there are other turbomachinery applications experiencing large deformations during their duty cycles. In those cases, the evaluation of the plasticity corrections in post-processing of the FEM linear solver would be inaccurate, and its extension to the variational description for finite deformations is recommended [172]. In this case, the visco-plastic regime could be included in the analysis, in order to address also the creep related issues.

The present thesis focuses on the prediction of the crack-initiation event as a robust criterion to address the lifetime problem for the turbocharger turbine rotor. The development relies on the well-established Morrow model, whose material fatigue properties are available in literature. However, some approximations to the temperature dependent characteristics of the material are necessary in the model when it comes to the evaluation of a cyclic manoeuver, introducing some limitations historically experienced by the isothermal fatigue estimations. A possible improvement to the accuracy of the fatigue lifetime prediction is offered by the Chaboche model [164], whose higher complexity allows modelling more reliably the TMF problem. However, the implementation of this technique must be supported by a comprehensive dataset of material properties.

Finally, an extension to the development of crack-propagation models, hence addressing the damage modelling, would provide a less conservative means of controlling the durability of the component for those materials exhibiting a significant lifetime left after the initial appearance of cracks on the surface. Such technique could be expanded also to the evaluation of the uncertainties associated to the properties of the material, with the aim of further reducing the engineering margins over the structural constraints and to address a more aggressive search for optimal shapes.

References

[1] “Paris agreement”, United Nations, 2015

[2] “Assembly 40th session WP/561 EX/238, agenda item 16: Environmental protection – International aviation and climate change – Policy and standardization”, International Civil Aviation Organization, 2019

[3] Gill, M.; “Waypoint 2050: An Air Transport Action Group project”, Air Transport Action Group, Geneva, Switzerland, 2020

[4] Pohorelsky, L.; Vondrak, A.; Turner, N.; Luard, N.; Cooper, B.; Lane, A.; Osborne, R.; “The coupling of advanced gasoline combustion and a fast-transient boost system to produce a low CO2 vehicle concept”, Honeywell & Jaguar Land Rover & Ricardo, in 23rd Supercharging Conference, pp. 397-421, Dresden, Germany, 2018

[5] “IATA Sustainable Aviation Fuels – Fact sheet”, International Air Transport Association, 2019

[6] Martins, J.R.R.A.; Lambe, A.B.; “Multidisciplinary design optimization: A survey of architectures”, AIAA Journal, Volume 51, Issue 9, pp. 2049-2075

[7] Weck, O.L.; Agte, J.; Sobieski, J.S.; Arendsen, P.; “State-of-the-art and future trends in multidisciplinary design optimization”, in the 48th AIAA/ASME/ASCE/AHS/ASC Structures, Structural Dynamics, and Materials, 2007

[8] Vassberg, J.C.; Jameson, A.; “Industrial application of aerodynamic shape optimization”, in von Karman Institute for Fluid Dynamics Lecture Series 2018-04, Sint-Genesius-Rode, Belgium, 2018

[9] Hildebrandt, T.; Thiel, P.; Suganuma, H.; “Multidisziplinäre und multikriterielle kennfeld optimierung eines turboladerverdichters für motorsport anwendungen”, in 23rd Supercharging Conference, pp. 355-371, Dresden, Germany, 2018

[10] Fröhlig, F.; Kech, J.; Lachenmaier, N.; Männle, T.; “The development of the ZR-turbocharger-family from MTU to increase efficiency and dynamic of the charging system”, in 24th Supercharging Conference, pp. 31-50, Dresden, Germany, 2019

[11] Wöhr, M.; Schneid, M.; Palenschat, T.; Dillmann, A.; Müller, M.; “Automated turbocharger compressor development at Daimler trucks”, in The 13th International Conference on Turbochargers and Turbocharging, pp. 153-165, London, UK, 2018

[12] Buske, C.; Krumme, A.; Schmidt, T.; Dresbach, C.; Zur, S.; Tiefers, R.; “Distributed multidisciplinary optimization of a turbine blade regarding performance, reliability and castability”, in ASME Turbo Expo 2016 – Volume 2C: Turbomachinery, Seoul, South Korea, 2016

[13] Shahpar, S.; “SOPHY: an integrated CFD based automatic design optimisation system”, in Rolls-Royce PLC REPORT-PNR, 2005

[14] Shahpar, S.; “Optimisation strategies used in turbomachinery design from an industrial perspective”, Introduction to Optimization and Multidisciplinary Design in Aeronautics and Turbomachinery, in von Karman Institute for Fluid Dynamics Lecture Series 2010-07, Sint-Genesius-Rode, Belgium, 2010

[15] Liu, X.; Furrer, D.; Kosters, J.; Holmes, J.; “Vision 2040: A roadmap for integrated, multiscale modeling and simulation of materials and systems”, NASA/CR-2018-219771, 2018

[16] Lotz, R.D.; Andrews, D.N.; McHenry, J.P.; Van Saun, D.; Watson, J.P.; “Further development of a high-efficiency compressor stage suited to post Euro VI emissions and fuel economy legislation”, in The 13th International Conference on Turbochargers and Turbocharging, pp. 139-151, London, UK, 2018

[17] Ioannou, E.; Costall, A.W.; Khairuddin, U.; Ramasamy, P.; Haigh, E.; “Turbocharger turbine aerodynamic optimization for reduced fuel consumption and CO2 emissions from heavy-duty diesel engines: Experimental validation and flow field analysis”, in The 13th International Conference on Turbochargers and Turbocharging, pp. 373-388, London, UK, 2018

[18] Seshadri, P.; Yuchi, S.; Parks, G.; Shahpar, S.; “Supporting multi-point fan design with dimension reduction”, The Aeronautical Journal, Volume 124(1279), pp. 1371-1398, 2020

[19] Abbas, H.A.; Sarker, R.; Newton, C.; “PDE: A Pareto-frontier Differential Evolution approach for multi-objective optimization problems”, in Proceedings of the Congress of Evolutionary Computation, Volume 2, pp. 971-978, Piscataway, New Jersey, USA (2001)

[20] Verstraete, T.; “Introduction to optimization and multidisciplinary design”, in von Karman Institute for Fluid Dynamics Lecture Series 2018-04, Sint-Genesius-Rode, Belgium, 2018

[21] Craven, B.D.; “Control and optimization”, Chapman & Hall, 1995

[22] Gamkrelidze, R.; “Principles of optimal control theory”, Plenum Press, 1978

[23] Knowles, G.; “An introduction to applied optimal control”, Academic Press, 1981

[24] Macki, J.; Strauss, A.; “Introduction to optimal control theory”, Springer, 1982

[25] Bungartz, H.J.; Schäfer, M.; “Fluid-Structure Interaction: Modelling, simulation, optimization”, Springer-Verlag, 2006

[26] Sigrist, J.F.; “Fluid-Structure Interaction: An introduction to Finite Element coupling”, Wiley, 2015

[27] Mueller, L.; Prinsier, J.; Verstraete, T.; Racca, A.; “CAD based multidisciplinary adjoint optimization of a radial compressor impeller”, in the 24th supercharging conference, Dresden, Germany, 2019

[28] O’Daniel, J.; “Benefits (and problems) of one-way “loose” coupling”, WIT Transactions on The Built Environment, Volume 71, 10 pp., 2003

[29] Benra, F.K.; Dohmen, H.J.; Pei, J.; Schuster, S.; Wan, B.; “A comparison of one-way and two-way coupling methods for numerical analysis of Fluid-

Structure Interactions", Journal of Applied Mathematics, Volume 2011 (853560), 16 pp., 2011

[30] Novascone, S.R.; Spencer, B.W.; Hales, J.D.; Williamson, R.L.; "Evaluation of coupling approaches for thermomechanical simulations", Nuclear Engineering and Design, Volume 295, pp. 910-921, 2015

[31] Rastrigin, L.A.; "The convergence of the random search method in the extremal control of a many parameter system", Automation and Remote Control, Volume 24, Issue 10, pp. 1337–1342, 1963

[32] Dyer, M.; Frieze, A.; Kannan, A.; "Random polynomial time algorithm for estimating the volumes of convex bodies", Journal of the ACM, Volume 38, pp. 1–17, 1991

[33] Kirkpatrick, S.; Gelatt, C.D.; Vecchi, M.P.; "Optimization by Simulated Annealing", Science, Volume 1, n. 220, pp. 671-680, 1983

[34] Kennedy, J.; Eberhart, R.; "Particle Swarm Optimization", Proceedings of ICNN'95 - International Conference on Neural Networks, Perth, WA, Australia, Volume 4, pp. 1942-1948, 1995

[35] Slowik, A.; Kwasnicka, H.; "Evolutionary Algorithms and their applications to engineering problems", Neural Comput & Applic, Volume 32, pp. 12363–12379, 2020

[36] Deb, K.; "Multi-objective optimization using Evolutionary Algorithms", Wiley, New York, NY, USA, 2001

[37] Emmerich, M.; Giotis, A.; Özdemir, M.; Bäck, T.; Giannakoglou, K.; "Metamodel-assisted evolution strategies", in: Guervós, J.J.M.; Adamidis, P.; Beyer, H.G.; Schwefel, H.P.; Fernández-Villacañas, J.L.; (eds) "Parallel problem solving from nature" — PPSN VII. PPSN 2002. Lecture Notes in Computer Science, Volume 2439, Springer, Berlin, Heidelberg, 2002

[38] T. Verstraete, "CADO: A Computer Aided Design and optimization tool for turbomachinery applications", in 2nd International Conference on Engineering Optimization, pp. 6-9, Lisbon, Portugal, 2010

[39] Pierret, S.; "Designing turbomachinery blades by means of the function approximation concept based on artificial neural network, genetic algorithm, and the Navier-Stokes equations", Ph.D. Thesis, Faculte Polytech Mons, Mons, Belgium, 1999

[40] Dwight, R.P.; De Baar, J.; Azijli, I.; "Introduction to optimization and multidisciplinary design – Adaptive surrogate modelling for global optimization", in von Karman Institute for Fluid Dynamics Lecture Series 2018-04, Sint-Genesius-Rode, Belgium, 2018

[41] Martin, J.D.; Simpson, T.W.; "Use of Kriging models to approximate deterministic computer models", AIAA Journal, Volume 43, Issue 4, pp. 853-863, 2005

[42] Vanti, F.; Pinelli, L.; Arnone, A.; Schneider, A.; Astrua, P.; Puppo, E.; "Aeroelastic optimization of an industrial compressor rotor blade geometry", in Proceedings of ASME Turbo Expo 2018, Oslo, Norway, 2018

[43] Trunk, G.V.; “A problem of dimensionality: A simple example”, IEEE Transaction on Pattern Analysis and Machine Intelligence; Volume 1, Issue 3, pp. 306–307; IEEE: Piscataway, NJ, USA, 1979

[44] Lee, D.S.; “Uncertainty based multiobjective and multidisciplinary design optimization in aerospace engineering”, Ph.D. Thesis, The University of Sydney, Sydney, Australia, 2008

[45] Whitney, E.J.; “A modern evolutionary technique for design and optimization in aeronautics”, Ph.D. Thesis, The University of Sydney, Sydney, Australia, 2003

[46] Jameson, A.; “Aerodynamic design via control theory”, J. Sci. Comput., Volume 3, pp. 233-260, 1988

[47] Giles, M.B.; Pierce, N.A.; “An introduction to the adjoint approach to design”, Flow Turbul. Combust., Volume 65, pp. 393-415, 2000

[48] Nocedal, J.; Wright, S.J.; "Numerical optimization - Second edition", Springer, New York, NY, USA, 2006

[49] Mueller, J.D.; “Shape optimization with gradient-based methods”, in von Karman Institute for Fluid Dynamics Lecture Series 2018-04, Sint-Genesius-Rode, Belgium, 2018

[50] Martins, J.R.R.A.; Sturdza, P.; Alonso, J.J.; “The complex-step derivative approximation”, in ACM Transactions on Mathematical Software, Volume 29, Issue 3; Association for Computing Machinery: New York, NY, USA, 2003.

[51] Giles, M.B.; Pierce, N.A.; “Adjoint equations in CFD: Duality, boundary conditions and solution behavior”, AIAA-CP 97-1850, 1997

[52] Luo, J.; Xiong, J.; Liu, F.; McBean, I.; “Three-dimensional aerodynamic design optimization of a turbine blade by using an adjoint method”, J. Turbomach., Volume 133, 011026, 2011

[53] Pironneau, O.; “On optimum design in fluid mechanics”, J. Fluid Mech., Volume 64, pp. 97-110, 1974

[54] Mueller, L.; “Adjoint-based optimization of turbomachinery applied to axial and radial turbines”, Ph.D. Thesis, Université Libre de Bruxelles, Bruxelles, Belgium, 2019

[55] Griewank, A.; Walther, A.; “Evaluating derivatives: Principles and techniques of Algorithmic Differentiation, 2nd ed.”, Siam: Philadelphia, PA, USA, 2008

[56] Everett III, H.; “Generalized Lagrange multiplier method for solving problems of optimum allocation of resources”, Oper. Res., Volume 11, pp.399-417, 1963

[57] Elliott, J.; Peraire, J.; “Practical 3D aerodynamic design and optimization using unstructured meshes”, AIAA Journal, Volume 35(9), pp. 1479-1485, 1997

[58] Sagebaum, M.; Albring, T.; Gauger, N.R.; “High-performance derivative computations using CoDiPack”, arXiv preprint arXiv:1709.07229, 2017

[59] Xu, S.; Timme, S.; “Robust and efficient adjoint solver for complex flow conditions”, Comput. Fluids, Volume 148, pp. 26-38, 2017

[60] Mueller, J.D.; Hueckelheim, J.; Mykhaskiv, O.; “STAMPS: a Finite-Volume solver framework for adjoint codes derived with source-transformation AD”, in AIAA 2018 Multidisciplinary and Analysis and Optimization Conference, Atlanta, Georgia, USA, 2018

[61] Xu, S.; Radford, D.; Meyer, M.; Mueller, J.D.; “Stabilisation of discrete steady adjoint solvers”, J. Comput. Phys., Volume 299, pp. 175-195, 2015

[62] Schwalbach, M.; Mueller, L.; Verstraete, T.; Gauger, N.R.; “CAD-based adjoint multidisciplinary optimization of a radial turbine under structural constraints”, in Proceedings of the 2018 Global Power and Propulsion Forum, Montreal, QC, Canada, 2018; Paper No. GPPS-NA-2018-133

[63] Pini, M.; Persico, G.; Dossena, V.; “Robust adjoint-based shape optimization of supersonic turbomachinery cascades”, in Proceedings of the ASME Turbo Expo, Dusseldorf, Germany, 2014

[64] He, L.; Wang, D.X.; “Concurrent blade aerodynamic-aero-elastic design optimization using adjoint method”, J. Turbomach., Volume 133, 011021, 2011

[65] Aissa, M.H.; Maffulli, R.; Mueller, L.; Verstraete, T.; “Optimization of a turbine inlet guide vane by gradient-based and metamodel-assisted methods”, International Journal of Computational Fluid Dynamics, Volume 33(6:7), pp. 302-316, 2019

[66] El-Mihoub, T.; Hopgood, A.; Nolle, L.; Battersby, A.; “Hybrid genetic algorithms: A review”. In Engineering Letters, 13:2, 2006

[67] Chatel, A.; Verstraete, T.; Coussement, G.; “Multipoint optimization of an axial turbine cascade using a hybrid algorithm”, in ASME Turbo Expo, Phoenix, USA, 2019

[68] Heywood, J.B.; “Internal combustion engine fundamentals”, McGraw-Hill International Editions – Automotive Technology Series, New York, NY, USA, 1988

[69] van Basshuysen, R.; Schäfer, F.; “Internal combustion engine handbook – Basics, components, systems, and perspectives”, SAE International, Warrendale, PA, USA, 2004

[70] Watson, N.; Janota, M.S.; “Turbocharging the internal combustion engine”, Macmillan, London, UK, 1982

[71] Baines, N.C.; “Fundamentals of turbocharging”, Concepts, ETI, 2005

[72] Culy, D.G.; Heldenbrand, R.W.; Richardson, N.R.; “Final report for the advanced turbocharger desig study program”, NASA CR-174633, NASA Lewis Research Center, Cleveland, OH, USA, 1984

[73] Prevost, F.; Le Moual, Y.; Maiboom, A.; Payet-Burin, T.; Davodet, O.; Fosse, F.; “Improvement of turbocharger model in 1D engine simulation: Comparison with experiments under constant and pulsating flows”, in Global GT Virtual Conference 2020, 2020

[74] Lethwala, Y.; Sharma, N.; Jain, R.; “Engine performance simulation of Ricardo WAVE for GTDI optimization”, International Journal of Engineering and Advanced Technology, 2019

[75] Galindo, J.; Serrano, J.R.; Arnau, F.J.; Piqueras, P.; “Description and analysis of a one-dimensional gas-dynamic model with independent time

discretization", ASME 2008 Internal Combustion Engine Division Spring Technical Conference, 2008

[76] Checcucci, M.; Becciani, M.; Bellucci, J.; Bianchini, A.; Ferrara, G.; Arnone, A.; Cencherle, F.; De Luca, M.; Marmorini, L.; Montesino, S.; Pini, N.; "An integrated design approach for turbocharger turbines based on the performance optimization in transitory conditions", in Proceedings of ASME Turbo 2018, Oslo, Norway, 2018

[77] Christmann, R.; Gugau, M.; Weiske, S.; "Gasoline VGT - a new trend for gasoline Miller engines?", Borg-Warner Turbo Systems Germany, in Proceedings of the 13th International Conference on Turbochargers and Turbocharging, pp. 563-576, London, UK, 2018

[78] Lachenmaier, N.; Baumgärtner, D.; Schiffer, H.P.; Kech, J.; "Gradient-free and Gradient-based optimization of a radial turbine", in Proceedings of the 13th European Conference on Turbomachinery Fluid dynamics & Thermodynamics, Lausanne, Switzerland, 2019

[79] Mueller, L.; Verstraete, T.; Racca, A.; "Multidisciplinary adjoint optimization of radial turbine rotors", in Proceedings of the 14th International Conference on Turbochargers and Turbocharging, IMechE, London, OK, 2021

[80] Aissa, M.H.; Verstraete, T.; Racca, A.; Williams, C.E.; "Optimization of a centrofugal turbine rotor for robustness and reliability against manufacturing tolerances", in Proceedings of the 14th International Conference on Turbochargers and Turbocharging, IMechE, London, OK, 2021

[81] Diefenthal, M.; Rakut, C.; Tadesse, H.; Wirsum, M.; "Temperature distribution in a radial turbine wheel during transient operation", MTZ Worldwide, Volume 76, pp. 50-55, 2015

[82] Makhija, D.S.; Beran, P.S.; "Concurrent shape and topology optimization for unsteady Conjugate Heat Transfer", Struct. Multidiscip. Optim., Volume 62, pp.1275-1297, 2020

[83] Jaksch, P.; "Implementation of an adjoint thermal solver for inverse problems", in Proceedings of the 12th European Conference on Turbomachinery Fluid Dynamics & Thermodynamics, Stockholm, Sweden, 2017

[84] Subramaniam, V.; Dbouk, T.; Harion, J.-L.; "Topology optimization of Conjugate Heat Transfer systems: A competition between heat transfer enhancement and pressure drop reduction", Int. J. Heat Fluid Flow, Volume 75, pp.165-184, 2019

[85] Perelmann, L.T.; "On conjugate problems of heat transfer", International Journal of Heat and Mass Transfer, Volume 3, pp. 293-303, 1961

[86] Luikov, A.V.; "Conjugate convective heat transfer problems", International Journal of Heat and Mass Transfer, Volume 17, pp. 257-265, 1974

[87] Gkaragkounis, K.T.; Papoutsis-Kiachagias, E.M.; Giannakoglou, K.C.; "The continuous adjoint method for shape optimization in Conjugate Heat Transfer problems with turbulent incompressible flows", Appl. Therm. Eng., Volume 140, pp.351-362, 2018

[88] Mousavi, S.A.; “Constrained aerodynamic and heat transfer optimization of gas turbine blades using an adjoint approach”, Ph.D. Thesis, McGill University, Montreal, QC, Canada, 2012

[89] Burghardt, O.; Albring, T.; Gauger, N.R.; “Computation of accurate adjoint-based gradients for optimization in Conjugate Heat Transfer problems”, in Proceedings of the 6th European Conference on Computational Mechanics, Glasgow, UK, 2018

[90] Burghardt, O.; Gauger, N.R.; Economon, T.D.; “Coupled adjoints for Conjugate Heat Transfer in variable density incompressible flows”, in Proceedings of the AIAA Aviation 2019 Forum, Dallas, TX, USA, 2019

[91] Towara, M.; Lotz, J.; Naumann, U.; “Discrete adjoint approaches for CHT applications in OpenFOAM”, in Proceedings of the Eurogen 2019, Guimarães, Portugal, 2019

[92] Nocedal, J.; Wright, S.J.; “Numerical Optimization – Volume 2”, Springer Science & Business Media, LLC: Berlin/Heidelberg, Germany, 2006

[93] SAE J1826, “Turbocharger gas stand test code”, SAE standard, 1995

[94] SAE J922, “Turbocharger nomenclature and terminology”, SAE standard, 1995

[95] PTC 10-1997, “Performance test code on compressors and exhausters”, American Society of Mechanical Engineers, New York, 1997

[96] Romagnoli, A.; Manivannan, A.; Rajoo, S.; Chiong, M.S.; Feneley, A.; Pesiridis, A.; Martinez-Botas, R.F.; “A review of heat transfer in turbochargers”, Renewable and Sustainable Energy Reviews, Volume 79, pp. 1442-1460, 2017

[97] Romagnoli, A.; Martinez-Botas, R.; “Heat transfer analysis in a turbocharger turbine: an experimental and computational evaluation”, Applied Thermal Engineering, Volume 38, pp. 58–77, 2012

[98] Aghaali, H.; Angstrom, H.E.; Serrano, J.R.; “Evaluation of different heat transfer conditions on an automotive turbocharger”, International Journal of Engine Research, Volume 16, Issue 2, pp. 137-151, 2015

[99] Baines, N.; Wygant, K.D.; Dris, A.; “The analysis of heat transfer in automotive turbochargers”, J. Eng Gas Turb Power; Volume 132: 042301, 8 pp., 2010

[100] Dimelow, A.; “Steady and transient conjugate heat transfer analysis of a turbocharger”, in the 13th International Conference on Turbochargers and Turbocharging, London, UK, 2018

[101] Heuer, T.; Engels, B.; Wollscheid, P.; “Thermomechanical analysis of a turbocharger based on Conjugate Heat Transfer”, in Proceedings of ASME Turbo Expo 2005: Power for Land, Sea and Air, Reno-Tahoe, Nevada, USA, 2005

[102] Sharp, K.; Matschinsky, F.; Translation of Ludwig Boltzmann’s Paper “On the relationship between the second fundamental theorem of the mechanical theory of heat and probability calculations regarding the conditions for thermal equilibrium”, Sitzungberichte der Kaiserlichen Akademie der Wissenschaften. Mathematisch-Naturwissen Classe. Abt. II, LXXVI 1877, pp 373-435 (Wien. Ber. 1877, 76:373-435). Reprinted in Wiss. Abhandlungen, Vol. II, reprint 42, p. 164-223, Barth, Leipzig, 1909. Entropy 2015, 17, 1971-2009

[103] Schlichting, H.; “Boundary-layer theory”, McGraw-Hill Series in Mechanical Engineering – Seventh Edition; McGraw-Hill, New York, 1979

[104] Kassab, A.J.; Kapat, J.S.; “Investigation of Conjugate Heat Transfer in turbine blades and vanes”, NASA NRA-99-GRC-2 Final Report, NASA

[105] Verdicchio, J.A.; Chew, J.W.; Hills, N.J.; “Coupled fluid/solid heat transfer computation for turbine discs”. In Proceedings of the ASME Turbo Expo, New Orleans, LA, USA, 4–7 June 2001; Volume 3. Paper No. 2001-GT-0205

[106] Luff, I.K.; McGuirk, J.J.; “Conjugate heat transfer predictions of a combustor heatshield containing pedestals”, NATO RTO-AVT Symposium on advanced flow management, Norway, 2001

[107] Croce, G.; “A Conjugate Heat Transfer procedure for gas turbine blades”, in Heat Transfer in Gas Turbine Systems, Annals of NY Academy of Sciences, Vol. 934, pp.273-280, 2001

[108] Montomoli, F.; Adami, P.; Martelli, F.; “A finite volute method for the conjugate heat transfer in film cooling device”, in Proceedings of the Institution of Mechanical Engineers, Part A: Journal of Power and Energy, Volume 223, Issue 2, pp.191-200, 2008

[109] Węcel, G.; “BEM-FVM solution of the conjugate radiative and convective heat transfer problem”, ARCO, Volume 13, pp. 171–248, 2006

[110] Li, H.; Kassab, A.J.; “A coupled FVM/BEM approach to conjugate heat transfer in turbine blades”, in the 6th Joint Thermophysics and Heat Transfer Conference, AIAA, 2012

[111] He, M.; Kassab, A.J.; Bishop, P.J.; Minardi, A.; “An iterative FDM/BEM method for the conjugate heat transfer problem - parallel plate channel with constant outside temperature”, Engineering Analysis with boundary Elements, Vol. 15, 1995

[112] Divo, E.; Kassab, A.J.; “An efficient localized radial basis function meshless method for fluid flow and Conjugate Heat Transfer”, ASME. J. Heat Transfer, Volume 129, Issue 2, pp. 124-136, 2007

[113] Horvat, A.; Mavko, B.; Catton, I.; “The Galerkin method solution of the conjugate heat transfer”, in the Proceedings of the ASME-ZSIS International Thermal Science Seminar II, Bled, Slovenia, 2004

[114] Chiappini, D.; Festuccia, A.; Bella, G.; “Coupled lattice Boltzmann finite volume method for conjugate heat transfer in porous media”, in Numerical Heat Transfer, Part A: Applications, Volume 73, Issue 5, pp. 291-306, 2018

[115] Wesseling, P.; “An introduction to multigrid methods”, Volume in Pure and Applied Mathematics, John Wiley & Sons, New York, 1992

[116] Gordon, W.; Thiel, L.; “Transfinite mapping and their application to grid generation”, Applied Mathematics and Computation, Volume 10–11, pp. 171–233, 1982

[117] Delaunay, B.; “Sur la sphère vide”, Bulletin de l’Académie des Sciences de l'URSS, Classe des Sciences Mathématiques et Naturelles, Volume 6, pp. 793–800, 1934

[118] Verstraete, T.; Mueller, L.; Mueller, J.D.; “CAD-based adjoint optimization of the stresses in a radial turbine”, in Proceedings of the ASME

Turbo Expo 2017, Charlotte, NC, USA, 2017; Volume 2C, Paper No. GT2017-65005

[119] Verstraete, T.; "Multidisciplinary turbomachinery component optimization considering performance, stress, and internal heat transfer", Ph.D. Thesis, Universiteit Gent, Gent, Belgium, 2008

[120] Stephard, D.; "A two-dimensional interpolation function for irregularly spaced data", in the Proceedings of the 23rd ACM National Conference, pp. 517-524, 1968

[121] Giles, M.B.; "Stability analysis of numerical interface conditions in fluid-structure thermal analysis", International Journal of Numerical Methods in Fluids, Volume 25, pp. 421-436, 1997

[122] Verstraete, T.; Scholl, S.; "Stability analysis of partitioned methods for predicting Conjugate Heat Transfer", Int. J. Heat Mass Transf., Volume 101, pp. 852–869, 2016

[123] Duchaine, F.; Corpon, A.; Pons, L.; Mounreau, V.; Nicoud, F.; Poinsot, T.; "Development and assessment of a coupled strategy for conjugate heat transfer with large eddy simulation: application to a cooled turbine blade", Int. J. Heat Fluid Flow, Volume 30, pp. 1129-1141, 2009

[124] Divo, E.; Steinthorsson, E.; Rodriguez, F.; Kassab, A.J.; Kapat, J.S.; "Glenn-HT/BEM conjugate heat transfer solver for large-scale turbomachinery models", NASA-Report CR212195, NASA, 2003

[125] Heselhaus, A.; Vogel, D.T.; Karain, H.; "Coupling of 3D N-S external flow calculatios and internal 3D heat conduction calculations for cooled turbine blades", in Proceedings of the Propulsion Energetics Panel 80th Symposium, Antalya, Turkey, 1992

[126] Verstraete, T.; Van den Braembussche, R.; "A novel method for the computation of Conjugate Heat Transfer with coupled solvers", in Proceedings of the International Symposium on Heat Transfer in Gas Turbine Systems, Antalya, Turkey, 2009

[127] Scholl, S.; Janssens, B.; Verstraete, T.; "Stability of the static conjugate heat transfer coupling approaches using Robin interface conditions", Computers and Fluids, Volume 172, pp. 209–225, 2018

[128] Bathe, K.J.; Khoshgoftaar, M.R.; "Finite Element formulation and solution of nonlinear heat transfer", Nucl. Eng. Des., Volume 51, pp. 389–401, 1979

[129] Dhondt, G.; "The Finite Element Method for three-dimensional thermomechanical applications"; John Wiley & Sons Ltd, Chichester, UK, 2004

[130] Zienkiewicz, O.C.; Taylor, R.L.; Zhu, J.Z.; "The Finite Element Method: Its basis and fundamentals - 7th edition", Butterworth-Heinemann, Oxford, UK, 2013

[131] Saad, Y.; "Iterative methods for sparse linear systems - Second edition", SIAM: Philadelphia, PA, USA, 2003

[132] Blazek, J.; "Computational Fluid Dynamics: Principles and applications – 2nd edition", Elsevier Science Ltd, Amsterdam, The Netherlands, 2001

[133] Hirsch, C.; “Numerical computation of internal and external flows, Volume 1: Fundamentals of computational fluid dynamics – Second edition”, Butterworth-Heinemann, Oxford, UK, 2007

[134] Schwalbach, M.; Verstraete, T.; Gauger, N.R.; “Adjoint optimization of turbomachinery components under mechanical constraints”, in The 8th VKI PhD Symposium, von Karman Institute for Fluid Dynamics, Sint-Genesius-Rode, Belgium (2017)

[135] Taguchi, G.; “Introduction to quality engineering: Designing quality into products and processes”; Asian Productivity Organization/UNIPUB: White Plain, NY, USA; Unipub/Kraus: New York, NY, USA, 1986

[136] Prautzsch, H.; Boehm, W.; Paluszny, M.; “Bézier and B-Spline techniques”, Springer Berlin Heidelberg, Berlin, Germany, 2002

[137] Torreguitart, I.S.; Verstraete, T.; Mueller, L.; “CAD kernel and grid generation algorithmic differentiation for turbomachinery adjoint optimization”, in Proceedings of the 7th European Congress on Computational Methods in Applied Sciences and Engineering (ECCOMAS), Crete Island, Greece, 2016

[138] Martins, J.R.R.A.; Alonso, J.J.; Reuther, J.J.; “A coupled-adjoint sensitivity analysis method for high-fidelity aero-structural design”, Optim. Eng., Volume 6, pp. 33–62, 2005

[139] Bücker, H.M.; Corliss, G.F.; “A bibliography on automatic differentiation”, in Automatic Differentiation: Applications, Theory, and Implementations, Springer, pp.321–322, 2005

[140] Griewank, A.; Walther, A.; “Evaluating derivatives: Principles and techniques of Algorithmic Differentiation, 2nd ed.”, Siam: Philadelphia, PA, USA, 2008

[141] M.A. Neto; A.A.L. Roseiro; J.C.R. Leal; “Engineering computation of structures: The Finite Element Method”, Springer International Publishing AG Switzerland, Switzerland, 2015

[142] Tadjouddine M.; Forth S.A.; Keane A.J.; “Adjoint differentiation of a structural dynamics solver. Automatic Differentiation: Applications, theory, and implementations”, Springer, pp. 309-319, 2006

[143] Varella, R.A.; Giechaskiel, B.; Sousa, L.; Duarte, G.; “Comparison of portable emissions measurement systems (PEMS) with laboratory grade equipment”, Applied Sciences, 8(9), 2018

[144] Halford, G.R.; “Low-Cycle Thermal Fatigue”, NASA Technical Memorandum 87225, NASA Lewis Research Center, Cleveland, Ohio, USA, 1986

[145] Hull, D.; Bacon, D.J.; “Introduction to dislocations - Fifth edition”, Butterworth-Heinemann, Oxford, UK, 2011

[146] Anderson, P.M.; Hirth, J.P.; Lothe, J.; “Theory of dislocations - Third edition”, Cambridge University Press, New York, USA, 2017

[147] Manson, S.S.; Halford, G.R.; “A method of estimating high temperature low cycle fatigue behavior of materials”, NASA Technical Memorandum X-52270, NASA Lewis Research Center, Cleveland, OH, USA, 1967

[148] Bill, R.C.; “Micromechanisms of thermomechanical fatigue: A comparison with isothermal fatigue”, NASA Technical Memorandum 87331, NASA Lewis Research Center, Cleveland, OH, USA, 1986

[149] Halford, G.R.; Saltsman, J.F.; “Calculation of thermomechanical fatigue life based on isothermal behavior”, NASA Technical Memorandum 88864, NASA Lewis Research Center, Cleveland, OH, USA, 1987

[150] Coffin, L.F.; “A study of the effects of cyclic thermal stresses on a ductile metal”, Trans. ASME, Volume 76, Issue 6, pp. 931-950, 1954

[151] Manson, S.S.; “Thermal stress and Low-Cycle Fatigue”, McGraw-Hill, New York, USA, 1966

[152] Ashby, M.F.; Shercliff, H.; Cebon, D.; “Materials engineering, science, processing and design”, Elsevier, 2007

[153] Brun, M.; “Low Cycle Fatigue in turbines”, NASA Technical Memorandum 75264, Washington D.C., USA, 1978

[154] Halford, G.R.; McGaw, M.A.; Bill, R.C.; Fanti, P.D.; “Bithermal fatigue - A link between isothermal and thermomechanical fatigue”, NASA Technical Report 19880048691, NASA Lewis Research Center, Cleveland, OH, USA, 1988

[155] Fuchs, H.O.; Stephens, R.I.; “Metal fatigue in engineering”, Exp. Mech., pp. 65-82, 1965

[156] Timoshenko, S.; “Strength of materials, part II - Advanced theory and problems, third edition”, Robert E. Krieger Publishing Company, pp. 393-430, 1983

[157] Coffin, L.F.; Tavernelli, J.F.; “The cyclic straining and fatigue of metals”, Trans. Metall. Soc. of AIME, Volume 215, pp. 794-807, 1959

[158] Tavernelli, J.F.; Coffin, L.F.; “Experimental support for generalized equation predicting Low Cycle Fatigue”, Trans. ASME, J. Basic Engineering, Volume 84, Issue 4, p. 533, 1962

[159] Manson, S.S.; Hirschberg, M.H.; “Low-Cycle Fatigue of notched specimens by consideration of crack initiation and propagation”, NASA Technical Note D-3146, NASA Lewis Research Center, Cleveland, OH, USA, 1967

[160] Graham, J.A.; “Fatigue design handbook”, SAE, 1968

[161] Landgraf, R.W.; Morrow, J.D.; Endo, T.; “Determination of cyclic stress-strain curve”, J. Mater., Volume 4, Issue 1, pp. 176-188, 1969

[162] Goodman, J.; “Mechanics applied to engineering – Eight edition”, Longman Green & Co., London, UK, 1914

[163] Morrow, J.D.; Tuler, F.R.; “Low Cycle Fatigue evaluation of Inconel 713C and Waspaloy”, ASME J. Basic Engineering, Volume 87, Issue 2, pp. 275-289, 1965

[164] Chaboche, J.L.; “A review of some plasticity and viscoplasticity constitutive theories”, International Journal of Plasticity, Volume 24, pp. 1642-1693, 2008

[165] Halfpenny, A.; Anderson, R.; Lin, X.; “Isothermal and Thermo-Mechanical Fatigue of automotive components”, SAE Technical Paper 2015-01-0548, 2015

[166] He, L.; Oldfield, M.; “Unsteady conjugate heat transfer modeling”, Journal of Turbomachinery, Volume 133, Issue 3: 31022, 2011

[167] Errera, M.P.; Baqué, B.; “A quasi-dynamic procedure for coupled thermal simulations”, Int. J. Numer. Meth. Fluids, Volume 72, pp. 1183-1206, 2013

[168] Sun, Z.; Chew, J.W.; Barnes, C.J.; “Efficient Finite Element Analysis/Computational Fluid Dynamics thermal coupling for engineering applications”, Journal of Turbomachinery, Volume 132, Issue 3: 031016 (9 pages), 2010

[169] Meng, F.; Dong, S.; Wang, J.; Guo, D.; “A new algorithm of global tightly-coupled transient heat transfer based on quasi-steady flow to the conjugate heat transfer problem”, Theoretical & Applied Mechanics Letters, Volume 6, pp. 233-235, 2016

[170] Radenac, E.; Gressier, J.; Millan, P.; “A conservative coupling numerical method for transient conjugate heat transfer”, in International Conference on Computational Methods for Coupled Problems in Science and Engineering, Santorin, Greece, 2005

[171] He, L.; Fadl, M.; “Multi-scale time integration for transient Conjugate Heat Transfer”, International Journal for Numerical Methods in Fluids, Volume 83, Issue 12, pp. 887-904, 2017

[172] Zienkiewicz, O.C.; Taylor, R.L.; “The Finite Element Method, Volume 2: Solid mechanics – 5th edition”, Butterworth-Heinemann, Oxford, UK, 2000

[173] Newmark, N.; “A method of computation for structural dynamics”, Journal of Engineering Mechanics, ASCE, Volume 85, pp. 67-94, 1959

[174] Tavernelli, J.F.; Coffin, L.F.; “A compilation and interpretation of cyclic strain fatigue tests on metals”, Trans. ASME, Volume 51, pp. 438-453, 1959

[175] Suresh, S.; “Fatigue of materials”, Cambridge University Press, The Edinburgh Building, Cambridge, UK, 1998

[176] Lee, D.; Kang, T.; Koo, J.M.; Seok, C.S.; Song, S.J.; “A study of the LCF characteristics of the Ni-based superalloy IN738LC”, Int. J. Precis. Eng. Manuf., Volume 16, pp. 775-780, 2015

[177] Hazra, S.b.; Schulz, V.; “Simultaneous pseudo-timestepping for PDE-model based optimization problems”, BIT Numerical Mathematics, Volume 44, pp. 457-472, 2004

[178] Ta’asan, S.; Kuruvila, G.; Salas, M.D.; “Aerodynamic design and optimization in one shot”, AIAA 92-0025, 1992

[179] Maenchen, G.; Sacks, S.; “The tensor code”, in Methods in Computational Physics, Volume 3, pp. 181-210, Academic Press, New York, NY, USA, 1964

[180] Lubliner, J.; “Plasticity theory”, Macmillan, London, UK, 1990

[181] Chaboche, J.L.; Lin, X.B.; Private communication, 2002

Appendix A

Basic tools for fluid and solid solvers

A.1 Isoparametric formulation

The energy balance equation in the solid domain (Eq. 2.7) is solved through the application of the Finite Element Method. The weak formulation presented in Eq. (2.14) is treated by dividing the entire volume V in N infinitesimal elements, such that:

$$V = \sum_{e=1}^{N} V_e \,. \tag{A.1}$$

In the present study, each element (named "finite element") is represented by a tetrahedron, with one node per vertex in the case of "first order elements".

The temperature field within the finite element is defined by a continuous function of the discrete temperature values detected at the nodes:

$$T(x) = \sum_i \varphi_i(x) T_i \tag{A.2}$$

with T_i as the temperature detected at node i, and $\varphi_i(x)$ indicating the corresponding shape function. The number of shape functions equals the number of nodes in the element. Moreover, their formulation is compliant with the following equalities:

$$\sum_i \varphi_i(x) = 1 \tag{A.3}$$

$$\varphi_i(x_j) = \begin{cases} 1 & if\ i = j \\ 0 & if\ i \neq j \end{cases} \tag{A.4}$$

with the subscripts i and j respectively indicating one of the shape functions and the location of one of the nodes in the element. Hence, Eq. (A.2) is satisfied at each node.

Similarly to the case of the state variables, also a general position X in the global coordinates system can be described w.r.t. the discrete positions of the nodes in the element:

$$X = \sum_i \psi_i(x)\, X_i\,. \tag{A.5}$$

According to [130], if the shape functions adopted for the description of the state variables and for the positions in global coordinates are the same (i.e. $\varphi_i = \psi_i$), the formulation is called "isoparametric".

Figure A.1 presents two different schemes for the discretization of a tetrahedral finite element. In the first case, the number of nodes equals the number of vertices, and the shape functions define a linear interpolation of the temperatures detected at the nodes. If an intermediate node is added to each edge in the element, the number of shape functions increases and their formulation assumes a higher degree, generating quadratic interpolations of the temperature field along each edge. Therefore, the corresponding finite element is defined "quadratic". Despite the higher complexity, quadratic elements are preferred to linear ones because of their higher accuracy in discretizing curved physical domains.

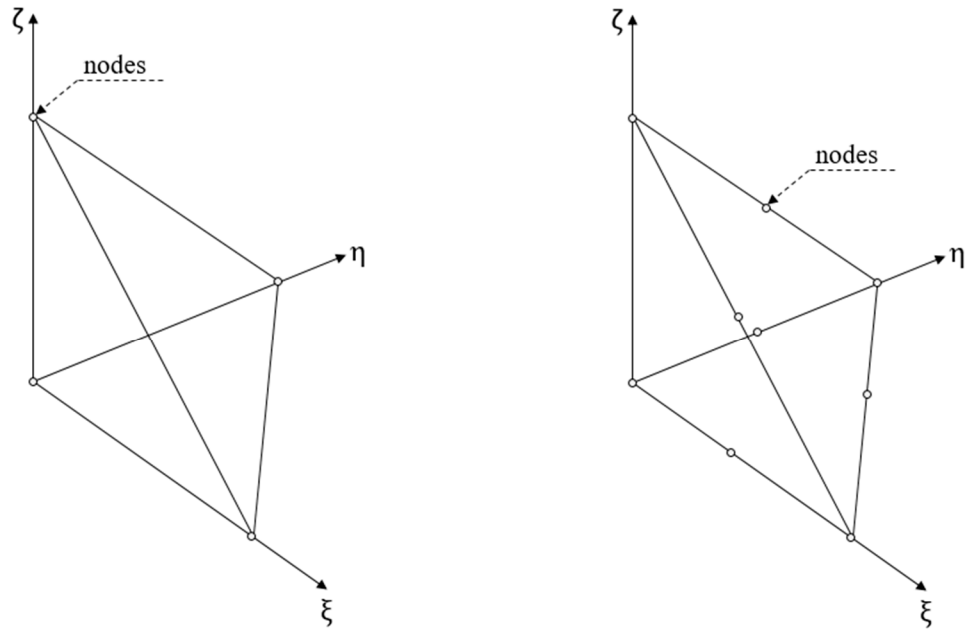

(a) Linear finite element **(b)** Quadratic finite element

Figure A.1 Linear and quadratic tetrahedral elements in local coordinates.

The choice of adopting tetrahedral elements for the discretization of the solid domain is justified by their high versatility in the reproduction of complex shapes, as necessary for turbomachinery components. Moreover, a robust meshing

technique based on the three-dimensional Delaunay method is available in the code CADO. Nevertheless, the number of discretization schemes of first and second order available in literature is not limited to such kind of finite element. The interested reader is invited to consult [129] for a thorough discussion about this topic.

A.2 Volume integral and surface integral

The system of equations (2.16) is adopted for the solution of the energy balance within the solid domain. The formulation involves volume integrals and surface integrals over each finite element in the three dimensional space. Since the shape of the domain may be rather complex and the elements irregular, it is convenient to apply a coordinates transformation to switch from the global reference system $X(x, y, z)$ to a local one associated to the finite element itself, $X(\xi, \eta, \zeta)$. In case of a tetrahedral element, the new coordinates satisfy the following relations:

$$0 \leq \xi, \eta, \zeta \leq 1 \tag{A.6}$$

$$\xi + \eta + \zeta \leq 1 \tag{A.7}$$

Figure A.2 presents the impact of the coordinates transformation to a tetrahedral element. Despite the curved edges in the physical domain, the regular shape resulting in the local coordinate system allows the straightforward application of a general formulation for the shape functions, such that:

$$\varphi(x, y, z) \quad \rightarrow \quad \varphi(\xi, \eta, \zeta) \, . \tag{A.8}$$

The full set of shape functions in the local coordinates system is reported in [129].

Therefore, Eq. (2.16) can be rewritten as follows:

$$\begin{aligned} \sum_e \sum_i \sum_j \underbrace{\left[\int_{V_e} \mathrm{k} \nabla\varphi_i \nabla\varphi_j \left| \frac{\partial X(x,y,z)}{\partial \gamma(\xi,\eta,\zeta)} \right| d\xi \, d\eta \, d\zeta \right]}_{A_{cond}} T_i \delta T_j \\ = -\sum_e \sum_i \sum_j \underbrace{\left[\int_{S_e} \tilde{h} \varphi_i \varphi_j \left| \frac{\partial X(x,y,z)}{\partial \gamma(\xi,\eta)} \right| d\xi \, d\eta \right]}_{A_{conv}} T_i \delta T_j \\ + \sum_e \sum_j \left[\int_{S_e} \tilde{h} T'_{fl} \varphi_j \left| \frac{\partial X(x,y,z)}{\partial \gamma(\xi,\eta)} \right| d\xi \, d\eta \right] \delta T_j \, . \end{aligned} \tag{A.9}$$

Eq. (A.9) presents at the LHS the determinant of the Jacobian defining the three-dimensional coordinates transformation from the global to the local reference system. This term is explicitly computed as:

$$J_V = \left|\frac{\partial X(x,y,z)}{\partial \gamma(\xi,\eta,\zeta)}\right| = \begin{vmatrix} \frac{\partial x}{\partial \xi} & \frac{\partial x}{\partial \eta} & \frac{\partial x}{\partial \zeta} \\ \frac{\partial y}{\partial \xi} & \frac{\partial y}{\partial \eta} & \frac{\partial y}{\partial \zeta} \\ \frac{\partial z}{\partial \xi} & \frac{\partial y}{\partial \eta} & \frac{\partial z}{\partial \zeta} \end{vmatrix} . \tag{A.10}$$

On the other hand, Eq. (A.9) shows at the RHS two surface integrals in the three dimensional space. Therefore, the determinant of the Jacobian accounting for the transformation from a three-dimensional reference system of a two-dimensional local one is reflected in the following formulation:

$$J_S = \left|\frac{\partial X(x,y,z)}{\partial \gamma(\xi,\eta)}\right| = \begin{vmatrix} \vec{\imath} & \vec{\jmath} & \vec{k} \\ \frac{\partial x}{\partial \xi} & \frac{\partial y}{\partial \xi} & \frac{\partial z}{\partial \xi} \\ \frac{\partial x}{\partial \eta} & \frac{\partial y}{\partial \eta} & \frac{\partial z}{\partial \eta} \end{vmatrix} . \tag{A.11}$$

In fact, if a surface S in the three-dimensional space is defined as a vector function of two parameters (ξ, η),

$$S = x(\xi,\eta)\,\vec{\imath} + y(\xi,\eta)\,\vec{\jmath} + z(\xi,\eta)\,\vec{k}\,, \tag{A.12}$$

then it is recognized its area is calculated as

$$area_S = \int \left|\frac{\partial S}{\partial \xi} \times \frac{\partial S}{\partial \eta}\right| d\xi d\eta = \int J_s\, d\xi d\eta\,. \tag{A.13}$$

Finally, since the shape of the solid domain may be complex, the solution of Eq. (A.9) would be hardly achievable through an analytical integration. Therefore, it is preferable to accept the integrals approximation offered by the numerical integration technique, as follows:

$$\begin{aligned} &\sum_e \sum_n \sum_i \sum_j \underbrace{\left[\left(\mathrm{k}\,\nabla\varphi_i(\xi_n,\eta_n,\zeta_n)\;\nabla\varphi_j(\xi_n,\eta_n,\zeta_n)\;J_V\right) w_{n_{vol}}\right]}_{A_{cond}} T_i \delta T_j \\ &= -\sum_e \sum_n \sum_i \sum_j \underbrace{\left[\left(\tilde{h}\varphi_i(\xi_n,\eta_n,\zeta_n)\;\varphi_j(\xi_n,\eta_n,\zeta_n)\;J_S\right) w_{n_{surf}}\right]}_{A_{conv}} T_i \delta T_j \\ &+ \sum_e \sum_n \sum_j \left[\left(\tilde{h} T'_{fl} \varphi_j(\xi_n,\eta_n,\zeta_n)\;J_S\right) w_{n_{surf}}\right] \delta T_j\,. \end{aligned} \tag{A.14}$$

In Eq. (A.14) the volume integral and the surface integrals are replaced by linear combinations of terms which are functions of *n* integration points located in the finite element (four points for the volume integral and three points for the surface one). Moreover, it is possible to note the shape functions are cyclically calculated w.r.t. the local coordinates (ξ_n, η_n, ζ_n) of each integration point. Finally, a weighting coefficient w_n is assigned to each point. The number and locations of the integration points, as well as their correspondent weights w_n, depend on several schemes available in literature, providing different levels of accuracy and computational cost. In the present work, the Gaussian scheme for tetrahedral elements is adopted [129].

A.3 Single Point Constraint and Multiple Point Constraint

The turbocharger turbine rotor herein analyzed is a geometry exhibiting a cyclic symmetry. Therefore, only a periodic sector is considered in the CHT framework (cf. Figure 2.3). The pairs of corresponding nodes on the two periodic surfaces are subjected to multiple point constraints (MPC), i.e. constraints involving more than one degrees of freedom (d.o.f.). Instead, single point constraints (SPC) are invoked if only one d.o.f. is affected by the boundary conditions, like in the case of a node with an imposed temperature.

The boundary conditions of type SPC or MPC can be efficiently treated by eliminating one d.o.f. per constraint, thus reducing the rank of the global stiffness matrix.

In principle, it is considered a system of equations with *N* d.o.f.

$$a_{ij}\, x_j = b_i, \qquad i, j \in (1, N) \tag{A.15}$$

presenting a subset of *K* MPC:

$$a_{kj}\, x_j = b_k, \qquad k \in (1, K);\ j \in (1, N);\ K < N. \tag{A.16}$$

For each equation (A.16) affected by such constraints, one d.o.f. x_S is selected and moved at the LHS:

$$a_{kS}\, x_S = b_k - \sum_{j \neq S} a_{kj}\, x_j, \qquad k \in (1, K);\ j \in (1, N). \tag{A.17}$$

From Eq. (A.17), it turns out that:

$$x_S = \sum_{j \neq S} \left(-\frac{a_{kj}}{a_{kS}}\right) x_j + \frac{b_k}{a_{kS}}, \qquad k \in (1, K);\ j \in (1, N). \tag{A.18}$$

All the d.o.f. x_S at the LHS are called "dependent parameters" and can be defined as a linear combination of the other d.o.f. $x_{j \neq S}$ (named "independent parameters").

Hence, Eq. (A.18) is substituted in Eq. (A.15), allowing the elimination of the set of dependent parameters from the global system of equations, thus reducing the computational cost of the system solution. In case of a SPC, Eq. (A.18) still holds, but only considering its second term at the RHS.

This concept is applied to all the FEM solvers involved in the present work, either in steady state or in transient mode, for the computation of the temperature field and the stresses in the material.

The reader interested in a rigorous treatment of the application of SPC and MPC to the global system of equations is invited to refer to [129], which discusses in details about the techniques implemented for the conservation of the symmetric structure of the global stiffness matrix during the elimination of the dependent parameters.

A.4 Flow transformation matrices at viscous walls

Section 2.3.2 discusses the linearization of the heat flux boundary condition at the fluid walls in order to comply with the structure of the implicit flow solver expressed by Eq. (2.18).

[54] explains that the contributions to the linearized flow residuals $\partial R/\partial U$ are computed from the Jacobian matrices of the viscous and the inviscid fluxes, calculated at the interfaces of all the cells involved in the respective stencils, following Eq. (2.20) repeated here for convenience:

$$\frac{dF_{bnd}}{dU_{D1}} = \left[\frac{\partial F_{bnd}}{\partial V_{D1}} + \frac{\partial F_{bnd}}{\partial V_{G1}}\frac{\partial V_{G1}}{\partial V_{D1}}\right]\frac{\partial V_{D1}}{\partial U_{D1}} \tag{A.19}$$

Eq. (A.19) presents at the RHS the term $\partial V_{G1}/\partial V_{D1}$, which is the 5x5 flow transformation matrix from the first ghost cell layer to the first inner layer of the physical fluid domain. In case of viscous fluxes at a solid wall, the no-slip condition holds and, therefore, the central terms in the matrix at (A.20) present a negative sign. Since the zero-order pressure extrapolation is assumed in this development, the last term in position (5,5) equals unity. The first term, related to the density differentiation, is discussed hereafter.

$$\frac{\partial V_{G1}}{\partial V_{D1}} = \begin{bmatrix} a & 0 & 0 & 0 & 0 \\ 0 & -1 & 0 & 0 & 0 \\ 0 & 0 & -1 & 0 & 0 \\ 0 & 0 & 0 & -1 & 0 \\ 0 & 0 & 0 & 0 & 1 \end{bmatrix} \tag{A.20}$$

The assignment of the heat flux q_{FW} to the wall follows the thin shear layer approximation. Therefore, the temperature in the first ghost cell layer is derived as:

$$T_{G1} = T_{D1} - q_{FW}\frac{\Delta n}{k_{fl}} \,. \tag{A.21}$$

The application of the ideal gas law and the assumption of a zero-order pressure extrapolation lead to

$$\begin{aligned}\rho_{G1} = \frac{p_{G1}}{RT_{G1}} = \frac{p_{D1}}{R\left(T_{D1} - q_{FW}\frac{\Delta n}{k_{fl}}\right)} = \frac{\frac{p_{D1}}{RT_{D1}}}{1 - q_{FW}\frac{\Delta n}{k_{fl}T_{D1}}} \\ = \rho_{D1}\frac{1}{1 - q_{FW}\frac{\Delta n}{k_{fl}T_{D1}}} \,.\end{aligned} \tag{A.22}$$

Hence, it is possible to conclude that

$$a = \frac{\partial \rho_{G1}}{\partial \rho_{D1}} = \frac{1}{1 - q_{FW}\frac{\Delta n}{k_{fl}T_{D1}}} \,. \tag{A.23}$$

In alignment with this development, section 3.3.5 refers to the flow transformation matrix $\partial V_{bnd}/\partial V_{D1}$, relating the primitive variables detected at the wall boundary to the first inner layer of the fluid domain. The new 5x5 matrix assumes the following formulation:

$$\frac{\partial V_{bnd}}{\partial V_{D1}} = \begin{bmatrix} a_{bnd} & 0 & 0 & 0 & 0 \\ 0 & 0 & 0 & 0 & 0 \\ 0 & 0 & 0 & 0 & 0 \\ 0 & 0 & 0 & 0 & 0 \\ 0 & 0 & 0 & 0 & 1 \end{bmatrix}. \tag{A.24}$$

Because of the no-slip condition, the velocity terms at the boundary are null. Moreover, the derivative of the density term is affected by the computation of the temperature at the boundary, replacing Eq. (A.21) with the following one:

$$T_{bnd} = T_{D1} - q_{FW}\frac{0.5\,\Delta n}{k_{fl}} \,. \tag{A.25}$$

Thus, the a_{bnd} term is obtained:

$$a_{bnd} = \frac{\partial \rho_{bnd}}{\partial \rho_{D1}} = \frac{1}{1 - 0.5\,q_{FW}\frac{\Delta n}{k_{fl}T_{D1}}} \,. \tag{A.26}$$

Appendix B

Steady state adjoint solvers

B.1 Adjoint strain matrix

The present section discusses the development of the contributions of the strain matrix to the sensitivities of the solid grid coordinates, as presented in Eq. (3.20) and repeated here for convenience:

$$\bar{X}_{sl} \mathrel{+}= \bar{B}\ \frac{dB}{dX_{sl}}. \tag{B.1}$$

The first term at the RHS of Eq. (B.1) is the adjoint strain matrix, whose evaluation is discussed in Section 3.3.2. Here the focus is on the computation of the gradients of the strain matrix w.r.t. the solid grid coordinates dB/dX_{sl}, which is performed by walking in reverse mode the matrix assembly process.

The strains ε in a finite element are obtained from the differentiation of the displacements u:

$$\varepsilon_i = \frac{du}{dX} = B(i,j)\,u(j) = \sum_j \frac{\partial \varphi_{i,j}}{\partial X}\,u_j \tag{B.2}$$

with the index i identifying one of the six components of the element strain vector, and $j \in (1,\ num\_nodes \cdot num\_dofs)$.

In accordance with the isoparametric formulation presented in Section A.1, the strain matrix consisting in the derivatives of the shape functions w.r.t. the global coordinates $\partial\varphi/\partial X$ appears in Eq. (B.2). For each node, such derivatives are computed from the corresponding derivatives of the shape functions in local coordinates $\partial\varphi/\partial\gamma(\xi,\eta,\zeta)$, presented in Eq. (A.8), as follows:

$$
\begin{aligned}
J_V &= \left|\frac{\partial X(x,y,z)}{\partial \gamma(\xi,\eta,\zeta)}\right| \\
J_x &= \begin{vmatrix} \dfrac{\partial \varphi_i}{\partial \xi} & \dfrac{\partial y}{\partial \xi} & \dfrac{\partial z}{\partial \xi} \\ \dfrac{\partial \varphi_i}{\partial \eta} & \dfrac{\partial y}{\partial \eta} & \dfrac{\partial z}{\partial \eta} \\ \dfrac{\partial \varphi_i}{\partial \zeta} & \dfrac{\partial y}{\partial \zeta} & \dfrac{\partial z}{\partial \zeta} \end{vmatrix} \\
J_y &= \begin{vmatrix} \dfrac{\partial x}{\partial \xi} & \dfrac{\partial \varphi_i}{\partial \xi} & \dfrac{\partial z}{\partial \xi} \\ \dfrac{\partial x}{\partial \eta} & \dfrac{\partial \varphi_i}{\partial \eta} & \dfrac{\partial z}{\partial \eta} \\ \dfrac{\partial x}{\partial \zeta} & \dfrac{\partial \varphi_i}{\partial \zeta} & \dfrac{\partial z}{\partial \zeta} \end{vmatrix} \\
J_z &= \begin{vmatrix} \dfrac{\partial x}{\partial \xi} & \dfrac{\partial y}{\partial \xi} & \dfrac{\partial \varphi_i}{\partial \xi} \\ \dfrac{\partial x}{\partial \eta} & \dfrac{\partial y}{\partial \eta} & \dfrac{\partial \varphi_i}{\partial \eta} \\ \dfrac{\partial x}{\partial \zeta} & \dfrac{\partial y}{\partial \zeta} & \dfrac{\partial \varphi_i}{\partial \zeta} \end{vmatrix} \\
\rightarrow \quad & \frac{\partial \varphi_i}{\partial x} = \frac{J_x}{J_V}; \qquad \frac{\partial \varphi_i}{\partial y} = \frac{J_y}{J_V}; \qquad \frac{\partial \varphi_i}{\partial z} = \frac{J_z}{J_V} \,.
\end{aligned}
\tag{B.3}
$$

Hence, the derivatives of the shape functions in global coordinates are obtained by applying Cramer's method, with J_V indicating the determinant of the Jacobian of the three-dimensional coordinates transformation presented in Eq. (A.10).

In reverse mode, the accumulation of the sensitivities to the grid coordinates takes place through the Algorithmic Differentiation of Eq. (B.3). Hence, for each node *i* in the finite element, from Eq. (B.1) it follows that

$$
\begin{cases}
\bar{X}_{sl}(i) \mathrel{+}= \overline{\dfrac{\partial \varphi_\iota}{\partial x}}\, J_x \left(-\dfrac{1}{J_V^2}\right) \dfrac{dJ_V}{dX_{sl}} + \overline{\dfrac{\partial \varphi_\iota}{\partial x}}\, \dfrac{1}{J_V}\, \dfrac{dJ_x}{dX_{sl}} \\
\bar{X}_{sl}(i) \mathrel{+}= \overline{\dfrac{\partial \varphi_\iota}{\partial y}}\, J_y \left(-\dfrac{1}{J_V^2}\right) \dfrac{dJ_V}{dX_{sl}} + \overline{\dfrac{\partial \varphi_\iota}{\partial y}}\, \dfrac{1}{J_V}\, \dfrac{dJ_y}{dX_{sl}} \\
\bar{X}_{sl}(i) \mathrel{+}= \overline{\dfrac{\partial \varphi_\iota}{\partial z}}\, J_z \left(-\dfrac{1}{J_V^2}\right) \dfrac{dJ_V}{dX_{sl}} + \overline{\dfrac{\partial \varphi_\iota}{\partial z}}\, \dfrac{1}{J_V}\, \dfrac{dJ_z}{dX_{sl}}
\end{cases}
\tag{B.4}
$$

The derivatives d/dX_{sl} in Eq. (B.4) refer to the derivatives w.r.t. the three global coordinates (x, y, z) respectively, here reported in a compact form for sake of simplicity. Hence, $\bar{X}_{sl} = (\bar{x}, \bar{y}, \bar{z})_{sl}$. Moreover, the components of the adjoint strain matrix $\bar{B}$ explicitly appear herein.

B.2 Adjoint mechanical solver

The adjoint development for a FEM iterative linear system solver is presented in Section 3.3.2. The primal solver is not directly differentiated in reverse mode, but the formulation according to [142] is adopted. The present section offers the demonstration leading to Eq. (3.21) and Eq. (3.22).

The linear system in primal mode in Eq. (B.5) presents the stiffness matrix *S* and the load vector *f* in input. The system solution returns the displacements field *u* in output.

$$S\,u = f \tag{B.5}$$

In reverse mode, the adjoint displacement field $\bar{u}$ is known. Moreover, the stiffness matrix *S* and the load vector *f* are available in input, from the solution in primal mode. The requested outputs are the adjoint stiffness matrix $\bar{S}$ and the adjoint load vector $\bar{f}$. For sake of clarity, $\bar{f}$ indicates the perturbation in the load vector *f* necessary to achieve a perturbation in the displacements field *u* equal to the one observed in the known vector $\bar{u}$. Similarly for $\bar{S}$.

The solution to the system in (B.5) depends on the values of the load vector:

$$u_i = u_i(f_j), \qquad j = (1, \dots, N) \tag{B.6}$$

with *N* as the total number of nodes.

It follows that:

$$\bar{f_j} = \frac{dJ}{df_j} = \sum_{i=1}^{N} \bar{u}_i \frac{du_i}{df_j}. \tag{B.7}$$

In order to compute the second term at the RHS of Eq. (B.7), the system in (B.5) is differentiated:

$$S \frac{du}{df_j} = \begin{bmatrix} 0 \\ \vdots \\ 1 \\ \vdots \\ 0 \end{bmatrix} = e_j \qquad \rightarrow \qquad \frac{du}{df_j} = S^{-1} e_j \,. \tag{B.8}$$

From Eq. (B.7) it is possible to conclude that for each node *j*

$$\bar{f_j} = \frac{dJ}{df_j} = \sum_{i=1}^{N} \bar{u}_i \frac{du_i}{df_j} = \bar{u}^T \frac{du}{df_j} = \bar{u}^T S^{-1} e_j \,. \tag{B.9}$$

Hence, in general:

$$\bar{f}^T = \bar{u}^T S^{-1} \qquad \rightarrow \qquad S^T \bar{f} = \bar{u} \,. \tag{B.10}$$

Eq. (B.10), equivalent to Eq. (3.21), allows to compute the adjoint load vector $\bar{f}$.

Concerning the evaluation of the adjoint stiffness matrix, since

$$u_i = u_i(S_{ij}), \qquad i, j = (1, \dots, N) \tag{B.11}$$

its components are computed as

$$\bar{S}_{ij} = \frac{dJ}{du_k}\frac{du_k}{dS_{ij}}\,, \qquad k = (1, \dots, N)\,. \tag{B.12}$$

It is necessary to compute the second term at the RHS of Eq. (B.12), i.e. the perturbation to the displacement u_k corresponding to the perturbation of the component of the stiffness matrix S_{ij}.

Starting from Eq. (B.5) and differentiating by the component S_{ij}, it turns out that

$$\frac{dS}{dS_{ij}}u + S\,\frac{du}{dS_{ij}} = 0\,. \tag{B.13}$$

$$\frac{dS}{dS_{ij}} = e_{ij} \qquad \rightarrow \qquad e_{ij}u = \begin{bmatrix} 0 \\ \vdots \\ u_j \\ \vdots \\ 0 \end{bmatrix}. \tag{B.14}$$

Hence, from Eq. (B.13) it follows that

$$S\,\frac{du}{dS_{ij}} = -\begin{bmatrix} 0 \\ \vdots \\ u_j \\ \vdots \\ 0 \end{bmatrix} \qquad \rightarrow \qquad \frac{du}{dS_{ij}} = -S^{-1}\begin{bmatrix} 0 \\ \vdots \\ u_j \\ \vdots \\ 0 \end{bmatrix} \tag{B.15}$$

Substituting Eq. (B.15) in Eq. (B.12)

$$\bar{S}_{ij} = \frac{dJ}{du_k}\frac{du_k}{dS_{ij}} = -\left(\frac{dJ}{du}\right)^T S^{-1}\begin{bmatrix} 0 \\ \vdots \\ u_j \\ \vdots \\ 0 \end{bmatrix} = -\bar{u}^T S^{-1}\begin{bmatrix} 0 \\ \vdots \\ u_j \\ \vdots \\ 0 \end{bmatrix}. \tag{B.16}$$

Finally, substituting Eq. (B.10) in Eq. (B.16), the adjoint stiffness matrix is obtained:

$$\bar{S}_{ij} = -\bar{u}^T S^{-1}\begin{bmatrix} 0 \\ \vdots \\ u_j \\ \vdots \\ 0 \end{bmatrix} = -\bar{f}^T\begin{bmatrix} 0 \\ \vdots \\ u_j \\ \vdots \\ 0 \end{bmatrix} = -\bar{f}_i\,u_j\,. \tag{B.17}$$

Eq. (B.17) is equivalent to Eq. (3.22). Since $\bar{S}$ is non-symmetric, it is possible to replace it with a symmetric matrix, such that $\bar{S}_{symm} = 0.5(\bar{S} + \bar{S}^T)$.

Once the adjoint stiffness matrix and the adjoint load vector are available, their contributions to the sensitivities of the solid grid coordinates are computed, as described in the next section.

B.3 Grid sensitivities contributions from the adjoint mechanical solver

The FEM system assembly process is algorithmically differentiated to accumulate the sensitivities contributions to the solid grid points coordinates. This process is summarized in Eq. (3.23), repeated here for convenience:

$$\bar{X}_{sl} \mathrel{+}= \bar{S}\ \frac{dS}{dX_{sl}} + \bar{f}\ \frac{df}{dX_{sl}}. \tag{B.18}$$

The two derivatives at the RHS of Eq. (B.18) are discussed hereafter.

In their explicit form, the stiffness matrix and the load vector are defined in Eq. (2.27) as:

$$\begin{aligned}\sum_e \sum_i \sum_j \left[\int_{V_e} B^T \mathrm{E}\ \mathrm{B}\, dV_e\right] u_i \delta u_j \\ = \sum_e \sum_j \left[\int_{V_e} \rho \varphi_j b(\omega) dV_e\right] \delta u_j \\ + \sum_e \sum_j \left[\int_{V_e} B^T E \varepsilon_{th} dV_e\right] \delta u_j \\ + \sum_e \sum_j \left[\int_{S_e} \varphi_j t\ dS_e\right] \delta u_j\end{aligned} \tag{B.19}$$

Starting from the stiffness matrix at the LHS, according to the discussion in Section A.2, the three-dimensional coordinates transformation from the global to the local reference system and the application of the numerical integration technique return the following definition:

$$\begin{aligned}&\sum_e \sum_i \sum_j \left[\int_{V_e} B^T \mathrm{E}\ \mathrm{B}\, dV_e\right] u_i \delta u_j \\ &= \sum_e \sum_i \sum_j \left[\int_{V_e} B^T \mathrm{E}\ \mathrm{B} \left|\frac{\partial X(x,y,z)}{\partial \gamma(\xi,\eta,\zeta)}\right| d\xi\ d\eta\ d\zeta\right] u_i \delta u_j \\ &= \sum_e \sum_n \sum_i \sum_j \underbrace{\{w_n [B^T(X_{sl}(\xi_n,\eta_n,\zeta_n))\ \mathrm{E}\ \mathrm{B}(X_{sl}(\xi_n,\eta_n,\zeta_n))\ J_V]\}}_{S_e} u_i \delta u_j\end{aligned} \tag{B.20}$$

with n indicating the number of integration points located in the finite element.

Hence, the differentiation of the element stiffness matrix follows:

$$\begin{aligned}\frac{dS_e}{dX_{sl}} = w_n \Big\{ J_V\ \frac{d}{dX_{sl}} [B^T(X_{sl}(\xi_n,\eta_n,\zeta_n))\ \mathrm{E}\ \mathrm{B}(X_{sl}(\xi_n,\eta_n,\zeta_n))\ ] \\ +\ [B^T(X_{sl}(\xi_n,\eta_n,\zeta_n))\ \mathrm{E}\ \mathrm{B}(X_{sl}(\xi_n,\eta_n,\zeta_n))]\ \frac{dJ_V}{dX_{sl}}\ \Big\}.\end{aligned} \tag{B.21}$$

The operator d/dX_{sl} is a compact form indicating the derivatives respect to the global coordinates (x, y, z). In Eq. (B.21) the second term presents the derivatives of the determinant of the Jacobian matrix of the three-dimensional coordinates transformation, already encountered in section B.1. Instead, the first term involves the derivatives of the strain matrix *B*, whose explicit formulation is the following:

$$B = \begin{bmatrix} \frac{\partial \varphi_1}{\partial x} & 0 & 0 & \cdots & \frac{\partial \varphi_N}{\partial x} & 0 & 0 \\ 0 & \frac{\partial \varphi_1}{\partial y} & 0 & & 0 & \frac{\partial \varphi_N}{\partial y} & 0 \\ 0 & 0 & \frac{\partial \varphi_1}{\partial z} & & 0 & 0 & \frac{\partial \varphi_N}{\partial z} \\ \frac{\partial \varphi_1}{\partial y} & \frac{\partial \varphi_1}{\partial x} & 0 & & \frac{\partial \varphi_N}{\partial y} & \frac{\partial \varphi_N}{\partial x} & 0 \\ 0 & \frac{\partial \varphi_1}{\partial z} & \frac{\partial \varphi_1}{\partial y} & & 0 & \frac{\partial \varphi_N}{\partial z} & \frac{\partial \varphi_N}{\partial y} \\ \frac{\partial \varphi_1}{\partial z} & 0 & \frac{\partial \varphi_1}{\partial x} & & \frac{\partial \varphi_N}{\partial z} & 0 & \frac{\partial \varphi_N}{\partial x} \end{bmatrix} \tag{B.22}$$

with *N* indicating the number of nodes in the finite element and $\partial \varphi_i / \partial X_{sl}$ the shape function derivatives defined in the global coordinates system. Therefore, the contribution to the sensitivities of the grid coordinates through the strain matrix *B* boils down to the derivatives of the matrix in (B.22), by application of the algorithmic differentiation technique to the assembly process of each term.

The RHS of Eq. (B.19) accounts for three loads, which are separately treated for the computation of the derivatives df/dX_{sl} in Eq. (B.18). Also in this case, the coordinates transformations along with the numerical integration scheme are applied.

The first term of the load vector in Eq. (B.19) refers to the centrifugal forces, which are a function of the wheel rotational speed ω:

$$\sum_e \sum_j \left[\int_{V_e} \rho \varphi_j b(\omega) dV_e \right] \delta u_j = \sum_e \sum_n \sum_j \underbrace{\left\{ w_n \rho \left[\varphi_j b_n(\omega)\ J_V \right] \right\}}_{\Omega_e} \delta u_j \, . \tag{B.23}$$

The differentiation of Eq. (B.23) is the following:

$$\frac{d\Omega_e}{dX_{sl}} = w_n \rho \left\{ J_V \frac{d}{dX_{sl}} \left[\varphi_j b_n(\omega) \right] + \left[\varphi_j b_n(\omega) \right] \frac{dJ_V}{dX_{sl}} \right\} . \tag{B.24}$$

The centrifugal force applied to a node P of the solid mesh is proportional to

the distance of P from the rotation axis and to the square of the angular speed. Hence,

$$b_n(\omega) = (P - Q)\omega^2 \tag{B.25}$$

with Q indicating the location of the point representing the projection of P on the rotational axis. As discussed in [129], if R is another point located on the same axis, and $\vec{e}$ is the axis versor (i.e. its unit vector), then Eq. (B.25) can be written in extensive form as

$$b_n(\omega) = \{(P - R) - [(P - R) \cdot \vec{e}]\, \vec{e}\}\, \omega^2 \,. \tag{B.26}$$

Eq. (B.26) is evaluated at each integration point and its contribution is assigned to the nodes of the finite element by multiplication for the respective shape function φ_j, as reported in Eq. (B.23). The derivative of the centrifugal force appearing at the first term in eq. (B.24) is computed in each node as:

$$\begin{aligned} &\frac{d}{dX_{sl}}\left[\varphi_j b_n(\omega)\right] = \frac{d\varphi_j}{dX_{sl}} b_n(\omega) + \varphi_j \frac{d}{dX_{sl}} b_n(\omega) = \frac{d\varphi_j}{dX_{sl}} b_n(\omega) + \\ &\varphi_j \left\{\frac{d}{dX_{sl}}(P - R) - \frac{d}{dX_{sl}}[(P - R) \cdot \vec{e}]\, \vec{e}\right\} \omega^2 \,. \end{aligned} \tag{B.27}$$

Concerning the first term in the curly brackets at the RHS of Eq. (B.27), since the point R does not belong to the solid mesh, it does not pertain to the derivate. It turns out that

$$\begin{aligned} \frac{d}{dX_{sl}(i)}(P - R) &= \frac{d}{dX_{sl}(i)}\begin{bmatrix}(P_x - R_x)\\ (P_y - R_y)\\ (P_z - R_z)\end{bmatrix} = \frac{d}{dX_{sl}(i)}\begin{bmatrix}P_x\\ P_y\\ P_z\end{bmatrix} \\ &= \begin{cases} \dfrac{dP}{dx(i)} = \left[\varphi_i + x_i \dfrac{\partial \varphi_i}{\partial x}, 0, 0\right] \\ \dfrac{dP}{dy(i)} = \left[0, \varphi_i + y_i \dfrac{\partial \varphi_i}{\partial y}, 0\right] \\ \dfrac{dP}{dz(i)} = \left[0, 0, \varphi_i + z_i \dfrac{\partial \varphi_i}{\partial z}\right] \end{cases} \end{aligned} \tag{B.28}$$

since $P(x, y, z) = P(\sum_i \varphi_i x_i \,, \sum_i \varphi_i y_i \,, \sum_i \varphi_i z_i)$ in the finite element.
The second term in the curly brackets at the RHS of Eq. (B.27) equals to

$$\begin{aligned} &\frac{d}{dX_{sl}}[(P - R) \cdot \vec{e}]\, \vec{e} \\ &\qquad = \frac{d}{dX_{sl}}\left[(P_x - R_x)e_1 + \left(P_y - R_y\right)e_2 \right. \\ &\qquad \left. + (P_z - R_z)e_3\right] \vec{e} \,. \end{aligned} \tag{B.29}$$

Since there is no contribution from point R to the solid grid, the derivatives in the global coordinates are the following:

$$\begin{cases} \dfrac{d}{dx(i)}\left[(P_x - R_x)e_1 + (P_y - R_y)e_2 + (P_z - R_z)e_3\right]\vec{e} = \dfrac{d}{dx(i)}[P_x e_1]\,\vec{e} = e_1\left(\varphi_i + x_i\dfrac{\partial\varphi_i}{\partial x}\right)\vec{e} \\ \dfrac{d}{dy(i)}\left[(P_x - R_x)e_1 + (P_y - R_y)e_2 + (P_z - R_z)e_3\right]\vec{e} = \dfrac{d}{dy(i)}[P_y e_2]\,\vec{e} = e_2\left(\varphi_i + y_i\dfrac{\partial\varphi_i}{\partial y}\right)\vec{e} \\ \dfrac{d}{dz(i)}\left[(P_x - R_x)e_1 + (P_y - R_y)e_2 + (P_z - R_z)e_3\right]\vec{e} = \dfrac{d}{dz(i)}[P_z e_3]\,\vec{e} = e_3\left(\varphi_i + z_i\dfrac{\partial\varphi_i}{\partial z}\right)\vec{e} \end{cases}$$

Finally, the second term in Eq. (B.24) is simply the derivative of the determinant of the Jacobian matrix of the coordinates transformation, as already discussed before.

The second term at the RHS of Eq. (B.19) refers to the thermal loading. The application of the coordinates transformation and the numerical integration technique result in Eq. (B.31):

$$\sum_e \sum_j \left[\int_{V_e} B^T E \varepsilon_{th} dV_e\right] \delta u_j = \sum_e \sum_n \sum_j \underbrace{\{w_n [B^T E \varepsilon_{th}\ J_V]\}}_{D_e}\ \delta u_j\,. \quad \text{(B.31)}$$

The derivative of the element matrix D_e, re-evaluated at each integration point, is the following:

$$\frac{dD_e}{dX_{sl}} = w_n \left\{ J_V \frac{d}{dX_{sl}}[B^T E \varepsilon_{th}] + [B^T E \varepsilon_{th}] \frac{dJ_V}{dX_{sl}} \right\}. \quad \text{(B.32)}$$

The first derivative in Eq. (B.32) pertains to the elements of the strain matrix *B*, as presented in (B.22). The second term is the derivative of the determinant of the Jacobian transformation matrix.

Finally, the third term at the RHS of Eq. (B.19) is the boundary condition of the imposed displacements or tractions. In this case, the derivative involves only the numerical integration term J_S, which refers to the surface integral (ref. Section A.2), instead of the volumetric one.

Eq. (B.19) presents some material properties that are temperature-dependent and expressed by polynomial functions. Moreover, the thermal strains appear in the load vector, bringing a direct dependence over the temperature as well. When propagating the adjoint variables in opposite direction, some contributions to the temperature sensitivities $\bar{T}$ are accumulated:

$$\bar{T} += \bar{S}\frac{dS}{dT} + \bar{f}\frac{df}{dT}. \quad \text{(B.33)}$$

Starting from the stiffness matrix in Eq. (B.20), the temperature derivative involves the elasticity matrix:

$$\frac{dS_e}{dT} = w_n\ J_V\ \frac{d}{dT}[B^T(X_{sl}(\xi_n,\eta_n,\zeta_n))\ \mathrm{E(T)}\ \mathrm{B}(X_{sl}(\xi_n,\eta_n,\zeta_n))\ ] \\ = w_n\ J_V\ B^T(X_{sl}(\xi_n,\eta_n,\zeta_n))\frac{dE(T)}{dT}\ \mathrm{B}(X_{sl}(\xi_n,\eta_n,\zeta_n))\,. \tag{B.34}$$

In fact, $E(T) = f(\epsilon(T), \nu(T))$, with $\epsilon(T)$ indicating the Young's modulus, and $\nu(T)$ the Poisson's ratio.

Concerning the load vector *f*, the first term related to the centrifugal forces brings a contribution to the adjoint temperatures through the density. Hence,

$$\frac{d\Omega_e}{dT} = w_n J_V \varphi_j b_n(\omega)\frac{\partial\rho(T)}{\partial T}\,. \tag{B.35}$$

The second term, associated to the thermal loading, contributes to $\bar{T}$ through the elasticity matrix *E(T)* and the thermal strain ε_{th}:

$$\frac{dD_e}{dT} = w_n J_V\ B^T\frac{d}{dT}[E(T)\ \varepsilon_{th}]\ . \tag{B.36}$$

The thermal strain, defined in Eq. (2.28), is $\varepsilon_{th}(T) = g\big(T, \alpha(T)\big)$, hence presenting a direct dependence over the temperature and an indirect one through the thermal expansion coefficient of the material.

Eventually, the elements of the global stiffness matrix affected by Single or Multiple Point Constraints do not appear explicitly in the adjoint stiffness matrix $\bar{S}$, because of its consistency with the elimination of the dependent parameters prior to the system solve taking place in primal mode (ref. Section A.3). However, the contributions of the dependent parameters to the grid sensitivities are accounted for by the back-propagation of the adjoint variables through the assembly process of the boundary conditions. In particular, the reverse algorithmic differentiation of the SPC assembly process leads to the coordinate transformation matrix, adopted in primal mode to switch from the global rectangular system to the cylindrical coordinates system in bodies exhibiting cyclic symmetry for sake of easiness in the imposition of the boundary conditions. Hence, the contributions to $\bar{X}_{sl}$ are accumulated from there.

B.4 Adjoint post-processing routine for the heat fluxes in the solid domain

Figure 3.6 shows that a post-processing routine is invoked once the solution of the temperature field is available. Its purpose is to compute the heat fluxes q_{SW} at the surface of the solid domain, which are then interpolated by the DWI procedure and imposed as boundary condition to the fluid solver.

The procedure is delineated as follows. First, the thermal solver is run till

convergence in order to obtain the temperature field in the solid domain. Then, all the elements with at least one face laying on the surface (therefore, exposed to the convective loading) are processed to evaluate the heat fluxes q_{SW} to be exchanged at the interface. This operation takes place by computing the nodal heat flux through Fourier's law and the shape functions interpolation, resulting in the three components in the global coordinates system: $q_{SW} = (q_x, q_y, q_z)$. Finally, the heat flux is projected on the element face normal unit vector and the resulting quantity is passed to the DWI routine.

Hence, in reverse mode, the interpolated adjoint heat flux $\bar{q}_{SW}$ from the adjoint fluid solver is propagated through the DWI procedure in opposite direction. It follows the projection routine is algorithmically differentiated, providing in output the adjoint components of the heat flux in the global coordinate system $(\bar{q}_x, \bar{q}_y, \bar{q}_z)$, and contributing to the solid grid sensitivities by walking in reverse mode the assembly of the unit vector normal to the finite element face. After that, the reverse calculation of the nodal heat fluxes returns the adjoint temperatures $\bar{T}$ assigned to the nodes laying on the solid surface, and the accumulation of the grid sensitivities $\bar{X}$ through the adjoint shape functions derivatives in global coordinates appearing in Fourier's law.

B.5 Grid sensitivities contributions from the adjoint thermal solver

The system assembly process for the heat transfer solver is algorithmically differentiated in reverse mode in order to accumulate the sensitivities of the solid grid points coordinates. The concept is expressed by Eq. (3.26), repeated here for convenience:

$$\bar{X}_{sl} \mathrel{+}= \bar{A}\ \frac{dA}{dX_{sl}} + \bar{b}\ \frac{db}{dX_{sl}}. \tag{B.37}$$

While $\bar{A}$ and $\bar{b}$ derive from Section 3.3.3, herein the focus is on the computation of the derivatives w.r.t. the grid coordinates.

The system of equations in primal mode from (A.9) is the following:

$$\begin{aligned} \sum_e \sum_i \sum_j \Bigg[& \underbrace{\int_{V_e} \mathrm{k}\, \nabla\varphi_i \nabla\varphi_j \left|\frac{\partial X(x,y,z)}{\partial \gamma(\xi,\eta,\zeta)}\right| d\xi\, d\eta\, d\zeta}_{Ae_{cond}} + \\ & \underbrace{\int_{S_e} \tilde{h}\varphi_i\varphi_j \left|\frac{\partial X(x,y,z)}{\partial \gamma(\xi,\eta)}\right| d\xi\, d\eta}_{Ae_{conv}} \Bigg] T_i \delta T_j = \\ & \sum_e \sum_j \left[\int_{S_e} \tilde{h} T'_{fl} \varphi_j \left|\frac{\partial X(x,y,z)}{\partial \gamma(\xi,\eta)}\right| d\xi\, d\eta\right] \delta T_j \,. \end{aligned} \tag{B.38}$$

The application of the numerical integration technique to the volume and

surface integrals returns the following formulation:

$$\sum_e \sum_n \sum_i \sum_j \Bigg\{ \underbrace{\left[\left(\nabla\varphi_i(X(\xi_n,\eta_n,\zeta_n))\ \mathrm{k}\ \nabla\varphi_j(X(\xi_n,\eta_n,\zeta_n))\ J_V\right)\right] w_{n_{vol}}}_{Ae_{cond}} + \underbrace{\left[\left(\tilde{h}\varphi_i(\xi_n,\eta_n,\zeta_n)\ \varphi_j(\xi_n,\eta_n,\zeta_n)\ J_S\right)\right] w_{n_{surf}}}_{Ae_{conv}} \Bigg\} T_i \delta T_j = \sum_e \sum_n \sum_j \left[\left(\tilde{h} T'_{fl} \varphi_j(\xi_n,\eta_n,\zeta_n)\ J_S\right) w_{n_{surf}}\right] \delta T_j \,. \tag{B.39}$$

Hence, the derivative of the stiffness matrix involves three terms:

$$\begin{aligned} \frac{dA_e}{dX_{sl}} &= \frac{dA_{e\_cond}}{dX_{sl}} + \frac{dA_{e\_conv}}{dX_{sl}} \\ &= \left(\frac{d\left[\nabla\varphi_i(X(\xi_n,\eta_n,\zeta_n))\ \mathrm{k}\ \nabla\varphi_j(X(\xi_n,\eta_n,\zeta_n))\right]}{dX_{sl}}\ J_V \right. \\ &+ \left. \frac{dJ_V}{dX_{sl}} \left[\nabla\varphi_i(X(\xi_n,\eta_n,\zeta_n))\ \mathrm{k}\ \nabla\varphi_j(X(\xi_n,\eta_n,\zeta_n))\right] \right) w_{n_{vol}} \\ &+ \left(\frac{dJ_S}{dX_{sl}} \left[\tilde{h}\ \varphi_i(\xi_n,\eta_n,\zeta_n)\ \varphi_j(\xi_n,\eta_n,\zeta_n)\right] \right) w_{n_{surf}} \,. \end{aligned} \tag{B.40}$$

The first term at the RHS of Eq. (B.40) features the shape functions derivatives in the global coordinate system $\partial\varphi/\partial X_{sl}$. Therefore, their algorithmic differentiation follows the path derived in Section B.1, tracing back the grid coordinates contributions in the Jacobian transformation matrices.

Similarly, the second and third terms in Eq. (B.40) present direct differentiations of the J_V and J_S matrices, in accordance with the development discussed in Section B.3.

The load term in Eq. (B.39) provides two contributions. The first one is related to the accumulation of the grid sensitivities:

$$\frac{db_e}{dX_{sl}} = \frac{dJ_S}{dX_{sl}} \left[\tilde{h} T'_{fl} \varphi_j(\xi_n,\eta_n,\zeta_n)\right] w_{n_{surf}} \,. \tag{B.41}$$

The second one refers to the calculation of the adjoint virtual bulk fluid temperature, as mentioned in Eq. (3.27), that is passed to the hFFB loop:

$$\frac{db_e}{dT'_{fl}} = \tilde{h}\ \varphi_j(\xi_n,\eta_n,\zeta_n)\ J_S\ w_{n_{surf}} \,. \tag{B.42}$$

B.6 Grid sensitivities contributions from the interface perturbations

The calls to the differentiated DWI routine within the hFFB procedure, while propagating the adjoint variables in reverse mode, seed the mapped distances between solid nodes and fluid cells. Thus, the impact of any interface perturbation to the response function is taken into account. In particular, two adjoint clusters result from this operation.

In the first case, in primal mode the solid domain returns the heat fluxes at the interface, to be interpolated in order to impose the boundary condition to the fluid walls. Hence, for each target fluid cell center, a list of solid nodes is considered (its neighbors), with their relative distances computed as

$$dist\left(cell_i \,/\, node_j\right) = \sqrt{\left(x_{fl}(i) - x_{sl}(j)\right)^2 + \left(y_{fl}(i) - y_{sl}(j)\right)^2 + \left(z_{fl}(i) - z_{sl}(j)\right)^2} \,. \tag{B.43}$$

Hence, in reverse mode the adjoint distances $\overline{dist_{fl-sl}}$ contribute to the accumulation of the sensitivities of the solid and fluid grid coordinates by the algorithmic differentiation of Eq. (B.43).

In the second case, in primal mode the fluid domain provides the wall temperatures to be interpolated and transferred to the solid for the imposition of the Robin boundary condition. In this case, Section 2.2.3 discusses the development of a network of virtual fluid points aimed at distributing the temperature information in an isotropic fashion, before selecting the mating solid nodes – virtual fluid points for the weighted interpolation. Hence, the definition of the mutual distances changes to

$$dist\left(node_i \,/\, virtual\ fluid\ point_j\right) = \sqrt{\left(x_{sl}(i) - x_{Virt\_fl}(j)\right)^2 + \left(y_{sl}(i) - y_{Virt\_fl}(j)\right)^2 + \left(z_{sl}(i) - z_{Virt\_fl}(j)\right)^2} \,. \tag{B.44}$$

In reverse mode, the contributions to the solid grid coordinates are directly available from the differentiation of Eq. (B.44). On the other hand, the virtual fluid points involved in the interpolation process are seeded, returning the vector $\bar{X}_{Virt_{fl}}(j)$. Their adjoint information is carried to the routine responsible for the generation of the network of evenly distributed points between close cell centers. Thus, the back propagation of the adjoint variables passes through the reversed interpolation routine, finally contributing to the sensitivities of the "true" fluid grid points coordinates.

Therefore, the sensitivities of the grids coordinates obtained from the distances seeded by the reverse DWI procedure are accumulated to the contributions separately collected from the adjoint solid and fluid solvers, as described in Section 3.3.7. The resulting $\bar{X}_{fl}$ and $\bar{X}_{sl}$ are finally plugged into Eq. (3.2) for the evaluation of the cost function sensitivities w.r.t. the CAD variables.

Appendix C

Quasi-dynamic TMF solvers

C.1 The unsteady non-linear heat transfer solver – Primal mode

The unsteady heat transfer solver invoked by the quasi-dynamic approach is expressed by the non-linear system of equations (4.5), repeated here for convenience:

$$M(T_k^{n+1})\,\frac{T_k^{n+1}-T^n}{\Delta t}+A(T_k^{n+1})\,T_k^{n+1}=b(T_k^{n+1})\,. \tag{C.1}$$

An implicit time integration scheme is selected for sake of robustness in the numerical stability of the solver. Hence, Eq. (C.1) is linearized in order to process it through a Newton-Raphson method. In principle, the residual form of Eq. (C.1) is the following:

$$R\left(T_{k+1}^{n+1}\right)=M\left(T_{k+1}^{n+1}\right)\frac{T_{k+1}^{n+1}-T^n}{\Delta t}+A\left(T_{k+1}^{n+1}\right)T_{k+1}^{n+1}-b\left(T_k^{n+1}\right)=0\,, \tag{C.2}$$

which is equivalent to

$$R(T_{k+1}^{n+1})\cong\ R(T_k^{n+1})+\frac{\partial R(T_k^{n+1})}{\partial T_k^{n+1}}\,\Delta T=0\,. \tag{C.3}$$

Eq. (C.3) is iteratively solved w.r.t. the independent variable ΔT and at each loop the predicted temperature T_k^{n+1} is corrected, thus updating the residual vector and the Jacobian matrix. The algorithm is schematically represented as

$$
\begin{aligned}
&\text{do}\\
&\{\\
&\quad \frac{\partial R\left(T_k^{n+1}\right)}{\partial T_k^{n+1}}\,\Delta T = -R\left(T_k^{n+1}\right)\\
&\quad T_{k+1}^{n+1} = T_k^{n+1} + \Delta T\\
&\}\ \text{while}\ (\Delta T > tolerance)
\end{aligned}
\tag{C.4}
$$

with the index *k* indicating the iterations to convergence.

The Jacobian term on the LHS of Eq. (C.4) is obtained by linearizing the residual formulation in Eq. (C.2):

$$
\begin{aligned}
\frac{\partial R\left(T_k^{n+1}\right)}{\partial T_k^{n+1}} = \frac{\partial M\left(T_{k+1}^{n+1}\right)}{\partial T_{k+1}^{n+1}}\,\frac{T_{k+1}^{n+1} - T^n}{\Delta t} + M\left(T_{k+1}^{n+1}\right)\,\frac{I}{\Delta t} + \frac{\partial A\left(T_{k+1}^{n+1}\right)}{\partial T_{k+1}^{n+1}}\,T_{k+1}^{n+1}\\
+ A\left(T_{k+1}^{n+1}\right) I - \frac{\partial b\left(T_{k+1}^{n+1}\right)}{\partial T_{k+1}^{n+1}} = 0\,.
\end{aligned}
\tag{C.5}
$$

The terms $\partial M/\partial T \in R^{N,N,N}$ and $\partial A/\partial T \in R^{N,N,N}$ are tensors: hence, a tensor per vector product follows. For instance, in the case of the mass matrix

$$
\frac{\partial M(T^{n+1})}{\partial T^{n+1}}\,\frac{T^{n+1} - T^n}{\Delta t} = \sum_{i=1}^{N} \frac{\partial M}{\partial T_i}\,\frac{T_i^{n+1} - T_i^n}{\Delta t}
\tag{C.6}
$$

with the pedix "*i*" referencing to each grid node. The derivatives of the mass matrix *M* boil down to the density and heat capacity coefficients (both described as polynomial functions of the nodal temperature), while the derivatives of the stiffness matrix *A* refer to the thermal conductivity.

The element "*I*" appearing at the second and fourth terms on the RHS of Eq. (C.5) indicates the identity matrix.

Finally, the linearization of the load vector is derived as

$$
\frac{\partial b(T_{k+1}^{n+1})}{\partial T_{k+1}^{n+1}} = \frac{\partial}{\partial T_{k+1}^{n+1}}\left[\int_S \tilde{h}\left(T'_{fl} - \varphi^T \varphi T_{k+1}^{n+1}\right) dS\right] = -\int_S \tilde{h}\,\varphi^T \varphi\; dS\,.
\tag{C.7}
$$

Once the algorithm in (C.4) reaches convergence, T^{n+1} initializes the temperature field at the following time step. In case the conjugate coupling is traversing the last hFFB loop to convergence, at each time step the converged temperature field is passed to the thermo-mechanical solver for the computation of the unsteady thermal strains.

C.2 The unsteady non-linear heat transfer solver – Adjoint mode

The development of the adjoint framework for the unsteady heat transfer solver benefits from the linearization of the governing equation already performed in primal mode. In fact, starting from the system solve in (C.4), a procedure aimed at seeding the RHS vector is developed coherently with the demonstrations offered in Section B.2.

In principle, at each time step the governing equation is linearized around the converged field solution. Therefore, starting from the last temperature update, it follows that

$$T_{k+1}^{n+1} = T_k^{n+1} + \Delta T \quad \rightarrow \quad \begin{cases} \overline{\Delta T} = \bar{T}_{k+1}^{n+1} \\ \bar{T}_k^{n+1} = \bar{T}_{k+1}^{n+1} \end{cases} . \tag{C.8}$$

Since

$$\frac{\partial R(T_k^{n+1})}{\partial T_k^{n+1}} \Delta T = -R(T_k^{n+1}) \tag{C.9}$$

is a linear system, if we indicate the Jacobian matrix with the compact notation $\partial R/\partial T = C$, then it is possible to demonstrate that

$$C\ \Delta T = -R \tag{C.10}$$

$$C\ \frac{d\Delta T}{dR_i} = -e_i \tag{C.11}$$

$$\bar{R}_i = \overline{\Delta T}^T \frac{d\Delta T}{dR_i} = \overline{\Delta T}^T C^{-1}(-e_i) = -{e_i}^T\ C^{-T}\overline{\Delta T} = -{e_i}^T\ V \tag{C.12}$$

$$\left.\begin{aligned} \bar{R}_i = -{e_i}^T \quad &\rightarrow \quad \bar{R} = -V \\ V = C^{-T}\overline{\Delta T} \quad &\rightarrow \quad C^T\ V = \overline{\Delta T} \end{aligned}\right\} \ - C^T\ \bar{R} = \overline{\Delta T}\ . \tag{C.13}$$

Eq. (C.13) returns the adjoint residual vector, from which the contributions to the temperature sensitivities are finally obtained:

$$\bar{T}_k^{n+1} += \left(\frac{dR}{dT_k^{n+1}}\right)^T \bar{R}\ . \tag{C.14}$$

Hence, the transposed form of the Jacobian matrix previously computed in primal mode in Eq. (C.5) is directly implemented in Eq. (C.13) and Eq. (C.14).

In this case, $\bar{T}_k^{n+1}$ is considered as the initial temperature at the current time step, i.e. $\bar{T}_k^{n+1} = \bar{T}^n$. In fact, in reverse mode the linearization around the fully converged solution (which is expected to be the attractor point) allows neglecting the path to convergence walked in primal mode by the iterative solver. Only the sensitivities of the solution w.r.t. the input variables are relevant during the

evaluation in reverse mode. Hence, for the principle of the reverse accumulation the adjoint solver, which is linear, does not need to perform any accumulation through the inner iterations executed by the primal one.

Differently from the steady state development, no contributions to the adjoint temperatures are extracted from the LHS matrix in (C.4). Indeed, such matrix is a Jacobian that would bring second order derivatives of the temperature. Thus, only the RHS term, which is the residual form of the governing equation, contributes to $\bar{T}$. This procedure is confirmed by the same definition of the adjoint state variable from Eq. (1.9), repeated here as:

$$\bar{y} = \left(\frac{\partial J}{\partial y}\right)^T = \left(\frac{\partial R}{\partial y}\right)^T \psi. \tag{C.15}$$

In Eq. (C.15) only the derivatives of the residual form of the governing equation contribute to $\bar{y}$.

Hence, it is possible to draw back the consistency with the steady state adjoint development presented in Section 3.3.3, extracting the contributions to the temperature sensitivities not only from the RHS vector b, but also from the LHS matrix A. In fact, they both belong to the residual formulation of the energy balance equation $R = A\,T - b = 0$ (cf. Eq. 2.17).

Following the same principle, the contributions to the solid grid sensitivities are obtained from the seeded residual as well:

$$\bar{X}_{sl} \mathrel{+}= \bar{R}\ \frac{dR}{dX_{sl}} = \bar{M}\ \frac{dM}{dX_{sl}} + \bar{A}\ \frac{dA}{dX_{sl}} - \bar{b}\ \frac{db}{dX_{sl}}. \tag{C.16}$$

The application of the numerical integration technique to Eq. (4.4) leads to the following form:

$$\begin{aligned}
&\sum_e \sum_n \sum_i \sum_j \underbrace{\left[\left(\rho(T) c_p(T)\ \varphi_i\left(X(\xi_n,\eta_n,\zeta_n)\right) \varphi_j(X(\xi_n,\eta_n,\zeta_n))\ J_V\right)\right] w_{n_{vol}}}_{M_e} \frac{dT_i}{dt}\delta T_j \\
&+ \sum_e \sum_n \sum_i \sum_j \Bigg\{ \underbrace{\left[\left(\nabla\varphi_i(X(\xi_n,\eta_n,\zeta_n))\ \mathrm{k}(T)\ \nabla\varphi_j(X(\xi_n,\eta_n,\zeta_n))\ J_V\right)\right] w_{n_{vol}}}_{Ae_{cond}} \\
&+ \underbrace{\left[\left(\tilde{h}\varphi_i(\xi_n,\eta_n,\zeta_n)\ \varphi_j(\xi_n,\eta_n,\zeta_n)\ J_S\right)\right] w_{n_{surf}}}_{Ae_{conv}} \Bigg\} T_i \delta T_j \\
&= \sum_e \sum_n \sum_j \left[\left(\tilde{h} T'_{fl} \varphi_j(\xi_n,\eta_n,\zeta_n)\ J_S\right) w_{n_{surf}}\right] \delta T_j\,.
\end{aligned} \tag{C.17}$$

The first term in Eq. (C.17) is the mass matrix, whose contributions to the grid sensitivities are computed by differentiating the determinant of the transformation matrix J_V:

$$\frac{dM_e}{dX_{sl}} = \left(\frac{dJ_V}{dX_{sl}} \left[\rho(T) c_p(T)\ \varphi_i\left(X(\xi_n,\eta_n,\zeta_n)\right) \varphi_j(X(\xi_n,\eta_n,\zeta_n))\right]\right) w_{n_{vol}} \tag{C.18}$$

The contributions of the stiffness matrix A (including the conduction and convection terms) are derived according to Eq. (B.40), while the load vector follows the development presented in Eq. (B.41).

Finally, the load vector b accumulates its contributions to the sensitivities of the virtual bulk fluid temperature, as expressed in Eq. (B.42). However, in unsteady computations, the instantaneous $\bar{T}'_{fl}$ refers to the seeded value interpolated between the two fluid loads computed in primal mode at the extreme points of the current stretch of manoeuver. Hence, the interpolation routine itself needs to be algorithmically differentiated in order to accumulate the sensitivities of the true fluid bulk temperatures.

C.3 Constitutive model for inelastic deformations

The constitutive model introduced in Section 4.3.5 is invoked in post-processing of the FEM linear solver in order to analyze the occurrences of small inelastic deformations.

The problem is treated in primal mode following the definition by [172], here repeated for sake of convenience in preparation to the discussion of the adjoint development.

In principle, during the solution of an unsteady loading phenomenon the stress field is updated at each time step according to the following equation:

$$\sigma_{n+1} = \sigma_n + \Delta\sigma_n = \sigma_n + \int_0^{\Delta\varepsilon_n} D \; d\varepsilon \tag{C.19}$$

with D representing the elastoplastic tangent matrix, in replacement of the elasticity matrix E presented in Section 2.3.3. D is defined as

$$D = K\vec{m}\vec{m}^T + 2G\left(I - \frac{1}{3}\vec{m}\vec{m}^T\right) \tag{C.20}$$

with K as the elastic bulk modulus (or elastic tangential modulus), G indicating the plastic shear modulus, I as the identity matrix, and $\vec{m} = [1\ 1\ 1\ 0\ 0\ 0\ 0\ 0\ 0]^T$.

The implicit integration of Eq. (C.19) leads to

$$\Delta\sigma_{n+1}^k = D_{n+1}^k \Delta\varepsilon_{n+1}^k \tag{C.21}$$

with D_{n+1}^k representing the estimate of the tangent matrix at the end of the time step. In order to solve such equation, complex derivatives of the tangent matrix should be accounted for. This complication may be circumvented by the adoption of the "Return-Map Algorithm" by [179], presenting a predictor-corrector approach.

At first, a trial prediction of the stresses is performed assuming an elastic behavior:

$$\sigma_{n+1}^{trial} = E\left(\varepsilon_{n+1} - \varepsilon_n^p\right) \tag{C.22}$$

in which ε_{n+1} is the total strain at the end of the time step as computed by the FEM solver, and ε_n^p is the plastic strain known at the beginning of the time step. In the predictor step, only the elastic component modulus is considered.

The next step involves the evaluation of the Yield function *F*, defined as:

$$F = f(\sigma, \kappa, \nu) \tag{C.23}$$

with κ indicating the kinematic hardening parameter and ν the isotropic hardening parameter.

The yield criterion is satisfied when $F = 0$, and can be visualized as a surface in the n-dimensional space of stresses, whose shape depends on the values of κ and ν.

In the case of an isotropic material, several candidate formulations for the Yield surface are available in literature. The present work refers to the definition by Huber – von Mises, providing a satisfactory correlation for the plasticity in metals:

$$F = \sqrt{2J_2} - \sigma_Y = \sqrt{2J_2} - \sqrt{\frac{2}{3}}\, Y(\nu) \tag{C.24}$$
$$with\ \ 2J_2 = s_{ij}\, s_{ji} = \frac{1}{6}\left[(\sigma_{xx} - \sigma_{yy})^2 + (\sigma_{yy} - \sigma_{zz})^2 + (\sigma_{xx} - \sigma_{zz})\right.$$

in which σ_Y is a scalar constant representing the radius of the Yield function [180], J_2 represents the second invariant of the deviatoric stress tensor $\boldsymbol{s}$, and $Y(\nu)$ indicates a function for the description of the isotropic hardening (for instance, a linear polynomial definition such as $Y(\nu) = Y_0 + H_i\nu$, with H_i as the isotropic hardening module).

Hence, the evaluation of the Yield function follows:

$$F = f\left(\sigma_{n+1}^{trial}, \kappa_n, \nu_n\right) \begin{cases} if\ \ \leq 0 \ \ \rightarrow \ \ elastic \\ if\ \ > 0 \ \ \rightarrow \ \ plastic \end{cases} \tag{C.25}$$

In case of an elastic behavior, the update at the end of the time step is straightforward:

$$\sigma_{n+1} = \sigma_{n+1}^{trial}\,, \quad \kappa_{n+1} = \kappa_n\,, \quad \nu_{n+1} = \nu_n\,. \tag{C.26}$$

Otherwise, the yield constraint is violated and the trial state is inadmissible. Hence, the plastic behavior is to be modelled. The stress correction over the time step is defined in incremental form as follows:

$$\Delta\sigma_{n+1} = E\left(\Delta\varepsilon_{n+1} - \Delta\varepsilon_{n+1}^p\right). \tag{C.27}$$

The plastic strain rate is formulated as

$$\dot{\varepsilon} = \dot{\lambda}\frac{\partial F}{\partial \sigma} \tag{C.28}$$

with a proportionality constant $\dot{\lambda}$ known as the "plastic consistency" parameter. In the present demonstration, it is assumed to treat only cases of associative plasticity.

When considering a pseudo time step $dt = t_{n+1} - t_n$, it is possible to define the increment of plastic strain as $d\varepsilon = \dot{\varepsilon}\, dt$. Hence, the implicit integration of Eq. (C.28) leads to

$$\Delta\varepsilon^p_{n+1} = \Delta\lambda \frac{\partial F}{\partial \sigma}\bigg|_{n+1} \tag{C.29}$$

Substituting Eq. (C.29) in Eq. (C.27), it follows that

$$\Delta\varepsilon_{n+1} - \frac{\Delta\sigma_{n+1}}{E} - \Delta\lambda \frac{\partial F}{\partial \sigma}\bigg|_{n+1} = R_\sigma \,. \tag{C.30}$$

Eq. (C.30) represents the first non-linear residual form.

Concerning the kinematic hardening, its rate form is

$$\dot{\kappa} = -\dot{\lambda}\boldsymbol{H}\frac{\partial F}{\partial \kappa} \tag{C.31}$$

with $\boldsymbol{H}$ indicating an invertible set of constant hardening parameters. Once integrated in implicit form and rearranged, Eq. (C.31) provides the second non-linear residual form:

$$-\frac{\Delta\kappa_{n+1}}{\boldsymbol{H}} - \Delta\lambda \frac{\partial F}{\partial \kappa}\bigg|_{n+1} = R_\kappa \,. \tag{C.32}$$

Finally, the third non-linear residual form is obtained by enforcing the plastic solution, expressed as

$$-F_{n+1} = r_i \,. \tag{C.33}$$

The three equations (C.30), (C.32) and (C.33) generate a non-linear system whose solution satisfies $R_\sigma = 0, R_\kappa = 0, r_i = 0$. Such system can be solved by application of the Newton-Raphson method, leading to

$$\begin{cases} -E^{-1}\, d\sigma - \Delta\lambda \dfrac{\partial}{\partial \sigma}\left(\dfrac{\partial F}{\partial \sigma}\bigg|_{n+1}\right) d\sigma - \Delta\lambda \dfrac{\partial}{\partial \kappa}\left(\dfrac{\partial F}{\partial \sigma}\bigg|_{n+1}\right) d\kappa - \dfrac{\partial F}{\partial \sigma}\bigg|_{n+1} d\lambda = -R_\sigma \\ -\Delta\lambda \dfrac{\partial}{\partial \sigma}\left(\dfrac{\partial F}{\partial \kappa}\bigg|_{n+1}\right) d\sigma - \boldsymbol{H}^{-1} d\kappa - \Delta\lambda \dfrac{\partial}{\partial \kappa}\left(\dfrac{\partial F}{\partial \kappa}\bigg|_{n+1}\right) d\kappa - \dfrac{\partial F}{\partial \kappa}\bigg|_{n+1} d\lambda = -R_\kappa \\ -\dfrac{\partial F_{n+1}}{\partial \sigma} d\sigma - \dfrac{\partial F_{n+1}}{\partial \kappa} d\kappa + H_i d\lambda = -r_i \end{cases} \tag{C.34}$$

in which the total strain variation $\Delta\varepsilon_{n+1}$ from the FEM linear solver is treated like a constant. Hence, it follows in matrix form

$$\begin{bmatrix} E^{-1} + \Delta\lambda F_{,\sigma\sigma} & \Delta\lambda F_{,\sigma\kappa} & F_{,\sigma} \\ \Delta\lambda F_{,\kappa\sigma} & \boldsymbol{H}^{-1} + \Delta\lambda F_{,\kappa\kappa} & F_{,\kappa} \\ F^T_{,\sigma} & F^T_{,\kappa} & -H_i \end{bmatrix}^k_{n+1} \begin{Bmatrix} d\sigma \\ d\kappa \\ d\lambda \end{Bmatrix} = \begin{Bmatrix} R_\sigma \\ R_\kappa \\ r_i \end{Bmatrix}^k_{n+1} . \tag{C.35}$$

In each iteration, the incremental forms are updated, i.e. $\Delta\sigma_{n+1} \mathrel{+}= d\sigma, \Delta\kappa_{n+1} \mathrel{+}= d\kappa, \Delta\lambda_{n+1} \mathrel{+}= d\lambda$.

Once at convergence, all the residuals are null, with the updated stress σ_{n+1} exactly satisfying the yielding criterion. However, such stress would not satisfy the equilibrium condition in the residual form

$$R_{n+1} = M\ddot{u}_{n+1} + P_{n+1} - f = 0 \tag{C.36}$$

with the term $P_{n+1} = \int_V B^T \sigma_{n+1} dV$.

Hence, Eq. (C.36) is invoked one more time with the imposed stiffness term P_{n+1}accumulated in the load vector:

$$\begin{gathered} M\ddot{u}_{n+1} = Q \\ with\ Q = f - P_{n+1} \end{gathered} \tag{C.37}$$

Eq. (C.37) is solved through a direct integration method [141]. In this case, the central difference algorithm is adopted, such that

$$\frac{1}{\Delta t^2} M\, u_{n+1} = 2Q + \frac{1}{\Delta t^2} M(2u_n - u_{n-1}) \tag{C.38}$$

The updated displacements allow evaluating the total strains and, therefore, the updated total strain increment ${\Delta\varepsilon_{n+1}}^{k+1}$ follows. This increment, when inserted in Eq. (C.30), brings a non-zero residual $R_\sigma = {\Delta\varepsilon_{n+1}}^{k+1} - {\Delta\varepsilon_{n+1}}^{k} = d\varepsilon \neq 0$, while $R_\kappa = 0$ and $r_i = 0$ still hold.

Finally, given the solutions of the incremental forms, the system in (C.35) is manipulated as follows:

$$\begin{gathered} A = \begin{bmatrix} E^{-1} + \Delta\lambda F_{,\sigma\sigma} & \Delta\lambda F_{,\sigma\kappa} \\ \Delta\lambda F_{,\kappa\sigma} & \boldsymbol{H}^{-1} + \Delta\lambda F_{,\kappa\kappa} \end{bmatrix} \\ \nabla F = \begin{Bmatrix} F_{,\sigma} \\ F_{,\kappa} \end{Bmatrix} \\ A^* = H_i + \nabla F^T A^{-1} \nabla F \end{gathered} \tag{C.39}$$

resulting in the following formulation:

$$\begin{Bmatrix} d\sigma \\ d\kappa \end{Bmatrix} = A^{-1} \begin{Bmatrix} R_\sigma \\ R_\kappa \end{Bmatrix} - \frac{1}{A^*}\, A^{-1}\nabla F \left[\nabla F^T A^{-1} \begin{Bmatrix} R_\sigma \\ R_\kappa \end{Bmatrix} - r_i\right]. \tag{C.40}$$

Eq.(C.40) can be simplified. In fact, the previous incremental forms return $R_\kappa = 0$ and $r_i = 0$. Moreover, with the updated strain increment we obtain $R_\sigma \neq 0 = d\varepsilon$. Hence, Eq. (C.40) is rewritten in the following form:

$$\begin{Bmatrix} d\sigma \\ d\kappa \end{Bmatrix} = \left[A^{-1} - \frac{1}{A^*} A^{-1}\nabla F\, \nabla F^T A^{-1}\right] \begin{Bmatrix} R_\sigma \\ 0 \end{Bmatrix} = \begin{bmatrix} D & \vdots \\ \cdots & \cdots \end{bmatrix} \begin{Bmatrix} d\varepsilon \\ 0 \end{Bmatrix} \tag{C.41}$$

The upper diagonal block in (C.41) equals to the elastoplastic tangent matrix. Therefore, it follows that

$$d\sigma = D\, d\varepsilon \tag{C.42}$$

and finally

$$\sigma_{n+1}^{k+1} = \sigma_{n+1} + d\sigma \tag{C.43}$$

which now detaches from the Yield surface, extending in the inelastic region.

In reverse mode, the lifetime model discussed in Section 4.3.6 seeds the

increment in total strains $\Delta\varepsilon^{tot} = \Delta\varepsilon^{e} + \Delta\varepsilon^{p}$. If in primal mode the reference finite element at the determined time step presented an elastic behavior, the development would follow the standard reverse algorithmic differentiation of $\Delta\varepsilon^{e}$ discussed in Section 4.4.2. Instead, in case of an inelastic occurrence, the routine in post-processing of the displacements field updated by Eq. (C.38) comes into play.

Starting from the differentiated Morrow model, the algorithmic differentiation of the p-norm functions in Eq. (4.12) and of the averaging function for the stresses results in the following

$$\begin{cases} \overline{\Delta\varepsilon}^{tot} & \rightarrow \quad \bar{\varepsilon} \\ \bar{\sigma}_{mean} & \rightarrow \bar{\sigma} \end{cases} . \tag{C.44}$$

The adjoint stresses in Eq. (C.44) contribute to seeding Eq. (C.43) and Eq. (C.42):

$$\begin{cases} \overline{d\sigma} = \bar{\sigma}_{n+1}^{k+1} \\ \bar{\sigma}_{n+1} = \bar{\sigma}_{n+1}^{k+1} \end{cases} \tag{C.45}$$

$$\begin{cases} \overline{d\varepsilon} = D\ \overline{d\sigma} \\ \bar{D} = d\varepsilon\ \overline{d\sigma} \end{cases} . \tag{C.46}$$

In Eq. (C.46) both terms contributing to the computation of the stress correction are seeded. Concerning the adjoint elastoplastic tangent matrix, it brings contributions to the stresses through the first order and second order derivatives of the Yield surface *F*. Hence, the accumulation of sensitivities of the stresses follows the reverse algorithmic differentiation of the derivatives of Eq. (C.24), omitted here for sake of simplicity.

Instead, the adjoint strain correction $\overline{d\varepsilon}$ is propagated backwards to seed the strain increments computed upstream and downstream the system solve in Eq. (C.38):

$$d\varepsilon = {\Delta\varepsilon_{n+1}}^{k+1} - {\Delta\varepsilon_{n+1}}^{k} \quad \rightarrow \quad \begin{cases} \overline{\Delta\varepsilon}_{n+1}^{k+1} = \overline{d\varepsilon} \\ \overline{\Delta\varepsilon}_{n+1}^{k} = \overline{d\varepsilon} \end{cases} . \tag{C.47}$$

The second equation in (C.47) seeds the total strain increment directly obtained by the FEM liner solve. Instead, the first equation seeds the total strain increment computed in post-processing of the system in (C.38). Hence, the algorithmic differentiation of such post-processing routine returns the adjoint displacements $\bar{u}_{n+1}$.

From the system in (C.38) and the reverse differentiation procedure discussed in Section B.2, it follows that

$$\begin{gathered} A^{T}\,\bar{b} = \bar{u}_{n+1} \\ with\ A^{T} = A = \frac{1}{\Delta t^{2}} M\ . \end{gathered} \tag{C.48}$$

$\bar{b}$ is the adjoint vector associated to the load at the RHS of (C.38). Hence, it contributes to the adjoint stiffness term as follows

$$\begin{aligned} \bar{Q} &= 2\bar{b} \\ \bar{P}_{n+1} &= -\bar{Q}\,. \end{aligned} \tag{C.49}$$

The stiffness term is algorithmically differentiated in order to obtain the adjoint vector $\bar{\sigma}_{n+1}$, which is accumulated to the sensitivities computed in (C.45). Additionally, contributions to the grid sensitivities $\bar{X}_{sl}$ derive from the differentiation of the terms enclosed in the *B* matrix.

The reverse differentiation of the load vector contributes also to the accumulation of the adjoint displacements $\bar{u}_n$ and $\bar{u}_{n-1}$, as well as to the grid sensitivities and temperature sensitivities, as reported in Section C.5. Similar contributions are also obtained by seeding the LHS matrix *A* in (C.48).

Since in primal mode $\sigma_{n+1} = \sigma_n + \Delta\sigma_{n+1}$ (cf. system in C.35), it turns out that $\overline{\Delta\sigma}_{n+1} = \overline{d\sigma}_{n+1} = \bar{\sigma}_{n+1}$.

Considering the system in (C.35) and the algorithmic differentiation approach discussed in Section C.2, it follows that

$$-C^T\bar{R} = \bar{b} \tag{C.50}$$

with

$$\begin{aligned} C^T &= \begin{bmatrix} E^{-1} + \Delta\lambda F_{,\sigma\sigma} & \Delta\lambda F_{,\sigma\kappa} & F_{,\sigma} \\ \Delta\lambda F_{,\kappa\sigma} & \boldsymbol{H}^{-1} + \Delta\lambda F_{,\kappa\kappa} & F_{,\kappa} \\ F_{,\sigma}^T & F_{,\kappa}^T & -H_i \end{bmatrix}^T \\ \bar{b} &= \begin{Bmatrix} \overline{d\sigma}_{n+1} \\ 0 \\ 0 \end{Bmatrix}. \end{aligned} \tag{C.51}$$

The system (C.50) returns the adjoint residual vector $\bar{R}$, whose first component is $\bar{R}_\sigma$. Therefore, the reverse differentiation of Eq. (C.30) returns $\overline{\Delta\varepsilon}_{n+1} = \bar{R}_\sigma$, which is accumulated with the adjoint total strain obtained in the second equation of C.47.

Finally, since $\Delta\varepsilon_{n+1} = \varepsilon_{n+1} - \varepsilon_n$, the adjoint total strains are computed:

$$\begin{aligned} \bar{\varepsilon}_{n+1} &+= \overline{\Delta\varepsilon}_{n+1} \\ \bar{\varepsilon}_n &+= \overline{\Delta\varepsilon}_{n+1} \end{aligned} \tag{C.52}$$

In conclusion, $\bar{\varepsilon}_{n+1}$ and $\bar{\varepsilon}_n$ are passed to the post-processing routine of the adjoint structural solver at the two time steps t^n and t^{n+1}, where the accumulation of the contributions to the sensitivities of the displacements field takes place, as anticipated in Section 4.4.3.

C.4 Chaboche fatigue lifetime model

The Chaboche crack-initiation model is an interesting alternative to the Morrow model, as it can surpass the isothermal limitations discussed in Section 4.3.6.

The basic isothermal formulation introduced by Chaboche is the following:

$$N_f = \frac{\sigma_{UTS} - \sigma_{max}}{a\left((\sigma_{max} - \sigma_{mean}) - \sigma_{l_0}(1 - b\sigma_{mean})\right)} \left[\frac{\sigma_{max} - \sigma_{mean}}{C_0(1 - b\sigma_{mean})}\right]^{-\beta}. \quad \text{(C.53)}$$

From Eq. (C.53) it is possible to deduce this fatigue model belongs to the family of "stress life" models. Hence, the number of cycles to failure N_f is referred to the stress amplitude this time, as qualitatively described in Figure C.1. The exemplary curves herein reported are temperature dependent. Moreover, it is possible to perceive there may be some fatigue curves demonstrating an almost flat behavior for high stress amplitudes and at high temperatures. Since it would be difficult to identify a unique solution in this range of low number of cycles, it is evident the preference of analyzing the LCF phenomena through a strain life model (like the Morrow one).

However, the Chaboche model presented in this section may circumvent this issue when the isothermal assumption is relieved, as discussed later.

Concerning the second term in Eq. (C.53), it represents the finite fatigue definition according to Basquin, with β as the Basquin's exponent already encountered in the Morrow model. The numerator in this term expresses the alternating stress, while the denominator returns the intercept of the fatigue curve from Figure C.1 with the y-axis, after a correction for the mean stress over the cycle. In fact, the term C_0 indicates the intercept of the fatigue curve with the y-axis in case of zero mean stress; the coefficient b is a material property standing for its sensitivity to the mean stress correction.

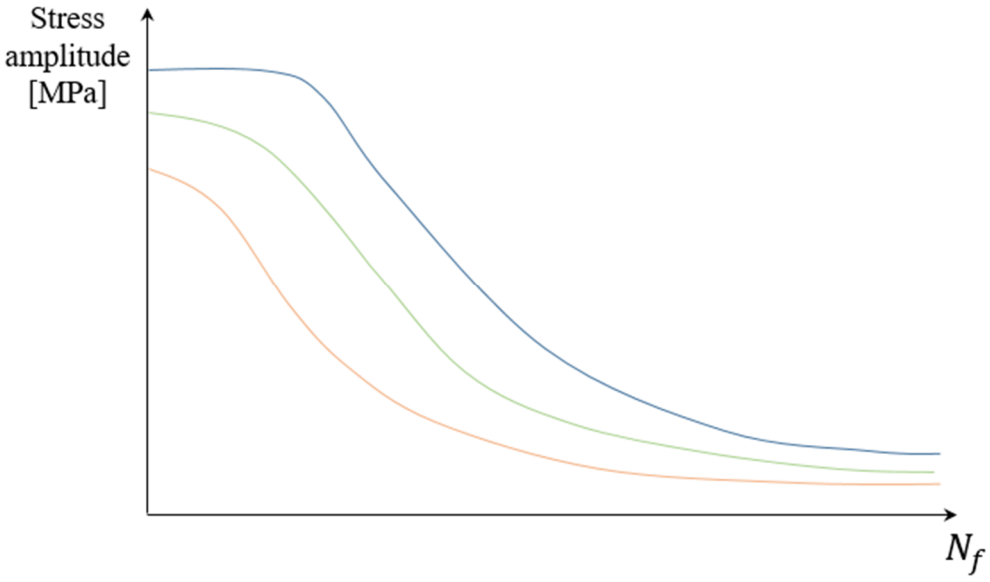

Figure C.1 Qualitative representation of temperature dependent Chaboche fatigue curves.

The first term in Eq. (C.53) is the inverse of the expression representing the

damage evolution. Hence, the lower the accumulated damage, the higher the expected number of cycles to failure. In particular, this fraction presents at the numerator the difference between the limit strength at a specific temperature and the maximum stress along the cycle: if the latter reaches the value of the material limit strength, the component exhibits immediate failure. At the denominator the stress amplitude appears, detracted from the durability limit σ_l (also known as "endurance limit", which is here corrected for the mean stress). The coefficient *a* is typically equal to 0.9.

Hence, it is evident the Chaboche model provides a prediction of the component lifetime which is more grounded on the actual evolution of the thermo-mechanical stresses in the material. Therefore, it may be eligible to replace the simpler Morrow model, provided that the full set of material fatigue properties is available. Unfortunately, it is not the case in the present work, which relies on the dataset pertinent to the strain life model, available in literature [163].

Finally, Chaboche [181] offers a useful means to circumvent the limitations of the isothermal modelling. In particular, all the temperature dependent fatigue curves in Figure C.1 are collapsed in a unique one by application of a temperature compensation. Thus, the concept of "effective stress" is introduced:

$$\sigma' = \frac{\sigma}{P(T)} \tag{C.54}$$

with $P(T)$ indicating the temperature dependent equivalent ratio. Such ratio is specific for each temperature and is necessary to collapse each fatigue curve in Figure C.1 on the unique temperature independent master curve obtained by interpolating all the fatigue data in a unique chart, as qualitatively indicated in Figure C.2.

Hence, the fatigue lifetime from Eq. (C.53) is modified in the following formulation:

$$N_f = \frac{\sigma'_{UTS} - \sigma'_{max}}{a\left((\sigma'_{max} - \sigma'_{mean}) - \sigma'_{l_0}(1 - b\sigma'_{mean})\right)} \left[\frac{\sigma'_{max} - \sigma'_{mean}}{C'_0(1 - b\sigma_{mean})}\right]^{-\beta}, \tag{C.55}$$

in which all the terms with an apex are corrected through the equivalence ratio

$$x' = \frac{x(T)}{P(T)} . \tag{C.56}$$

In reverse mode, the adjoint lifetime $\overline{N}_f$ seeds the TMF model in Eq. (C.55), ending up in the accumulated sensitivities of the effective maximum stress $\overline{\sigma'}_{max}$ and of the effective average stress $\overline{\sigma'}_{mean}$. Such adjoint variables seed the correspondent temperature dependent stresses (i.e. $\overline{\sigma'}_{max}$ and $\overline{\sigma'}_{mean}$) while a contribution to the nodal temperature sensitivities derives from the differentiation of the polynomial representation of the equivalence ratio *P(T)*.

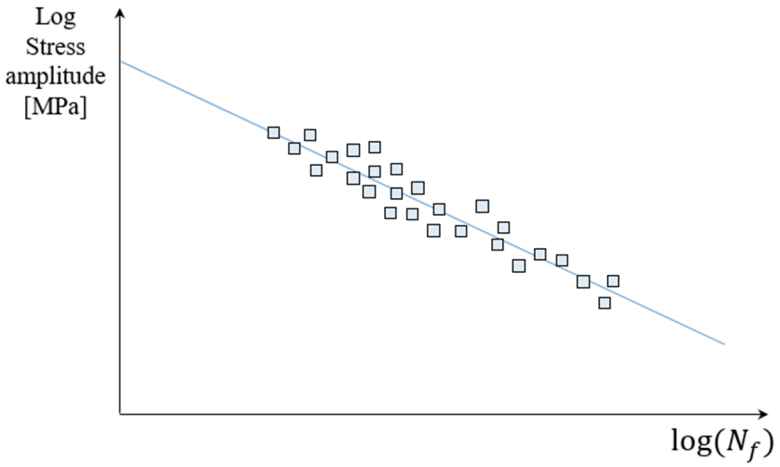

Figure C.2 Qualitative representation of Chaboche master curve for computation of effective stress.

Finally, the adjoint maximum stresses contribute to the accumulation of the sensitivities of the nodal stresses through the differentiation of the p-norm function, while the adjoint mean stresses through the differentiation of the averaging routine. Hence, the field for the FEM mechanical solver is seeded by walking in backward direction the routine discussed in Section C.3.

C.5 Unsteady thermo-mechanical solver: System assembly differentiation

The adjoint unsteady thermo-mechanical solver introduced in Section 4.4.3 delivers in Eq. (4.18) the seeded LHS matrix and RHS vector from the linear system, as repeated here for convenience:

$$\begin{cases} [M + \beta\Delta t^2 S]^T \ \bar{F}_{n+1} \ = \ \bar{a}_{n+1} \\ \overline{[M + \beta\Delta t^2 S]}_{ij} \ = \ -a_{n+1}(j)\ \bar{F}_{n+1}(i) \end{cases} . \tag{C.57}$$

Hence, the differentiation of the system assembly routine results in the contributions to the grid sensitivities and to the temperature sensitivities. Therefore, it follows that

$$\bar{X}_{sl} \mathrel{+}= \ \overline{LHS}\ \frac{dLHS}{dX_{sl}} + \ \bar{F}\ \frac{dF}{dX_{sl}} . \tag{C.58}$$

The differentiation of the LHS matrix accounts for two terms:

$$\frac{dLHS}{dX_{sl}} = \frac{dM}{dX_{sl}} + \ \beta\Delta t^2\ \frac{dS}{dX_{sl}} . \tag{C.59}$$

The first term in Eq. (C.59) is about the differentiation of the mass matrix, which is introduced in Eq. (4.7) as

$$M = \sum_{e} \sum_{n} \sum_{i} \sum_{j} \underbrace{\{w_n[\rho(T)\varphi^T \varphi J_V]\}}_{M_e} . \tag{C.60}$$

Thus, the derivatives w.r.t. the grids coordinates involves only the determinant of the Jacobian matrix of the coordinates transformation J_V.

The second term in Eq. (C.59) refers to the differentiation of the stiffness, as discussed in Eq. (B.21).

The differentiation of the RHS vector involves two terms as well:

$$\frac{dF}{dX_{sl}} = \frac{df_{n+1}}{dX_{sl}} - \hat{u}_{n+1} \frac{dS}{dX_{sl}}. \tag{C.61}$$

The first term in Eq. (C.61) is the differentiation of the load vector f_{n+1}. Since the load vector contains multiple contributions, the differentiation procedure outlines in Section B.3 follows.

The second term in Eq. (C.61) is again the differentiation of the stiffness matrix multiplied by the predictor $\hat{u}_{n+1}$. Hence, Eq. (B.21) is invoked once more.

Therefore, the computation of the contributions to the grid sensitivities is complete.

The evaluation of the temperature sensitivities follows:

$$\bar{T} += \overline{LHS} \frac{dLHS}{dT} + \bar{F} \frac{dF}{dT}. \tag{C.62}$$

The temperature derivatives of the LHS matrix accounts for the derivative of the mass matrix (which reduces to the derivative of the density term in Eq. C.60) and the derivative of the stiffness matrix, in compliancy with Eq. (B.34). Concerning the temperature derivatives of the vector *F*, they comprise the temperature derivatives of the components of the load vector f_{n+1}, as discussed in Eq. (B.35) and (B.36), and the temperature derivatives of the stiffness matrix. Thus, the accumulation of the temperature sensitivities through the adjoint mechanical solver is accomplished.